



Iranian Association of Electrical
and Electronics Engineers



Shahid Chamran
University of Ahvaz

Journal of Applied Research in Electrical Engineering



Vol. 3, No. 1, Winter and Spring 2024



PUBLISHER: SHAHID CHAMRAN UNIVERSITY OF AHVAZ

E-ISSN: 2783-2864

P-ISSN: 2717-414X



**Iranian Association of
Electrical and Electronics
Engineers**

Journal of Applied Research in Electrical Engineering

E-ISSN: 2783-2864

P-ISSN: 2717-414X



**Shahid Chamran
University of Ahvaz**

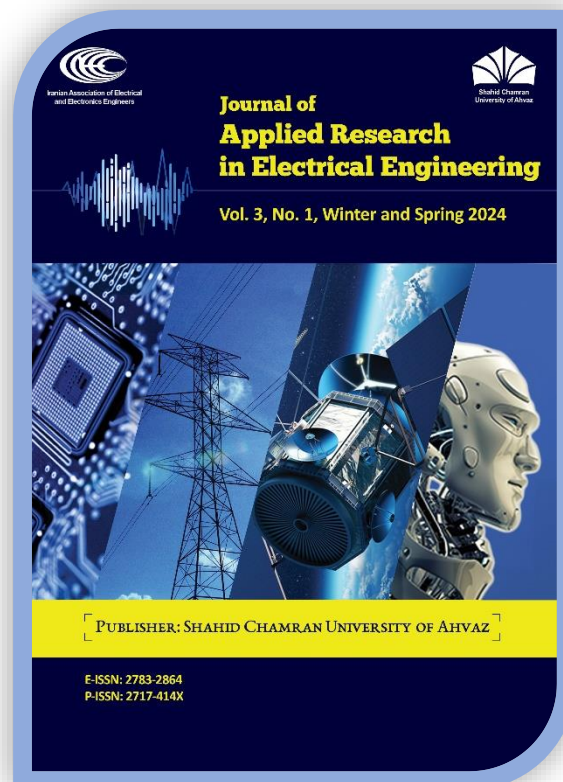
**Journal of Applied Research in Electrical Engineering (JAREE),
Volume 3, Number 1, Winter and Spring 2024**

Publisher: Shahid Chamran University of Ahvaz, Iran

This magazine is the result of a formal partnership of **Shahid Chamran University of Ahvaz** and **Iranian Association of Electrical and Electronics Engineers**

Website: <https://jaree.scu.ac.ir>

E-mails: jaree@scu.ac.ir; jaree.scu@gmail.com



Address: Department of Electrical Engineering, Faculty of Engineering, Shahid Chamran University of Ahvaz, Golestan Street, Ahvaz, Iran

P.O. Box: 61357-85311

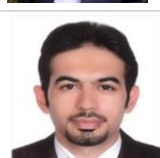
Tel: +986133226782, +989122876375

Fax: +986133226597

Managing Committee and Staff

	<p style="text-align: center;">Editor-in-Chief</p> <p>Prof. Mahmood Joorabian Shahid Chamran University of Ahvaz, Ahvaz, Iran</p> <p><i>Power System Planning, Renewable Energy and Smart Grid, FACTS Devices</i> mjoorabian@scu.ac.ir</p>		<p style="text-align: center;">Director-in-Charge</p> <p>Prof. Seyed Ghodratoollah Seifossadat Shahid Chamran University of Ahvaz, Ahvaz, Iran</p> <p><i>Power System Protection, Power Electronics, Power Quality</i> seifossadat@yahoo.com</p>
	<p style="text-align: center;">Managing Editor</p> <p>Dr. Alireza Saffarian (Associate Professor) Shahid Chamran University of Ahvaz, Ahvaz, Iran</p> <p><i>Power System Protection, Power System Stability, Power Quality, Distribution Systems</i> a.saffarian@scu.ac.ir</p>		<p style="text-align: center;">Executive Assistant</p> <p>Dr. Mohammad Nabipour (Associate Professor) Shahid Chamran University of Ahvaz, Ahvaz, Iran</p> <p><i>Reliability of Power Systems, Microgrids and Distributed Energy Sources, Smart Grids</i> farzin@scu.ac.ir</p>
	<p style="text-align: center;">Associate Editor (Electronics and Telecommunications)</p> <p>Prof. Yousef Seifi Kavian Shahid Chamran University of Ahvaz, Ahvaz, Iran</p> <p><i>Digital Circuits and Systems, Communication Networks and Distributed Systems</i> y.s.kavian@scu.ac.ir</p>		<p style="text-align: center;">Associate Editor (Power and Control)</p> <p>Dr. Mohsen Saniei (Associate Professor) Shahid Chamran University of Ahvaz, Ahvaz, Iran</p> <p><i>Power System Dynamics, High Voltage Engineering, Electricity Market, Microgrid</i> m.saniei@scu.ac.ir</p>
	<p style="text-align: center;">Language Editor</p> <p>Majid Sadeghzadeh Hemayati English Language Editing</p> <p>m_s_hemayati@yahoo.com</p>		<p style="text-align: center;">Page Designer</p> <p>Mehdi Mohammadian Mehr Shahid Chamran University of Ahvaz, Ahvaz, Iran</p> <p>eng.mohammadianmehr@gmail.com</p>
		<p style="text-align: center;">Executive Director</p> <p>Masoomeh Shaygan Shahid Chamran University of Ahvaz, Ahvaz, Iran</p> <p>masoomeh.shaygan@gmail.com</p>	

Editorial Board

	<p>Prof. Mahmood Joorabian Shahid Chamran University of Ahvaz, Ahvaz, Iran</p> <p><i>Power System Planning, Renewable Energy and Smart Grid, FACTS Devises</i> mjoorabian@scu.ac.ir</p>		<p>Prof. Seyed Ghodratoollah Seifossadat Shahid Chamran University of Ahvaz, Ahvaz, Iran</p> <p><i>Power System Protection, Power Electronics, Power Quality</i> seifossadat@yahoo.com</p>
	<p>Prof. Saeedallah Mortazavi Shahid Chamran University of Ahvaz, Ahvaz, Iran</p> <p><i>Intelligent Control Systems, Power System Control, Automation, Fuzzy Logic, Neural Networks</i> mortazavi_s@scu.ac.ir</p>		<p>Prof. Abdolnabi Kosarian Shahid Chamran University of Ahvaz, Ahvaz, Iran</p> <p><i>Solid State Electronic Devices, Solar Cell Fabrication Technology</i> a.kosarian@scu.ac.ir</p>
	<p>Prof. Ebrahim Farshidi Shahid Chamran University of Ahvaz, Ahvaz, Iran</p> <p><i>Analog and Digital Integrated Circuits, Data Converters, Microelectronics</i> farshidi@scu.ac.ir</p>		<p>Prof. Naser Pariz Ferdowsi University of Mashhad, Mashhad, Iran</p> <p><i>Nonlinear Control, Hybrid Systems, Aeronautics, Industrial Control, Applied Mathematics</i> n-pariz@um.ac.ir</p>
	<p>Prof. Yousef Seifi Kavian Shahid Chamran University of Ahvaz, Ahvaz, Iran</p> <p><i>Digital Circuits and Systems, Communication Networks and Distributed Systems</i> y.s.kavian@scu.ac.ir</p>		<p>Dr. Mohsen Sanieci (Associate Professor) Shahid Chamran University of Ahvaz, Ahvaz, Iran</p> <p><i>Power System Dynamics, High Voltage Engineering, Electricity Market, Microgrid</i> m.sanieci@scu.ac.ir</p>
	<p>Prof. Reza Ghaderi Shahid Baheshti University, Tehran, Iran</p> <p><i>Control Theory, System Identification, Control Systems, Fuzzy Engineering</i> r_ghaderi@sbu.ac.ir</p>		<p>Dr. Edris Pouresmaeil (Associate Professor) Aalto University, Espoo, Finland</p> <p><i>Integration of Renewable Energies into the Power Grid</i> edris.pouresmaeil@aalto.fi</p>
	<p>Prof. Abbas Zarifkar Shiraz University, Shiraz, Iran</p> <p><i>Optical Electronics</i> zarifkar@shirazu.ac.ir</p>		<p>Prof. Fushuan Wen Tallinn University of Technology, Tallinn, Estonia</p> <p><i>Power Systems and Power Economics</i> fushuan.wen@taltech.ee</p>
	<p>Prof. Majid Sanaye-pasand University of Tehran, Tehran, Iran</p> <p><i>Power Systems Protection, Digital Protective Relays, Power Systems Automation, Power System Transients</i> msanaye@ut.ac.ir</p>		<p>Prof. Zabih (Fary) Ghassemlooy North Umbria University, Newcastle upon Tyne, United Kingdom</p> <p><i>Optical Communications, Visible Light, Communication Systems</i> z.ghassemlooy@northumbria.ac.uk</p>
	<p>Prof. Mahdi Tavakoli University of Alberta, Alberta, Canada</p> <p><i>Robotics and Telerobotics, Haptics and Teleoperation Control, Surgical and Therapeutic Robotics, Image-Guided Surgery</i> mahdi.tavakoli@ualberta.ca</p>		<p>Prof. Mohamad Hassan Modir Shanechi Illinois Institute of Technology, Chicago, USA</p> <p><i>Nonlinear and intelligent systems, Power system dynamics and security, Power system planning and maintenance scheduling</i> shanechi@iit.edu</p>
	<p>Prof. Mohammad Shahidehpour Illinois Institute of Technology, Chicago, USA</p> <p><i>Power Systems, Microgrids, Power System Operation, Power System Planning</i> ms@iit.edu</p>		<p>Prof. Gholamreza Akbarizadeh Shahid Chamran University of Ahvaz, Ahvaz, Iran</p> <p><i>Image Processing, Machine Vision, SAR Satellite Imaging Systems and Remote Sensing, Machine Learning and Deep Learning</i> g.akbari@scu.ac.ir</p>
	<p>Prof. Mohammad Soroosh Shahid Chamran University of Ahvaz, Ahvaz, Iran</p> <p><i>Photonic Crystals, Optoelectronics, Plasmonic Devices, Graphene, Photodetectors</i> m.soroosh@scu.ac.ir</p>		<p>Dr. Alireza Saffarian (Associate Professor) Shahid Chamran University of Ahvaz, Ahvaz, Iran</p> <p><i>Power System Protection, Power System Stability, Power Quality, Distribution Systems</i> a.saffarian@scu.ac.ir</p>

About Journal

Journal of Applied Research in Electrical Engineering (J. Appl. Res. Electr. Eng.) is a single-blind peer-reviewed, **open access** and **free of charge** international journal published by Shahid Chamran University of Ahvaz in cooperation with Iranian Association of Electrical and Electronics Engineers (IAEEE). The JAREE is a medium for global academics to exchange and spread the latest discoveries and advances in their applied research in electrical engineering. The JAREE aims at presenting important results of analytical, computational and experimental works within all specialized fields of electrical engineering (electronics, power, control and telecommunications). It welcomes high quality original research papers from contributors throughout the world. All papers are subject to a peer reviewing procedure. Submission, processing and publication of the papers in JAREE is **free of charge**.

Types of accepted papers include:

- Research articles
- Review articles
- Applied articles

Research papers are expected to present innovative solutions, novel concepts, or creative ideas that can help to address existing or emerging technical challenges in electrical engineering.

Application papers are expected to share valuable industry experiences on dealing with challenging technical issues, developing/adopting new standards, applying new technologies or solving complex problems. JAREE welcomes application papers that can have a significant impact on industry practices in the coming years.

Review papers are expected to provide insightful and expert reviews, tutorials, or study cases on an important, timely and widely-interested topic in electrical engineering.

All researchers in the fields of electrical science are invited to publish their scientific and research achievements in this journal. Interested authors can submit their manuscripts in the journal's website. More information is available in the website on how to prepare and submit the manuscripts.

Amis and Scope

The *Journal of Applied Research in Electrical Engineering* aims to provide a medium for dissemination of innovative and consequential papers that present analytical, computational and experimental works within all specialized fields of electrical engineering (electronics, power, control and telecommunications). The scope of the journal includes, but is not limited to, the following topic areas:

Electronics:

- Optical electronics, photonics and solar cells
- Integrated analog circuits and mixed signals
- Integrated radio frequency circuits
- Digital electronics (VLSI)
- Semiconductor devices
- Sensor technology

Power:

- Dynamics and stability of the power systems
- Power system protection
- Electric power quality
- Operation and planning of the power systems
- High voltage insulation technology
- Flexible AC Transmission Systems (FACTS)
- Electric power distribution systems
- Smart grids, micro-grids, renewable energies and distributed generation
- Reliability of electrical energy systems
- Energy management and electricity market
- Electric machines and transformers
- Power electronic and electric drives

Control:

- Linear and non-linear control systems
- Adaptive, optimal and stochastic control
- Fuzzy systems, neural networks and intelligent control
- Robotic and mechatronic
- Modeling, Identification and optimization of systems
- Guidance and navigation systems
- Automation, industrial control and instrumentation

Telecommunications:

- Signal and image processing
- Wireless and cellular communication systems
- Telecommunication networks
- Radar and sonar
- Information theory and coding
- Cognitive radio
- Antenna design
- Microwave devices
- Wave propagation and electromagnetic compatibility

Indexing Databases and Social Networks

	<p>Islamic World Science Citation Center (ISC): https://mjil.isc.ac/Searchresult.aspx?Cond=2&SrchTxt=27832864</p>
	<p>Iran Ministry of Science, Research and Technology Scientific Journals: (Journal Rank: International) https://journals.msrt.ir/home/detail/16058/</p>
	<p>Directory of Open Access Journals (DOAJ): https://doaj.org/toc/2783-2864</p>
	<p>Google Scholar: https://scholar.google.com/citations?user=F7KQPtYAAAAJ&hl=en&authuser=1</p>
	<p>Directory of Open Access Scholarly Resources (ROAD): https://portal.issn.org/resource/ISSN/2783-2864</p>
	<p>Elton B. Stephens Company (EBSCO): https://jaree.scu.ac.ir/news?newsCode=204</p>
	<p>CIVILICA: https://en.civilica.com/I/140583/</p>
	<p>National Publications Information Bank (magiran): https://www.magiran.com/magazine/8471</p>
	<p>Digital Object Identifier (DOI): https://www.doi.org/</p>
	<p>LinkedIn: https://www.linkedin.com/in/journal-of-applied-research-in-electrical-engineering-jaree-7540871b2/</p>
	<p>Academia: https://shahidchamranahwaz.academia.edu/JournalAppliedResearchinElectricalEngineering</p>
	<p>Mendeley: https://www.mendeley.com/profiles/journal-of-applied-res-in-electrical-engineer/</p>
	<p>Twitter: https://twitter.com/jaree_scu</p>
	<p>Facebook: https://www.facebook.com/jaree.scu</p>
	<p>Researchgate: https://www.researchgate.net/profile/Jaree_Engineering</p>
	<p>Telegram: https://t.me/jareescu</p>
	<p>Instagram: https://www.instagram.com/jaree.scu/</p>
	<p>Journal homepage: https://jaree.scu.ac.ir</p>

Guide for Authors

How to submit a manuscript

For the initial submission, the authors have to just send the main manuscript file and the signed [Copyright Form](#) of the journal. While preparing manuscripts for initial submission, authors are kindly requested to follow the guidelines, described below:

- The manuscript should be written in a Microsoft Word file (.doc or .docx).
- The file should include text (preferably in 10 points, “Times New Roman” font) and all figures (figures can be placed within the text at the appropriate point or at the end of the text).
- The manuscript pages should be prepared either using a double-column single-line spacing layout or a single-column double-line spacing layout. A margin of at least 1.5 cm on each side is required.
- All papers should be composed of Title, Author Name, Affiliation, Corresponding author email, Abstract, Keywords, Body, and References.
- The manuscript should be written in good English. It should have been carefully checked for clarity, conciseness, the correctness of grammar, and typographical errors.
- The corresponding author should sign the journal copyright form on behalf of any and all co-authors and upload it to the Journal’s Submission System when submitting the manuscript. The journal copyright form can be downloaded from [here](#).
- The corresponding author can use the [JAREE Template for Cover Letter](#) as a default text for the cover letter when submitting the manuscript.
- It is recommended that the title of the paper does not contain abbreviations or formulae.
- The abbreviations used in the abstract should be introduced both in the abstract and again on first use in the body.
- References should be numbered in the order they are mentioned in the text.

Manuscript Submission

Submission to this journal proceeds totally online and you will be guided stepwise through the creation and uploading of your files. All correspondence, including notification of the Editor's decision and requests for revision, takes place by e-mail. To submit your manuscript, click on the [Submit Manuscript](#) link on the journal's homepage. Then, click on [Register](#) to create an author account. A message is sent to your email address containing your username and password. Then, login to the Journal’s Submission System at the [User's login](#) page using the username and password to submit your new manuscript. Once you have logged in, you can change your password by clicking on the My Home link at the top menu.

Copyright and Open Access License

An author submitting a paper should ensure that he or she has the right to publish the paper and that it contains nothing defamatory. The JAREE will assume that all co-authors have agreed to the submission of any paper received. The corresponding author should sign the journal copyright form on behalf of any and all co-authors and upload it to the Journal’s Submission System when submitting the manuscript.

Contents

Article Title and Authors	Page No.
Improving the Performance of a VSG in the Distorted Grid Using Third-Order Generalized Integrator Ramin Arjmandzadeh, Mahdi Banejad, Ali Akbarzadeh Kalat	1
Voltage and Frequency Control Considering Disturbance in Input Power of DG Ali Morsagh Dezfuli, Mahyar Abasi, Mohammad Esmail Hasanzadeh, Mahmood Joorabian	9
Solving Combined Economic Emission Dispatch Problem Using the Rain Optimization Algorithm Narges Yousefi, Mahmood Joorabian, Mahyar Abasi	19
A New Topological Method for Output Voltage Clamping of Immittance-based Constant Current Load Resonant Converters Alireza Khoshsaadat, Mohammad Abedini	33
Analysis of the Potential of Different Air Conditioner Brands for Piezoelectric Energy Harvesting Daniel Kwegyir, Francis Boafu Effah, Daniel Opoku, Peter Asigri, Yoosi Hayford, Eliezer Owusu Boateng, Kwaku Kessey-Antwi, Nana Maryam Abdul-Bassit Munagah, Kelvin Worlanyo Tamakloe	40
Efficient Responding to Demand and Robust Voltage Control of an Islanded DC Microgrid Under Variations in Load and Supply Sajed Derakhshani Pour, Reza Eslami	51
Conventional DC-DC Converters Through Duality Approach for Current-Based Applications Zahra Gholami, Rahim Ildarabadi, Hamed Heydari-doostabad	64
Consensus-Based Algorithm for Distributed Continuous-Time Convex Optimization Over Undirected and Directed Networks Ehsan Nazemorroaya, Mohsen Shafieirad, Mahdi Majidi, Mahdiah Adeli	74
Improvement of IBC-SHJ Solar Cell Efficiency Based on Back Contacts Geometry Engineering Pegah Paknazar, Maryam Shakiba, Gholamreza Shaloo	83
Demand Response Design for Healthy Operation of Transformers in Heavy-Load and High-Temperature Conditions Arash Moghadami, Davood Azizian, Amin Karimi	90
Assessing Power System Adequacy and Generation Expansion Planning in the Presence of Wind Power Plants Considering Uncertainties in the DIgSILENT Software Environment Hamid Reza Safa, Ali Asghar Ghadimi, Mohammad Reza Miveh	99
Reliability Evaluation of Power Systems Including Pumped-Storage Generation Units Amir Ghaedi, Mehrdad Mahmoudian	110

Copyrights

© 2024 Licensee Shahid Chamran University of Ahvaz, Ahvaz, Iran. This article is an open-access article distributed under the terms and conditions of the Creative Commons Attribution –Non-Commercial 4.0 International (CC BY-NC 4.0) License (<http://creativecommons.org/licenses/by-nc/4.0/>).





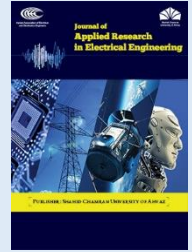
Iranian Association of
Electrical and Electronics
Engineers

Journal of Applied Research in Electrical Engineering

E-ISSN: 2783-2864

P-ISSN: 2717-414X

Homepage: <https://jaree.scu.ac.ir/>



Research Article

Improving the Performance of a VSG in the Distorted Grid Using Third-Order Generalized Integrator

Ramin Arjmandzadeh, Mahdi Banejad ^{*} , and Ali Akbarzadeh Kalat 

Faculty of Electrical Engineering, Shahrood University of Technology, Shahrood, Iran

** Corresponding Author: m.banejad@shahroodut.ac.ir*

Abstract: In conventional power systems, most of the power is produced by synchronous generators in the electric grid that have heavy and rotating rotors. As a result, there is an inherent inertia in the rotor of these generators. The presence of inertia in the grid prevents sudden frequency changes during imbalance situations, thus, the frequency stability of the grid is maintained. Today, with the increase of renewable energy sources that are usually connected to the network by power electronic equipment. Such resources do not have rotating materials, therefore, the overall inertia of the grid decreases and the stability of the system deteriorates. To solve the problem of lack of inertia in the power electronic-based grid, the notion of the virtual synchronous generator (VSG) technology has been introduced in recent years. This technology can imitate the behavior of traditional synchronous generators for inverters connected to the grid. In this way, the inverters connected to the grid act like a synchronous generator during imbalance. One of the problems associated with the converters-based microgrid is the existence of DC deviations and additional harmonics, which disrupt the work of the converters. Therefore, in this article, a third-order generalized integrator (TOGI)-based VSG for grid-connected inverters is employed so that the system stability is maintained in the conditions of additional harmonics and DC deviation. To show the effectiveness of the proposed method, time domain simulations have been performed in Simulink/MATLAB software. The results of the simulation verify the performance of the proposed method.

Keywords: Virtual synchronous generator, grid stability, distributed resources, dc deviations, additional harmonics.

Article history

Received 24 November 2023; Revised 11 December 2023; Accepted 05 January 2024; Published online 05 March 2024.

© 2024 Published by Shahid Chamran University of Ahvaz & Iranian Association of Electrical and Electronics Engineers (IAEEE)

How to cite this article

R. Arjmandzadeh, M. Banejad, and A. Akbarzadeh Kalat, "Improving the performance of a VSG in the distorted grid using third-order generalized integrator," *J. Appl. Res. Electr. Eng.*, vol. 3, no. 1, pp. 1-8, 2024.

DOI: 10.22055/jaree.2024.45355.1091



1. INTRODUCTION

In traditional power systems, synchronous generators with heavy and rotating rotors are commonly used to generate power. The rotational motion of these rotors is primarily responsible for providing the inertia for the entire power systems inertia, which is crucial for maintaining stability. When there is an imbalance between power generation and consumption within the grid, the speed of the rotor adjusts to accommodate this imbalance, resulting in frequency deviations. However, due to the inherent inertia of these rotors, sudden changes in speed are prevented, ensuring the stability of the network's frequency. Besides inertia, another key factor is the damping coefficient resulting from

mechanical friction and electrical losses in the motor of synchronous generators. This can significantly impact the stability of the electrical network. Currently, there is a global shift toward utilizing more renewable resources in power systems. As distributed energy sources are increasingly connected to grids via power electronic devices, which usually do not have inherent inertia, the overall rotational inertia of the network is decreasing. This is because renewable resources are usually interfaced through electronics that lack of the physical spinning components compared to traditional synchronous generators that have rotational masses.

As inertia levels decrease across the grid, it becomes more sensitive to disturbances and imbalances. The network

reacts faster to these disturbances, posing greater stability challenges for the system. Even minor imbalances causes cascading failures, widespread blackouts, and the need for power outages. One solution to enhancing stability under these conditions is providing virtual inertia from non-inertial resources. Recent work has acknowledged virtual synchronous generators as an approach that can mimic the behavior of a synchronous generator using power inverters connected to the network. By emulating synchronous generator characteristics, non-inertial sources act similarly to high inertia synchronous machines, compensating for the lack of physical rotating masses. This helps stabilize grid frequency in the cases of electrical disturbance [1].

By adjusting key parameters such as virtual inertia and damping rate, the output reaction of a VSG can be altered. The experts have examined different control setups with the goal of eliminating fluctuations in both power and frequency. A variety of control architectures have been evaluated as a way to reduce variations and keeping stability through the VSG response. By modifying the virtual inertia and damping emulated by the inverter, the VSG output response can be tailored to best maintain system frequency and power transfer under varying conditions of the electrical network. The virtual inertia and damping have been modeled by the inverter can allow the VSG to adapt its behavior by changing grid situations [2, 3]. A general overview and detailed investigation of various VSG designs and their structures have been given in [4], that has outline different VSG models as well as an in-depth discussion of their architectures. The concept of adaptive virtual inertia has been introduced in [5], which can effectively suppress the power and frequency fluctuations in VSGs. A small signal model of the VSG control loop has been analyzed to tune parameters in [6], obtaining optimal inertia (J) and damping (D) values. Also, in [7], the problems of designing VSG parameters have been discussed and a method based on Lyapunov has been presented for designing VSG parameters. A VSG-based approach has been presented in [8] to address the reduced inertia challenge in distribution grids. In this reference a virtual inertial control has been developed to increase the inertia of a DC microgrid and reduce voltage fluctuation rates. The VSGs can produce significant damping torque to eliminate low-frequency oscillations in grids [9]. The inertia response characteristics of permanent magnet wind energy conversion systems using VSG control have been evaluated and comparing them to synchronous generators in in [10]. While virtual resistance helps synchronous resonance suppression, it has negative impacts on VSG transient stability [11]. As a result virtual resistance effects on transience has been investigated in this reference and has been proposed a method for suppressing transient fluctuations using virtual resistance. A microgrid model with several VSGs and real synchronous generators have been used in [12] to define the voltage angle deviations from the center of inertia angle to analyze transient stability. Also, in [13], a control method has been presented to improve transient power angle stability (TPAS) and suppression fault current when a fault occurs in the grid.

As mentioned earlier, in recent times, there has been significant growth in grid-connected microgrid systems driven by the need to improve renewable energy availability and reliability during high demand periods. To ensure

accurate synchronization of renewable sources with the main grid, Phase-Locked Loop (PLL) controllers have emerged as a key solution [14]. The PLL technique is one of the most widely used and established methods for synchronization in power systems [15]. However, if DC deviation components exist in the voltage and current signals, they can induce frequency and phase fluctuations estimated by the PLL. Eliminating these low frequency oscillations has posed a challenge [16].

The novelty of this paper is to use a VSG-based control method for grid-connected inverters is which can provide virtual inertia for new microgrids, it can also maintain the stability of the system and enhances the stability of dynamics of the system in the presence of DC deviation component and additional harmonics in the voltage and current VSG signals. In this design, instead of the voltage and current signals being used directly to calculate the power, first they pass through a TOGI and the harmonic and DC deviation removal operation takes place, and then the signals without DC deviation and additional harmonics are used to calculate the transmitted power.

The remaining Sections of the article are organized as follows: Section 2 provides a concise conceptual description and overview of the general structure of a VSG. Section 3 introduces a proposed method aiming at eliminating the DC deviation component from VSG signals, ensuring that its performance remains unaffected. Section 4 focuses on carrying out the time domain simulations based on the principles outlined in Section 3, validating the effectiveness of the proposed approach through simulation results. Finally, Section 5 concludes the article, summarizing the key findings and implications of the study.

2. GENERAL CONCEPT AND STRUCTURE OF A VSG

Fig. 1 illustrates the concept of a VSG. Based on the information depicted in this figure, it can be inferred that distributed energy sources like solar and wind energy can be regarded as providing the necessary energy that is an analogy to the rotor of synchronous generators. Additionally, inverters can be viewed as analogous to synchronous generators within the framework of VSG, according to the principles of VSG, when the VSG control method and theory are implemented in all grid-connected inverters, they can be treated collectively as an equivalent synchronous generator [17]. VSG is comprised of three primary components. An inverter, an energy storage system typically utilizing capacitors, and VSG control, as depicted in Fig. 2. When an imbalance in power occurs within the grid, the capacitor is utilized to either release or store energy. Thereby preventing frequency deviations. If power consumption exceeds generation, the required power is drawn from the capacitor. Conversely, if generation surpasses consumption, the surplus energy is stored in the capacitor. This process is controlled by the VSG control. The VSG control Section incorporates the oscillation equation of synchronous generators, which can be expressed as follows:

$$P_0 - P_e + D(\omega_0 - \omega) = J\omega \frac{d\omega}{dt} \quad (1)$$

where, P_0 , P_e , D , J , ω and ω_0 are the active power reference, VSG active power, damping coefficient, virtual inertia, VSG angular frequency and nominal frequency, respectively.

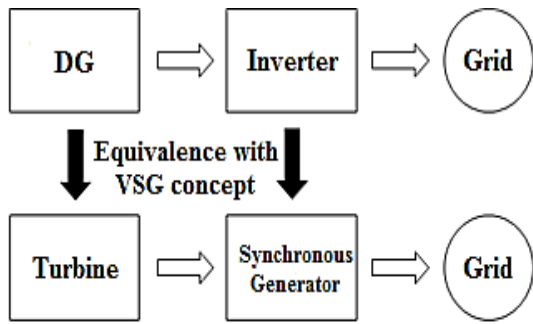


Fig. 1: Concept of a VSG.

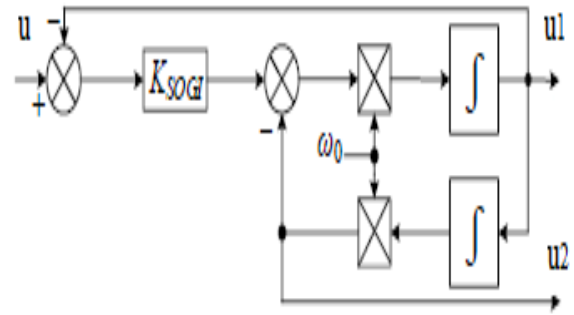


Fig. 3: General structure of a SOGI.

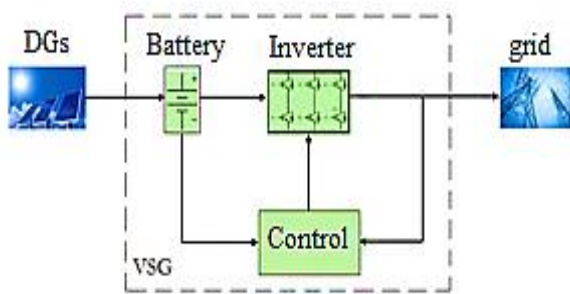


Fig. 2: General structure of a VSG.

3. PROPOSED METHOD FOR REMOVING THE DC DEVIATION COMPONENT AND ADDITIONAL HARMONICS TO IMPROVE VSG PERFORMANCE

As stated previously, the PLL plays a crucial role in the synchronization and closed-loop control of single-phase grid-connected systems (SPGCS), including photovoltaic systems, fuel cells, batteries, and wind systems [18, 19]. PLLs are responsible for accurately detecting the frequency and phase angle, which directly impacts the power quality, reliability, and stability of SPGCS [20]. The second-order generalized integrator (SOGI) algorithm depicted in Fig. 3 is considered one of the most effective PLL techniques for converters is being connected to a single-phase grid. In Fig. 3, u , K_{SOGI} , and ω_0 are the input signal, damping coefficient, and resonance frequency, respectively.

When examining the output signals u_1 and u_2 in TPFI, it is observed that they possess identical amplitudes but exhibit a phase shift of 90 degrees. Both u_1 and u_2 share the same amplitude and phase characteristics. However, in the presence of a DC offset component within the input signal, a notable distinction emerges. Specifically, u_1 has no DC offset while u_2 is significantly influenced by the DC offset. This discrepancy in behavior can pose challenges and complications in some cases.

The existence of a DC offset in PLL input is a fundamental issue due to inducing frequency fluctuations in the acquired phase and frequency [21, 22]. The detrimental impact of DC offset components in the grid voltage on synchronization unit performance is evident. It manifests as oscillatory behavior and offset errors in the estimation of grid information [23]. DC offset can arise from: voltage sensor offsets, disparities between semiconductor devices. A/D conversion and so on. To tackle this problem, this section

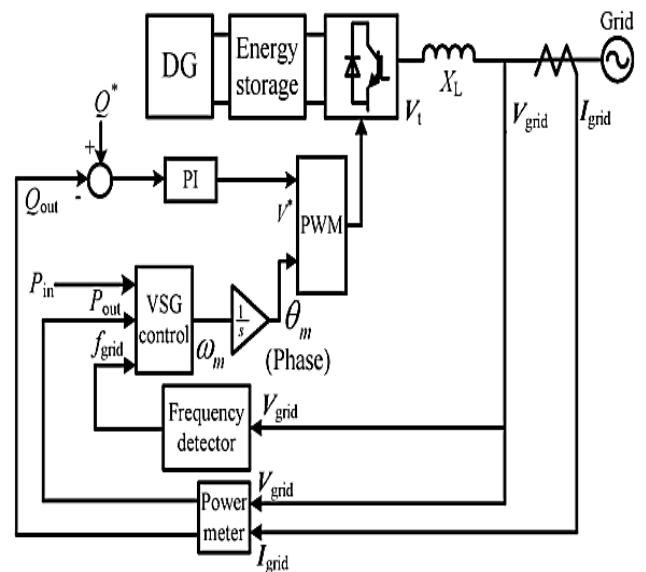


Fig. 4: General block diagram of a simple VSG.

introduces a method for eliminating the DC offset from the output voltage and current signals of VSG. Fig. 4 illustrates the general block diagram of a simplified VSG, serving as a visual representation for further discussion.

In the power calculation section, VSG power is calculated as follows:

$$P_{out} = V_a I_a + V_b I_b + V_c I_c \quad (2)$$

$$Q_{out} = \frac{1}{\sqrt{3}} (I_a (V_b - V_c) + I_b (V_c - V_a) + I_c (V_a - V_b)) \quad (3)$$

where V_a , V_b , and V_c are the voltages of phase a, b, and c, respectively, and I_a , I_b , and I_c are also the currents of phase a, b, and c. If there is a DC deviation in any of the parameters mentioned in (2) and (3), it can introduce calculation errors in power calculations. These errors can propagate through the VSG control cycle, leading to successive errors and potential instability. The dynamical coupling between frequency and voltage of a VSG a has been studied in [25]. In this reference a unified model is presented to study the voltage and frequency analysis. In reference [26], TOGI algorithm is introduced to address DC deviations in single-phase systems. The TOGI algorithm eliminates the influence of the DC offset component in u_2 by incorporating an additional loop to the SOGI. In this article, the TOGI-based

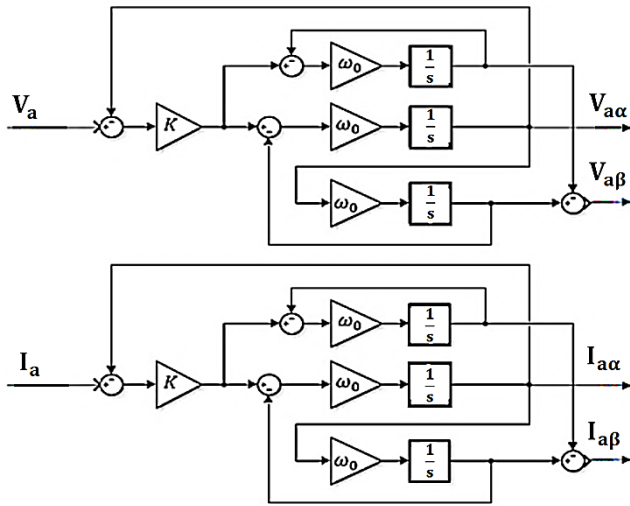


Fig. 5: Extraction of phase a $\alpha\beta$ components by TOGI in a VSG [26].

algorithm is utilized to generate the $\alpha\beta$ axes of voltage and current for the VSG, enabling the extraction of the fundamental components of voltage and current and facilitating power calculation. To achieve this, six TOGIs are employed, with two TOGIs per phase (one for voltage and one for current). Fig. 5 illustrates the process of extracting the $\alpha\beta$ components of phase (a) voltage and current using the TOGI-based algorithm. Similarly, TOGI is considered in phases b and c. In this case, the VSG active and reactive powers can be calculated as follows.

$$P_{out} = \frac{(V_{a\alpha}I_{a\alpha} + V_{a\beta}I_{a\beta})}{2} + \frac{(V_{b\alpha}I_{b\alpha} + V_{b\beta}I_{b\beta})}{2} + \frac{(V_{c\alpha}I_{c\alpha} + V_{c\beta}I_{c\beta})}{2} \tag{4}$$

$$Q_{out} = \frac{(V_{a\alpha}I_{a\beta} + V_{a\beta}I_{a\alpha})}{2} + \frac{(V_{b\alpha}I_{b\beta} + V_{b\beta}I_{b\alpha})}{2} + \frac{(V_{c\alpha}I_{c\beta} + V_{c\beta}I_{c\alpha})}{2} \tag{5}$$

Using this approach, the VSG active and reactive powers are computed independent of any DC deviations, ensuring the delivery of power to the load with the desired quality and enhancing the system's stability. The modified version of Fig. 4 is represented as Fig. 6, incorporating the suggested method.

4. SIMULATIONS

Simulations are carried out using the Simulink/MATLAB software. This analyzes and compares the transient performance, steady state characteristics, and stability of the system in different sections, in comparison to conventional VSG control. The VSG was connected to the grid and operated alongside a local load of 15KW, with the simulation duration set for 6 seconds. Two scenarios are considered to evaluate the proposed design. The first scenario involved the presence of unwanted DC deviations in the VSG voltage and current signals. The second scenario is the connection of the studied VSG to a harmonic grid. Therefore, the proposed design should be able to perform well in both of these scenarios and maintain the stability of the system.

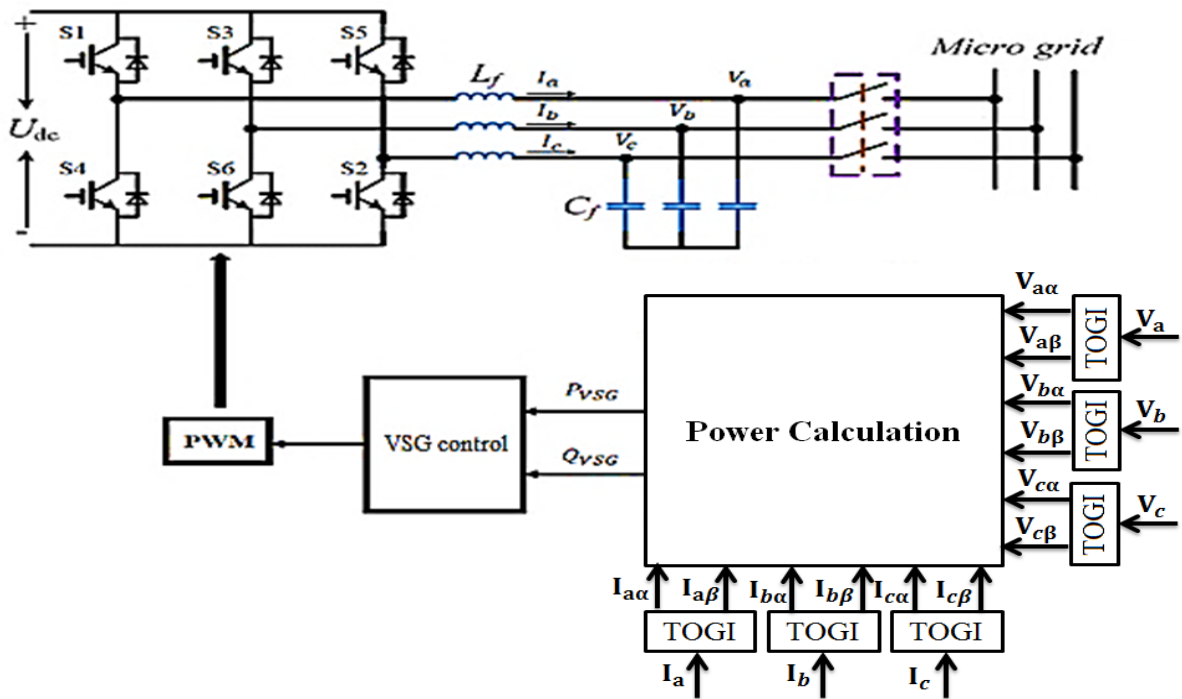


Fig. 6: Proposed VSG control scheme.

The simulation parameters for the proposed VSG are provided in Table 1. To assess the implementation and effectiveness of the proposed strategy, time domain simulations are conducted in the following under scenarios involving DC deviations in VSG voltage and current signals, as well as a harmonically distorted with harmonic content.

4.1. Scenario 1: DC Deviation in the Voltage and Current VSG Signals

In this Section, both the proposed VSG and conventional VSG are simulated while voltage and current signals have DC deviation and the results of the simulations are then compared. DC deviation can cause grid instability. Therefore, the proposed VSG should be able to reduce the effect of DC deviation. In 2.5s, a DC deviation is injected in the phase a voltage of both controllers (proposed VSG and normal VSG). The value of this deviation is 100V. Fig. 7 and Fig. 8 show the system frequency and output power of VSGs, respectively. As it can be seen from these figures, the proposed TOGI-based method removes the DC deviation value from its signals.

It becomes stable with an acceptable transient and follows its reference values without any fluctuations. However, the DC deviation greatly affected the control performance of conventional VSG. The performance of this controller fluctuates greatly in these conditions and even the frequency and power fluctuate outside the allowed range. This is despite the fact that the DC deviation occurred with a relatively low amplitude and only in phase (a). If it occurs in other phases with higher amplitudes, it can worsen the situation.

4.2. Scenario 2: Performance of the Proposed VSG Connected to a Harmonically Grid

In scenario 2, the simulations are carried out for both the proposed VSG and conventional VSG in the presence of a harmonic grid. The grid to which the VSG is connected is considered to have a third order harmonic with an amplitude of 0.2pu and a phase of -25 degrees, spanning from 2s to 4s seconds. Both the proposed and conventional VSG controls are connected to this grid, enabling a comparison of their respective responses. Fig. 9 displays the system frequency, while Fig. 10 illustrates the output power of the VSGs. Both figures are for the conditions that the third harmonic is present. These simulation results provide a basis for evaluating the performance and effectiveness of each control approach in the presence of harmonic distortion.

Table 1: Simulation parameters.

Parameter	Value
Nominal frequency	50 Hz
switching frequency	14 KHz
Grid voltage	220 V
DC bus voltage	800 V
Virtual inertia J	0.023
Damping coefficient D	796
Filter inductance L_f	1.5 mH
Filter capacitor C_f	150 μ F

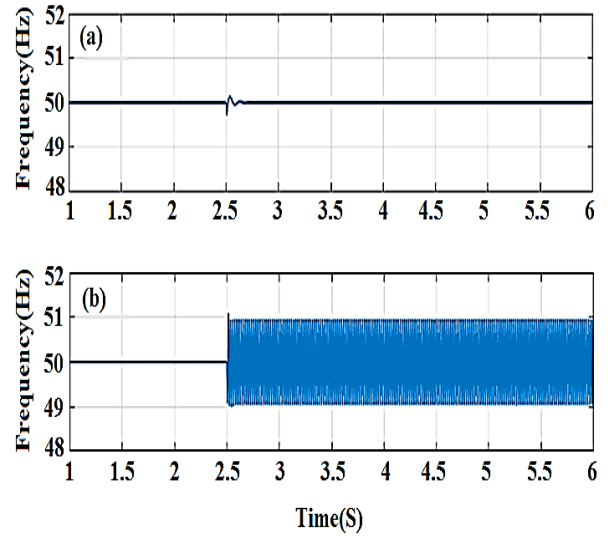


Fig. 7: System frequency: (a) proposed VSG control, (b) conventional VSG control.

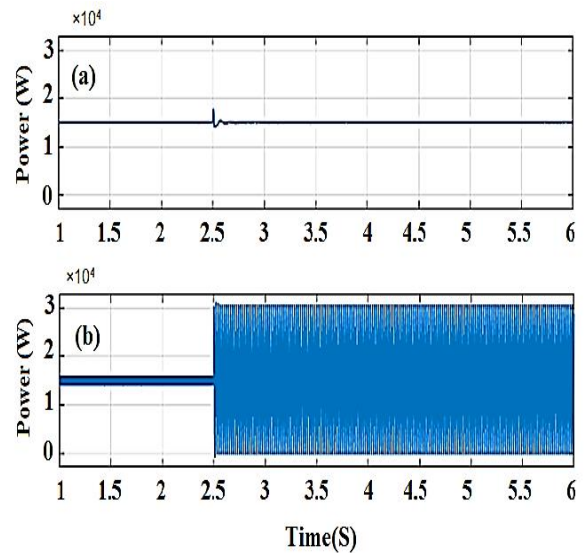


Fig. 8: Output power of VSGs: (a) proposed VSG control, (b) conventional VSG control.

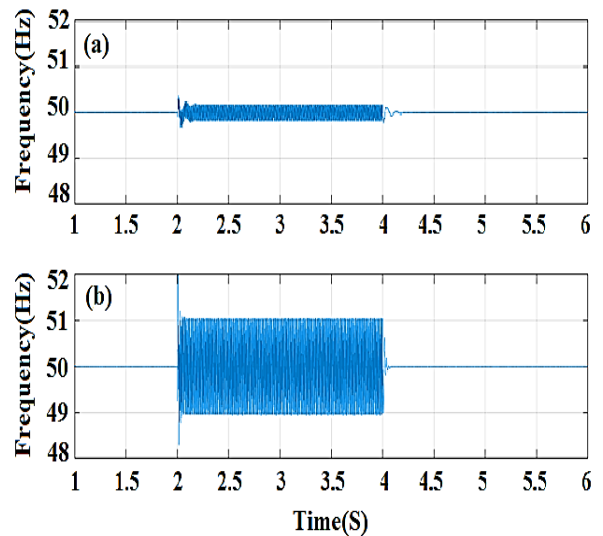


Fig. 9: System frequency: (a) proposed VSG control, (b) conventional VSG control.

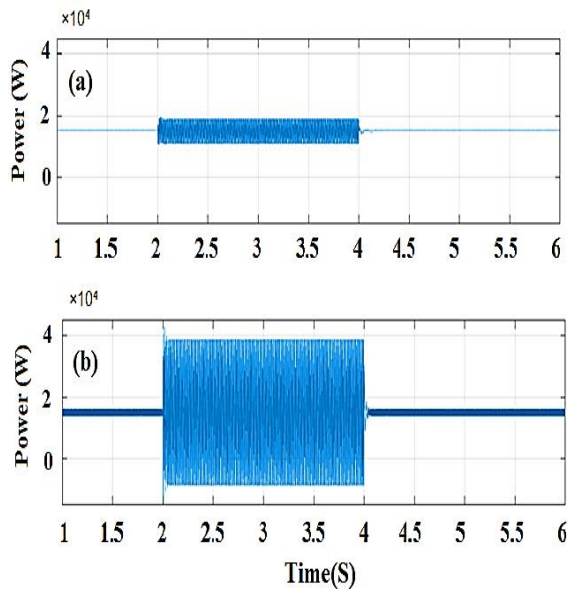


Fig. 10: Output power of VSGs: (a) proposed VSG control, (b) conventional VSG control.

As Fig. 9 and Fig. 10 show, in time interval between 2s to 4s, when the additional harmonic is injected, the proposed VSG remove the effect of the excess harmonic well and has only a very small fluctuation, which is within the permissible range. but the conventional VSG has not been able to remove the additional harmonic effect and as it is known, the system has a strong oscillation in 2 to 4 seconds. The advantages of the proposed design include easy implementation, low calculation time, improvement of VSG stability in harmonic conditions and the presence of DC deviations in voltage signal, applicable for single-phase and three-phase inverters, without the need to connect with other system components and low cost.

5. CONCLUSION

This article focuses on enhancing the stability of a VSG in the presence of harmonically distorted conditions and DC deviations in its voltage and current signals. It begins by providing a brief overview of the general and conceptual structure of a VSG. Subsequently, a method utilizing TOGI is introduced to eliminate DC deviations from the VSG's voltage and current signals. To evaluate the effectiveness and efficiency of this proposed approach, the time domain simulations are conducted in Simulink/MATLAB software, by considering two scenarios: 1) the presence of DC deviations in the VSG's voltage and current signals, and 2) the VSG connected to a harmonically distorted grid. The simulation results clearly indicate the effectiveness of the proposed design in enhancing the stability of the VSG.

CREDIT AUTHORSHIP CONTRIBUTION STATEMENT

Ramin Arjmandzadeh: Conceptualization, Data curation, Formal analysis, Methodology, Software, Visualization, Roles/Writing - original draft. **Mahdi**

Banejad: Formal analysis, Methodology, Project administration, Supervision, Validation, Roles/Writing - original draft, Writing - review & editing. **Ali Akbarzadeh Kalat:** Investigation, Methodology, Resources, Supervision.

DECLARATION OF COMPETING INTEREST

The authors declare that they have no known competing financial interests or personal relationships that could have appeared to influence the work reported in this paper. The ethical issues; including plagiarism, informed consent, misconduct, data fabrication and/or falsification, double publication and/or submission, redundancy has been completely observed by the authors.

REFERENCES

- [1] H. Bevrani, "Robust power system frequency control." Springer, 2009.
- [2] Y. Xiang-Zhen, S. Jian-Hui, D. Ming, L.-J. Wei, and D. Yan, "Control strategy for virtual synchronous generator in microgrid," in *Proc. 4th International Conference on Electric Utility Deregulation and Restructuring and Power Technologies (DRPT)*, Jul. 2011, pp. 1633–1637.
- [3] N. Xu, Y. Wang, M. Li, W. Wang, N. Wang, and J. Li "An optimal control method of virtual angular acceleration to improve transient response based on virtual synchronous generator," in *IEEE 3rd International IFEEC 2017 - ECCE Asia*, Jul. 2017.
- [4] C. Khalid Mehmood, "A comprehensive review of virtual synchronous generator," *International Journal of Electrical Power & Energy Systems*, vol. 120, 2020.
- [5] J. Alipoor, Y. Miura, and T. Ise, "Power system stabilization using virtual synchronous generator with alternating moment of inertia," *IEEE Journal of Emerging and Selected Topics in Power Electronics*, vol. 03, no. 02, 2015.
- [6] J. Fang, H. Li, Y. Tang, and F. Blaabjerg, "Distributed power system virtual inertia implemented by grid-connected power converters", *IEEE Transactions on Power Electronics*, vol. 30, no.10, pp. 8488-8499, 2017.
- [7] S. Chen, Y. Sun, Y., X. Hou, H. Han, S. Fu, S., and M. Su, "Quantitative parameters design of VSG oriented to transient synchronization stability," *IEEE Transactions on Power Systems*. vol. 38, no. 5, pp. 4978-4981, 2023.
- [8] X. Zhu, Z. Xie, S. Jing, H. Ren, "Distributed virtual inertia control and stability analysis of dc microgrid," *IET Generation, Transmission & Distribution*, vol. 12, no. 14, 2018, pp. 3477-3486.
- [9] L. Huang, , H. Xin, Z. Wang, "Damping low-frequency oscillations through VSC-HVdc stations operated as virtual synchronous machines," *IEEE Transactions on Power Electronics*, vol. 34, no. 6, 2018, pp. 5803-5818.

- [10] J. Xi, H. Geng, G. Yang, and S. Ma, "Inertial response analysis of PMSG-based WECS with VSG control," *The Journal of Engineering*, vol. 13, pp. 897-901.
- [11] S. Chen, et al. "A Modified VSG Control Scheme With Virtual Resistance to Enhance Both Small-Signal Stability and Transient Synchronization Stability," *IEEE Transactions on Power Electronics*, vol. 38, no. 5, pp. 6005-6014, 2023.
- [12] J. Alipoor, Y. Miura, and T. Ise, "Stability assessment and optimization methods for microgrid with multiple VSG units," *IEEE Transactions on Smart Grid*, vol. 9, no. 2, pp. 1462-1471.
- [13] W. Yang, C. Tu, F. Xiao, and Q. Guo, "A combined regulation method of transient power angle stability control and fault current suppression for VSG," *International Journal of Electrical Power & Energy Systems*, vol. 156, 2024.
- [14] S. V., Kulkarni, and D. N. Gaonkar. "An investigation of PLL synchronization techniques for distributed generation sources in the grid-connected mode of operation," *Electric Power Systems Research*, vol. 223, 2023.
- [15] S. Golestan, J. M. Guerrero, and J. C. Vasquez. "DC-offset rejection in phase-locked loops: A novel approach," *IEEE Transactions on Industrial Electronics*, vol. 63, no. 8, pp. 4942-4946, 2016.
- [16] H., Bevrani, T. Ise, and Y. Miura, "Virtual synchronous generators: A survey and new perspectives," *International Journal of Electrical Power & Energy Systems*, vol. 54, pp. 244-254, 2014.
- [17] B. Zhang, X. Yan, and S. Y. Althair. "Control design and small-signal modeling of multi-parallel virtual synchronous generators." in *2017 11th IEEE International Conference on Compatibility, Power Electronics and Power Engineering*, 2017.
- [18] T. Thacker, D. Boroyevich, R. Burgos, and F. Wang, "Phase-locked loop noise reduction via phase detector implementation for single-phase systems," *IEEE Transactions on Industrial Electronics*, vol. 58, no. 6, pp. 2482-2490, 2020.
- [19] I. Carugati, P. Donato, S. Maestri, D. Carrica, and M. Benedetti, "Frequency adaptive PLL for polluted single-phase grids," *IEEE Transactions on Power Electronics*, vol. 27, no. 5, pp. 2396-2404.
- [20] M. Karimi-Ghartemani, "A unifying approach to single-phase synchronous reference frame PLLs," *IEEE Transactions on Power Electronics*, vol. 28, no. 10, pp. 2012.
- [21] A. Kulkarni, and V. John. "Design of synchronous reference frame phase-locked loop with the presence of dc offsets in the input voltage," *IET Power Electronics*, vol. 8, no. 12, pp. 2435-2443, 2015.
- [22] F. Wu, D. Sun, D., L. Zhang, and J. Duan, "Influence of plugging DC offset estimation integrator in single-phase EPLL and alternative scheme to eliminate effect of input DC offset and harmonics," *IEEE Transactions on Industrial Electronics*, vol. 62, no. 8, pp. 4823-4831.
- [23] I. A. Smadi, E., I. E. Atawi, and A. A. Ibrahim. "An improved delayed signal cancelation for three-phase grid synchronization with dc offset immunity," *Energies*, vol. 16, no. 6, 2023.
- [24] S. A. Golestan, J. M. Guerrero, and J. C. Vasquez, "Three-phase PLLs: A review of recent advances," *IEEE Transactions on Power Electronics*, vol. 32, no.3, pp. 1894-1907, 2017.
- [25] H. Cheng, C. Li, A. M. Ghias, and F. Blaabjerg, "A dynamic coupling mechanism analysis between voltage and frequency in virtual synchronous generator system," *IEEE Transactions on Power Systems*, vol. 39, no. 1, pp. 2365 - 2368, 2024
- [26] C. Zhang, et al. "A grid synchronization PLL method based on mixed second-and third-order generalized integrator for DC offset elimination and frequency adaptability," *IEEE Journal of Emerging and Selected Topics in Power Electronics*, vol. 6, no. 3, pp. 1517-1526, 2018.

BIOGRAPHY



Ramin Arjmandzadeh was born in Bojnord, Iran in 1984. He finished his M. Sc in electric power engineering at Shahrood University of Technology, Shahrood, Iran. His research interests are renewable energies and microgrid control.



Mahdi Banejad (IEEE SM'15) received the Ph.D. degree in electrical engineering from the Queensland University of Technology, Brisbane, QLD, Australia, in 2004. He is currently an Associate Professor with the Faculty of Electrical Engineering, Shahrood University of Technology, Shahrood, Iran. His main research interests include distribution expansion planning, droop-based voltage and frequency control of microgrids, decentralized state estimation in the distribution system, and small signal stability of microgrids. He was also visiting scholar at QUT, Australia (2014 and 2017), at Aalborg university, Denmark (2016) and at SQU, Oman (2018).



Ali Akbarzadeh Kalat was born in Mashhad, Iran in 1969. He received his B.Sc. degree from Iran University of Science and Technology in 1992. He graduated in control engineering in M.Sc. and Ph.D. from Ferdowsi University, Mashhad, Iran and Tarbiat Modarres University, Theran, Iran in

1998 and 2007 respectively. He is with the Faculty of Electrical and Robotic Engineering at Shahrood University of Technology in Iran. His fields of interest include Neural, Fuzzy and Adaptive control systems and Nonlinear observer design.

Copyrights

© 2024 Licensee Shahid Chamran University of Ahvaz, Ahvaz, Iran. This article is an open-access article distributed under the terms and conditions of the Creative Commons Attribution –Non-Commercial 4.0 International (CC BY-NC 4.0) License (<http://creativecommons.org/licenses/by-nc/4.0/>).





Iranian Association of
Electrical and Electronics
Engineers

Journal of Applied Research in Electrical Engineering

E-ISSN: 2783-2864

P-ISSN: 2717-414X

Homepage: <https://jaree.scu.ac.ir/>



Research Article

Voltage and Frequency Control Considering Disturbance in Input Power of DG

Ali Morsagh Dezfuli¹ , Mahyar Abasi^{2,3,*} , Mohammad Esmaeil Hasanzadeh⁴ , and Mahmood Joorabian¹ 

¹ Department of Electrical Engineering, Faculty of Engineering, Shahid Chamran University of Ahvaz, Ahvaz 61357-85311, Iran

² Department of Electrical Engineering, Faculty of Engineering, Arak University, Arak 38156-8-8349, Iran

³ Research Institute of Renewable Energy, Arak University, Arak 38156-8-8349, Iran

⁴ Department of Electrical Engineering, Firouzabad Higher Education Center, Shiraz University of Technology, Shiraz, Iran

* Corresponding Author: m-abasi@araku.ac.ir

Abstract: The utilization of distributed generation (DG) in today's power systems has led to the emergence of the concept of microgrids, in addition to changing the mode of generating and supplying the energy required for network electrical loads. When a microgrid operates in the island mode, energy generation sources are responsible for controlling the microgrid's voltage and frequency. As the microgrid frequency is proportional to the amount of power generated by the DG, the microgrid requires a precise power-sharing strategy. Considering that DGs do not usually have stable output power despite the importance of power stability, the present paper addresses the voltage and frequency control of an islanded microgrid by considering the power generation uncertainties caused by disturbances and the varying power output of DGs. Given that the disturbance on the first DG's input current is 0.2 A, which is approximately 2.2% of the steady-state value, a simulation was performed, and it was observed that the maximum voltage variation of each bus in the worst case was 0.59% for the first bus and 0.53% for the second bus, which means that the controller could control the voltage and frequency values within the permissible range. If the controller is not used, the change in the frequency of each bus will be 10 times, and the voltage change will be 5 times as great as that of the case the controller is used.

Keywords: Microgrid, frequency control, voltage control, distributed generation.

Article history

Received 20 November 2023; Revised 20 January 2024; Accepted 12 February 2024; Published online 19 May 2024.

© 2024 Published by Shahid Chamran University of Ahvaz & Iranian Association of Electrical and Electronics Engineers (IAEEE)

How to cite this article

Ali Morsagh Dezfuli, Mahyar Abasi, Mohammad Esmaeil Hasanzadeh, and Mahmood Joorabian, "Voltage and frequency control considering disturbance in input power of DG," *J. Appl. Res. Electr. Eng.*, vol. 3, no. 1, pp. 9-18, 2024.

DOI: [10.22055/jaree.2024.45325.1088](https://doi.org/10.22055/jaree.2024.45325.1088)



1. INTRODUCTION

The incorporation of DGs in today's power systems has changed the mode of electrical energy generation and supply for electrical loads inside microgrids. This form of the use of DGs does not suffer from energy losses occurring in energy transmission lines, and it covers the discussion of reserve services and the provision of the demanded reactive power. Connecting these resources to the grid requires the adoption of power electronic converters. An electronic power converter can respond to fast load changes and provide fast and flexible control of voltage and frequency, so active and reactive power can be properly controlled. However, the use of DG units complicates the structure and brings about challenges in the operation, control, stability, protection, and security of power distribution networks [1]. Therefore, there are new strategies for connecting these resources to the power system. Islanded microgrids are inherently weak in frequency

and voltage stabilization. Frequency and voltage are highly variable concerning active and reactive power variations, respectively.

Ref. [2] proposed an optimization-based scheme for simultaneous frequency and voltage control in islanded microgrids in which the DG unit with the largest capacity served as the master controller, ensuring proper load sharing. In [3], a finite-time event-triggered control was proposed for frequency and voltage in islanded AC microgrids, enabling efficient power sharing among distributed generators. A two-stage economic plan was suggested in [4] for integrating synchronous distributed generations (SDGs) into distribution networks. The results on standard distribution networks confirmed improved protection coordination and economic indices compared to power flow studies. The authors in [5] attempted a control strategy for microgrid PV inverters, ensuring seamless transitions between grid-connected and

islanding modes. The approach enhanced overall microgrid reliability by mitigating transient variations in voltage, current, phase, frequency, and DC-link voltage. Ref. [6] focused on a washout filter-based power-sharing approach in microgrids, eliminating voltage and frequency deviations without secondary control or communication links. Ref. [7] introduced a multi-agent-based adaptive controller for microgrids, addressing uncertainties in distributed generating resources. Compared to a secondary voltage controller, it demonstrated faster convergence and improved performance in handling load changes. Researchers in [8] presented an event-triggered distributed control for islanded AC microgrids, allowing asynchronous communication without synchronization, effectively reducing communication rates. A fully distributed optimal control for AC microgrids was introduced in [9], emphasizing transient responses. The proposed two-loop control optimized local frequency and voltage adjustments, effectively solving the distributed optimization problem with ADMM and the Lyapunov function approach. Ref. [10] focused on a novel distributed control scheme for islanded microgrids, ensuring finite-time restoration of generator frequencies, active power sharing, and voltage regulation. Ref. [11] investigated efficient islanded microgrid frequency control by coordinating reactive power between a solid oxide fuel cell (SOFC) and a battery, reducing the need for energy storage and eliminating reserve capacity. Ref. [12] introduced a multi-agent adaptive controller for microgrids, comparing its performance with a secondary voltage controller. Ref. [13] explored improving microgrid control during grid-independent operation. It presented a novel optimization approach in which teaching-learning-based optimization and harmonic search algorithms were combined to enhance voltage and frequency regulation. Researchers in [14] introduced a novel evolutionary algorithm for unit commitment, addressing societal quality of life improvement with thermal and wind units. Ref. [15] proposed disturbance observer-based control for regulating frequency and voltage in a low-inertia microgrid with solar PV and a diesel generator. A distributed control approach was proposed in [16] for islanded microgrids, optimizing reactive power-sharing and addressing voltage/frequency drop issues. A decoupled double synchronous reference frame-based virtual synchronous generator (VSG) was introduced in [17] for improved performance in unbalanced conditions within an islanded microgrid. The method enhanced controllability, accuracy, and robustness under heavy loads by separating positive and negative components. Ref. [18] optimally allocated DG units in networks with unbalanced loads using a modified group search optimizer (GSO) algorithm. Ref. [19] investigated an efficient power control technique for inverter-based DG in an islanded microgrid and emphasized improved electricity quality during islanded operation. The control method integrated internal current and external power control loops. An adaptive virtual impedance control method optimized by the multi-objective particle swarm optimization (MOPSO) algorithm was considered for efficient voltage and frequency control in microgrids [20]. Ref. [21] introduced a fixed-time control approach for islanded AC microgrids that utilized a multi-agent consensus method with an adaptive fuzzy fixed-time secondary voltage controller and a secondary frequency controller based on the control barrier function. A disturbance-observer-based control (DOBC) was proposed in [22] for efficient frequency and voltage

regulation in power systems with high renewable energy sources (RES). Ref. [23] introduced two event-triggered fault-tolerant control (ETFTC) algorithms for voltage restoration in microgrids, addressing bias faults in distributed generators' actuators and reliability in distributed control applications. Researchers in [24] discussed an advanced power-sharing control method using sliding mode control in microgrids. It improved voltage quality and enhanced power-sharing accuracy among inverters, even during communication interruptions.

Noting that DGs usually lack stable output power, the present study aimed to design a controller for voltage and frequency control of the islanded microgrid by considering disturbance in the input power of DGs. Based on the literature review, it is evident that no study on voltage and frequency control of microgrids has ever considered the full dynamic model of the resources and microgrid, as well as power disturbances simultaneously. Many references have presented voltage and frequency control but neglected the dynamics of DGs or power input disturbances. Also, some previous studies have discussed input disturbances and the dynamics of DGs, but the only control challenge they have considered has been the frequency control of the microgrid. Indeed, none of the references has been completely modeled.

This paper considers the dynamics of each DG to eliminate power input disturbances, maintain the voltage and frequency within the permissible range, and consequently preserve the microgrid's stability (with electronic power converters). The controller also makes the necessary changes in power electronic settings to eliminate disturbances and accomplish the control objectives.

Accordingly, the highlights of this paper are as follows:

- Presentation of a method for voltage and frequency control of islanded microgrids
- Designing a multi-output controller
- Considering the dynamics of each DG with power converters and power generation uncertainties
- Changing and controlling the switching method of power converters of DGs
- Increasing the velocity of response to changes and maintaining the closed-loop stability.

The rest of the paper is organized as follows. Section 2 discusses multivariable systems and how to design controllers for these systems. In Section 3, the target microgrid is modeled, and mathematical equations are obtained. Section 4 studies the dynamic model of each DG and presents its mathematical equations. Section 5 provides the state-space model of the system and the system matrices for simulation. In Section 6, a simulation is performed according to the equations expressed in Section 5, and the results are presented. Section 7 concludes the paper.

2. DESIGNING MULTIVARIABLE CONTROLLERS

2.1. Multivariable Linear Systems

Most control system analysis and design systems are based on the system's mathematical model. A system model may be a mathematical and analytical model of the system. Physical

systems and many non-physical systems can be described by a system of nonlinear differential equations and algebraic equations [25, 26]. By linearizing these equations around operating points, we can obtain the system's differential and algebraic linear equations. This way, linear control systems are analyzed and designed around the designated operating points. In the study on multivariable control systems, the system is described by linear state-space models, transfer function matrix, system matrix, and fractional matrix. The description of the space state or internal description is given in (1) and (2) [27]:

$$\dot{x}(t) = A.x(t) + B.u(t) + E.w(t) \quad (1)$$

$$y(t) = C.x(t) + D.u(t) + F.w(t) \quad (2)$$

where vector x shows the state variables, u is the input vector, y is the output vector, w is the disturbance vector, and the matrices A , B , C , D , E , and F are dimensioned. The control systems are designed with two objectives: stabilizing and improving the closed-loop operation. If the open-loop system is stable, the main purpose during designing the control system will be to improve the performance of the set of system behaviors. If the exact model of the open-loop system is available, or in other terms, the system's behavior is not uncertain, the desired control objectives can be achieved without feedback. However, practical systems are always associated with some uncertainty, which needs the use of feedback.

2.2. Design of a PI Controller for Multivariable Systems

Consider a multivariable system described using the state-space equations and the output shown in Fig. 1.

The corresponding transfer function matrix for the system is obtained as (3) [27]:

$$G(s) = C.(sI - A)^{-1}B \quad (3)$$

where $G(S)$ is an $(m \times 1)$ transfer function matrix.

Note that the open-loop system must be stable and controllable for controller design. Therefore, all the eigenvalues of matrix A should be placed on the left half of the imaginary, which will be proven as follows.

Consider the multivariable system given in (1) and (2). Assuming that the assumptions are correct, the multivariable PI controller is considered as (4):

$$u(s) = (K_1 + \frac{K_2}{s}).e(s) \quad (4)$$

The matrices K_1 and K_2 are defined as:

$$K_1 = \alpha \varepsilon K \quad (5)$$

$$K_2 = \varepsilon K \quad (6)$$

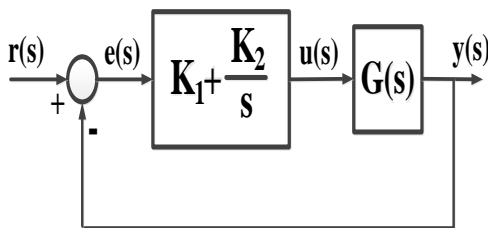


Fig. 1: A multivariable closed-loop system.

where ε is a setting parameter, α is a positive real number, and K as the design matrix is defined by (7):

$$K = G^T (GG^T)^{-1} \Sigma \quad (7)$$

Here $G = G(0)$ and Σ is:

$$\Sigma = \begin{bmatrix} \sigma_1 & 0 & \dots & 0 \\ 0 & \sigma_2 & \ddots & \vdots \\ \vdots & \ddots & \ddots & 0 \\ 0 & \dots & 0 & \sigma_m \end{bmatrix} \quad (8)$$

with $\sigma_i > 0$.

The most important advantage of the controller designed in this article is the control of multiple parameters, the stability of the closed loop system, and the appropriate response speed. The controller is designed below based on the system matrix.

3. MODELING AND MATHEMATICAL EQUATIONS OF THE MICROGRID

The islanded microgrid under study is shown in Fig. 2 [28]. This microgrid involves the interconnection of two DGs via a line and two local complex interconnected loads. This study modeled energy sources using a boost converter and an inverter to the main microgrid with constant loads. Different current (power) oscillations of DG1 are modeled as a disturbance that causes frequency and voltage deviations.

Current equations are written according to the matrix given in (9) [29]:

$$\begin{bmatrix} \vec{I}_1 \\ \vec{I}_2 \end{bmatrix} = \begin{bmatrix} Y_a + Y_c & -Y_c \\ -Y_c & Y_b + Y_c \end{bmatrix} \begin{bmatrix} \vec{V}_{r1} \\ \vec{V}_{r2} \end{bmatrix} \quad (9)$$

According to (9), equation (10) is obtained:

$$\vec{V}_r = Y^{-1} \vec{I} \quad (10)$$

If voltage and current equations are considered in the following sequence, equations (11) and (12) are obtained:

$$\vec{V}_r = V_{r_d} + jV_{r_q} \quad (11)$$

$$\vec{I} = I_d + jI_q \quad (12)$$

Equations (9) and (10) yield (13), (14), and (15):

$$Z_{11} = \frac{Z_a Z_c + Z_a Z_b}{Z_a + Z_b + Z_c} \quad (13)$$

$$Z_{12} = Z_{21} = \frac{Z_a Z_b}{Z_a + Z_b + Z_c} \quad (14)$$

$$Z_{22} = \frac{Z_a Z_b + Z_b Z_c}{Z_a + Z_b + Z_c} \quad (15)$$

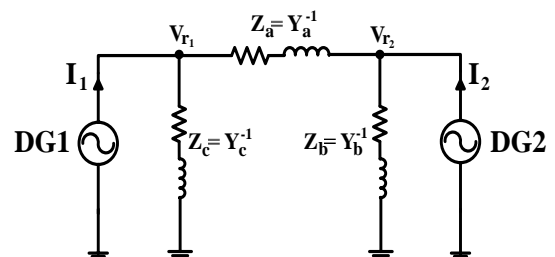


Fig. 2: The studied islanded microgrid [28].

These are also expressed as (16)-(19):

$$Z_{11} = R_{11} + jX_{11} \quad (16)$$

$$Z_{12} = R_{12} + jX_{12} \quad (17)$$

$$Z_{21} = R_{21} + jX_{21} \quad (18)$$

$$Z_{22} = R_{22} + jX_{22} \quad (19)$$

As a result, according to the above equations, equations (20)-(23) are obtained:

$$V_{d1} = R_{11}I_{1d} - X_{11}I_{1q} + R_{12}I_{2d} - X_{12}I_{2q} \quad (20)$$

$$V_{q1} = X_{11}I_{1d} + R_{11}I_{1q} + X_{12}I_{2d} + R_{12}I_{2q} \quad (21)$$

$$V_{d2} = R_{21}I_{1d} - X_{21}I_{1q} + R_{22}I_{2d} - X_{22}I_{2q} \quad (22)$$

$$V_{q2} = X_{21}I_{1d} + R_{21}I_{1q} + X_{22}I_{2d} + R_{22}I_{2q} \quad (23)$$

4. MODELING AND MATHEMATICAL EQUATIONS OF DG UNITS

Both DGs contain a DC/DC converter, an AC/DC inverter, and an LC filter, as shown in Fig. 3. The active power is controlled by the controller's switching function. DC-bus voltage is regulated by the switching function in the dq axis of the inverter. Therefore, the voltage and frequency of buses connected to resources are system outputs, and switching functions are controlled by converters and inverters of each DG. The input disturbance is also considered a change in the input current and, as a result, a change in the generating power of the first DG. The input voltage to the DC/DC converter is determined by the switching function (α_i) of each resource. DC-bus voltage (V_{DC}) and output current of the converter (I_{scr}) are indicated by the switch function (α_i) and DG current. The output voltage of each inverter (V_{d_i} and V_{q_i}) is expressed by the switching function (K_{d_i} and K_{q_i}) and the DC-bus voltage (V_{DC}). The input current of the inverter (I_m) is a function of the switching function (K_{d_i} and K_{q_i}) and the output current (I_{d_i} and I_{q_i}) of the AC bus. The input voltage sources are connected to a DC/DC converter by a resistor and inductor (R_{x_i} and L_{x_i}), as in Fig. 3. The input voltage to the converter (V_{h_i}) is a function of the input voltage (V_{in_i}), input current (I_{in_i}), and resistor and inductor (R_{x_i} and L_{x_i}). The DC/DC converter is filtered by a capacitor (C_{dc}) and connected to an AC/DC inverter. The input current to the inverter is equal to the difference between the output current of the converter (I_{scr}) and the capacitor current. The inverter output and AC side are modeled in this section. The inverter is connected to the grid by an RL filter, as shown in Fig. 3. The inverter output currents (I_{d_i} and I_{q_i}) are equivalent to the output currents I_1 or I_2 , as given in Fig. 2. In the equations, R_{ac_i} and L_{ac_i} are the resistance and inductance of the line, V_{d_i}

and V_{q_i} are voltages of the bus system in the dq axes, and V_{DC} is the DC-bus voltage.

In Fig. 3, the input source with an index $i = 1, 2$ is related to DG1 and DG2, respectively.

The power equation for each of the sources is obtained by (24):

$$P_i = V_{d_i} I_{d_i} + V_{q_i} I_{q_i} \quad (24)$$

Also, equations (25)-(29) are obtained considering the DC/DC converter and the AC/DC inverter:

$$V_{d_i} = K_{d_i} V_{DC_i} \quad (25)$$

$$V_{q_i} = K_{q_i} V_{DC_i} \quad (26)$$

$$I_{scr_i} = \alpha_i I_{in_i} \quad (27)$$

$$V_{h_i} = \alpha_i V_{DC_i} \quad (28)$$

$$I_{m_i} = K_{d_i} I_{d_i} + K_{q_i} I_{q_i} \quad (29)$$

By establishing KVL at the output of each inverter, equations (30) and (31) are expressed:

$$\dot{I}_{d_i} = \frac{-R_{ac_i}}{L_{ac_i}} I_{d_i} + \frac{1}{L_{ac_i}} V_{DC_i} K_{d_i} + \omega_i I_{q_i} - \frac{1}{L_{ac_i}} V_{rd_i} \quad (30)$$

$$\dot{I}_{q_i} = \frac{-R_{ac_i}}{L_{ac_i}} I_{q_i} + \frac{1}{L_{ac_i}} V_{DC_i} K_{q_i} + \omega_i I_{d_i} - \frac{1}{L_{ac_i}} V_{rq_i} \quad (31)$$

On the other hand, according to (27) and (28) and writing a KVL at the input of each converter, Equation (32) is provided:

$$\dot{I}_{in_i} = \frac{1}{L_{x_i}} V_{in_i} - \frac{1}{L_{x_i}} V_{DC_i} \alpha_i - \frac{R_{x_i}}{L_{x_i}} I_{in_i} \quad (32)$$

Also, by writing the KCL in the node to which the capacitor is connected and considering (28) and (29), we have:

$$\dot{V}_{DC_i} = \frac{1}{C_{DC_i}} \alpha_i I_{in_i} - \frac{1}{C_{DC_i}} (K_{d_i} I_{d_i} + K_{q_i} I_{q_i}) \quad (33)$$

The output frequency of each inverter is obtained using the droop character [28]:

$$\omega_i = \omega_{0_i} - K_{p_i} (P - P_{0_i}) \quad (34)$$

To ensure each inverter's voltage and frequency control, their output voltage and frequency are required.

These quantities are measured using a low-pass filter with a cut-off frequency of ω_f . According to Fig. 4, the power equation in the Laplace domain is formulated as [28]:

$$P_{meas}(s) = \frac{\omega_f}{s + \omega_f} P(s) \quad (35)$$

By substituting (35) in (34), we have:

$$\dot{\Delta\omega_i} = -\omega_{f_i} \Delta\omega_i - \omega_{f_i} K_{p_i} \Delta P_i \quad (36)$$

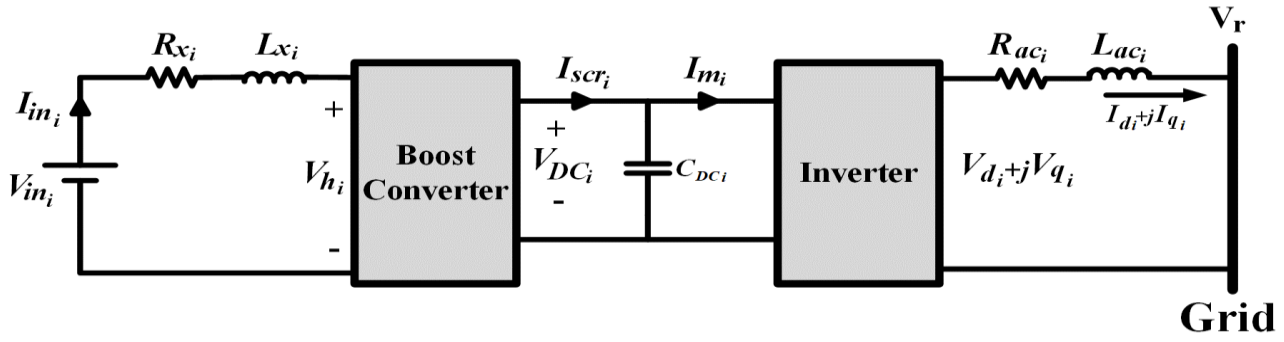


Fig. 3: The dynamics of each DG.

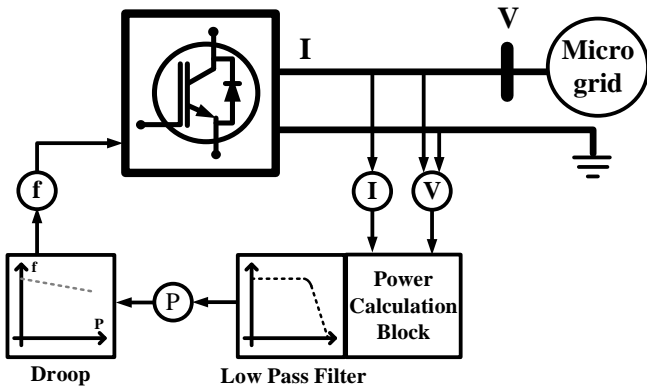


Fig. 4: Diagram of frequency control of each DG unit.

As is seen, these equations are nonlinear, but they should be linear and controllable in the form of state space equations to control the network. The following is allocated to this process.

Fig. 5 shows the performance flowchart of the proposed method.

5. STATE-SPACE MODEL OF THE SYSTEM

The state variables (Δx) include small variations in the DG's input current (ΔI_{in}), DC-bus voltage (ΔV_{DC}), inverter current in the d-axis direction (ΔI_d), inverter current in the q-axis direction (ΔI_q), and output frequency ($\Delta \omega$). Changes, also considered in the output (Δy), are the variation rate of each parameter from its steady state. Therefore, equations (30)-(33) are linearized around their initial stable points, so we have (37)-(40).

$$\Delta \dot{I}_d = \frac{-R_{ac_i}}{L_{ac_i}} \cdot \Delta I_d + \frac{1}{L_{ac_i}} \cdot V_{DC0_i} \cdot \Delta K_{d_i} + \frac{1}{L_{ac_i}} \cdot K_{d0_i} \cdot \Delta V_{DC_i} + \omega_{0_i} \cdot \Delta I_{q_i} + I_{q0_i} \cdot \Delta \omega_i - \frac{1}{L_{ac_i}} \cdot \Delta V_{rd_i} \quad (37)$$

$$\Delta \dot{I}_q = \frac{-R_{ac_i}}{L_{ac_i}} \cdot \Delta I_q + \frac{1}{L_{ac_i}} \cdot V_{DC0_i} \cdot \Delta K_{q_i} + \frac{1}{L_{ac_i}} \cdot K_{q0_i} \cdot \Delta V_{DC_i} + \omega_{0_i} \cdot \Delta I_{d_i} + I_{d0_i} \cdot \Delta \omega_i - \frac{1}{L_{ac_i}} \cdot \Delta V_{rq_i} \quad (38)$$

$$\Delta \dot{I}_{m_i} = \frac{1}{L_{x_i}} \cdot \Delta V_{in_i} - \frac{1}{L_{x_i}} \cdot \alpha_{0_i} \cdot \Delta V_{DC_i} - \frac{1}{L_{x_i}} \cdot V_{DC0_i} \cdot \Delta \alpha_i - \frac{R_{x_i}}{L_{x_i}} \cdot \Delta I_{m_i} \quad (39)$$

$$\Delta \dot{V}_{DC_i} = \frac{1}{C_{DC_i}} \cdot \alpha_{0_i} \cdot \Delta I_{in_i} + \frac{1}{C_{DC_i}} \cdot I_{in0_i} \cdot \Delta \alpha_i - \frac{1}{C_{DC_i}} (K_{d0_i} \cdot \Delta I_{d_i} + I_{d0_i} \cdot \Delta K_{d_i} + K_{q0_i} \cdot \Delta I_{q_i} + I_{q0_i} \cdot \Delta K_{q0_i}) \quad (40)$$

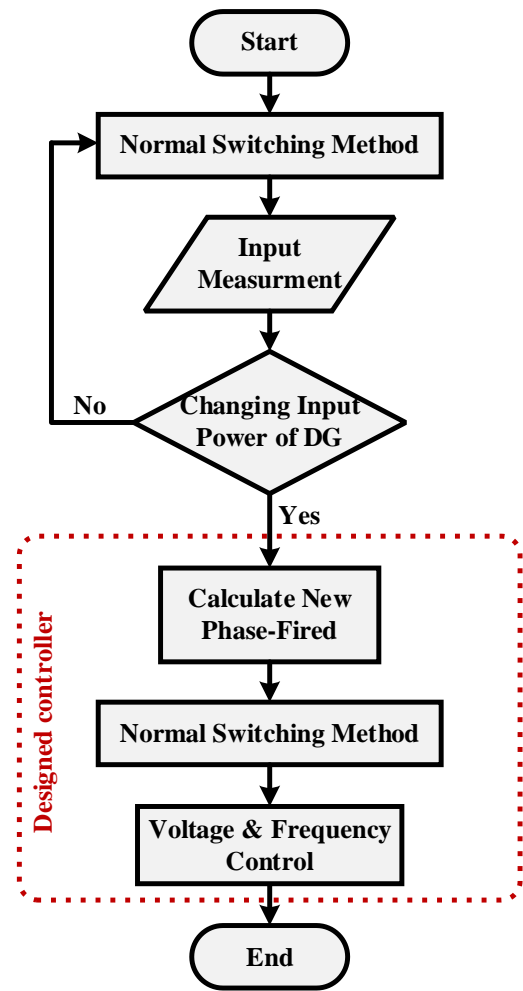


Fig. 5: The performance flowchart of the proposed method.

ΔV_{d_i} and ΔV_{q_i} in (37) and (38) are replaced by the network power flow equation given in (20)-(23). Also, after placing (25)-(26) in (24) and linearizing it, ΔP_i is obtained as (36), (see (41)).

In matrices A and B, values with zero indexes are initial values of parameters determined by the dynamics of DG sources and microgrid values, as listed below. In the case of matrices C and W, due to the small variations of voltage across the q-axis, the control of voltage in the q-axis direction is not considered in the literature, and only the control of voltage along the d-axis and the frequency control of each bus are the control objectives. Yet, voltage variations in the q-axis direction are considered in this study. Therefore, the purpose

is to control the frequency and voltage of buses in the d-axis. Therefore, the output matrix C is obtained as (46). Also, in the case of the matrix W, which is the disturbance matrix of the system, this disturbance is only related to the first DG. For the input disturbance to the system, only the change in the input current of the first DG is considered, and in this way, the disturbance matrix (W) is obtained as (47).

Considering the general form of state equations and concerning the linear equations observed in (36)-(41), (42), and (43) are formulated (see (42) and (43)).

Given matrices, matrices A and B are obtained as (44) and (45). Also, according to the dynamical equations of the system, the values of matrices D and F are zero.

$$\Delta \dot{\omega}_i = -\omega_{f_i} \cdot \Delta \omega_i - \omega_{f_i} \cdot K_{P_i} \cdot (I_{d0_i} \cdot (V_{DC0_i} \cdot \Delta K_{d_i} + K_{d0_i} \cdot \Delta V_{DC_i}) + V_{d0_i} \cdot \Delta I_{d_i} + I_{q0_i} \cdot (V_{DC0_i} \cdot \Delta K_{q_i} + K_{q0_i} \cdot \Delta V_{DC_i}) + V_{q0_i} \cdot \Delta I_{q_i}) \quad (41)$$

$$\Delta x = [\Delta I_{d1} \quad \Delta I_{q1} \quad \Delta I_{in1} \quad \Delta V_{DC1} \quad \Delta \omega_1 \quad \Delta I_{d2} \quad \Delta I_{q2} \quad \Delta I_{in2} \quad \Delta V_{DC2} \quad \Delta \omega_2]^T \quad (42)$$

$$\Delta u = [\Delta \alpha_1 \quad \Delta K_{d1} \quad \Delta K_{q1} \quad \Delta \alpha_2 \quad \Delta K_{d2} \quad \Delta K_{q2}]^T \quad (43)$$

$$A = \begin{bmatrix} \frac{-R_{ac1}}{L_{ac1}} - \frac{R_{11}}{L_{ac1}} & \omega_{01} - \frac{X_{11}}{L_{ac1}} & 0 & \frac{K_{d01}}{L_{ac1}} & I_{q01} & -\frac{R_{12}}{L_{ac1}} & \frac{X_{12}}{L_{ac1}} & 0 & 0 & 0 \\ \omega_{01} - \frac{X_{11}}{L_{ac1}} & \frac{-R_{ac1}}{L_{ac1}} - \frac{R_{11}}{L_{ac1}} & 0 & \frac{K_{q01}}{L_{ac1}} & I_{d01} & -\frac{X_{12}}{L_{ac1}} & -\frac{R_{12}}{L_{ac1}} & 0 & 0 & 0 \\ 0 & 0 & -\frac{R_{x1}}{L_{x1}} & -\frac{\alpha_{01}}{L_{x1}} & 0 & 0 & 0 & 0 & 0 & 0 \\ \frac{-K_{d01}}{C_{DC1}} & \frac{-K_{q01}}{C_{DC1}} & \frac{\alpha_{01}}{C_{DC1}} & 0 & 0 & 0 & 0 & 0 & 0 & 0 \\ -\omega_{f1} \cdot K_{P1} \cdot V_{d01} & -\omega_{f1} \cdot K_{P1} \cdot V_{q01} & 0 & -\omega_{f1} \cdot K_{P1} \cdot (I_{d01} \cdot K_{d01} + I_{q01} \cdot K_{q01}) & -\omega_{f1} & 0 & 0 & 0 & 0 & 0 \\ -\frac{R_{21}}{L_{ac2}} & \frac{X_{21}}{L_{ac2}} & 0 & 0 & 0 & -\frac{R_{ac2}}{L_{ac2}} - \frac{R_{22}}{L_{ac2}} & \omega_{02} - \frac{X_{22}}{L_{ac2}} & 0 & \frac{K_{d02}}{L_{ac2}} & I_{q02} \\ -\frac{X_{21}}{L_{ac2}} & -\frac{R_{21}}{L_{ac2}} & 0 & 0 & 0 & \omega_{02} - \frac{X_{22}}{L_{ac2}} & -\frac{R_{ac2}}{L_{ac2}} - \frac{R_{22}}{L_{ac2}} & 0 & \frac{K_{q02}}{L_{ac2}} & I_{d02} \\ 0 & 0 & 0 & 0 & 0 & 0 & 0 & -\frac{R_{x2}}{L_{x2}} & -\frac{\alpha_{02}}{L_{x2}} & 0 \\ 0 & 0 & 0 & 0 & 0 & \frac{-K_{d02}}{C_{DC2}} & \frac{-K_{q02}}{C_{DC2}} & \frac{\alpha_{02}}{C_{DC2}} & 0 & 0 \\ 0 & 0 & 0 & 0 & 0 & -\omega_{f2} \cdot K_{P2} \cdot V_{d02} & -\omega_{f2} \cdot K_{P2} \cdot V_{q02} & 0 & -\omega_{f2} \cdot K_{P2} \cdot (I_{d02} \cdot K_{d02} + I_{q02} \cdot K_{q02}) & -\omega_{f2} \end{bmatrix} \quad (44)$$

$$B = \begin{bmatrix} 0 & \frac{V_{DC01}}{L_{ac1}} & 0 & 0 & 0 & 0 & 0 & 0 & 0 & 0 \\ 0 & 0 & \frac{V_{DC01}}{L_{ac1}} & 0 & 0 & 0 & 0 & 0 & 0 & 0 \\ \frac{-V_{DC01}}{L_{x1}} & 0 & 0 & 0 & 0 & 0 & 0 & 0 & 0 & 0 \\ \frac{I_{in01}}{C_{DC1}} & \frac{-I_{d01}}{C_{DC1}} & \frac{-I_{q01}}{C_{DC1}} & 0 & 0 & 0 & 0 & 0 & 0 & 0 \\ 0 & -\omega_{f1} \cdot K_{P1} \cdot I_{d01} \cdot V_{DC01} & -\omega_{f1} \cdot K_{P1} \cdot I_{q01} \cdot V_{DC01} & 0 & 0 & 0 & 0 & 0 & 0 & 0 \\ 0 & 0 & 0 & 0 & 0 & \frac{V_{DC02}}{L_{ac2}} & 0 & 0 & 0 & 0 \\ 0 & 0 & 0 & 0 & 0 & 0 & 0 & \frac{V_{DC02}}{L_{ac2}} & 0 & 0 \\ 0 & 0 & 0 & 0 & \frac{-V_{DC03}}{L_{x2}} & 0 & 0 & 0 & 0 & 0 \\ 0 & 0 & 0 & 0 & \frac{I_{in02}}{C_{DC2}} & \frac{-I_{d02}}{C_{DC2}} & \frac{-I_{q02}}{C_{DC2}} & 0 & 0 & 0 \\ 0 & 0 & 0 & 0 & 0 & -\omega_{f2} \cdot K_{P2} \cdot I_{d02} \cdot V_{DC02} & -\omega_{f2} \cdot K_{P2} \cdot I_{q02} \cdot V_{DC02} & 0 & 0 & 0 \end{bmatrix} \quad (45)$$

$$C = \begin{bmatrix} 0 & 0 & 0 & 0 & 1 & 0 & 0 & 0 & 0 & 0 \\ R_{11} & -X_{11} & 0 & 0 & 0 & R_{12} & -X_{12} & 0 & 0 & 0 \\ X_{11} & R_{11} & 0 & 0 & 0 & X_{12} & R_{12} & 0 & 0 & 0 \\ 0 & 0 & 0 & 0 & 0 & 0 & 0 & 0 & 0 & 1 \\ R_{21} & -X_{21} & 0 & 0 & 0 & R_{22} & -X_{22} & 0 & 0 & 0 \\ X_{21} & R_{21} & 0 & 0 & 0 & X_{22} & R_{22} & 0 & 0 & 0 \end{bmatrix} \quad (46)$$

$$W = \begin{bmatrix} 0 & 0 & -\frac{R_{x1}}{L_{x1}} & \frac{\alpha_{01}}{C_{DC1}} & 0 & 0 & 0 & 0 & 0 & 0 \end{bmatrix}^T \quad (47)$$

In matrices A and B, values with zero indexes are initial values of parameters determined by the dynamics of DG sources and microgrid values, which are listed below.

In the case of matrices C and W, due to the small variation of voltage across the q-axis, the control of voltage in the q-axis direction is not considered in the literature, and only the control of voltage along the d-axis and the frequency control of each bus are the control objectives. Yet, the voltage changes in the q-axis direction are considered in this study. Therefore, the purpose is to control the frequency and voltage of buses in the d-axis. Thus, the output matrix C is obtained as (46). Also, in the case of matrix W, which is the disturbance matrix of the system, this disturbance is only related to the first DG. For the input disturbance to the system, only the change in the input current of the first DG is considered, and in this way, the disturbance matrix (W) is obtained as (47).

Given that the matrices A, B, C, and W are known and considering the values of the system as listed in Tables 1 and 2, and also assuming that the disturbance to the input current of the first generator is 0.15 A, i.e., almost 1.6% of its steady-state value, the simulations are performed.

Based on Tables 1 and 2, the system's controllability must be examined. According to Section 2.B, for controller design, all eigenvalues of matrix A must have a negative real part. In Table 3, the eigenvalues of matrix A are given.

Table 1: The values of the microgrid parameters.

Parameter	Value
Z_a	13+6i
Z_b	25+13i
Z_c	0.5+3i

Table 2: The values of DG parameters.

Parameter	Unit	Value for DG1	Value for DG2
R_{ac}	Ω	0.5	0.6
L_{ac}	mH	5	6
V_{DC0}	V	135	140
I_{d0}	A	6.4	5.9
I_{q0}	A	-3	-2.7
V_{d0}	V	127	129.9
V_{q0}	V	0	4.7
f_0	Hz	50	50
ω_0	rad/sec	100 π	100 π
ω_f	rad/sec	37.7	37.7
C_{CD}	μ F	5	4
K_p	Hz/watt	0.005	0.006
R_x	Ω	0.05	0.05
L_x	H	0.03	0.03
I_{in0}	A	9	9
V_{in0}	V	50	56

Table 3: The eigenvalues of matrix A.

The Eigenvalues of Matrix A
100.2 + 6457.80i
-100.2 - 6457.80i
-1682.1 + 6381.9i
-1682.1 - 6381.9i
-3002.8
-0.5
-123.6
-105.6
-36.9
-37.7

6. SIMULATION

It is observed that all eigenvalues of matrix A have a negative real part, so the system is stable and has the necessary conditions for controller design. For the system's stability and considering the values of the system matrices (A, B, C, and W), we can design a suitable controller for this system. According to Section 2.B, the controller is implemented using (4)-(8) and applied to the system.

A set of simulation studies is carried out in MATLAB to verify the performance of the proposed controller.

1) Case 1: Given that the disturbance on the first DG's input current is 0.2 A, which is approximately 2.2% of the steady-state value, simulation is performed. Initially, this disturbance was entered as an incremental step in 0.5 seconds.

It is seen that the maximum variation rate is 0.005% for the first bus and 0.007% for the second bus. Also, the maximum voltage variation of each bus in the worst case is 0.59% for the first bus and 0.53% for the second bus, which means the controller can control the voltage and frequency values within the permissible range. If the controller is not used, the change in the frequency of each bus is 10 times, and the voltage change is 5 times as great as that of the case the controller is used. Thus, the controller eliminated the disturbances caused by the variation in input power of the DG and improved the transient and steady-state stability, as illustrated in Figs. 6-8.

2) Case 2: In the next step, the disturbance is applied to the system as a ramp function in 5 seconds. After 3 seconds, the amount of disturbance on the input current of the first DG reaches 0.2 A.

In this case, it is also observed that the controller, while maintaining the transient and steady-state stability, like in case 1, has managed to hold the maximum overshoot of the microgrid frequency in 0.004% and maintain the settling time at time 8 s where the overshoot and settling time decreased 10% and 2 seconds compared to uncontrolled mode. In addition, in this case, frequency changes in buses 1 and 2 are 0.003% and 0.004%, and their voltage changes are 0.02% and 0.025%, respectively, reflecting the proper performance of the designed controller, as shown in Figs. 9-11.

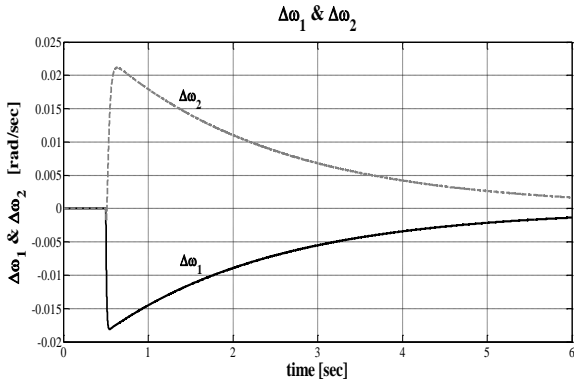


Fig. 6: Angle frequency variations for buses 1 and 2 when applying stepping disturbance in the input current of DG1.

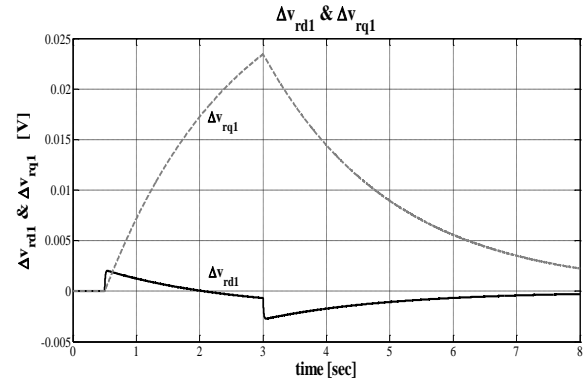


Fig. 10: Voltage variation for bus 1 when applying ramping disturbance in the input current of DG1.

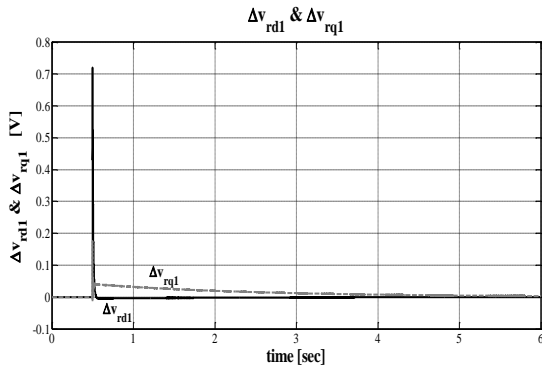


Fig. 7: Voltage variation for bus 1 when applying stepping disturbance in the input current of DG1.

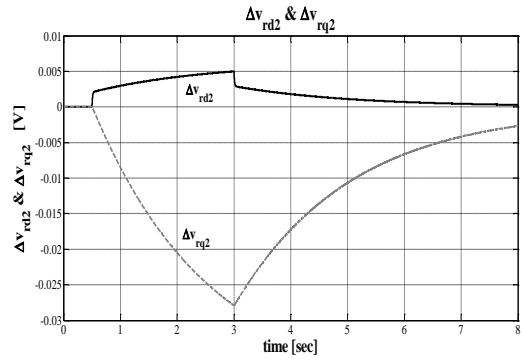


Fig. 11: Voltage variation for bus 2 when applying stepping disturbance in the input current of DG1.

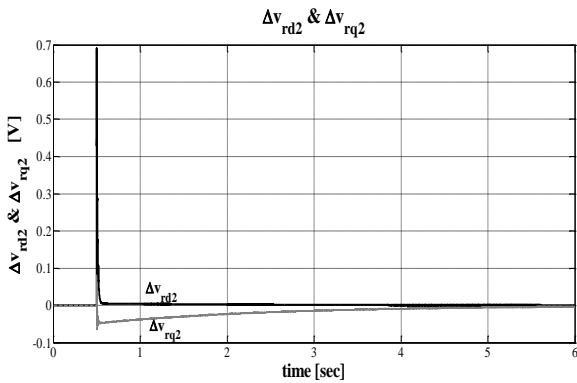


Fig. 8: Voltage variation for bus 2 when applying stepping disturbance in the input current of DG1.

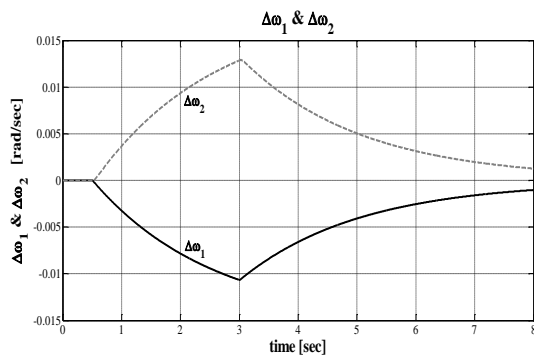


Fig. 9: Angle frequency variations for buses 1 and 2 when applying ramping disturbance in the input current of DG1.

7. CONCLUSION

In this research, a method was proposed for controlling the voltage and frequency in the islanded microgrid supplied by multiple DGs, considering the uncertainties of the productive power of DGs. Many references have proposed the dynamics of sources by considering the generality of sources. It was observed that the controller can control the frequency and voltage oscillations of each bus caused by the disturbance on the input current of the DG1 and reduce it to zero, where the microgrid supplied the load without any problem. It is worth noting that if the proposed controller is not used, the frequency and voltage of each bus will have a slower response, and higher changes will occur (voltage and frequency have been higher overshoot). Given that the disturbance on the first DG's input current is 0.2 A, which is approximately 2.2% of the steady-state value, simulation was performed, and it was observed that the maximum voltage variation of each bus in the worst case was 0.59% for the first bus and 0.53% for the second bus, which means the controller could control the voltage and frequency values within the permissible range. If the controller is not used, the change in the frequency of each bus will be 10 times and the voltage change will be 5 times as great as that of the case in which the controller is used. In contrast, these changes are greater in other references, so the controller improves frequency and voltage variations. Also, it was observed that the changes in voltage and frequency were dependent on the microgrid parameters and the power change characteristics (amount and duration of change). Voltage and frequency variations depended on the change in power generation and system parameters. In this paper, it was also observed that the controller maintained the closed-loop stability of the system.

In terms of the stability and performance indices against the uncertainties of the input current (input power), it is sufficiently robust and maintains both the bus frequency and voltage in the allowed range. Also, for the controller design, only frequency and output voltage of the inverters are required, so more sensors should be adopted.

CREDIT AUTHORSHIP CONTRIBUTION STATEMENT

Ali Morsagh Dezfuli: Conceptualization, Data curation, Formal analysis, Methodology, Software, Roles/Writing - original draft, Writing - review & editing. **Mahyar Abasi:** Conceptualization, Methodology, Project administration, Supervision, Validation, Roles/Writing - original draft, Writing - review & editing. **Mohammad Esmail Hasanzadeh:** Conceptualization, Methodology, Validation. **Mahmood Joorabian:** Conceptualization, Methodology, Project administration, Roles/Writing - original draft.

DECLARATION OF COMPETING INTEREST

The authors declare that they have no known competing financial interests or personal relationships that could have appeared to influence the work reported in this paper. The ethical issues; including plagiarism, informed consent, misconduct, data fabrication and/or falsification, double publication and/or submission, redundancy has been completely observed by the authors.

REFERENCES

- [1] M. Abasi, M. Joorabian, A. Saffarian, and S. G. Seifossadat, "A comprehensive review of various fault location methods for transmission lines compensated by FACTS devices and series capacitors," *Journal of Operation and Automation in Power Engineering*, vol. 9, no.3, pp. 213-225, 2021.
- [2] R. Dhua, S. K. Goswami, and D. Chatterjee, "An optimized frequency and voltage control scheme for distributed generation units of an islanded microgrid," in *Innovations in Energy Management and Renewable Resources*, 2021.
- [3] J. Choi, S.I. Habibi, and A. Bidram, "Distributed finite-time event-triggered frequency and voltage control of AC microgrids," *IEEE Transactions on Power Systems*, vol. 37, no. 3, 2022.
- [4] S. M. Sadeghi, M. Daryalal, and M. Abasi, "Two-stage planning of synchronous distributed generations in distribution network considering protection coordination index and optimal operation situation," *IET Renewable Power Generation*, vol. 16, no. 11, p.p. 2338-2356, 2022.
- [5] A. Saltouh, T. ME, A. El-Shafy A. Nafeh, A. Abou El-Ela, F. H. Fahmy, and Sherif K. Nawar, "Control strategy for seamless transition between grid-connected and islanding modes in microgrid-based PV inverters," *Energy Systems*, vol. 14, no. 4, p.p.1135-1162, 2023.
- [6] M. Yazdani, et al. "Small signal stability of washout filter-based power sharing for an inverter-based microgrid," *The Journal of Engineering*, vol. 2023, no. 2, 2023.
- [7] S. Arunima, and B. Subudhi, "Distributed control for accurate voltage/frequency regulation and power sharing in a microgrid," in *5th International Conference on Energy, Power and Environment: Towards Flexible Green Energy Technologies (ICEPE)*. IEEE, 2023.
- [8] K. Mohammadi, et al, "Asynchronous periodic distributed event-triggered voltage and frequency control of microgrids," *IEEE Transactions on Power Systems*. vol. 36, no. 5, p.p. 4524-4538, 2021.
- [9] Lin, Shin-Wen, and Chia-Chi Chu, "Distributed optimal consensus-based secondary frequency and voltage control of isolated AC microgrids," in *2nd International Conference on Smart Technologies for Power, Energy and Control (STPEC)*, 2021.
- [10] Ning, Boda, Qing-Long Han, and Lei Ding, "Distributed finite-time secondary frequency and voltage control for islanded microgrids with communication delays and switching topologies," *IEEE Transactions on Cybernetics*, vol. 51, no. 8, p.p. 3988-3999, 2020.
- [11] S. Aminzadeh, M. T. Hagh, and H. Seyedi, "Reactive power coordination between solid oxide fuel cell and battery for microgrid frequency control." *Journal of Applied Research in Electrical Engineering*, vol. 1, no. 2, p.p. 121-130, 2022.
- [12] S. Arunima, and B. Subudhi, "Distributed control for accurate voltage/frequency regulation and power sharing in a microgrid," in *5th International Conference on Energy, Power and Environment: Towards Flexible Green Energy, Technologies (ICEPE)*, 2023.
- [13] E. Akbari, "A novel frequency and voltage control method for islanded micro-grid," in *9th Iranian Conference on Renewable Energy & Distributed Generation (ICREDG)*, 2022.
- [14] M. Abasi, M. F. Nezhadnaeini, M. Karimi, N. Yousefi, "A novel meta heuristic approach to solve unit commitment problem in the presence of wind farms," *Revue roumaine des sciences techniques Série Électrotechnique et Énergétique*, vol. 60, no. 3, p.p. 253-262, 2015.
- [15] G. Himanshu, A. Verma, and T. S. Bhatti, "DOBC-based frequency & voltage regulation strategy for PV-diesel hybrid microgrid during islanding conditions," *Renewable Energy*, vol. 196, p.p.883-900, 2022.
- [16] Sh. Hou, J. Chen, and G. Chen, "Distributed control strategy for voltage and frequency restoration and accurate reactive power-sharing for islanded microgrid," *Energy Reports*, vol. 9, p.p. 742-751, 2023.
- [17] M.H. Mousavi, H. M. Cheshmeh Beigi, and M. Ahmadi, "A DDSRF-based VSG control scheme in islanded microgrid under unbalanced load conditions," *Electrical Engineering*, vol. 105, no. 6, p.p. 4321-4337, 2023.
- [18] M. F. Nezhadnaeini, M. Hajivand, M. Abasi, S. Mohajerami, "Optimal allocation of distributed generation units based on different objectives by a novel version group search optimizer algorithm in unbalance load system," *Revue roumaine des sciences techniques*

Série Électrotechnique et Énergétique. vol. 61, no. 4, pp. 338–342, 2016.

- [19] M. Dashtdar, et al, "Improving the power quality of island microgrid with voltage and frequency control based on a hybrid genetic algorithm and PSO," *IEEE Access*, vol. 10, p.p. 105352-105365, 2022.
- [20] Sepehrzad, Reza, et al, "Optimal energy management of distributed generation in micro-grid to control the voltage and frequency based on PSO-adaptive virtual impedance method," *Electric Power Systems Research*, vol. 208, 2022.
- [21] Zh. Wu, and H. Cheng, "Fixed-time control of distributed secondary voltage and frequency for microgrids considering state-constrained," *Electrical Engineering*, p.p. 1-13, 2023.
- [22] Grover, Himanshu, Ashu Verma, and T. S. Bhatti, "A fast and robust DOBC based frequency and voltage regulation scheme for future power systems with high renewable penetration." *Energy Conversion and Economics*, vol. 4, no. 4, p.p. 276-291, 2023.
- [23] M. Zhai, et al, "Distributed secondary voltage control of microgrids with actuators bias faults and directed communication topologies: Event-triggered approaches," *International Journal of Robust and Nonlinear Control*, vol. 32, no.7, p.p. 4422-4437, 2022.
- [24] Pham, Xuan Hoa Thi, "Improved power controller for enhancement of voltage quality in microgrid," *The Journal of Engineering*, vol. 2022, no. 8, p.p. 773-787, 2022.
- [25] M. Abasi, A. T. Farsani, A. Rohani, and M. A. Shiran, "Improving differential relay performance during cross-country fault using a fuzzy logic-based control algorithm," in *5th Conference on Knowledge-Based Engineering and Innovation, Iran*, 2019. IEEE Index.
- [26] M. Abasi, A. T. Farsani, A. Rohani, and A. Beigzadeh, "A novel fuzzy theory-based differential protection scheme for transmission lines," *International Journal of Integrated Engineering*, vol. 12, no. 8, pp. 149-160, 2020.
- [27] M. M. Seron, J. H. Braslavsky, and G.C. Goodwin, "MIMO control. In: Fundamental limitations in filtering and control," *Communications and Control Engineering*. Springer, London, 1997.
- [28] E. A. A. Coelho, P. C. Cortizo, and P. F. D. Garcia, "Small-signal stability for parallel-connected inverters in stand-alone AC supply systems," *IEEE Transactions on Industry Applications*, vol.38, Issue.2, 2002.
- [29] M. Abasi, N. Heydarzadeh, and A. Rohani, "Broken conductor fault location in power transmission lines using GMDH function and single-terminal data independent of line parameters," *Journal of Applied Research in Electrical Engineering*, vol. 1, no. 1, 2021.

BIOGRAPHY



Ali Morsagh Dezfali was born in Dezfal, Iran in 1992. He received his B.Sc. degree from the Jundi-Shapur University of Technology of Dezfal, Dezfal, Iran in 2015 and his M.Sc. degree from Shahid Rajae Teacher Training University, Tehran, Iran in 2017, both in Power Electrical Engineering. He is currently a Ph.D. candidate in Power Electrical Engineering at Shahid Chamran University, Ahvaz, Iran. His research interests are voltage and frequency control of microgrids, power electronics, FACTS devices, and power system protection.



Mahyar Abasi was born in 1989 in Iran. He graduated with a Ph.D. in Electrical Power Engineering from Shahid Chamran University, Ahvaz, Iran in 2021. He has more than 60 published journal and conference papers, more than 10 authored books, 11 industrial research projects, and a patent in power systems. In 2021, he was introduced as the top researcher of Khuzestan province, Iran, and in the years 2021 to 2023, he was successful in receiving four titles from the membership schemes of the National Elite Foundation in Iran. He is currently an assistant professor in the Electrical Engineering department of Arak University, Arak, Iran. His specialized interests are fault protection, detection, classification, and location in HVAC and HVDC transmission lines, control of reactive power and FACTS devices, evaluation and improvement of power quality, and power system studies.



power electronics.

Mohammad Esmail Hassanzadeh received his MSc. and Ph.D. degrees from the Shiraz University of Technology, Iran, in 2015 and 2022, respectively. He is currently an assistant professor in electrical engineering at Firouzabad Higher Education Center, Shiraz University of Technology. His research interests include power system stability and optimization, microgrids, renewable energies, FACTS devices, and

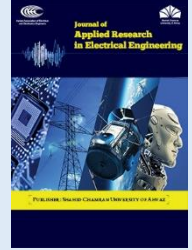


Mahmood Joorabian was born in Iran in 1961. He received his BEE degree from the University of New Haven, CT, USA, M.Sc. degree in Electrical Power Engineering from Rensselaer Polytechnic Institute, NY, USA, and a Ph.D. degree in Electrical Engineering from the University of Bath, Bath, UK in 1983, 1985 and 1996, respectively. He has been with the Department of Electrical Engineering at Shahid Chamran University, Ahvaz, Iran, as a Senior Lecturer (1985), Assistant Professor (1996), Associate Professor (2004), and Professor (2009). His main research interests are fault location, FACTS devices, power system protection, power quality, and applications of intelligence techniques in power systems.

Copyrights

© 2024 Licensee Shahid Chamran University of Ahvaz, Ahvaz, Iran. This article is an open-access article distributed under the terms and conditions of the Creative Commons Attribution NonCommercial 4.0 International (CC BY-NC 4.0) License (<http://creativecommons.org/licenses/by-nc/4.0/>).





Research Article

Solving Combined Economic Emission Dispatch Problem Using the Rain Optimization Algorithm

Narges Yousefi¹, Mahmood Joorabian^{2,*}, and Mahyar Abasi^{3,4}

¹ Department of Electrical Engineering, Institute for Higher Education, ACECR, Khuzestan, Iran

² Department of Electrical Engineering, Faculty of Engineering, Shahid Chamran University of Ahvaz, Ahvaz 61357-85311, Iran

³ Department of Electrical Engineering, Faculty of Engineering, Arak University, Arak 38156-8-8349, Iran

⁴ Research Institute of Renewable Energy, Arak University, Arak 38156-8-8349, Iran

* Corresponding Author: mjoorabian@scu.ac.ir

Abstract: An obstacle in managing economic dispatch is the integration of diverse factors such as pollution and heat. By introducing the price penalty coefficient, this class of two-objective problems is transformable to a single-objective form. The formulation considers various practical constraints of the system, including non-smooth cost functions, the balance of production, demand, and losses, and the limitation of power generation by active generators. One of the fundamental difficulties in tackling these types of complex problems lies in the algorithms and solvers employed to identify optimal solutions for a range of operation problems. The rain optimization algorithm (ROA) has been utilized in this paper. ROA is derived from the inherent tendency of raindrops to seek out the lowest areas on the earth's surface. This algorithm possesses exceptional efficacy in resolving problems characterized by stringent constraints and is adept at circumventing local optima. To validate the proposed method for cost and emission reduction, the scheme under consideration has been developed using software on standard systems. The implementation of the scenarios has revealed that the limits of the power system have led to a decrease in the overall generation cost of fossil fuel generation units. In this article, the ROA algorithm managed to plan the production with an optimal cost of 38481.54 dollars in case 1, which obtained a more optimal value than all the compared algorithms. This reduction in cost is considered one of the triumphs of the optimization problems. The results showcased and juxtaposed in the software simulation verify the effective performance of the suggested approach in comparison to prior research.

Keywords: Economic Emission Dispatch (EED), smooth cost function, penalty coefficient, rain optimization algorithm.

Article history

Received 17 January 2024; Revised 23 April 2024; Accepted 14 May 2024; Published online 26 June 2024.

© 2024 Published by Shahid Chamran University of Ahvaz & Iranian Association of Electrical and Electronics Engineers (IAEEE)

How to cite this article

Narges Yousefi, Mahmood Joorabian, and Mahyar Abasi, "Solving combined economic emission dispatch problem using the rain optimization algorithm," *J. Appl. Res. Electr. Eng.*, vol. 3, no. 1, pp. 19-32, 2024.

DOI: [10.22055/jaree.2024.45869.1102](https://doi.org/10.22055/jaree.2024.45869.1102)



NOMENCLATURE	
Variables	Description
F_i	i-th power plant fuel cost
F_{cost}	Total power plant fuel cost
a_i, b_i, c_i, d_i	Cost coefficients of i-th power plant
P_d	System consuming power
P_L	Transmission line loss
	Minimum admissible power generation in i-th power plant
$P_{i,min}$	

$P_{i,max}$	Maximum admissible power generation in i-th power plant
n	Number of power plants
e_i, f_i	Return coefficients of knee points of i-th power plant cost
B_{ij}, B_{oi}, B_{oo}	Transmission line loss function coefficients
h_i	Utilization factor
φ_T	The value of the balance coefficient
w_1, w_2	Wight coefficient
E_{cost}	Total power plants pollution amount

α	drop percentage volume that can be absorbed, depending on the soil property
$\beta_i . \gamma_i . c_i . \lambda_i$	power plants pollution coefficient
M	Daily hours
m	An hour of the day and night
UR_i	Maximum ramp rate
E_{cost}	Total power plant emission cost
B	Inequality constraints
PS	Pattern Search
L	Transmission line losses
R	Ramp rate
LR	Lagrange relaxation
LI	Lambda Iteration
MHBA	Hybridizing bat algorithm with artificial bee colony
QP	Quadratic Programming
NR	Newton-Raphson
ANN	Artificial Neural Networks
AHNN	Adaptive Hopfield neural network
DHS	Differential harmony search method
HPSO-GSA	Hybrid Particle swarm optimization and Gravitational search algorithm
JAYA-TLBO	JAYA and Teaching learning-based optimization

P_G	Power plants total power generation based on pollution power flow
r_1 and r_2	Drop radius
R	Total radius
DR_i	Minimum ramp rate
A	Constraints of equality
V	Valve-point loading effects
N	Voltage limits
P	Prohibited Operating Zones
T	Start time limit
BBO	Biogeography-based optimizer
GA-WOA	Genetic algorithm-whale optimization algorithm
DE-CQPSO	Differential evolution-crossover quantum PSO
IABC	Incremental artificial bee colony
CBBO	Improved biogeography-based optimization
GA	Genetic algorithm
PSO	Particle swarm optimization
DE	Differential evolution
DE-BBO	Differential evolution-Biogeography-based optimizer

1. INTRODUCTION

1.1. Research Motivation

Industrialized nations have endeavored to substitute renewable energies for fossil fuels since the 19th century, driven by concerns over air pollution, climate change, and escalating fuel expenses. The studies on power system operation indicate that the concern of economic-emission dispatch (EED) is focused on efficiently supplying the anticipated generation for loads while maintaining a balance between generation and demand. The utilization of contractive methods typically yields favorable outcomes. However, when the research space becomes non-linear and non-continuous, the problem-solving process gets highly intricate and the convergence of this strategy to find the ideal solution occurs at a notably slow pace. One of the issues that is important for the power grid today is the cost of production, but with international commitments, the issue of reducing pollutant emissions has also become one of the concerns of producers. Therefore, manufacturers should think of a method for cheap production and at the same time without producing pollution. One of the solutions that can help to solve this problem is the optimal planning of the production of power plant units. Various methods have been proposed to solve these problems. In general, these methods are divided into three categories: classical, meta-heuristic and artificial intelligence. Among them, artificial intelligence and meta-heuristic methods are more popular than classical methods due to their speed and accuracy. In this article, ROA meta-heuristic method is used to solve the EED problem.

1.2. Research Background and Literature Review

The EED problem has been solved by various optimization methods based on numerical and metaheuristic methods, which have been briefly examined in this section. In general, these methods can be classified into three categories, which include classic or traditional, modern, and combined methods. The objective of optimization is to identify the optimal solution that meets the constraints and requirements of the problem. Multiple options may exist, and the ideal solution is chosen after conducting a thorough comparison. Traditional methods are generally based on iteration techniques, which face issues such as high number of iterations and huge calculations, and finally, even in different states of the system, there is a possibility of divergence. The other category is the new methods which are defined based on the search space and have subsets of stochastic, heuristic, metaheuristic, etc., where all possible solutions are examined and finally the best solution is selected. Yet, in multi-objective problems where the objective function is transformed into a single function with defined variables, and considering the need to correct the problems of the previous two methods, the combined method helps significantly in the optimization problem and ultimately leads to more accurate solutions. However, not all these methods can solve all the optimization problems with non-smooth, non-continuous functions in the nonlinear solution space with acceptable efficiency, considering that research space is evolving and innovating. In the following, articles related to the described methods are reviewed. Power plants use the process of energy conversion to produce electricity, and the main costs of electricity production have roots in fuel costs. On the one hand, the ability to produce electricity with a high capacity is important, which can be achieved by using coal-fueled

steam power plants. Moreover, reducing the negative effects on the environment is an issue that can be investigated. It is necessary to manage the system by optimizing the economic problem and reducing greenhouse gas emissions. In recent years, economic power distribution in systems has been the focus of researchers, but the problem of pollution caused by fossil fuels has not been paid special attention in these studies. In the proposed model, the problem will be transformed into an economic-emission multi-objective function, and in the same way, a new model of the said problem will be presented, where the optimization algorithm will be investigated to solve the economic power distribution problem by considering the pollution function in multi-area power systems, the general concept of which can be defined in different structures. Algorithms used are classified according to their results into traditional, modern, and combined methods, each of which has been investigated to solve the issues of the previous methods. To validate the efficacy and application of the suggested approaches, different test systems have been used under different practical conditions. Table 1 summarizes the widely used systems in power planning problems.

1.2.1. Review of conventional EED methods

Conventional (traditional) techniques are among the common methods when it comes to solving the economic power/pollution problem. Among them are quadratic programming method, Newton-Raphson method, Lambda iteration, and Lagrangian relaxation [1-5]. The quadratic programming method was first developed [1-2] to deal with the economic dispatch problem by taking the line current limitations into account. The formulation of the problem with this method enables adopting a linear network model and operational constraints besides the explicit presentation of the costs exposed by transmission loss. After that, the Newton-Raphson technique was adopted [3] to address the economic dispatch problem by observing the same line current constraints. This method was formulated based on a Jacobian replacement matrix with transmission losses in terms of sensitivity factors, line current, and line resistance. The convergence of the mentioned method was achieved linearly with a very low speed. Next, the Lambda iteration technique was discussed [4] and implemented on 3, 6, 13, and 26-unit test systems. The method presented directly calculates the optimal value of Lambda for a certain power demand and is considered an efficient method for online information transmission.

In that method, generator limitations and transmission line losses were considered as problem constraints to prove its efficiency. Among other traditional methods, one can mention the technique based on Lagrangian relaxation for the EED problem [5]. In this reference, limitation on the generator, line current, and transmission line losses were considered. To perform this dispatch, the operation point of the system and network losses are also considered in the optimization process.

Issues such as the limitation of generators, line current, voltage profile, line losses, etc. are considered in these methods for the EED problem and finding the best optimal solution [6]. By carefully examining the mentioned methods, it can be seen that all of them have a high

Table 1: Introducing the test systems adopted for solving the economic/emission dispatch problem.

TEST SYSTEM	NUMBER OF THERMAL GENERATION UNITS
Test system 1	3- IEEE3 ELD
Test system 2	4- GENERATION
Test system 3	5- IEEE14 BUS
Test system 4	6- IEEE30 BUS
Test system 5	6- IEEE26 BUS
Test system 6	7- IEEE57 BUS
Test system 7	8- IEEE25 BUS
Test system 8	10- IEEE39 BUS
Test system 9	10- IEEE24 BUS
Test system 10	13- IEEE13 ELD
Test system 11	14 -GENERATION
Test system 12	15- GENERATION
Test system 13	19- IEEE118 BUS
Test system 14	20 GENERATION
Test system 15	26 GENERATION
Test system 16	30 GENERATION
Test system 17	38 GENERATION
Test system 18	40- IEEE13 ELD
Test system 19	54 GENERATION
Test system 20	57 GENERATION
Test system 21	69- IEEE300 BUS
Test system 22	110 GENERATION
Test system 23	120 GENERATION
Test system 24	140 GENERATION

dependence on the initial solutions and also have a weak convergence or finally converge with some local optima, even in some solutions, the solution diverges. Regrettably, this technique is also accompanied by two fundamental limitations. Firstly, this approach is unsuitable for resolving non-convex or non-linear problems. Secondly, due to the high calculation time and sometimes exponential calculation time, it was unable to effectively handle a significant amount of inequality constraints, and it controlled and improved only one solution in one run, failing to solve two-variable problems.

1.2.2. Review of recent EED methods

The methods that are included in this category are based on education-oriented, innovative, or meta-heuristic methods. Among the famous techniques of this category that were used for the EED problem are the methods of artificial neural networks, improved artificial bee colony optimization algorithm, improved biogeography optimization algorithm based on the Cauchy operator, the differential evolutionary optimization algorithm, the elitist multi-objective evolutionary optimization algorithm, and the particle swarm optimization algorithm [7-14]. Solving the economic dispatch problem by considering the piecewise quadratic cost function, based on the adaptive Hopfield artificial neural networks method, was proposed [7]. The method was tested on 3, 4, 40 and 120-unit test systems and its successful results confirmed the performance of the suggested scheme. An improved incremental artificial bee colony method was used to deal with the EED problem by observing the constraints of generators and transmission line losses [8]. Based on the local search with better convergence efficiency, modifications to the classical artificial bee colony algorithm further improved the performance and provided near-optimal solutions. In [9-10], the biogeography-based

optimizer algorithm and improved biogeography-based optimization methods were presented to address the EED problem. In [9], the problem of the convex nonlinear cost function minimization was considered, where the voltage and current constraints of the transmission line were added to the problem constraints. In [10], based on the Cauchy operator with improved capabilities of local and global exploration and convergence rate, the biogeography optimization algorithm applied to the EED problem achieved more suitable results. In another study, the EED problem was addressed using a differential evolutionary optimization algorithm in the form of a multifaceted nonlinear problem [11]. The results of this technique showed that the solution converged on the local optimum and performed poorly for more complex calculations. The EED problem was presented [12-13] using the basic method of genetic optimization algorithm as well as its improved method in the form of an elitist multi-objective evolutionary algorithm. This technique provided possible solutions and, as a result, a more suitable Pareto optimal front than the multi-objective problem, which presented a better view of the solution space. Another stochastic optimization approach called particle swarm optimization was employed by [13]. This approach offers numerous benefits that are well-suited for non-convex optimization problems characterized by stringent constraints. The effectiveness of the suggested technique was assessed in a system consisting of 10 units, taking into account limitations on the generator, valve-point loading effects, and transmission losses. In another study, the economic-environmental dynamic dispatching problem including wind energy, solar photovoltaic, thermal and water power plants, taking into account the limits of slope rate limits and the influence of valve-point loading, was solved by adopting the multi-objective particle swarm optimization [14].

1.2.3. Review of combined EED methods

In the combined methods, several algorithms are used to benefit their advantages and reduce their weaknesses in solving more complicated problems. So, they are impactful in finding global optimal solutions of economic power/pollution problems with different constraints. In [15], the combination of differential evolutionary and biogeographic algorithms was presented to solve the problem of EED of thermal power plants in power systems. The combination of both methods increased the accuracy and speed of the implementation results on the EED problem. In [16], the challenge of non-convex economic dispatching was solved by combining differential evolutionary mechanisms and harmony search algorithm. In that study, the proposed method was tested on 6, 10, 13, 15, 24, and 40 generation units with constraints such as the effects of valve-point loading, multi-fuel, slope rate limits, and prohibited operating zones. In [17], a new combination of Java methods and teaching-learning-based optimization was utilized to solve the challenge of economic distribution in non-convex and non-smooth conditions. The method was tested and evaluated on 5, 10 and 40-unit systems. The accuracy and speed of the results compared to other methods were also examined. Reference [18] presented a combination of the non-dominant elitist sorting algorithm and a modified distance-crowding sorting method to obtain a Pareto optimal front with a uniform distribution for EED

problem. In that reference, the slope rate limits and the prohibited operating ones were modeled on three standard IEEE 6, 19, and 57-unit systems to evaluate the proposed method. In [19], a method based on the combination of bat-inspired algorithm and artificial bee colony with search strategy to solve large-scale, highly nonlinear, non-convex, non-smooth, non-differential, and non-continuous problems related to EED problem was introduced. In [20], a method composed of genetic algorithm and whale optimization was presented to obtain global optimal results for EED problems. The efficacy of this proposed methodology was examined on four distinct test systems and its performance was contrasted with other heuristic approaches. In [21], to solve the challenge of EED, a method relying on the combination of particle swarm optimization and time-varying acceleration coefficient was proposed.

The distribution of greenhouse gas emissions considered in this reference consisted of multi-objective optimization problems of combined economic-environmental dispatching of heat and power and dynamic economic-environmental dispatching taking into account various operational limitations. The main theoretical solutions and innovations presented in that study proposed a new test case by observing the maximum practical limitations such as the limits of the slope rate, the prohibited operating zones, and the creation of a novel methodology to choose the most optimal compromise options and guarantee a diverse range of Pareto solutions that are more suitable for economic-environmental dynamic dispatch problems. And finally, a hybrid method called Differential Evolutionary Crossover Quantum Particle Swarm Optimization Algorithm was introduced [22] to deal with the EED problem. In that research, the authors took advantage of the rapid convergence of the differential evolutionary approach and the diversity of particles of genetic algorithm crossover operators. Table 2 summarizes the methods presented in the reviewed references.

1.3. Contributions and Novelty

The contribution and innovation of this article is to solve EED problem based on rain optimization algorithm (ROA). In general, this article has two main contributions and objectives. The first objective is to formulate and solve the problem of economic dispatch combined with the pollution emission caused by the emission of greenhouse gases in fossil fuel power plants using the ROA method. The second objective is to consider the practical limitations in the EED problem. Since the cost function of a fossil fuel power plant is not smooth in practice and has knee-shaped points on the third curve, EED will be investigated considering this limitation. In summary, the innovations of this article are as follows:

- Solving the ED problem with two objective functions to reduce cost and pollutant
- Using the new ROA algorithm to optimize the ED problem
- Checking and verifying the results obtained with other methods

1.4. Paper Organization

The subsequent sections of the paper are structured as follows. Section 2 presents the modeling of the EED problem, and then using the ROA for deal with the problem is fully introduced. In Section 3, implementation of the scheme in standard networks in MATLAB software are presented. Also, in this section, the test results of the suggested algorithm and those presented in the background research are reviewed in detail, and eventually, Section 4 provides the conclusion of the paper.

2. PROPOSED METHOD

This section presents solving the emission dispatch problem based on the ROA method. In order to explain the problem, the equations and formulation of economic dispatch are first given, then the emission dispatch problem and the combination of these two dispatches are provided in the form of EED in the next subsections. In the rest of this section, the general theory of the ROA and finally the complete flowchart of the implementation of the EED problem are provided.

2.1. Economic Dispatch

The economic dispatch problem minimizes the fuel cost function for the generation of a certain amount of power while satisfying the restrictions governing the generation. In this paper, the fuel cost function is modelled using a smooth quadratic and a cubic function. However, in fact, the cost function is not smooth and has local maxima and minima. To show this feature of the quadratic cost function and the second part of the function, the absolute

value cost is a sinusoidal function, which are called non-smooth functions [14]. For this purpose, the cost of fuel used to produce P_i in the i th power plant is determined by F_i .

2.1.1. Smooth Quadratic Function of Fuel Cost

In this model, the smooth quadratic function of fuel cost is given in terms of the power generation of the power plant. Equations (1) and (2) show the model considered in this paper.

$$\text{minimize } F_{cost} = \sum_{i=1}^n (a_i + b_i P_i + c_i P_i^2) \tag{1}$$

$$F_{cost} = F_1 + F_2 + \dots + F_n \tag{2}$$

2.1.2. Non-smooth Function of Fuel Cost

The non-smooth function of fuel cost is provided in (3) for minimization purposes.

$$\text{minimize } F_{cost} = \sum_{i=1}^n a_i + b_i P_i + |e_i \times \sin(fi (P_{imin} - P_i))| \tag{3}$$

2.1.3. Constraints

The problem constraints, including the generation and consumption equality condition, taking into account losses, generation limits of generators, and applying the slope rate of power plants, are given in (4)-(8).

Table 2: Summary and summation of previously presented algorithms based on references

	Ref.	Optimization method	Test system	Abbreviated constraints											
				A	B	C	M	N	P	L	R	T	V	S	LF
Traditional methods	[1]	LR	1-4-8												
	[2]	LI	1 and 1-5												
	[3]	PS	3-1-10-18-3-8												
	[4]	QP	3-11-13-16-20												
Novel methods	[5]	NR	3-4-7												
	[7]	ANN	1-2-18-23												
	[8]	AHNN	1-4												
	[9]	BBO	1-4-5-10-14-18-22												
	[10]	IABC	1-3-4-18												
	[11]	CBBO	4-5-18												
	[12]	GA	1-4												
	[13]	PSO	1-3-4-13												
Combined methods	[14]	DE	5												
	[15]	DE-BBO	1-4												
	[16]	DHS	10-18												
	[17]	HPSO-GSA	1-10-18												
	[18]	JAYA-TLBO	5-9-10												
	[19]	MHBA	2-10												
	[20]	CSA-BA-ABC	8												
	[21]	GA-WOA	1-3-8-18-20												
	[22]	DE-CQPSO	4-9												

$$\sum_{i=1}^n P_i = P_d + P_L \quad (4)$$

$$P_L = \sum_{i=1}^n \sum_{j=1}^n P_i \cdot B_{ij} \cdot P_j + \sum_{i=1}^n B_{oi} \cdot P_i + B_{oo} \quad (5)$$

$$P_{i,\min} \leq P_i \leq P_{i,\max} \quad (6)$$

$$P_{i,m} - P_{i(m-1)} \leq UR_i \quad i \in n . m \in M \quad (7)$$

$$P_{i(m-1)} - P_{i,m} \leq DR_i \quad i \in n . m \in M \quad (8)$$

Fig. 1 shows the fuel cost function model of power plants with smooth functions considering the slope rate of power plants.

2.2. Emission Dispatch

The main goal of solving emission dispatch problems is to reduce the output emission of power plants. By examining the amount of pollutant, i.e., NO_x and SO_x output from power plants, it is seen that many factors impact the emission rate of power plants, the most important of which is the active power output. The relationship between these two variables is nonlinear.

The simplest emission model according to the ISO standard for emission dispatch is a quadratic function. However, the research shows that the emission cost function of a power plant is assumed to be the sum of a quadratic function and an exponential function in terms of active power generation so that a more accurate solution can be achieved [15].

2.2.1. Smooth quadratic function of fuel cost

Equations (9) and (10) express the minimization and smooth functions of fuel cost:

$$\text{minimize } Ecost = \sum_{i=1}^n (\alpha_i + \beta_i P_i + \gamma_i P_i^2) \quad (9)$$

$$E_{cost} = E_1 + E_2 + \dots E_n \quad (10)$$

2.2.2. Non-smooth function of fuel cost

Equation (11) presents the non-smooth function model of fuel cost.

$$\text{minimize } Ecost = \sum_{i=1}^n (\alpha_i + \beta_i P_i + \gamma_i P_i^2 + \delta_i e^{\lambda_i P_i}) \quad (11)$$

Fig. 2 illustrates the emission cost functions of plants using non-smooth functions.

2.3. EED Problem

Economic dispatch and emission dispatch problems are used together in this part of the paper to optimize fuel cost and reduce the amount of emission of power plants. The formulation of the EED problem is provided by considerations made on the objective functions of economic dispatch and emission dispatch.

The multi-objective EED problem becomes a single-objective problem by defining the price penalty coefficient.

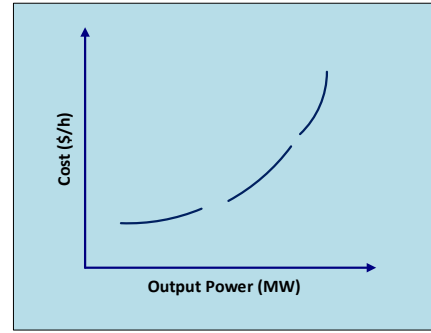


Fig. 1: Fuel cost functions of power plants with smooth functions by applying the slope rate of power plants.

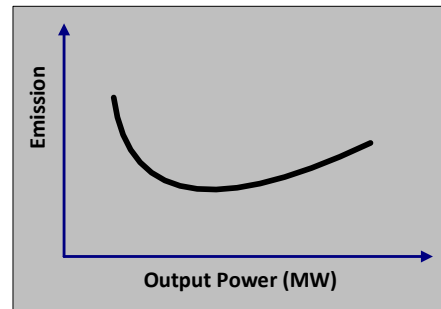


Fig. 2: Model of emission cost functions of power plants with non-smooth functions.

The price penalty coefficient method is proposed based on the PSO algorithm to obtain the optimal Pareto curve, which is one of the best possible solutions to solve the EED problem. The optimal Pareto curve shows the relationship between the results of economic and emission dispatches, and the optimal point of this curve is obtained by determining the penalty coefficient of power plants.

The EED can find the optimal point from the Pareto curve considering the objectives of the problem, i.e., the cost and emission reduction. To convert the multi-objective EED into a single-objective problem, the penalty coefficients of power plants must be obtained.

The necessary equations to implement the proposed method are given in Equations (12)-(17).

$$P_{G_i} = \frac{(\lambda - \beta_i)}{2\gamma_i} MW \quad (12)$$

$$\begin{cases} \min \Phi_T = \sum_{i=1}^n [F_i(PG_i) \cdot E_i(PG_i)] \\ \min \Phi_T = \sum_{i=1}^n [F_i(PG_i)] + h_i \sum_{i=1}^n [E_i(PG_i)] \end{cases} \quad (13)$$

$$h_i = \frac{F_i(P_{i,max})}{E_i(P_{i,max})} \quad (14)$$

Thus, the cost and emission functions in (13) are transformed into the objective function.

$$\left\{ \begin{array}{l} F_1 = \sum_{i=1}^n [F_i(PG_i)]; F_2 = \sum_{i=1}^n [E_i(PG_i)] \\ F_{total} = \sum_{i=1}^n (a_i + h_i\alpha_i) + (b_i + h_i\beta_i)P_i \\ \quad + (c_i + h_i\gamma_i)P_i^2 \\ F_{total} = F_1 + h_iF_2 \end{array} \right. \quad (15)$$

By defining the mass coefficient w_1 and w_2 , the relationship between the total cost of EED can be calculated based on the cost obtained from economic dispatch, F_1 , and emission dispatch, F_2 :

$$F_{total} = W_1F_1 + hW_2F_2 \quad (16)$$

$$if \left\{ \begin{array}{l} W_1 + W_2 = 1 \\ W_1 = W \end{array} \right. \rightarrow W_2 = 1 - W$$

$$F_{total} = W_1F_1 + (1 - W)hF_2 \quad (17)$$

$$if \left\{ \begin{array}{l} W = 1 \\ W = 0 \end{array} \right. \rightarrow \begin{array}{l} F_{tot} = F_1 \\ F_{tot} = F_2 \end{array}$$

For $w=1$ and $w=0$, the economic/emission dispatch equation is transformed into the economic and emission dispatch equations, respectively.

Overall, the aim of performing EED is to obtain the mass coefficient in the range of $0 \leq W \leq 1$ so that an optimal point is found on the Pareto curve [23].

2.4. Rain Optimization Algorithm

Metaheuristic optimization methods are employed to address intricate global challenges across several domains. These algorithms aim to replicate natural processes by employing iterative sequences to discover a rapid and efficient resolution to complex issues. This section aims to thoroughly investigate the behavior of rain.

A raindrop can serve as a model for any solution. In certain issue scenarios, certain points inside the solution space are chosen at random, analogous to the random distribution of raindrops on the ground. The primary characteristic of every raindrop is its radius. Over time, the radius of each raindrop undergoes a process of diminishing and subsequent enlargement when the raindrop merges with other drops. After the initial population of solutions is created, the radius of each drop can be randomly decided within an appropriate range.

During each iteration, every droplet examines its immediate environment based on its size. Isolated droplets without any connections just consider the largest area they cover. When a problem is resolved in n -dimensional space, every individual element comprises n variables. Hence, the initial stage involves scrutinizing the lower and upper bounds of the variable, as these bounds are dictated by the drop's radius.

Subsequently, the two endpoints of the second variable are subjected to testing, and this process is repeated until the final variable is reached.

Currently, the cost of the first descent is being revised as it descends. These declines are not yet in their ultimate

stage, and although the cost function is lowering, it is moving downward in a consistent path.

This process is carried out for every individual instance, after which the expense and location of each instance are ascertained. Based on (18) and (19), the radius of each drop undergoes modifications in two distinct states:

1. If two drops with radii r_1 and r_2 are close to each other and have a common area with each other; they can join together to form a larger drop of radius R :

$$R = (r_1^n + r_2^n)^{1/n} \quad (18)$$

where, n is the number of variables in each drop.

2. If a drop of radius r_1 does not move, a percentage of its volume can be absorbed, depending on the soil property, denoted by α .

$$R = (\alpha r_1^n)^{1/n} \quad (19)$$

where, α is the proportion of drop volume that can be absorbed in each iteration, ranging from 0 to 100%. The minimum drop radius is denoted as r_{min} , and any drops with radii smaller than this value are excluded. It is evident that the population size reduces over a few iterations, and more significant declines occur with bigger amplitudes. Expanding the research range for each drop leads to a proportional improvement in the local search capability of the drops, corresponding to the size of the drops.

Consequently, as the number of iterations grows, the weak drops with low amplitude will either vanish or merge with stronger drops that have a wider radius. This will lead to a significant reduction in the original population, thereby expediting the discovery of accurate solutions.

The subsequent discussion outlines the fundamental distinctions between ROA and search-based algorithms. In the context of the ROA, the starting population number undergoes changes in each iteration as a result of neighboring drops attaching or being absorbed by the soil, despite the implementation of various search algorithms.

This challenge improves the algorithm's search capability and significantly reduces the cost of optimization. Following each repetition, the dimensions of each droplet undergo modifications as a result of neighboring droplets adhering to them or being absorbed by the soil. This action enhances the search capability of each item and classifies the items based on their significance. In numerous other search algorithms, every population (drop) in each iteration is composed of randomly chosen neighboring points, and the drop is randomly enhanced by one step. Conversely, in ROA, every drop identifies the optimal route to reach the minimal point. Once the path is discovered, it descends gradually, with the cost function decreasing in a single iteration.

This results in the rapid departure of the original population from the incompatible sites. Essentially, the technique requires the user to input specified parameters such as the beginning number of raindrops (population size) and the initial radius of each raindrop (search space) in the first stage. Subsequently, a numerical value is allocated to every droplet based on the cost function.

Subsequently, every droplet commences its descent. Hence, the cost function scrutinizes the endpoints of each drop. Once a droplet is set in motion, it will persist in its trajectory until it reaches a point of minimal elevation along its course. This scenario is replicated for every individual drop.

Along the path, nearby drops can join each other and significantly increase the speed of the algorithm. When a drop reaches the minimum point, its radius gradually decreases, thus significantly enhancing the response accuracy. This strategy enables the algorithm to identify all the largest (end) points of the objective function.

When it rains, raindrops fall on the surface of the earth. After some time, it is observed that some of these drops connect to each other and form more significant drops that can move under the influence of their force on the surface to places with a lower level of the earth's surface. Along the path, other amazing things happen to these drops. Some drops may move to other drops and join them, or some of each drop may vaporize or be absorbed depending on different soil properties such as the nature of the soil surface, including permeability, leakiness, and soil moisture. In addition, a portion of the soil undergoes dissolution in the water.

During this process, the drops that land on the level surface can be fully absorbed by the soil and vanish, whereas the ones that fall on the inclined area descend and merge with other drops, resulting in the formation of a water stream. Certain streams have the potential to interconnect and create a river.

Obstacles in the passage of streams or rivers can lead to the formation of lakes, highlighting the significance of water volume in such cases. Following the cessation of rainfall, the water currents and rivers converge into nearby lakes, and over time, smaller lakes may dissipate as a result of water evaporation or absorption by the soil. Therefore, depending on the surface topology and soil characteristics, only a few significant lakes remain.

These lakes represent a local minimum and deeper lakes represent a global minimum. As the type of rain changes, the previous scenario may change slightly. For example, if heavy rain is accompanied by large drops, all the drops will connect very quickly and, without absorption and evaporation, will lead to flooding. Only the global minimum can be discerned in this scenario, as all the local minima are interconnected as a result of intense rainfall.

In contrast, in the presence of light rain characterized by little droplets, the soil has the capacity to absorb all the drops, so preventing any runoff. Hence, it is evident that establishing the parameters when utilizing the ROA holds great significance. The particle movement in the suggested technique bears resemblance to slope-based optimization methods and conventional single-point algorithms, such as hill climbing, slope optimization algorithm, and rainfall optimization. These strategies iteratively tweak a single parameter to determine if modifying it enhances the cost performance. Nevertheless, the ROA employs a collection of answers that all converge towards the optimal outcome concurrently.

During each iteration of this movement, certain traits undergo changes. For instance, their dimensions may undergo alterations or they may vanish. Furthermore, the ROA has the capability to identify all points of maximum rather than solely minimum or maximum points. Fig. 3 shows the flowchart of the ROA.

2.5. The Ultimate Flowchart of the Proposed Algorithm

In this subsection, the final flowchart for solving the EED problem based on the ROA is given in a general format. The flowchart is designed in two blocks according to Fig. 4.

3. SIMULATION AND RESULTS

This section applies the ROA to deal with the EED problem. For evaluation and comparison purposes, the results obtained from the implementation of the suggested design together with similar optimization algorithms are used. The successful results of the implementation of the proposed design in comparison with the rest of algorithms confirm the acceptable performance of the suggested. Five

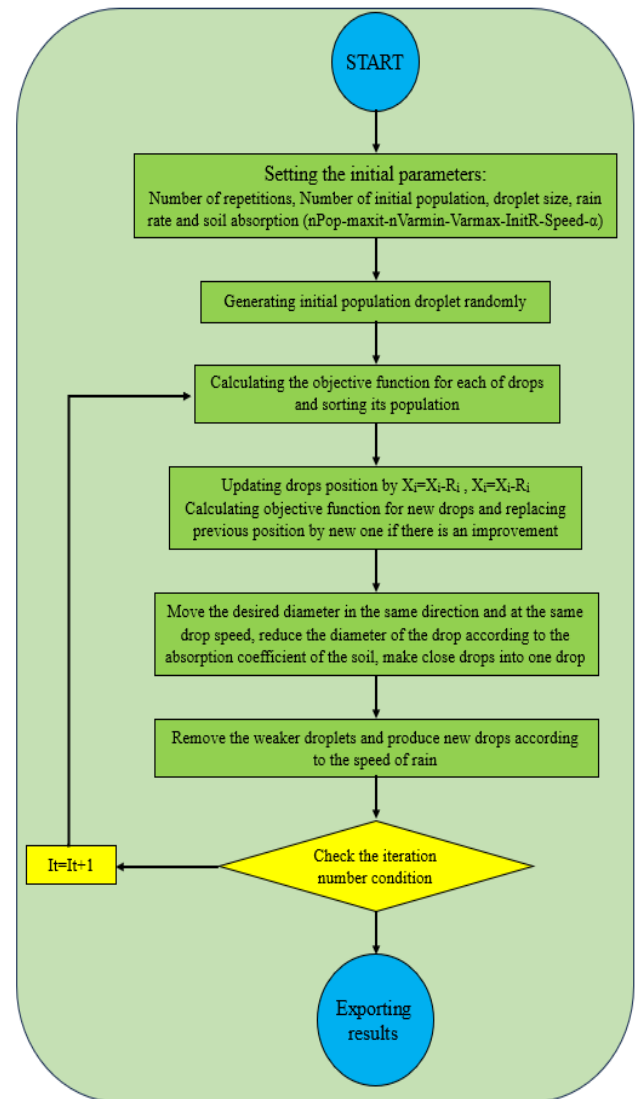


Fig. 3: Flowchart of the ROA [24].



Fig. 4: Flowchart of solving the EED problem by ROA.

different cases have been used for this evaluation. Table 1 lists the definitions of each of the cases. The information included for each case includes test system, number of units, power demand, heat demand, and system losses. In Table 3, the information required for each case is given. The power generation units provide function inputs in each case depending on the design of the problem so that it is possible to compare the emission rate and the fuel cost rate of each scenario according to the power consumption of the load. For each test system, the convergence behavior of the objective function can also be observed using the ROA method. All simulations were conducted on a computer using MATLAB software.

3.1. Evaluation of Case I

According to the information provided in Table 3, Case I includes three generator units. According to the results presented in Table 4, it can be seen in this test system that the technique proposed in this paper has outperformed the techniques presented in other references. According to the result obtained with the value of 11.658, the ROA optimized

the consumption of generator units to create a better fuel cost and emission rate and reduce losses. Next, Fig. 5 presents the convergence behaviour of the objective function by ROA. emission rate obtained using the ROA are presented in Table 5. By comparing the techniques mentioned in Table 5, it is observed that the ROA provides the lowest emission rate while the SFLA gives the best fuel cost.

3.2. Evaluation of Case II

In this scenario, simulations have been performed on the 10-bus test system. The optimal fuel cost and the target convergence behavior of the ROA for this scenario is shown in Fig. 6.

3.3. Evaluation of Case III Test System

Case III was simulated on the IEEE 30-bus system. Table 6 shows the optimal power allocation that provides the best fuel cost in this case. The convergence curve of the objective function concerning the best optimization report is provided in Fig. 7.

3.4. Evaluation of Case IV test system

Table 7 presents the outcomes of Case IV for various optimization strategies. The ROA yields the most favourable outcome for this system, while the CSOA ranks third in terms of performance. Fig. 8 illustrates the convergence of the objective function in this scenario.

3.5. Evaluation of Case V

For the experimental system of Case V, the power allocation achieved for fourteen generators is displayed in Table 8. Based on the comparison study and the data presented in the table, it can be concluded that the suggested algorithm has achieved the smallest fuel cost and emission rate. Furthermore, the Fig. 9 illustrates the convergence pattern of the objective function.

4. CONCLUSION AND FUTURE TRENDS

In this paper, the optimization of the EED problem was carried out using the ROA. To realize this, various limitations, such as cost functions with non-smooth points, reducing the amount of pollution, limitations of power generation, and considering losses as well as thermal power plants of the system are taken into account. In this research, the proposed algorithm was applied to reduce cost and emission in the EED model on 3, 10, 6, 40, and 15-unit systems. The findings of simulation confirmed the effectiveness of the ROA method in achieving the best solution for the problem. In this article, the ROA algorithm managed to plan the production with an optimal cost of 38481.54 dollars in case 1, which obtained a more optimal value than all the compared algorithms.

Also, in the case 2, the ROA algorithm was able to increase the value of the F_E function to 3886.7, which is much lower than other algorithms, and this shows the power of this algorithm in solving EED problems. In case 2, the ROA algorithm was able to reduce the value of the FC economic objective function to 1.1338, which is much lower compared to the PSO, GSA, KKO, etc. algorithms. In case 3, it can be seen that the FC and FE target function values for rain optimization algorithm are 603.65 and 0.2013, respectively. As the results of all three case studies showed, the ROA algorithm has been able to reduce the cost and environmental pollution in the best way in all cases, which indicates the strength and accuracy of this algorithm in finding the global optimum. A summary of the contributions of the paper include:

- Reduction of system losses compared to economic dispatch,
- Reduction of emission compared to economic dispatch, and
- Reduction of total cost compared to economic dispatch and emission dispatch

Table 3: Different cases considered for problem testing and evaluation

Problem	Case	No. of units	Power demand (MW)	Loss
CEED	Case I	3	500	∓
	Case II	10	2000	∓
	Case III	6	283.4	∓
	Case IV	40	10500	-
	Case V	19	950	∓

Table 4: Obtained results for Case I.

Case 1	G1	G2	G3	C	Fc	FE	LP
FA	128.884	192.585	190.282	39209.93	-	311.15	11.693
BA	128.828	192.579	190.285	39209.94	-	311.15	11.693
HYB	128.834	192.567	190.291	39209.96	-	311.15	11.693
GA	128.997	192.683	190.110	39220	-	311.27	11.696
PSO	128.984	192.645	190.063	39210.20	-	311.15	11.691
FPA	128.807	192.590	190.295	39210.15	-	311.155	11.693
MSFLA	128.338	191.946	191.389	32209.81	-	311.163	11.692
KKO	129.011	192.303	190.274	39199.7	25490.5	311.013	11.687
ROA	129.394	192.270	190.875	38481.54	25459.2	311.06	11.658

Table 5: Obtained results for Case II.

Case 2	NSGA-2	PDE	SPEA-2	GSA	PSO	EMOC	FPA	LFA	KKO	ROA
G1	51.9515	54.9853	5.97612	5.99924	55	55	53.188	5.99204	5.99234	57.654
G2	67.2584	79.3803	72.813	7.95869	80	80	79.975	7.86798	7.89148	79.548
G3	73.6879	83.9842	7.11288	7.43419	81.14	8.55943	78.105	7.71688	7.79468	83.538
G4	91.3554	86.5942	8.60883	85	84.213	8.60314	97.119	7.10558	8.74798	87.866
G5	134.0522	144.4386	1.24323	1.10634	1.33773	1.56324	152.74	1.62724	15.8149	145.79
G6	174.9504	165.7756	1.91887	1.56706	1.50866	1.24816	163.08	1.09365	16.5550	17.6510
G7	289.4350	283.2122	2.20238	2.87499	2.83389	300	258.61	2.99549	26.1742	288.77
G8	314.0556	312.7709	3.40232	3.23871	3.58241	3.34941	302.22	3.22190	30.8578	316.91
G9	455.6978	440.1135	4.88144	4.17754	4.33632	4.91831	433.21	4.32434	43.3070	430.88
G10	431.8054	432.6783	4.90252	4.63062	4.15984	4.31333	466.70	4.69473	46.0391	455.65
F _c	1.13539	1.1351	1.1352	1.1349	1.1342	1.13445	1.1337	1.13246	1.13481	1.1338
F _E	4130.2	4111.1	4109.1	4111.4	4120.1	4119.83	3997.7	4138.9	3988.52	3886.7

And, below are the suggestions for future studies:

- Implementing EED for systems with multi-piece fuel cost curve with non-smooth functions considering wind energy uncertainty, and
- Implementing EED by considering the dynamic model for the slope constraints of power plants and using virtual power plants for problem solving and investigating their effects.

Table 6: Obtained results for Case III.

Case 3	MHBA	FSBF	NSBF	KKO	ROA
G1	10.94	19.43	17.80	12.9546	13.6
G2	29.85	37.26	33.66	32.2445	38.7
G3	58.29	68.57	72.92	54.51935	70.5
G4	99.48	59.19	59.08	96.9029	87.6
G5	51.81	60.85	57.66	52.9564	58.9
G6	36.20	40.61	44.74	36.548	43.6
F_C	607.39	619.3679	619.6086	605.68	603.65
F_E	0.2208	0.2015	0.2027	0.217897	0.2013
LP	3.204	2.51	2.46	2.396	2.42

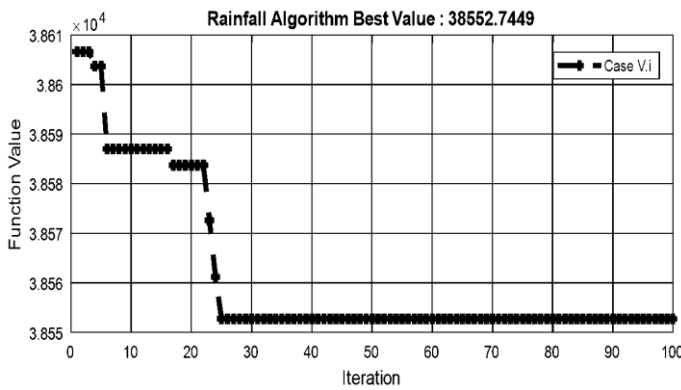


Fig. 5: Convergence behaviour of ROA objective function in Case I.

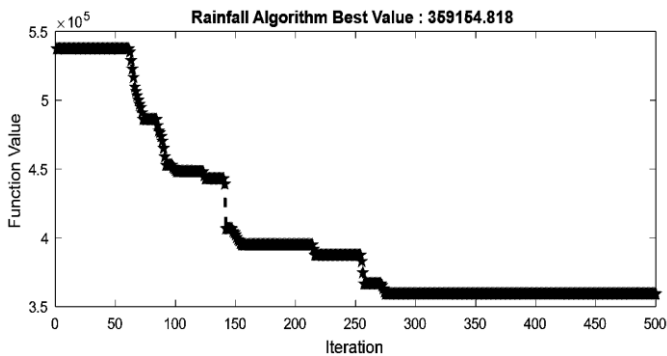


Fig. 6: Convergence behaviour of ROA objective function in Case II.

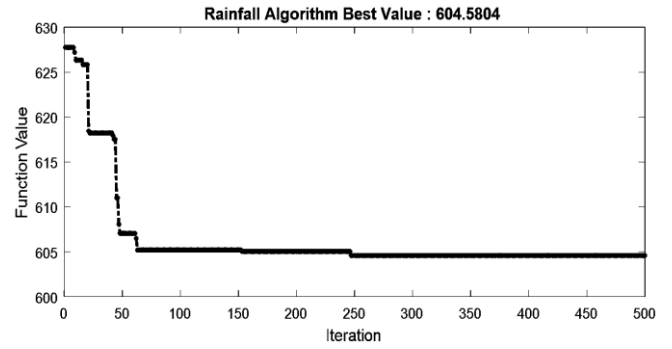


Fig. 7: Convergence behaviour of ROA objective function in Case III.

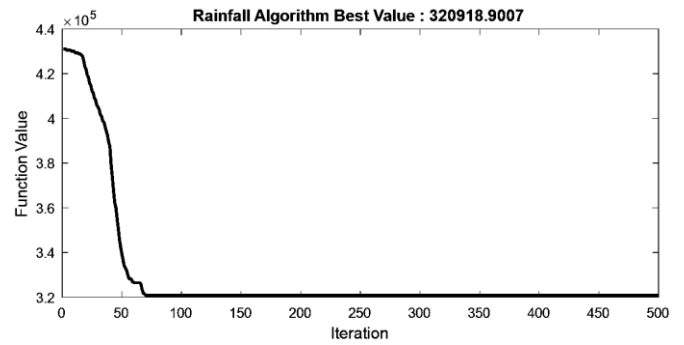


Fig. 8: Convergence behaviour of ROA objective function in Case IV.

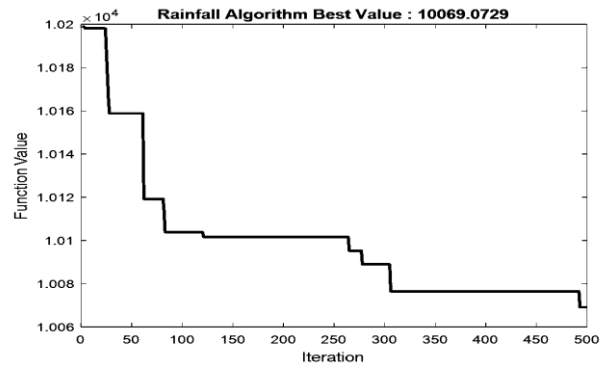


Fig. 9: Convergence behaviour of ROA objective function in Case V.

Table 7: Obtained results for Case IV.

Case 4	NSGA-II	SPEA-2	GSA	MABC	MABC	FPA	ISA	KKO	ROA
G1	113.8685	113.9694	113.9989	110.7998	110.8998	43.405	43.567	114	113.65
G2	113.6381	114	113.9896	110.7998	110.7998	113.95	113.56	113.045	113.47
G3	120	119.8719	199.9995	97.3999	97.3999	105.86	105.76	119.744	111.52
G4	179.94	179.9284	179.7857	174.5504	174.5486	169.65	169.43	181.102	180.6
G5	180.7887	97	97	87.7999	97	96.659	96.62	96.5081	96.66
G6	140	139.2721	139.0128	105.3999	105.3999	139.02	139.23	139.796	139.55
G7	300	300	299.9885	259.5996	259.9556	273.28	273.36	299.686	295.8
G8	299.0084	298.2706	300	284.5996	284.5996	285.15	285.15	298.619	288.76
G9	298.8890	290.5228	296.2025	284.5996	284.5996	241.96	241.54	289.447	290.5
G10	131.6132	131.4832	130.3850	130	130	131.26	131.26	131.386	132.5
G11	246.5138	244.6704	245.7475	318.1921	318.2129	312.13	312.12	241.114	250.6
G12	318.8748	317.2003	318.2101	243.5996	243.5996	362.58	362.45	318.381	350.3
G13	395.7224	394.7358	394.6257	394.2793	394.2793	346.24	346.34	395.689	395.8
G14	394.1369	394.6223	395.2016	394.2793	394.2793	306.06	306.06	393.82	395.1
G15	305.5781	304.7271	306.0014	394.2793	394.2793	358.78	358.54	305.891	355.4
G16	394.6968	394.7289	394.1005	394.2793	394.2793	260.68	260.23	394.283	394.8
G17	489.4234	487.9857	489.2569	399.5195	399.5195	415.19	415.26	489.706	489.43
G18	488.2701	488.5321	488.7598	399.5195	399.5195	423.94	423.56	487.897	488.3
G19	500.8	501.1683	499.2320	506.1985	506.1716	549.12	549.03	500.104	537.5
G20	455.2006	456.4324	455.2821	506.1985	506.2206	496.7	496.74	455.719	500.4
G21	434.6639	434.7877	434.45202	514.1472	514.105	539.17	538.76	434.334	520.4
G22	434.15	434.3937	433.8125	514.1455	514.1472	546.46	546.46	434.86	544.5
G23	445.8385	445.0772	445.5136	514.5237	514.5664	540.06	540.56	446.6	533.3
G24	450.7509	451.8970	452.0547	514.5386	514.4868	514.5	514.55	451	500.4
G25	491.2745	492.3946	492.8864	433.5196	433.5195	453.46	453.67	451.259	490.5
G26	436.3418	436.9926	433.3695	433.5195	433.5196	517.31	516.891	435.7721	500.6
G27	11.2457	10.7784	110.0026	10	10	14.881	14.345	11.079	12.45
G28	10	10.2955	10.0246	10	10	18.79	18.64	10.3466	15.4
G29	12.0714	13.7018	10.0125	10	10	26.611	26.578	12.2337	11.65
G30	97	96.2431	96.9125	97	87.8042	59.581	59.565	96.6001	96.1
G31	189.4926	190.0000	189.9689	159.733	159.733	183.48	183.36	189.436	188.76
G32	174.7971	174.2196	175	159.733	159.7331	183.39	182.87	175.188	176.5
G33	189.2845	190	189.0181	159.733	159.733	189.02	189.22	189.992	189.4
G34	200	200	200	200	200	198.73	198.65	198.679	199.8
G35	199.9138	200	200	200	200	198.77	198.76	199.89	198.6
G36	199.5066	200	199.9978	200	200	182.23	182.45	199.905	198.52
G37	108.3061	110	109.9969	89.1141	89.1141	39.673	39.635	108.554	109.89
G38	110	102.6912	109.0126	89.1141	89.1141	81.596	81.625	109.71	109.6
G39	107.7899	108.5560	109.4560	89.1141	89.1141	42.96	42.91	108.639	109.4
G40	421.5609	421.8521	421.9987	56.1879	506.1951	537.17	537.15	421.912	588.8
F _c	1.5283	1.2581	12.2587	1.24490903	1.2449116	1.23170	1.23034	1.25852	1.21
F _E	2.1095	2.1110	2.1093	2.56560267	2.5656026	2.0846	2.0643	2.10837	2.55

Table 8: Obtained results for Case V.

Case 5	CSAISA	ISA	HSA	DE	PSO	GA	KKO	ROA
G1	102.6468	100.3485	100.3839	100.5473	100.7363	100.8578	65.43	68.65
G2	59.1816	58.8270	58.6583	58.5372	58.2314	58.3547	75.2154	76.55
G3	50.0599	50.8309	50.8302	50.8474	50.5242	50.9973	69.7721	69.5
G4	70.3498	73.3932	73.5292	73.0932	73.3238	73.4352	76.7522	75.34
G5	63.1042	59.1153	59.1846	59.9323	59.7272	59.4636	78.5975	77.44
G6	51.0080	50.1468	50.9231	50.7397	50.2726	50.6254	74.8284	73.23
G7	50.0000	507470	50.2832	50.5360	50.8362	50.5363	64.9154	65.4
G8	51.0166	53.2494	53.0220	53.2324	53.5242	53.1321	64.005	65.5
G9	83.9497	85.1551	85.8231	85.4235	85.4355	85.3546	73.8251	70.43
G10	87.1409	92.1870	92.6484	92.5426	92.0388	92.7522	66.2354	60.33
G11	58.6019	61.3470	91.9233	61.5243	61.6493	61.4368	68.8125	70.4
G12	119.1476	121.8597	121.4353	121.6357	121.7468	121.2463	65.6357	66.53
G13	50.0000	50.0000	50.4352	50.5367	50.6484	50.7468	64.8102	66.42
G14	50.0000	50.0000	50.5327	50.6382	50.8202	50.4373	50.0000	50.33
G15	7.2070	7.2069	7.3536	7.6388	7.8447	7.4357	8.854	8.88
F _c	4352.39	4353.57	4366.27	4387.44	4427.26	4453.85	4304.62	4277.6
F _E	135.23	136.46	144.85	153.42	176.75	184.38	108.85	104.7

CREDIT AUTHORSHIP CONTRIBUTION STATEMENT

Narges Yousefi: Conceptualization, Data curation, Formal analysis, Investigation, Methodology, Resources, Software, Validation, Visualization, Writing - original draft. **Mahmood Joorabian:** Conceptualization, Funding acquisition, Validation, Visualization, Writing - review & editing. **Mahyar Abasi:** Methodology, Project administration, Supervision, Resources, Writing - original draft, Writing - review & editing.

DECLARATION OF COMPETING INTEREST

The authors declare that they have no known competing financial interests or personal relationships that could have appeared to influence the work reported in this paper. The ethical issues; including plagiarism, informed consent, misconduct, data fabrication and/or falsification, double publication and/or submission, redundancy has been completely observed by the authors.

REFERENCES

- [1] J. Fan, and L. Zhang, "Real-time economic dispatch with line flow and emission constraints using quadratic programming," *IEEE Transactions on Power Systems*, vol. 13, no. 2, pp. 320-325, 1998.
- [2] G. F. Reid, and L. Hasdorff, "Economic Dispatch Using Quadratic Programming," *IEEE Transactions on Power Apparatus and Systems*, vol. PAS-92, no. 6, pp. 2015-2023, 1973.
- [3] S. D. Chen, and J. F. Chen, "A direct Newton Raphson economic emission dispatch," *International Journal of Electrical Power & Energy*, vol. 25, no. 5, pp. 411-417, 2003.
- [4] P. Aravindhababu, and K. R. Nayar, "Economic dispatch based on optimal lambda using radial basis function network," *International Journal of Electrical Power and Energy Systems*, vol. 24, no. 7, pp. 551-556, 2002.
- [5] J. Nanda, L. Hari, and M. L. Kothari, "Economic emission load dispatch with line flow constraints using a classical technique," *IEEE Proceedings-Generation, Transmission and Distribution*, vol. 141, no. 1, pp. 1-10, 1994.
- [6] M. Ismail, G. Tawfik et al., "Combined economic emission dispatch with and without consideration of PV and wind energy by using various optimization techniques: a review," *Energies*, vol. 15, pp. 44-72, 2022.
- [7] T. Yalcinoz, and M. J. Short, "Neural networks approach for solving economic dispatch problem with transmission capacity constraints," *IEEE Transactions on Power Systems*, vol. 13, no. 2, pp. 307-313, 1998.
- [8] K. Y. Lee, A. Sode-Yome, and June Ho Park, "Adaptive Hopfield neural networks for economic load dispatch," *IEEE Transactions on Power Systems*, vol. 13, no. 2, pp. 519-526, 1998.
- [9] M. R. Lohokare, B. K. Panigrahi, S. S. Pattnaik, S. Devi, and A. Mohapatra, "Neighborhood search-driven accelerated biogeography-based optimization for optimal load dispatch," *IEEE Transactions on Systems, Man, and Cybernetics, Part C (Applications and Reviews)*, vol. 42, no. 5, pp. 641-652, 2012.
- [10] S. Özyön, and D. Aydın, "Incremental artificial bee colony with local search to economic dispatch problem with ramp rate limits and prohibited operating zones," *Energy Conversion and Management*, vol. 65, pp. 397-407, 2013.
- [11] I. Marouani, T. Guesmi, and HH. Abdallah, "An improved biogeography-based optimization for economic/environmental dispatch", *Iioab Journal*, vol. 10, no. 5, pp. 24-33, 2019.
- [12] S. Hussain, M. AI-Hitmi, S. Khaliq, A. Hussain, and M. A. Saqib, "Implementation and comparison of particle swarm optimization and genetic algorithm techniques in combined economic emission dispatch of an independent power plant," *Energies*, vol. 12, no. 11, pp. 2037, 2019.
- [13] M. A. Meziane, Y. Mouloudi, and A. Draoui, "Comparative study of the price penalty factors approaches for Bi-objective dispatch problem via PSO," *International Journal of Electrical and Computer Engineering*, vol. 10, no. 4, pp. 3343-3349, 2020.
- [14] X. Yu, X. Yu, Y. Lu, and J. Sheng, "Economic and emission dispatch using ensemble multi-objective differential evolution algorithm," *Sustainability*, vol. 10, no. 2, pp. 1-17, 2018.
- [15] A. Bhattacharya, and P. K. Chattopadhyay, "Solving economic emission load dispatch problems using hybrid differential evolution," *Applied soft computing*, vol. 11, no. 2, pp. 2526-2537, 2011.
- [16] L. Wang, and L.-p. Li, "An effective differential harmony search algorithm for the solving non-convex economic load dispatch problems," *International Journal of Electrical Power & Energy Systems*, vol. 44, no. 1, pp. 832-843, 2013.
- [17] S. Jiang, and Z. Ji, Y. Shen, "A novel hybrid PSO and gravitational search algorithm for solving economic emission load dispatch problems with various practical constraints," *International Journal of Electrical Power & Energy Systems*, vol. 55, pp. 628-44, 2014.
- [18] M. J. Mokarram, T. Niknam, J. Aghaei, M. Shafiekhah, and J. P. S. Catalão, "Hybrid optimization algorithm to solve the nonconvex multiarea economic dispatch problem," *IEEE Systems Journal*, vol. 13, no. 3, pp. 3400-3409, 2019.
- [19] R. Murugan, M. R. Mohan, C. C. A. Rajan, P. D. Sundari, and S. Arunachalam, "Hybridizing bat algorithm with artificial bee colony for combined heat

and power economic dispatch," *Applied Soft Computing*, vol. 72, pp. 189-217, 2018.

- [20] C.E.S Rex, M.M. Beno, and J Annrose, "A solution for combined economic and emission dispatch problem using hybrid optimization techniques," *Journal of Electrical Engineering & Technology*, pp. 1-10, 2019.
- [21] H. Nourianfar, and H. Abdi, "Solving the multi-objective economic emission dispatch problems using fast non-dominated sorting TVAC-PSO combined with EMA," *Applied Soft Computing*, vol. 85, 2019.
- [22] Z. Xin-gang, L. Ji, M. Jin, and Z. Ying, "An improved quantum particle swarm optimization algorithm for environmental economic dispatch," *Expert Systems with Applications*, vol. 152, 2020.
- [23] S. Deb, S. Fong, and Z. Tian, "Elephant search algorithm for optimization problems," in *2015 Tenth International Conference on Digital Information Management (ICDIM)*, 2015, pp. 249-255.
- [24] A. Shabani, B. Asgarian, and M. Salido, "Search and rescue optimization algorithm for size optimization of truss structures with discrete variables," *Numerical Methods in Civil Engineering*, vol. 3, no. 3, pp. 28-39, 2019.

Biography



Narges Yousefi was born in Iran, in 1993. She received his B.Sc. degree in Electronics Engineering from Behbahan Khatamolanbia Industrial University, Behbahan, Iran, in 2018. She is currently a master's student in Power Systems major at Department of Electrical Engineering, Institute for Higher

Education, ACECR, Ahvaz, Iran. Her main interests include

operation and planning of power system and applications of optimization algorithms in power system studies.



Mahmood Joorabian was born in Iran, in 1961. He received his B.E.E degree from University of New Haven, CT, USA, M.Sc. degree in Electrical Power Engineering from Rensselaer Polytechnic Institute, NY, USA and Ph.D. degree in Electrical Engineering from University of Bath, Bath, UK in 1983, 1985 and 1996, respectively. He has been with the Department of Electrical Engineering at Shahid Chamran University of Ahvaz, Ahvaz, Iran as Senior Lecturer (1985), Assistant Professor (1996), Associate Professor (2004) and Professor (2009). His main research interests are fault location, FACTS devices, power system protection, power quality, and applications of intelligence technique in power systems.

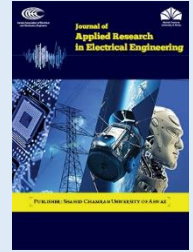


Mahyar Abasi was born in Iran in 1989. He graduated with a Ph.D. in Electrical Power Engineering from the Shahid Chamran University of Ahvaz, Ahvaz, Iran, in 2021. His research background is more than 60 published journal and conference papers, more than 10 authored books, 11 industrial research projects, and a patent in power systems. In 2021, he was introduced as the top researcher of Khuzestan province, Iran, and in the years 2021 to 2023, he successfully received four titles from the membership schemes of the National Elite Foundation in Iran. He is currently an Assistant Professor at the Electrical Engineering Department of Arak University, Arak, Iran. His specialized interests are fault protection, detection, classification, and location in HVAC and HVDC transmission lines, control of reactive power and FACTS devices, evaluation and improvement of power quality, and power system studies.

Copyrights

© 2024 Licensee Shahid Chamran University of Ahvaz, Ahvaz, Iran. This article is an open-access article distributed under the terms and conditions of the Creative Commons Attribution –NonCommercial 4.0 International (CC BY-NC 4.0) License (<http://creativecommons.org/licenses/by-nc/4.0/>).





Research Article

A New Topological Method for Output Voltage Clamping of Immittance-based Constant Current Load Resonant Converters

Alireza Khoshsaadat , and Mohammad Abedini * 

Department of Electrical Engineering, Faculty of Engineering, Ayatollah Boroujerdi University, Boroujerd, Iran

* Corresponding Author: m.abedini@abru.ac.ir

Abstract: In this paper a new improved diode-based circuit is introduced for output voltage limiting of immittance-based constant current Load Resonant Converters (LRCs). The proposed Diode-based Voltage-Limiter (DVL) is very reliable and simple, and also has the minimum number of components. Moreover, limiting values are flexible and can be varied according to the design requirements. All of the positive characteristics of the LRC operation are preserved in this technique, such as Zero Voltage Switching (ZVS) of the inverter switches and Zero Current Switching (ZCS) of the rectifier diodes. A 150W converter with a 300kHz switching frequency is considered as a sample prototype. The circuit simulation is presented based on the real model of the semiconductor devices in the OrCAD environment to have maximum accordance with the real conditions. Simulation results demonstrate an accurate clamping ability of the output voltage for overload conditions without any characteristics variation.

Keywords: Diode-based Voltage-Limiter (DVL), Immittance Passive Resonant Tank (IPRT), Load Resonant Converter (LRC).

Article history

Received 27 December 2023; Revised 20 May 2024; Accepted 25 June 2024; Published online October 9, 2024.

© 2024 Published by Shahid Chamran University of Ahvaz & Iranian Association of Electrical and Electronics Engineers (IAEEE)

How to cite this article

A. R. Khoshsaadat, and M. Abedini, "A New Topological Method for Output Voltage Clamping of Immittance-based Constant Current Load Resonant Converters," *J. Appl. Res. Electr. Eng.*, vol. 3, no. 1, pp. 33-39, 2024.

DOI: 10.22055/jaree.2024.45659.1096



1. INTRODUCTION

Load Resonant Converters (LRCs) [1], [2] are used widely as constant current or voltage sources in applications such as high-voltage power supplies [3], induction heaters [4], driver for illumination systems [5], electric arc welders [6], battery or capacitor chargers [7], [8], power factor correctors [9], and contactless power transfers [10]. Therefore, robust output against load variation is an important characteristic in the LRCs design [11], [12]. A simple and reliable technique to achieve load regulation ability in LRCs is utilization of Immittance Passive Resonant Tanks (IPRTs) in LRCs. This feature has been investigated deeply in previous works for IPRTs with various number of reactive component [13-16]. In this method, the robust load regulation capability can be achieved based on a topological technique; thus, utilization of complex controller can be eliminated. In the IPRT-based LRCs, the output voltage is varied according to the various load values and the output current remain constant based on the inherent load-independent operation of

the IPRT in a defined switching frequency. An important problem in this type of the LRCs is occurs when the load increases. In this condition, the output voltage increases accordingly to control the output current in a predefined constant value. This phenomenon can damage the load or the LRC in a specific application such as chargers and electric arc welders. For example, in the battery charger that is charged with a constant current LRC, the output voltage should be limited to a defined voltage when the battery charging procedure is near to the full-load condition. Otherwise, the output voltage increases to high values and the battery lifetime is reduced. Or, in the electric arc welders, if the arc is offed, the open-circuit condition occurs and the LRC can be damaged due to very high output voltage [17]. Therefore, in the IPRT-based LRCs, a voltage clamper should be considered to protect the converter properly.

To solve the mentioned drawback, a method is applying a control circuit to tune the output voltage based on a predefined reference value. In this way, the complexity and cost of the LRC controller increases. An alternative technique

is utilization of a clamping circuit, which limits the output voltage topologically. Based on this perspective, a simple circuit topology is presented in [17] using two clamping diode, which demonstrated in Fig. 1. As can be seen, if the IPRT output voltage is less than the V_{in} , two diodes are reverse biased; and if the IPRT output voltage is more that the V_{in} , two diode are direct biased and the output voltage is clamped to the V_{in} . Although, this circuit is not a general method for various IPRT topologies and conditions because a predefined assumption is considered, which the maximum output voltage of the IPRT in the full-load condition is equal to the V_{in} . This assumption is correct when the IPRT voltage gain is a specific value, which restricts degrees of freedom for the optimum design of the IPRT parameters value. Also, this topology is considered for clamping the output voltage to the V_{in} , while in some conditions it is wanted to clamp the output voltage to the higher values. In this paper, a new improve Diode-based Voltage-Limiter (DVL) is introduced, which have the follows feature that can be considered as its main features:

- It has high flexibility in variation the border of the clamping voltage that can be tunable according to the converter application and also can be applied in LRCs with various IPRT topologies.
- This flexible topological structure for voltage clamping has minimum number of components increment;
- The positive operation characteristics of the LRC, such as Zero Voltage Switching (ZVS) of the inverter switches and Zero Current Switching (ZCS) of the rectifier diode are preserved in case of utilizing DVL circuit.

Some other topologies have been offered in [17] with more operation flexibility. Although, they do not have the first circuit simplicity, reliability, and correctness, and also use the higher number of the components with more complicated structures. In [18] explores using a concept called duality to design new current-based DC-DC converters. Duality involves creating a mirror image of an existing circuit, where specific components are swapped. This paper applies this idea to traditional voltage-based DC-DC converters, including buck, boost, fly-back, cuk, sepic, and zeta designs. In [19] a tuneable band-pass filter built with an operational transconductance amplifier. This filter acts as an anti-aliasing filter for an analog-to-digital converter. An AAF is crucial to block unwanted signals before they reach the ADC, ensuring accurate digital conversion. Therefore, a new simple topology should be proposed to cover weaknesses of the presented circuit in Fig. 1 with the same simplicity.

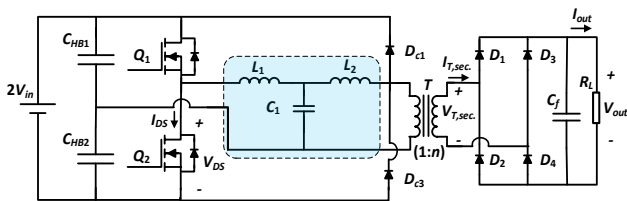


Fig. 1: The presented clamping circuit in [17].

2. PROPOSED DVL DESIGN

Table 1 provides samples of the appropriate type sizes and styles to use. The main paper sections must be organized as follows: The new proposed DVL is presented in Fig. 2 to clamp the output voltage of a typical IPRT-based LRCs, named LCCLC-LRC. The fifth-order LCCLC-IPRT topology is a sample and can be replaced with the other IPRT structures. This DVL is composed of the two diodes, similar to Fig. 1, and only two extra zener diodes that connected two the previous diodes directly. Each pair of two diodes (a usual and a zener) are act in half cycle of the LRC operation. Therefore, by analyzing of a pair, the similar condition exists for the other pair.

In the positive cycle, if the IPRT output voltage is less than V_{in} , D_{c2} in Fig. 2 is reverse biased and LRC is operated in the usual condition. If the IPRT output voltage is more than V_{in} , D_{c2} is forward biased and the LRC will operated in the clamping mode based on the following expression:

$$V_{break,Dc1\&Dc3} = V_{pri,full} - V_{in} \quad (1)$$

In which, $V_{pri,full}$ is the maximum output voltage of the IPRT in the full-load condition, and $V_{break,Dc1\&Dc2}$ is the breakdown voltage of the zener diodes that should be defined based on difference between the $V_{pri,full}$ and V_{in} to limit the output voltage of the LRC to the full-load condition.

Expression (1) is true for the condition that DVL clamps the output voltage to the full-load condition. To obtain a higher value for clamping of the output voltage, the breakdown voltage of the zener diodes should be increased by a required extra voltage (V_{extra}), which is considered in problem description. In this condition, the breakdown voltage of the DVL zener diodes is defined as:

$$V_{break,Dc1\&Dc3} = (V_{pri,full} - V_{in}) + V_{extra} \quad (2)$$

3. SIMULATION RESULTS

To demonstrate the proposed DVL ability and its operation correctness, a 150W LCCLC-LRC prototype with 300kHz switching frequency is considered as a sample circuit. In the designed converter, $V_{in}=24V$, $I_{out}=3.5A$, and $RL=12\Omega$. The detail design procedure and analysis of the LCCLC-LRC have been introduced in [8] and to avoid from prolongation, the operation characteristics and components value are considered similar. Therefore, the value of the components, according to Fig. 2, are defined as: $L1=L2=2.6\mu H$, $C1=C2=335nF$, $C3=168nF$, $Cf=47\mu F$, and n (transformer turn ratio) $=1.75$. A 48V supply is applied due to using half-bridge inverter at the input of the converter.

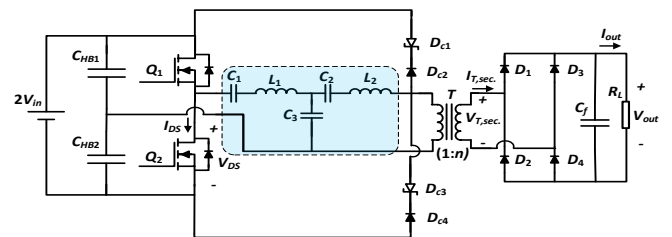


Fig. 2: The proposed DVL structure for output voltage clamping of the LCCLC-LRC.

The OrCAD software is applied for simulation of the LCCLC-LRC due to high ability in real modelling of the components circuit with more accordance to real experimental conditions in comparison with the other simulator. The LCCLC-LRC schematic is presented in Fig. 3. IRFP150 is used as the inverter switches, and IR2113 is applied as the switches driver. A 1Ω resistor is used to model the ohmic losses of the LCCLC-LRC. LCCLC-LRC prototype is presented in Fig. 3. Operation waveforms of the designed LCCLC-LRC in nominal load are presented in Fig. 4. The LCCLC-LRC operation waveforms in half-load, full-load, and twice of the full-load conditions are presented in Fig. 5, for clamping the output voltage to the full-load case. Therefore, the breakdown voltage of the zener diodes is the

difference between the maximum voltage of the IPRT output (43V) and V_{in} , which is equal to 18V according to (1). It is clear that the LCCLC-LRC has the normal operation in half-load and full-load conditions. In twice of full-load condition, the output voltage of the IPRT is clamped to 43V, which is the full-load condition voltage. Therefore, the LRC output voltage clamped to the predefined value in the full-load condition. As can be seen in Fig. 4, the voltage and current of the rectifier diodes are in phase and switching losses of this part is minimum. Also, the ZVS operation of the inverter switches is preserved in heavy loads. Thus, the switching losses in the inverter part is very low, and a low switching losses is due to the turn-off current of the switches.

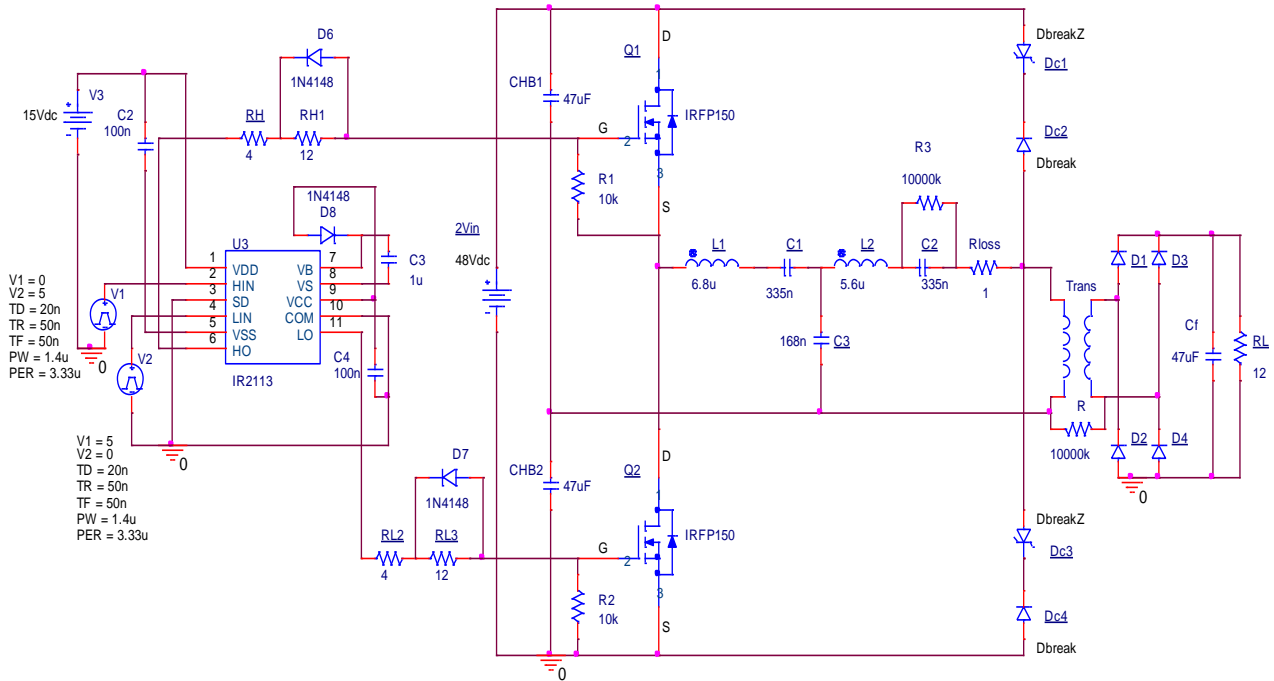
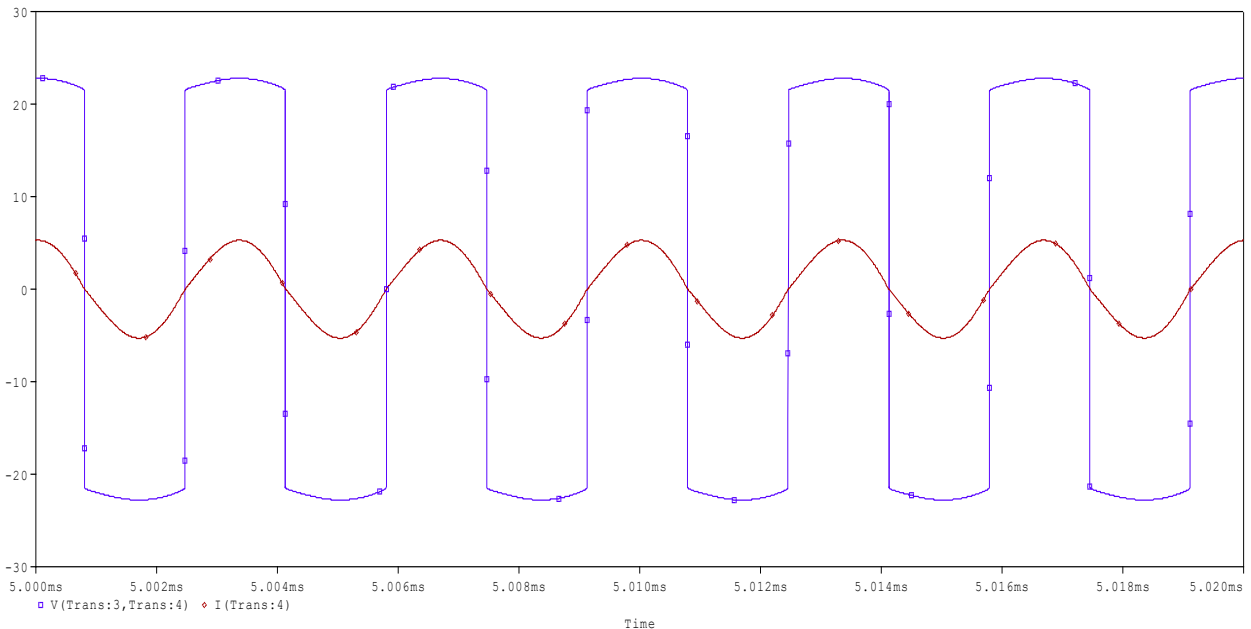
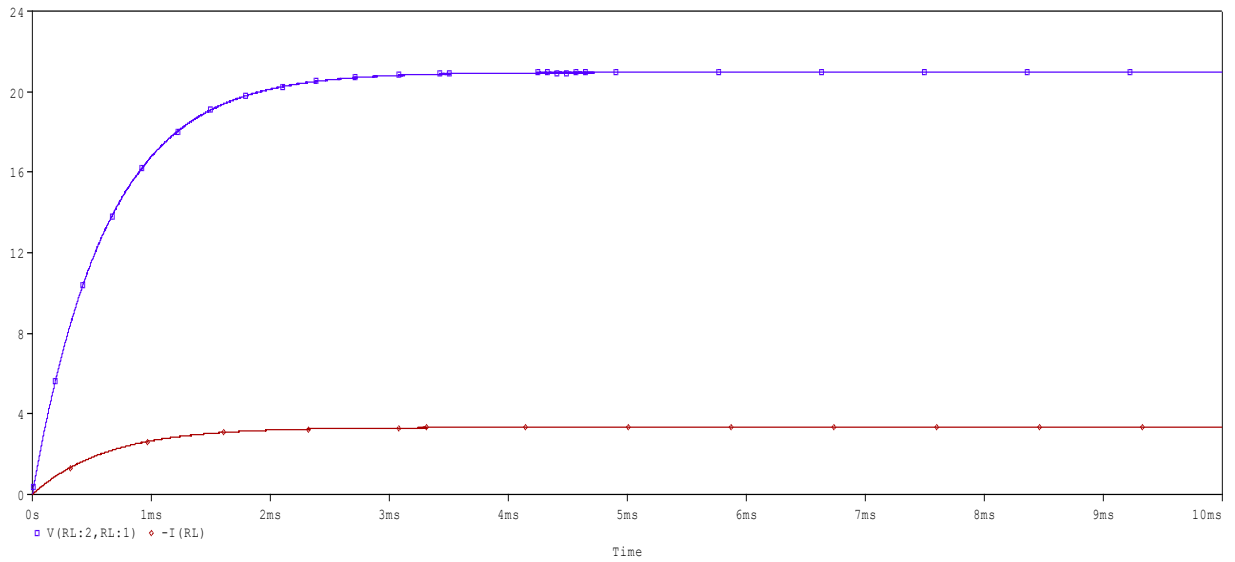


Fig. 3: The proposed DVL schematic circuit in OrCAD.

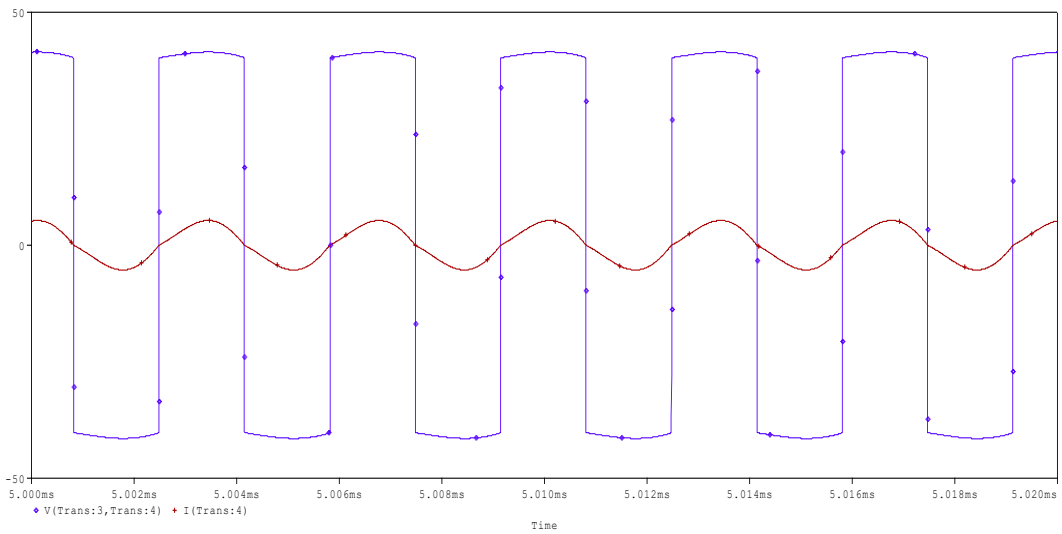


(a)

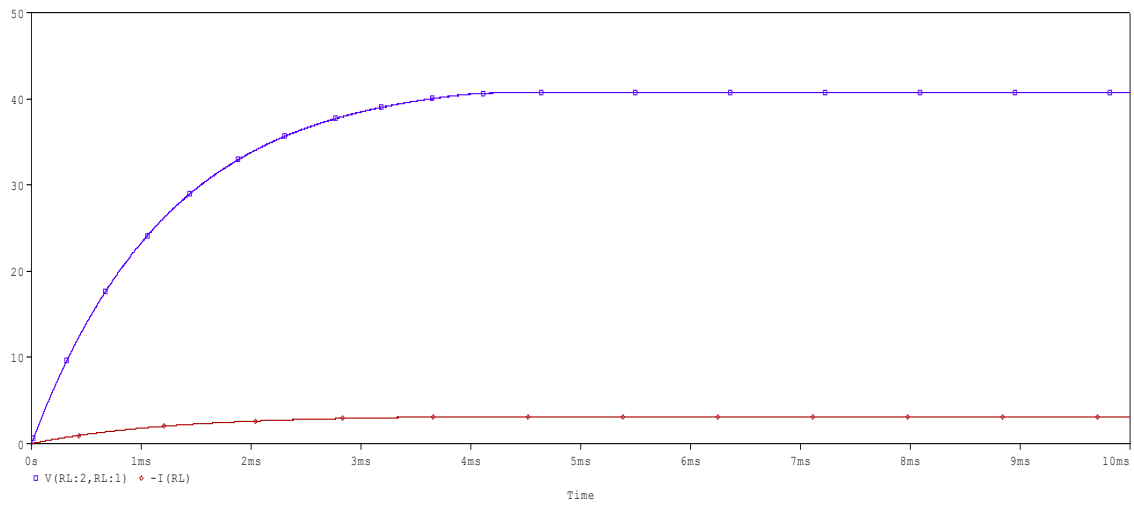


(b)

Fig. 4: Simulation waveforms of the LCCLC-LRC with the applied DVL in half-load condition for voltage claming in full-load. (a) Voltage and current at secondary side of the transformer; (b) output voltage and current. Blue: voltage, red: current.

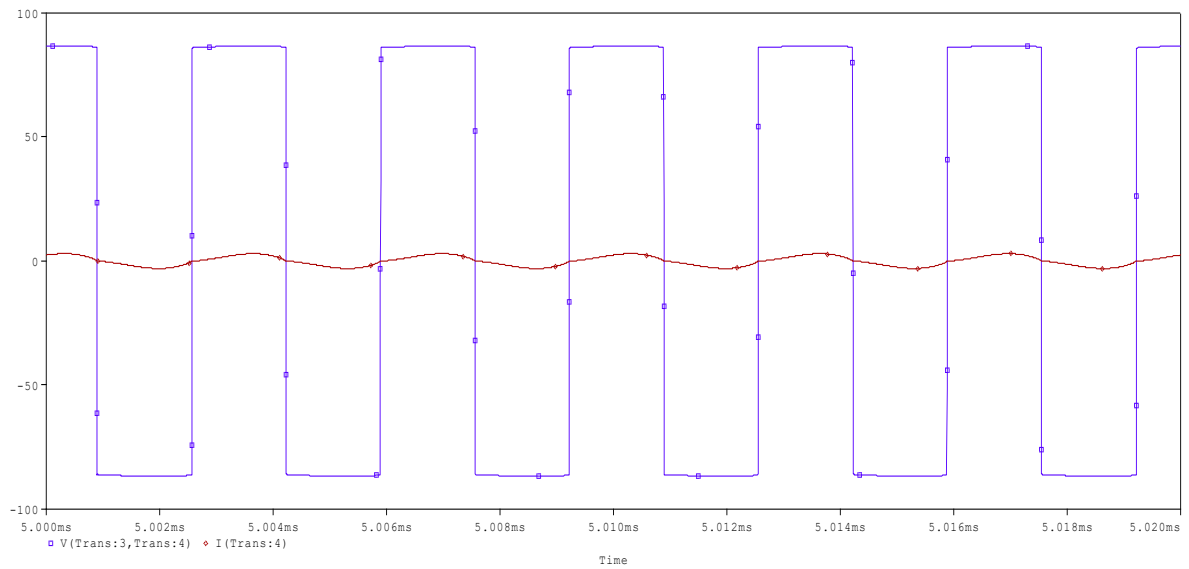


(a)

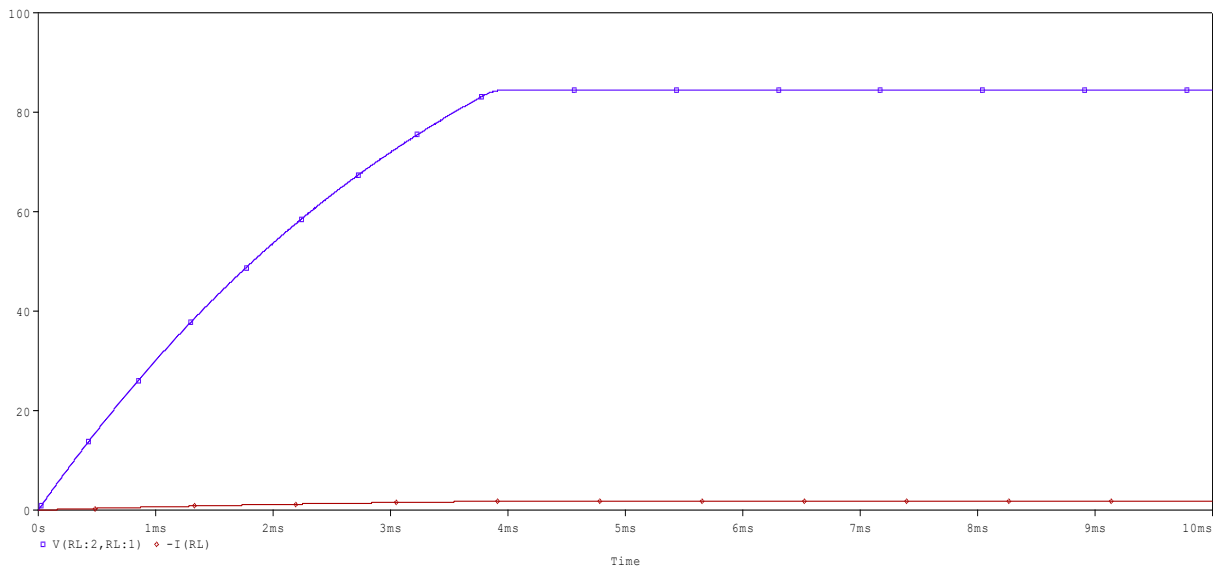


(b)

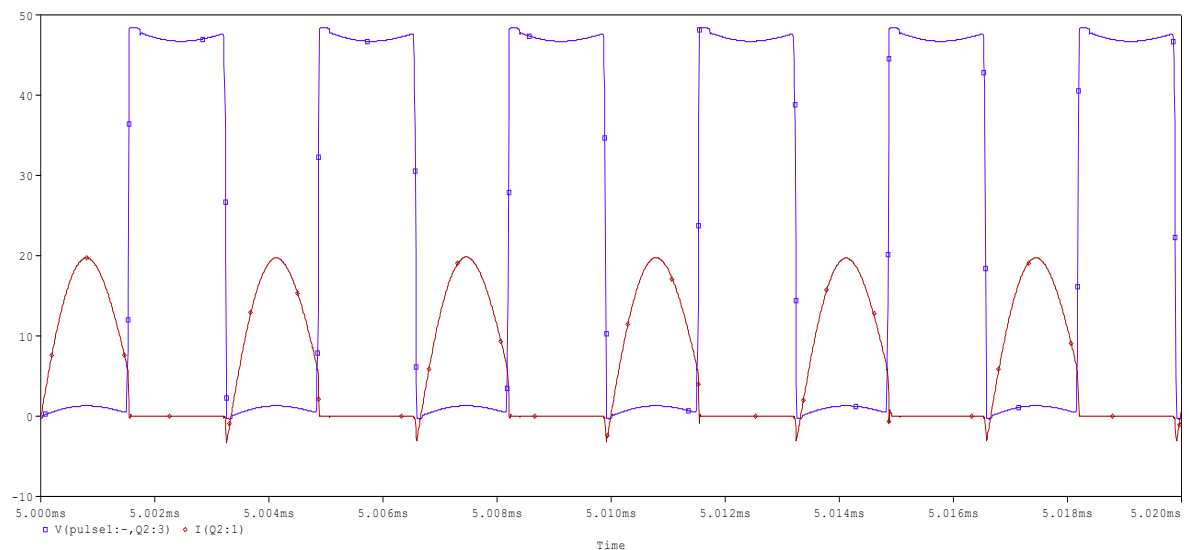
Fig. 5: Simulation waveforms of the LCCLC-LRC with the applied DVL in full-load condition for voltage clamping in full-load value. (a) Voltage and current at secondary side of the transformer; (b) output voltage and current. Blue: voltage, red: current.



(a)



(b)



(c)

Fig. 6: Simulation waveforms of the LCCLC-LRC with the applied DVL in the three times full-load condition (36Ω) for voltage claming in twice the full-load value (86V). (a) Voltage and current in the secondary side of the transformer; (b) output voltage and current; (c) voltage and current of the inverter switch. Blue: voltage, red: current.

To demonstrate the flexibility of the proposed DVL for various limiting conditions, another simulation is performed for a higher voltage limitation than the full-load condition. In this case, the limitation value is considered in twice the full-load condition (86V). The simulation results are presented in Fig. 6. It can be seen that the output voltage is in the normal condition until $R_L=24\Omega$. The output voltage is clamped to 86V in the higher values of the $2R_L$, such as 36Ω , without affecting the ZVS of the inverter switches and ZCS of the rectifier diodes. The output current and voltage of the LCCLC-LRC as a function of the R_L , are presented in Fig. 7 and also Fig. 8 respectively for voltage clamping in the full-load case. As can be seen, the output current is nearly constant in light- to full-load condition. When the load is higher than the full case, the constant current mode converts to the constant voltage mode. In this condition, the output voltage remain constant with the load increasing. Therefore, the output current decrease proportionally.

4. CONCLUSION

A new general diode-based circuit (DVL) is presented in this paper for clamping the output voltage of the constant current IPRT-based LRCs for protecting the load and converter in the heavy-load conditions. This topology is very simple and reliable with high precision. Due to applying only four diodes (two usual and two zener) the DVL cost and complexity is very low in comparison with other controller-based methods. The output voltage clamping ability of the proposed DVL is examined with a sample LRC (LCCLC-LRC) prototype that designed in the past works.

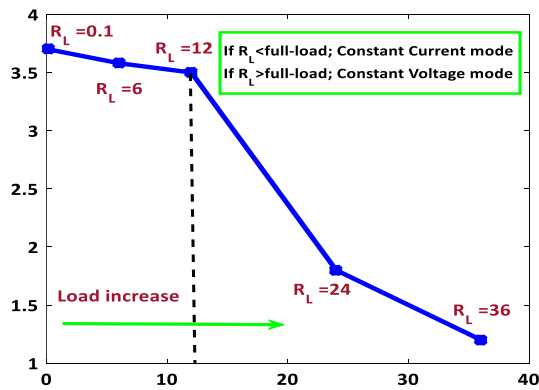


Fig. 7: LCCLC-LRC output current using DVL as a function of R_L .

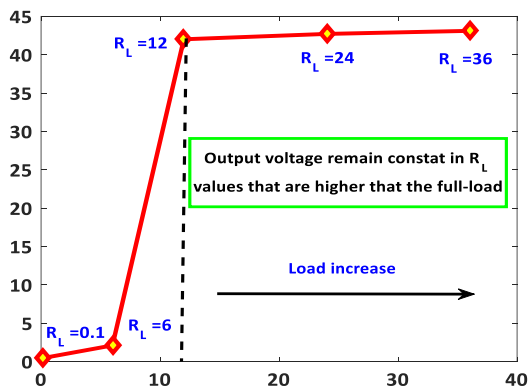


Fig. 8: LCCLC-LRC output voltage using DVL as a function of R_L .

The simulation results, using the OrCAD and real model of the components, demonstrates that the introduced circuit can operate successfully in the various load values without affecting the main positive characteristics of the basic converter, such as ZVS of the inverter switches and ZCS of the rectifier diodes.

CREDIT AUTHORSHIP CONTRIBUTION STATEMENT

Alireza Khoshsaadat: Conceptualization, Funding acquisition, Project administration. **Mohammad Abedini:** Data curation, Roles/Writing - original draft, Writing - review & editing.

DECLARATION OF COMPETING INTEREST

The authors declare that they have no known competing financial interests or personal relationships that could have appeared to influence the work reported in this paper. The ethical issues; including plagiarism, informed consent, misconduct, data fabrication and/or falsification, double publication and/or submission, redundancy has been completely observed by the authors.

REFERENCES

- [1] M. M. Jovanovic, "Merits and limitations of resonant and soft-switched converters," in *Proc. of Fourteenth International Telecommunications Energy Conference - INTELEC '92*, Washington, DC, USA, 1992, pp. 51-58.
- [2] M. Jovanović, "Resonant, quasi-resonant, multi-resonant and soft-switching techniques-merits and limitations," *Int. Journal of Electron.*, vol. 77, no. 5, pp. 537-554, Apr. 1994.
- [3] W. -C. Hsu, J. -F. Chen, Y. -P. Hsieh, and Y. -M. Wu, "Design and steady-state analysis of parallel resonant DC-DC converter for high-voltage power generator," *IEEE Transactions on Power Electronics*, vol. 32, no. 2, pp. 957-966, Feb. 2017.
- [4] B. Jaafari, and A. Namadmalan, "Design and parameter estimation of series resonant induction heating systems using self-oscillation tuning loop," *Journal of Applied Research in Electrical Engineering*, vol. 1, no. 1, pp. 42-49, 2022.
- [5] N. Molavi, and H. Farzanehfard, "Load-independent hybrid resonant converter for automotive LED driver applications," *IEEE Transactions on Power Electronics*, vol. 37, no. 7, pp. 8199-8206, 2022.
- [6] A. Navarro-Crespin, V. M. Lopez, R. Casanueva, and F. J. Azcondo, "Digital control for an arc welding machine based on resonant converters and synchronous rectification," *IEEE Transactions on Industrial Informatics*, vol. 9, no. 2, pp. 839-847, 2013.
- [7] H. Haga, and F. Kurokawa, "Modulation method of a full-bridge three-level LLC resonant converter for battery charger of electrical vehicles," *IEEE Transactions on Power Electronics*, vol. 32, no. 4, pp. 2498-2507, April 2017.

- [8] M. K. Borage, S. Tiwari, and S. Kotaiah, "A constant-current, constant-voltage half-bridge resonant power supply for capacitor charging," *IEE Proc. Electr. Power. Appl.*, vol. 153, no. 3, pp. 343-347, May 2006.
- [9] J. Hong, D. Maksimovic, R. W. Erickson, and I. Khan, "Half-cycle control of the parallel resonant converter operated as a high power factor rectifier," *IEEE Transactions on Power Electronics*, vol. 10, no. 1, pp. 1-8, Jan. 1995.
- [10] A. Namadmalan, "Bidirectional current-fed resonant inverter for contactless energy transfer systems," *IEEE Transactions on Industrial Electronics*, vol. 62, no. 1, pp. 238-245, Jan. 2015.
- [11] L. Li, Y. Gao, P. K. T. Mok, I. -S. M. Sun, and N. Park, "A 16–28-W 92.8%-efficiency monolithic quasi-resonant LED driver with constant-duty-ratio frequency regulator," *IEEE Transactions on Circuits and Systems II: Express Briefs*, vol. 62, no. 12, pp. 1199-1203, Dec. 2015.
- [12] C. -O. Yeon, J. -W. Kim, M. -H. Park, I. -O. Lee and G. -W. Moon, "Improving the light-load regulation capability of LLC series resonant converter using impedance analysis," *IEEE Transactions on Power Electronics*, vol. 32, no. 9, pp. 7056-7067, Sept. 2017.
- [13] L. Cao, J. Lin, X. Jiang, C. S. Wong, and K. H. Loo, "An immittance-network-based multiport ZVS bidirectional converter with power decoupling capability," *IEEE Transactions on Power Electronics*, vol. 37, no. 10, pp. 12729-12740, Oct. 2022.
- [14] A. Khoshsaadat, and J. S. Moghani, "Fifth-order t-type passive resonant tanks tailored for constant current resonant converters," *IEEE Transactions on Circuits and Systems I: Regular Papers*, vol. 65, no. 2, pp. 842-853, Feb. 2018.
- [15] A. Bagheri, H. Iman-Eini, and M. Emaneini, "Underwater arc discharge treatment using a high-voltage arc-robust supply," *IEEE Journal of Emerging and Selected Topics in Power Electronics*, vol. 11, no. 3, pp. 3261-3269, June 2023.
- [16] L. Yang et. al., "Underwater power conversion and junction technology for underwater wireless power transfer stations", *Journal of Marine Science and Engineering*, vol.12, no.4, pp.561, 2024.
- [17] M. Borage, S. Tiwari, and S. Kotaiah, "LCL-T resonant converter with clamp diodes: a novel constant-current power supply with inherent constant-voltage limit," *IEEE Transactions on Industrial Electronics*, vol. 54, no. 2, pp. 741-746, April 2007.
- [18] Z. Gholami; R. Ildarabadi; and H. Heydari-doostabad. "Conventional DC-DC converters through duality approach for current-based applications", *Journal of Applied Research in Electrical Engineering*, vol. 3, no. 1, pp. 64-73, 2024.
- [19] M. Ghaemmaghami, and S. Reyhani, "Design of a tunable 4th order OTA-C band-pass filter for use in front-end of ADC," *Journal of Applied Research in Electrical Engineering*, vol. 2, no. 2, pp. 152-157, 2023.

BIOGRAPHY



Alireza Khoshsaadat was born in Boroujerd, Iran, in 1986. He received the B.Sc. degree from Shahid Beheshti University (SBU), Tehran, Iran, in 2009, the M.Sc. degree from the Iran University of Science and Technology (IUST), Tehran, in 2011, and the Ph.D. degree from Amirkabir University of Technology (AUT), Tehran, in 2018, all in electrical engineering. He is currently a Faculty Member and an Assistant Professor with Ayatollah Boroujerdi University (ABRU), Boroujerd. His research interests include design of power electronics converters and chargers, and also electric vehicles (EVs) analysis and design.



Mohammad Abedini was born in Boroujerd, Iran, in 1986. He received his B.Sc degree in electrical engineering from the Islamic Azad university of Borujerd, Borujerd, Iran in 2006. M.Sc. and Ph.D degrees in electrical engineering from Bu-Ali Sina University in 2008 and 2010, respectively. He is currently an associate professor at ayatollah Borujerd university. His current research interest includes microgrids and distribution systems.

Copyrights

© 2024 Licensee Shahid Chamran University of Ahvaz, Ahvaz, Iran. This article is an open-access article distributed under the terms and conditions of the Creative Commons Attribution –NonCommercial 4.0 International (CC BY-NC 4.0) License (<http://creativecommons.org/licenses/by-nc/4.0/>).



Shahid Chamran
University of AhvazIranian Association of
Electrical and Electronics
Engineers

Journal of Applied Research in Electrical Engineering

E-ISSN: 2783-2864

P-ISSN: 2717-414X

Homepage: <https://jaree.scu.ac.ir/>

Research Article

Analysis of the Potential of Different Air Conditioner Brands for Piezoelectric Energy Harvesting

Daniel Kwegyir ^{*} , Francis Bofo Effah , Daniel Opoku , Peter Asigri , Yoosi Hayford, Eliezer Owusu Boateng, Kwaku Kessey-Antwi, Nana Maryam Abdul-Bassit Munagah, and Kelvin Worlanyo Tamakloe

Department of Electrical and Electronic Engineering, Kwame Nkrumah University of Science and Technology, Kumasi, Ghana

* Corresponding Author: daniel.kwegyir@knust.edu.gh

Abstract: Piezoelectric energy harvesting from air conditioner compressors is a promising technology for generating renewable electricity. This study comprehensively compares the energy harvesting potential derived from mechanical vibrations in compressors across various air conditioner brands, harnessing piezoelectric systems. Initially, a data collection system rooted in Internet of Things (IoT) technology is employed to capture vibration signals from different branded air conditioner compressors. The acquired data undergoes pre-processing and is subsequently analyzed in MATLAB Simulink to gauge its energy harvesting potential through a piezoelectric framework. Notably, the maximum voltage harvested demonstrated strong positive correlations with both the compressor vibrational frequency (0.7892) and velocity (0.7855), emphasizing their role in determining available mechanical energy for conversion to electrical power. Furthermore, a moderate positive correlation (0.0659) was observed between the harvested voltage and the compressor's rated power, indicating its influence on energy conversion. An additional positive correlation (0.2839) between temperature and harvested voltage was attributed to the increased electrical conductivity of compressor materials at higher temperatures. Conclusively, the compressor's frequency and velocity emerged as primary determinants of the maximum voltage harnessed, with rated power having a less pronounced yet contributory effect. This research provides valuable insights for optimizing energy harvesting from air conditioner compressors, highlighting the pivotal role of operational parameters.

Keywords: Piezoelectric energy harvesting, air conditioners, simscape

Article history

Received 22 November 2023; Revised 25 May 2024; Accepted 26 May 2024; Published online October 9, 2024.

© 2024 Published by Shahid Chamran University of Ahvaz & Iranian Association of Electrical and Electronics Engineers (IAEEE)

How to cite this article

D. Kwegyir *et al.*, "Analysis of the Potential of Different Air Conditioner Brands for Piezoelectric Energy Harvesting," *J. Appl. Res. Electr. Eng.*, vol. 3, no. 1, pp. 40-50, 2024.

DOI: [10.22055/jaree.2024.45352.1089](https://doi.org/10.22055/jaree.2024.45352.1089)



1. INTRODUCTION

While reliable, conventional electricity generation methodologies, like hydroelectric and thermal power stations, pose significant environmental challenges. These include the depletion of natural resources, emission of greenhouse gases, and contribution to air pollution [1]. In pursuit of more eco-friendly alternatives, nations globally are turning to

renewable energy sources, including solar, wind, and nuclear fusion. Although these renewables offer reduced environmental footprints, their reliability can be compromised by unpredictable environmental conditions, such as fluctuating sunlight and wind patterns [2].

Recently, piezo energy harvesting has emerged as a promising avenue for energy generation. This technique captures renewable, environmentally friendly electricity from

mechanical vibrations, movements, and pressure, positioning it as a sustainable energy alternative [3]. Many mechanical devices in daily use, for instance, air conditioners, dispense several joules of mechanical energy as vibrations. This energy, primarily overlooked and wasted, holds the potential for conversion into usable power. Consequently, piezoelectric energy harvesting has attracted considerable research interest recently [4], as evidenced by numerous studies and publications.

Y. Li et al. [5] introduced a hybrid energy harvester that combines electromagnetic, piezoelectric, and triboelectric mechanisms to harness ocean wave energy. Their approach utilised a shaking energy harvesting mechanism, encompassing gear and pendulum components, supplemented by piezoelectric and electromagnetic generators. While the system could power at least 90 LEDs and environmental sensors, its effectiveness was constrained by the low frequency of ocean waves. W.M. Jayarathne et al. [6] presented a piezoelectric vibration energy harvester tailored for vehicular energy extraction. The model employed lead zirconate titanate as the piezoelectric medium and resonant frequency analysis within a cantilever configuration. Despite Finite Element Analysis (FEA) projecting an output of 5.99V, real-world motorcycle tests produced only 3.56V. Such discrepancies underscored the influence of dynamic road conditions and material inconsistencies. In their work, Abishek Ray et al. [7] explored the applicability of a modified cantilever design for vibration energy harvesting using piezoelectric sensors. They incorporated unique structural features, including a stair-shaped sidewall and a beam-integrated hole, to modulate the resonant frequency. The subsequent Finite Element Analysis, employing unimorph PZT-5H piezoelectric material, suggested promising outcomes, though structural modifications did pose challenges to the system's mechanical integrity. V.J. Caetano et al. [8] embarked on an experimental journey to engineer versatile piezoelectric devices that accommodate varied environmental excitation frequencies. Their innovative designs, especially the pizza-shaped prototype, were contrasted against conventional beam structures. The results favored the novel designs, especially when subjected to harmonic excitations. Corina et al. [9] ventured into optimizing a dual-stage piezoelectric energy harvesting circuit tailored for the SMD10T2R111WL transducer's SPICE model. Although their approach, encompassing synchronous buck configuration, showcased improved efficiency, specific results stemming from the piezoelectric transducer appeared unfeasible. Delving into the domain of human-centric energy harnessing, S. Mariem et al. [10] investigated the potential of converting human breathing patterns into electricity via piezoelectric systems. Their simulations underscored the impact of cantilever dimensions on energy optimization, revealing some insightful correlations. Z. Wang et al. [11] showcased a piezoelectric energy harvester leveraging rotational magnetic excitation. Despite the promising voltage outcomes, the generated power remained suboptimal due to the resonance frequency constraints inherent to their design.

Contrasting conventional piezoelectric structures, R. Newton et al. [12] championed the efficacy of an E-shaped design. Their comparative analysis, rooted in simulation, posited the superiority of the E-shaped model, though it

necessitated further efficiency refinements. Lastly, N. Burham et al. [4] delved into vehicular energy harvesting using piezoelectric mechanisms. Their empirical assessments highlighted the pronounced influence of vehicle attributes, such as weight and speed, on voltage outputs while underscoring the longevity challenges transducers face in such dynamic environments.

This study comprehensively compares the energy harvesting potential derived from mechanical vibrations in compressors across various air conditioner brands, harnessing piezoelectric systems. Initially, a data collection system rooted in Internet of Things (IoT) technology is employed to capture vibration signals from different branded air conditioner compressors. The acquired data undergoes pre-processing and is subsequently analyzed in MATLAB Simulink to gauge its energy harvesting potential through a piezoelectric framework. This paper is outlined as follows: Section 2 introduces the foundational theory of piezoelectric energy harvesting. Section 3 presents the proposed block diagram for the experimental design, detailing each block's component selection and functionalities. Section 4 discusses the experimental approach for data collection, while Section 5 delves into the related simulations. Results are discussed in Section 6, ending with conclusions in Section 7.

2. PIEZOELECTRIC ENERGY HARVESTING

Piezoelectricity refers to a unique phenomenon where certain materials, upon experiencing mechanical stress, generate an internal electric charge separation. These materials often possess crystal lattices devoid of central symmetry. When subjected to pressure, the relative movement of their positive and negative ions creates an electric voltage. Even though the material remains electrically neutral, the charge displacement induces an electric field, producing electricity. The resultant piezoelectric voltage exhibits pulsatory characteristics, requiring extensive processing for real-world applications [13].

2.1. Electrical and Mechanical Behaviour of Piezoelectric Material

The electrical and mechanical behaviour of the piezoelectric material can be represented by (1) and (2).

$$S = s^E T + d_t E \quad (1)$$

$$D = d_t T + \varepsilon^T E \quad (2)$$

Equations (1) and (2) contain the following parameters: 'S' represents mechanical strain, 'E' denotes the electric field, 'T' signifies the applied mechanical stress, and 'D' is the electric displacement. Meanwhile, ' s^E ' is the elasticity matrix maintained at a constant electric field, ' ε^T ' stands for the permittivity matrix under consistent mechanical strain, and ' d_t ' is the matrix defining the piezoelectric coefficient.

2.2. Inertia Mass and Resonant Frequency in Vibrational Analysis

The power density of a piezoelectric material is related strongly to the vibration's frequency and amplitude by (3).

$$P_{res} = 4\pi^3 m f_{res}^3 y z_{max} \quad (3)$$

Equation (3) includes parameters pivotal to vibrational dynamics for piezoelectric energy harvesting. Here, 'm' stands

for the inertia mass, which reflects the resistance of an object to any change in its velocity, including a change in direction. Inertia mass is central to understanding how vibrations will affect the piezoelectric material. The term ' f_{res} ' represents the resonant frequency. It is the specific frequency at which a system naturally oscillates with maximum amplitude due to external periodic driving forces. In piezoelectric systems, aligning the resonant frequency with expected external vibrations can substantially optimize energy capture. The parameter ' y ' denotes the amplitude of the vibrations, indicating the maximum displacement of a point on the beam from its rest position. In many scenarios, the amplitude correlates directly with the amount of energy that can be harvested: larger amplitudes often mean more significant energy potential. Lastly, ' z_{max} ' is the paramount amplitude of vibrations, signifying the utmost extent to which a point on the beam can deviate from its equilibrium state during oscillation.

From (3), the resonance can significantly amplify the vibrations of the beam, leading to a larger deflection and, in the piezoelectric materials, a higher generated voltage or power. Thus, designing a piezoelectric cantilever beam to have a natural frequency that matches or is close to the frequency of expected vibrations can optimize energy harvesting.

From the Euler-Bernoulli Beam theory, the natural frequency of a cantilever beam can be determined by (4) [14].

$$f_n = \frac{k_n}{2\pi} \sqrt{\frac{EI}{l^4}} \quad (4)$$

In (4), ' E ' is Young's modulus of elasticity, provides a measure of the stiffness of a material. The parameter ' I ', is the area moment of inertia used for determining a beam's resistance to bending and deflection. Also, ' l ' is the length of the beam, and ' k_n ', a constant, relies on the mode of vibration being analyzed. The value ' k_n ' is taken as 3.52 for the first mode of vibration (mode 1).

3. METHODS AND MATERIALS FOR EXPERIMENTAL DESIGN AND SETUP

This study adopted a four-phase methodology to guarantee meticulous and thorough investigations. A summary of these phases is presented in Fig. 1. This study randomly selected various air conditioner brands to ensure a representative sample of popular models in Ghana's market. A robust Internet of Things (IoT) system was developed to capture vibrational data from these air conditioners. The system interfaced directly with the compressors, logging vibrational data into an Excel sheet. After data collection, pre-processing techniques were employed to extract essential features. These features were then integrated into a piezoelectric energy harvester model in MATLAB Simulink. This methodology enabled the simulation of the vibrational dynamics, offering profound insights into the energy generation capabilities of the examined air conditioner units. Details of each step in the proposed methodology are explained in the sub-sections.

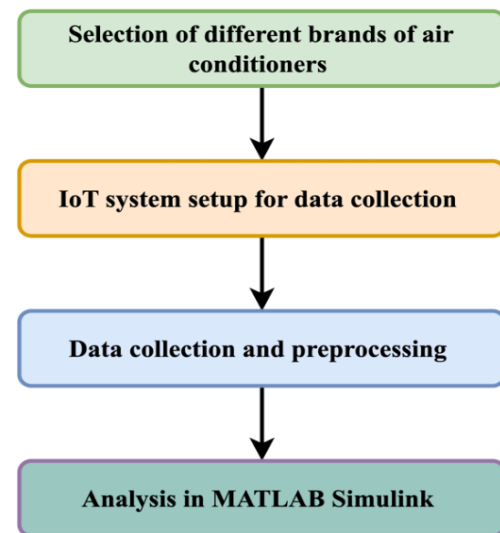


Fig. 1: Block diagram for experimental design.

3.1. Selection of Different Air Conditioner Brands for Experimental Setup

This study purposefully selected seven different air conditioner brands to ensure the representation of commonly used air conditioner types in Ghana. This was aimed at diversifying the array of air conditioning systems in the energy harvesting analysis. Each air conditioner unit was installed at different locations, each characterized by unique patterns of operation that could influence the voltage generated over time: Details of the location and usage patterns of each unit is provided in Table 1.

Again, the electrical specifications i.e., rated input power, rated input current of the air conditioners are given in Table 2.

3.2. IoT System Set-up for Data Collection

In this study, we developed an Internet of Things (IoT) framework to acquire and document vibrational data from multiple air conditioner models. The system incorporates numerous pivotal elements and methodologies, ensuring precise and trustworthy data gathering. The setup consists of a sensor, microcontroller, and computer with Arduino IDE and Microsoft Excel installed. This setup was integral to the experiment process, enabling the subsequent analysis of energy generation potential based on the recorded vibrations. Fig. 2 depicts the aforementioned setup, and details of the data collection processes are elaborated below.

A critical component of the IoT setup is the selection of an appropriate sensor capable of accurately detecting and measuring mechanical vibrations. For this purpose, an MPU-6050 GYRO+ACCELEROMETER sensor was selected due to its dual-axis accelerometer and gyroscope, which enabled comprehensive measurement of linear accelerations and rotational movements, aligning with the experiment's objective of capturing air conditioner vibrations in detail [15]. This sensor is connected physically and interfaced between the air conditioner compressor and an Arduino Uno microcontroller to sense vibrations. Also, to ensure precise

and consistent measurements, a calibration process is carried out on the MPU-6050 to adjust its sensitivity and offset parameters to eliminate any potential biases or inaccuracies in the collected data. The Arduino UNO is a central processing unit responsible for data acquisition and communication with the sensor. It is programmed to read the sensor data from the AC compressor continuously and sends it to a connected computer for storage in Excel and further analysis. The connection of MPU-6050 GYRO+ACCELEROMETER sensor to the Arduino Uno microcontroller is shown in Fig. 3. The physical setup of the IoT system which involves connection to AC compressor and laptop is shown in Fig. 4.

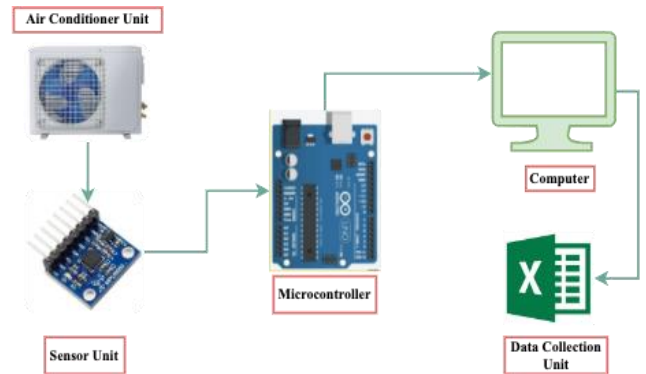


Fig. 2: IoT setup for data collection.

Table 1: Description of AC brands.

AC Brand	Location	Usage pattern
Chigo	Lecture’s office	Operates intermittently aligned with lecturer’s office hours
Nasco	Lecturer’s office	Operates intermittently aligned with lecturer’s office hours
LG	Lecturer’s office	Operates intermittently aligned with lecturer’s office hours
Beko	Student’s room on university campus	Operates based on student’s daily routine but remained operational throughout the evenings.
Frigidaire	Installed in a laboratory	Operates throughout the daytime during lab hours and remain off in the evening.
TCL	Lecturer’s office	Operates when the room is needed for activities
Hisense	Office of teaching assistants	Operates throughout the daytime during office hours

Table 2: Ratings of selected air conditioners.

Air Conditioner Type	Rated Input Power (W)	Rated Input Current (A)	Year of Installation
TCL	3430	12	>10 years
Beko	1800	9.5	>10 years
Hisense	1010	4.5	< 3years
LG	5000	8.5	> 5 years
Frigidaire	2122	9.46	>10 years
Nasco	1561	8.5	> 5 years
Chigo	1730	7.9	> 10 years

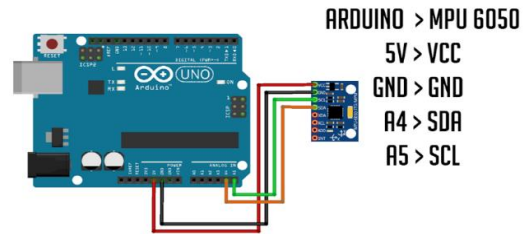


Fig. 3: Arduino Uno connected to MPU6050 GYRO+ Accelerometer.



Fig. 4: Physical set of IoT system for data collection.

3.3. Data Collection and Pre-processing

Vibration data was gathered at temperatures of 16°C, 20°C, and 24°C specifically for TCL, Beko, and Hisense while maintaining a steady 17°C for other units. Every data entry in the Excel file was marked with a timestamp of 0.01s to ensure accurate alignment with the air conditioner units’ respective operational states and usage patterns. This data was securely stored in a designated Excel file, allowing further analysis and processing. The data underwent a fast Fourier transform (FFT) treatment during the pre-processing phase. This involved importing the data into MATLAB and executing an FFT through custom code. The output of this transformation was a complex dataset, capturing the signal in its frequency, phase and acceleration spectrum. This FFT outcome was subsequently recorded in the Excel file. Sample outputs of vibration data analysis from the AC brands are shown in Figs. 5-7.

Tables 3 and 4 provide information about the different air conditioner types, the operating temperatures at which the vibrational data was collected, the frequency of the dominant vibration and its velocity from the Fourier analysis. The

maximum frequency and velocity are fed into the piezoelectric model in Simulink to harness the energy for further analysis.

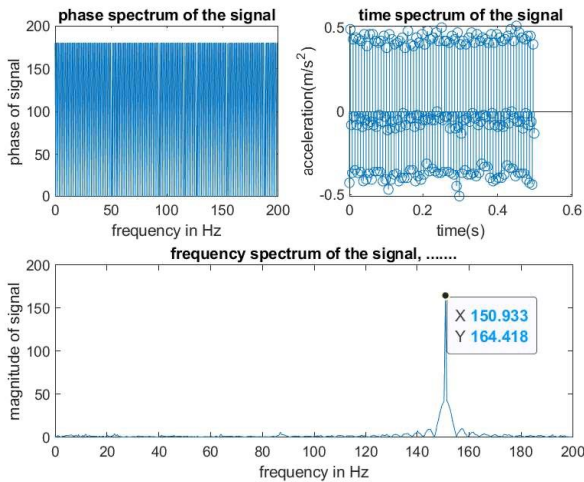


Fig. 5: Frequency, phase and time spectrum of Hisense vibrational data at an operating temperature of 24°C

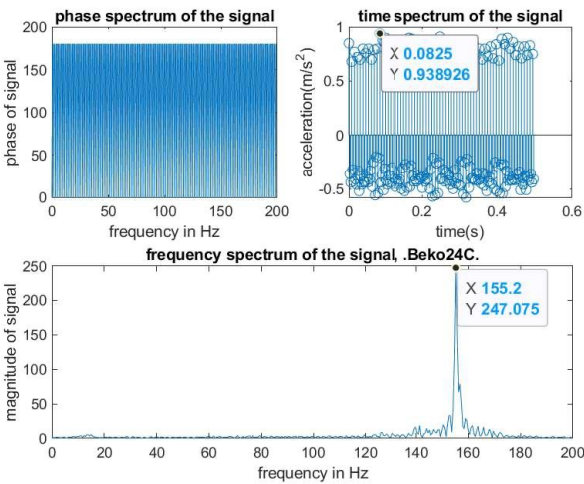


Fig. 6: Frequency, phase and time spectrum of Beko vibrational data at an operating temperature of 24°C

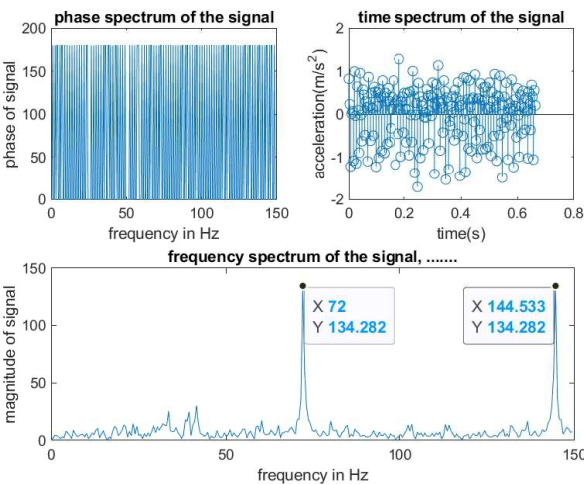


Fig. 7: Frequency, phase and time spectrum of TCL vibrational data at an operating temperature of 24°C

3.4. Simulation and Analysis in MATLAB Simulink

The block diagram in Fig. 8 is employed to model the piezoelectric energy harvester in MATLAB Simulink software.

3.5. Description of Each Block

Air conditioner vibration data and piezoelectric transducer: this serves as the source of vibrational data for energy harvesting. The vibration energy in a piezoelectric harvesting system consists of two parts, which are the mechanical and electrical parts. The mechanical part provides energy from the surrounding environment, which in this work represents the air conditioner compressor. This is transferred into the piezo device or transducer to vibrate its input and harvest energy. The vibrational source is modelled as a sinusoidal signal used to represent engines that rotate at a constant speed which is the case of an air conditioner compressor when set at a certain temperature shown in Fig.9.

The process of harvesting the vibrations from the air conditioner compressor is further modelled as a piezo bender connected to a vibration system within the energy harvesting system, as illustrated in Fig. 10. The piezo bender block shows a piezoelectric bimorph cantilever beam device, with its parameters used for the simulation detailed in Table 3. This device is modelled to vibrate and generate electrical potential by harnessing vibrational energy. Furthermore, the piezo bender has a tip mass and an unencumbered rotational free end on its right side. Including the tip mass serves multiple purposes, including the modulation of the system's resonance frequency, thereby optimizing its performance. Additionally, it enhances the mechanical responsiveness of the system, particularly during low-amplitude vibrations, thereby augmenting the overall output power. Applying an external force induces mass displacement, leading to deformation in the interconnected piezo element. These deformations yield a charge accumulation and voltage differential across the electrical terminals of the piezo bender, which are efficiently harvested as electrical power.

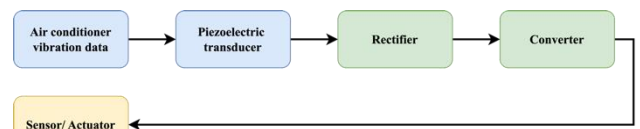


Fig. 8: Block diagram of piezoelectric energy harvester.

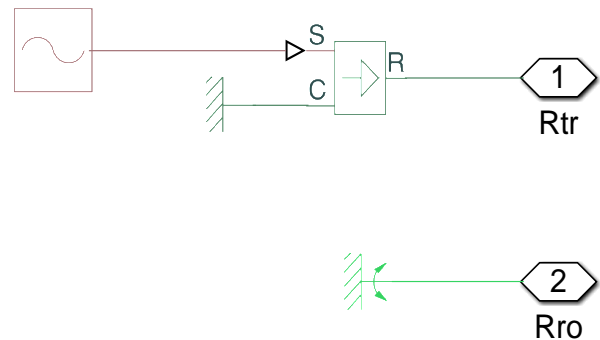


Fig. 9: Sinusoidal vibration source subsystem.

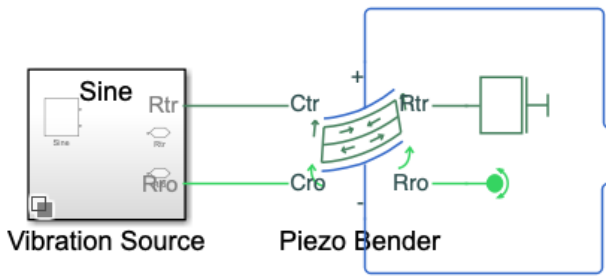


Fig. 10: Piezo bender connected to a vibrational source in Simulink.

Again, in this work, the vibration data collected from the different brands of air conditioners are used. Specifically, the dominant frequency component of the vibration and its velocity are set to the sinusoidal subsystem in Simulink shown in Fig. 11 to simulate the production of mechanical vibrations from the AC compressor.

Rectifier: In this research, a full-wave bridge rectifier is employed in conjunction with a piezo bender to facilitate the conversion of alternating current or voltage (AC) generated during the bending of the piezo device into direct current (DC). The rectification process transforms the sinusoidally varying AC input generated by the piezo bender into a pulsating DC voltage. The rectifier assembly comprises four diodes and a capacitor, serving as a filtering component to attenuate voltage ripple, as illustrated in Fig. 12. The resultant pulsating DC output voltage from the rectifier subsequently undergoes further refinement through a low pass filter, effectively reducing distortions and ensuring a smoother output.

Table 3: Cantilever beam parameters.

Parameter	Dimension
Beam Length	31.75mm
Beam Width	12.7mm
Beam thickness	0.5mm
Capacitance	15nF
Rated Drive Voltage, V_{rated}	180V
Free deflection at V_{rated}	0.233mm
Blocking Force at V_{rated}	-0.414N

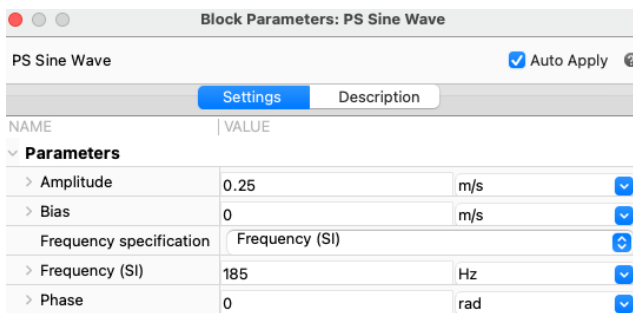


Fig. 11: Sinusoidal vibration source parameters.

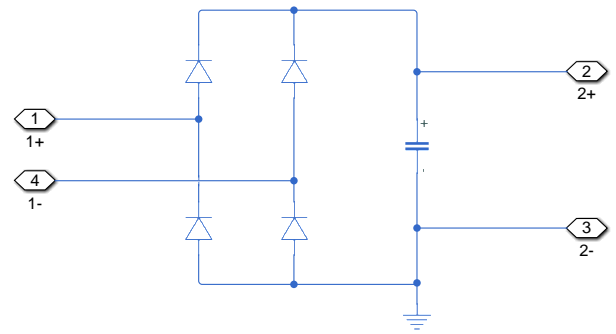


Fig. 12: Full-wave rectifier bridge subsystem with four diodes and one capacitor

Converter: In this study, the DC-DC converter is represented by a buck converter block, as depicted in Fig. 13. The buck converter regulates the voltage to transfer the maximum possible power to the load and ensures that the power transfer is unidirectional. Also, a pulse generator controls the converter in an open loop with a fixed switching frequency and duty cycle.

Actuator/Sensor: The DC voltage generated is applied to power a battery and a load depicted in Fig. 14. Initially, the energy harvester charges a battery. Then, the energy harvester and the battery power up a constant load. The battery cannot hold a charge since its voltage source varies with the amount of charge and resistance connected in series. The source battery's output will be precisely or very close to 3 volts if the internal resistance is adjusted to 2 ohms and the nominal voltage is 3 volts. This is the case since the nominal voltage is also 3 volts.

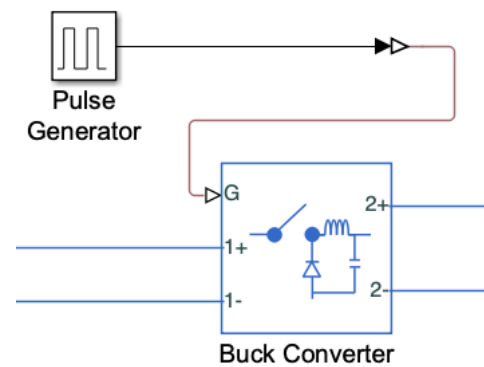


Fig. 13: Simscape buck converter model.

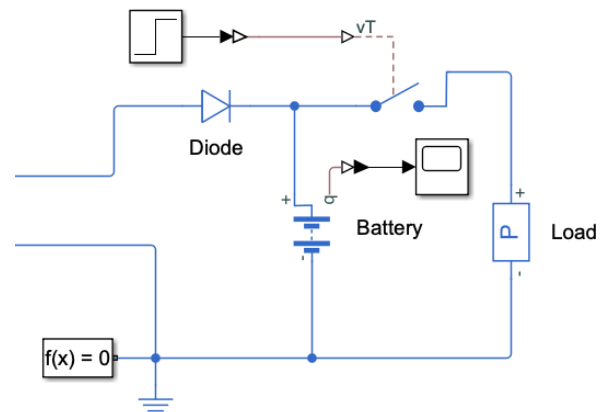


Fig. 14: Actuator circuit of battery and load.

4. SIMSCAPE MODEL OF PIEZOELECTRIC HARVESTER

The Simscape model in Fig. 15 from the existing literature was utilized to simulate energy harvesting from the air conditioner compressors.

5. RESULTS AND ANALYSIS

In this section, a detailed exploration of the maximum DC voltage outputs harvested from air conditioner compressors under varying conditions, encompassing different temperature settings and diverse compressor brands is presented. Again, the findings from the experimentation are analyzed and interpreted. The primary objective of this study was to assess the energy harvesting capabilities of seven prominent air conditioner compressor brands—TCL, Beko, LG, NASCO, Frigidaire, Chigo and Hisense on the Ghanaian market—while subjecting them to different operating temperatures. As energy harvesting from air conditioner compressors gains increasing significance in the context of sustainable and energy-efficient technologies, understanding the variables that influence their performance becomes paramount. The results presented in the preceding subsections summarize the intricate relationship between temperature and these compressors' maximum DC voltage output that can be harvested with a piezoelectric harvester. Additionally, these findings shed light on the disparities in energy harvesting potential across the assessed brands, serving as a valuable guide for decision-making in various applications reliant on air-conditioner compressor energy output.

5.1. Comparison of the Output Voltages of TCL, Beko and Hisense at an Operating Temperature of 16°C

The results in Table 4 present the maximum DC voltage harvested from the air conditioner units of three brands (TCL, Beko and Hisense) operating at a temperature of 16°C, 20°C and 24°C. This data is crucial in understanding how various factors such as vibration frequency, signal velocity, rated power, and the year of installation of the ACs influence their energy harvesting capabilities. Again, Table 4 shows the comparison of the average values of the frequency, velocity and maximum DC voltage harvested from the brands of ACs across all temperatures.

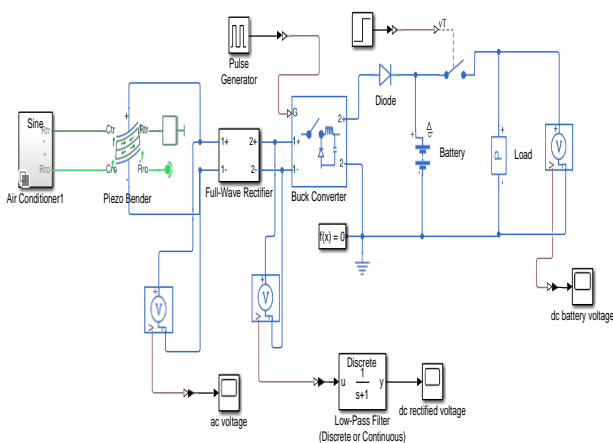


Fig. 15: Simscape model of piezoelectric harvester.

Table 4: Maximum voltage harnessed from different brands of air conditioners.

Air conditioner type	Temperature (°C)	Maximum Frequency (Hz)	Velocity of Signal (m/s)	Maximum DC Voltage Harvested (V)
TCL	16	140.80	0.60	5.03
Beko	20	141.11	0.90	6.52
Hisense	24	144.53	0.70	6.01
Beko	16	152.53	0.84	8.61
Frigidaire	20	154.13	0.74	8.29
Nasco	24	155.20	0.90	10.01
Hisense	16	125.33	0.50	3.24

TCL: At 16°C, the maximum frequency is 140.80 Hz, the velocity of the signal is 0.60 m/s, and the maximum DC voltage harvested is 5.03 V. As the temperature rises to 20°C, there is a slight increase in frequency to 141.11 Hz, a rise in signal velocity to 0.90 m/s, and an increase in harvested voltage to 6.52 V. At 24°C, the frequency further increases to 144.53 Hz, the velocity drops slightly to 0.70 m/s, while the harvested voltage drops marginally to 6.01 V.

Beko: Starting at 16°C, the maximum frequency is 152.53 Hz with a signal velocity of 0.84 m/s, and the harvested voltage is 8.61 V. At 20°C, the frequency slightly increases to 154.13 Hz, the signal velocity decreases to 0.74 m/s, but the harvested voltage decreases slightly to 8.29 V. By 24°C, the frequency has increased to 155.20 Hz, the signal velocity rises to 0.90 m/s, and the harvested voltage notably jumps to 10.01 V.

Hisense: At 16°C, Hisense shows the lowest frequency of 125.33 Hz compared to the other two brands, with a signal velocity of 0.50 m/s and harvested voltage of 3.24 V. At 20°C, there is a significant jump in frequency to 149.87 Hz, but the signal velocity remains the same at 0.50 m/s, leading to a harvested voltage of 5.74 V. At 24°C, the frequency slightly rises to 150.93 Hz, the velocity decreases to 0.40 m/s, and the voltage drops to 5.02 V.

Among the three brands, Beko consistently demonstrates the highest maximum frequency and harvested voltage across all temperatures. The high vibration velocity and frequency in the Beko and TCL air conditioners leading to higher voltage outputs can also be due to the wear and tear in some AC components, such as the fan, motor or compressor since they were installed about ten years ago. The low vibration velocity and frequency in the case of Hisense AC may be due to how new it is. Technological advancements have led to the developing of quieter and more efficient air conditioning units such as the Hisense brand. Again, modern air conditioners often incorporate features that minimize vibrations, such as better insulation, improved motor designs, and advanced compressor technologies. Clearly, the efficiency and capability of air conditioners to harness voltage vary based on the brand, year of installation and temperature. This information could be crucial for users or

industries aiming to optimize energy harnessing from air conditioners. The output voltage of the rectifier at temperatures of 16°C, 20°C and 24°C for TCL, Beko and Hisense are shown in Figs. 16-18.

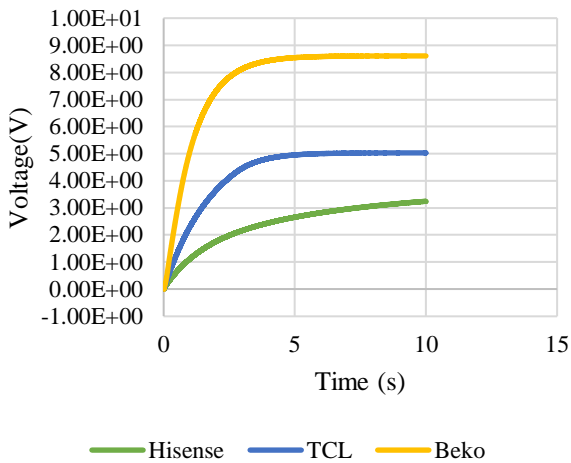


Fig. 16: Rectified voltage at 16°C.

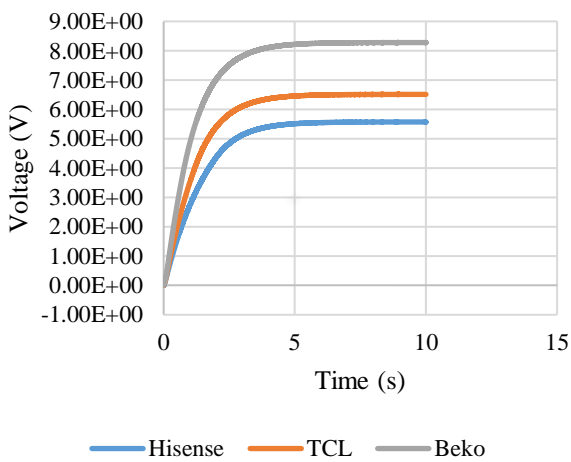


Fig. 17: Rectified voltage at 20°C.

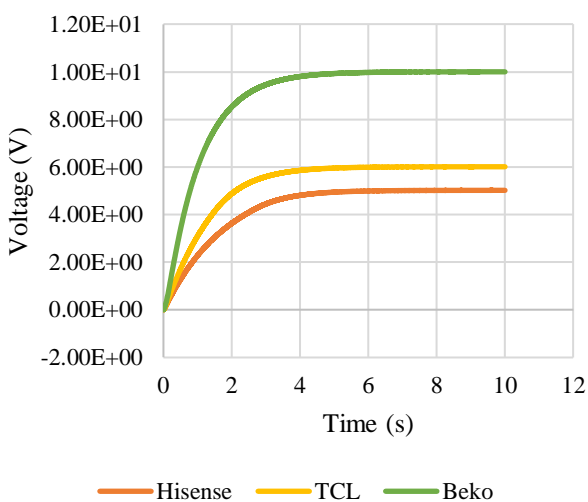


Fig. 18: Rectified voltage at 24°C.

5.2. Comparison of the Output Voltage Harvested from LG, NASCO, Frigidaire and ChIGO Air Conditioners at Different Operating Temperatures

Table 5 shows the maximum DC voltage harvested from LG, NASCO, Frigidaire, and ChIGO air conditioner vibrations at a constant temperature of 17°C. The results show that the maximum voltage harvested increases with frequency and velocity. A more detailed discussion is given below.

From Table 5, there is notable variations in vibrational frequency and velocity among the four brands of AC producing significant variation in the voltage harvested. Frigidaire, with the highest frequency of 252.27 Hz and velocity of 0.70m/s, demonstrates the highest maximum DC voltage harvested, measuring 6.72 V. With the next highest frequency of 145.60 Hz and a velocity of 0.6m/s, LG generates a maximum DC voltage of 5.60 V, showcasing a similar trend of higher frequency resulting in higher voltage output. Chicago, with a frequency of 133.87 Hz and velocity of 0.70m/s, and NASCO, at 128.00 Hz and a velocity of 0.50m/s, yield lower DC voltage outputs of 4.78 V and 3.53 V, respectively, further supporting the correlation between frequency and harvested voltage. It is clear that the amount of electricity that can be generated is limited by the frequency and velocity of the vibration, as well as the year of installation of the air conditioner. The output voltage of the rectifier is shown in Fig. 19.

Table 5: Maximum voltage harvested from vibrations of different air conditioners at a constant temperature.

Air conditioner type	Temperature (°C)	Maximum Frequency (Hz)	Velocity of Signal (m/s)	Maximum DC Voltage Harvested (V)
LG	17	145.60	0.60	5.60
NASCO	17	128.00	0.50	3.53
Frigidaire	17	252.27	0.70	6.72
ChIGO	17	133.87	0.70	4.78

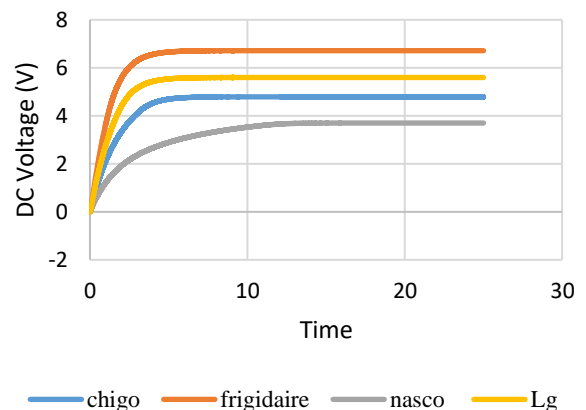


Fig. 19: Rectified output voltage at 17°C.

5.3. Correlation Between Maximum DC Voltage Harnesses and Temperature, Power Rating, Frequency and Velocity

The correlation table to study the impact of operating temperature (T), power rating (P), frequency (F) and velocity (S) of vibration signal on the amount of voltage (M) harvested from the ACs is shown in Table 6.

The results from Table 6 shows a strong positive correlation of 0.7892 and 0.7855 between the maximum voltage harnesses and the frequency and velocity respectively of the air conditioner compressor signal. This is because the frequency and velocity of the compressor determine the amount of mechanical energy available to be converted into electrical energy. The higher the frequency and velocity, the more mechanical energy is available and the higher the maximum voltage harnesses. There is also a positive correlation of 0.0659 between the maximum voltage harnesses and the rated power of the air conditioner compressor. This is because the rated power of the compressor is a measure of the amount of mechanical power it consumes. The higher the rated power, the more mechanical power can be converted into electrical energy. However, the correlation between the maximum voltage harnesses and the rated power is less intense than the correlation between the maximum voltage harnesses and the frequency and velocity of the compressor. Again, there is a positive correlation of 0.2839 between temperature and maximum voltage harvested, which can be explained by the fact that the electrical conductivity of the materials used in the compressor increases with temperature. This means more electrons can flow through the circuit, producing higher voltage output. The Table shows that the compressor's frequency and velocity primarily determine the maximum voltage harnesses from an air conditioner compressor. The rated power of the compressor also has a positive effect on the maximum voltage harnesses, but the effect is not more substantial.

6. CONCLUSION

The energy harvesting potential of various air conditioner brands on the Ghanaian market has been explored. The study unveiled significant insights into the eco-friendly energy-harnessing landscape through systematic experimentation and analysis. It was evident that different air conditioner brands, each with unique design and operational characteristics, exhibit varying energy harvesting capabilities. The study established a strong positive correlation between the frequency and velocity of air conditioner compressor vibrations and the maximum voltage harnesses.

Table 6: Correlation matrix.

	T	P	F	S	M
T	1.0000				
P	0.0000	1.0000			
F	0.4893	-0.1187	1.0000		
S	0.0466	0.4898	0.3218	1.0000	
M	0.2839	0.0659	0.7892	0.7855	1.0000

This correlation underlines the significance of mechanical energy, available in vibrations, in influencing the electrical energy output. Moreover, factors like the rated power of the compressor and the operating temperature also correlate with the amount of voltage harnesses. The rated power, indicative of the compressor's mechanical power consumption, revealed a less intense yet positive correlation with the harvested voltage. Simultaneously, the positive correlation between temperature and harvested voltage points towards the increased electrical conductivity of compressor materials at higher temperatures. Again, the year of installation also manifested as a significant determinant of energy harvesting efficiency.

Furthermore, brand-specific analyses showcased brands like Beko consistently outperforming others, emphasizing the brand-to-brand variability in energy-harnessing capabilities. The technological strides made in recent years, with brands focusing on quieter and more efficient units, were also evident in the research findings. This research is paramount in light of the growing global emphasis on sustainable energy solutions. The detailed insights from the study can guide consumers and industries in optimizing energy harnessing from everyday appliances like air conditioners. Moreover, the findings can spur further innovations in piezoelectric energy harvesting, pushing the boundaries of eco-friendly energy generation. In essence, this research not only underscores the untapped potential of mechanical vibrations in energy generation but also paves the way for more comprehensive studies and technological advancements in this domain.

7. FURTHER RESEARCH

While this study analyzed selected brands of air conditioners available in the Ghanaian market, further research should encompass a broader range of local and international brands. This would provide a more comprehensive understanding of the energy harvesting potential across different manufacturing and design philosophies. Long-term studies on air conditioner units should be conducted to understand the wear and tear effects on energy harvesting capabilities over extended periods. This would provide insights into the longevity and sustainability of such energy harvesting methods.

CREDIT AUTHORSHIP CONTRIBUTION STATEMENT

Daniel Kwegyir: Conceptualization, Formal analysis, Project administration. **Francis Bofo Effah:** Investigation, Validation. **Daniel Opoku:** Resources, Supervision. **Peter Asigri:** Funding acquisition, Roles/Writing - original draft. **Yoosi Hayford:** Data curation, Roles/Writing - original draft. **Eliezer Owusu Boateng:** Conceptualization, Software. **Kwaku Kessey-Antwi:** Conceptualization. **Nana Maryam Abdul-Bassit Munagah:** Conceptualization, Methodology. **Kelvin Worlanyo Tamakloe:** Conceptualization, Methodology.

DECLARATION OF COMPETING INTEREST

The authors declare that they have no known competing financial interests or personal relationships that could have appeared to influence the work reported in this paper. The ethical issues; including plagiarism, informed consent, misconduct, data fabrication and/or falsification, double publication and/or submission, redundancy has been completely observed by the authors.

REFERENCES

- [1] I. D. Ibrahim et al., "A review on Africa energy supply through renewable energy production: Nigeria, Cameroon, Ghana and South Africa as a case study," *Energy Strategy Reviews*, vol. 38. Elsevier Ltd, Nov. 01, 2021. doi: 10.1016/j.esr.2021.100740.
- [2] W. Strielkowski, E. Tarkhanova, M. Tvaronavič, and Y. Petrenko, "Renewable Energy in the Sustainable Development of Electrical," *Energies*, vol. 14, no. 24, article 8240, 2021.
- [3] N. Sezer, and M. Koç, "A comprehensive review on the state-of-the-art of piezoelectric energy harvesting," *Nano Energy*, vol. 80, no. August 2020, p. 105567, 2021.
- [4] N. Burham, M. N. A. Malek, A. A. Aziz, N. I. Shuhaimi and A. M. Markom, "Development of piezoelectric energy harvesting via vehicle movements," in *2019 IEEE 13th International Conference on Telecommunication Systems, Services, and Applications*, Bali, Indonesia, 2019, pp. 128-131.
- [5] Y. Li et al., "An electromagnetic-piezoelectric-triboelectric hybridized energy harvester towards blue energy**Research supported by ABC foundation," in *Proceedings of the 16th Annual IEEE International Conference on Nano/Micro Engineered and Molecular Systems*, Institute of Electrical and Electronics Engineers Inc., Apr. 2021, pp. 1070-1073.
- [6] W. M. Jayarathne, W. A.T. Nimansala, and S. U. Adikary, "Development of a vibration energy harvesting device using piezoelectric sensors," in *4th International Multidisciplinary Moratuwa Engineering Research Conference*, Sri Lanka, 2018, pp. 197-202.
- [7] A. Ray, V. Butram, N. Gupta, and A. Naugarhiya, "Non-conventional cantilever for piezoelectric energy harvesting at ultra low resonant frequency," in *9th Annu. Inf. Technol. Electromechanical Eng. Microelectron. Conf.*, 2019, pp. 90-93.
- [8] V. J. Caetano, and M. A. Savi, "Multimodal pizza-shaped piezoelectric vibration-based energy harvesters," *J. Intell. Mater. Syst. Struct.*, vol. 32, no. 20, pp. 2505-2528, Dec. 2021.
- [9] C. Covaci, and A. Gontean, "Two-stage converter for piezoelectric energy harvesting using buck configuration," in *2020 IEEE 26th International Symposium for Design and Technology in Electronic Packaging*, Oct. 2020, pp. 408-411.
- [10] M. Saida, G. Zaibi, M. Samet, and A. Kachouri, "Design and study of piezoelectric energy harvesting cantilever from human body," in *2018 15th Int. Multi-Conference Syst. Signals Devices*, 2018, pp. 164-168.
- [11] Z. Wang, L. He, Z. Zhang, Z. Zhou, J. Zhou, and G. Cheng, "Research on a Piezoelectric Energy Harvester with Rotating Magnetic Excitation," *J. Electron. Mater.*, vol. 50, no. 6, pp. 3228-3240, Jun. 2021.
- [12] N. Rai, M. J. Nagaraj, A. M. Morey, and V. Shantha, "Construction and simulation of various structures of unimorph piezoelectric cantilever for energy harvest," in *Proceedings of the 4th International Conference on Communication and Electronics Systems, ICCES 2019*, 2019, pp. 651-655.
- [13] C. Team, "Piezoelectric Effect Discovery of Piezoelectric Effect," pp. 1-6, 2023.
- [14] G. C. Mekalke, and A. V. Sutar, "Modal analysis of cantilever beam for various cases and its analytical and FEA analysis," *Int. J. Eng. Technol. Manag. Appl. Sci.*, vol. 4, no. 2, pp. 60-66, 2016.
- [15] C. I. Nwakanma, F. B. Islam, M. P. Maharani, D. S. Kim, and J. M. Lee, "IoT-based vibration sensor data collection and emergency detection classification using long short term memory (LSTM)," in *3rd Int. Conf. Artif. Intell. Inf. Commun. ICAIIC 2021*, pp. 273-278, 2021.
- [16] J. A. B. Gripp, and D. A. Rade, "Vibration and noise control using shunted piezoelectric transducers: A review," *Mech. Syst. Signal Process.*, vol. 112, pp. 359-383, 2018.
- [17] S. Sivakumar, M. J. Sathik, P. S. Manoj, and G. Sundararajan, "An assessment on performance of DC-DC converters for renewable energy applications," *Renew. Sustain. Energy Rev.*, vol. 58, pp. 1475-1485, 2016.
- [18] [A. Zablocki, "Energy Storage," Environmental and Energy Study Institute, 2019. \[Online\]. Available: https://www.researchgate.net/publication/354613849_Energy_Storage_2019](https://www.researchgate.net/publication/354613849_Energy_Storage_2019)

BIOGRAPHY

Daniel Kwegyir received his master's degree in Power Systems Engineering in 2020 and a bachelor's in Electrical and Electronic Engineering, all at the Kwame Nkrumah University of Science and Technology (KNUST), Ghana, in 2018. He is an Assistant lecturer at the Department of Electrical and Electronic Engineering, KNUST. His research interests include Artificial Intelligence and its application in power systems and renewable energy.



Francis Bofo Effah received the BSc. Electrical and Electronic Engineering degree at the Kwame Nkrumah University of Science and Technology (KNUST), Kumasi, in 2001, the MSc in Electrical Engineering from the University of Nottingham, UK, in 2009, and the PhD in Electrical and Electronic Engineering, from the University of Nottingham, UK, in 2014. He is working in the Department of Electrical and Electronic Engineering of KNUST, Kumasi, as a Senior Lecturer and currently the Head of Department. His research interests include control and modulation of power converters, application of power converters in power



systems, and electrical technologies for sustainable and renewable energy systems.



Daniel Opoku received his doctorate in Automation and Controls at North Carolina A & T State University, USA, in 2013 and a Bachelor's in Electrical and Electronic Engineering at the Kwame Nkrumah University of Science and Technology (KNUST), Ghana, in 2007. He is a Senior lecturer at the Department of

Electrical and Electronic Engineering, KNUST. His research interests include Modern Controls Theories and Applications for Unmanned Aerial Vehicles Sensors, Actuators, and Instrumentation, Artificial Intelligence, and Applications in Renewable Energy.



Peter Asigri received his master's degree in Renewable Energy at the University of Hull, UK, in 2017 and a Bachelor's in Electrical and Electronic Engineering at the Kwame Nkrumah University of Science and Technology (KNUST), Ghana, in 2015. He is an Assistant lecturer at the Department of

Electrical and Electronic Engineering, KNUST. His research interests include Performance Analysis of Solar PV systems, Renewable Energy Grid Integration, Wind Resource Assessment, and Power Systems



Yoosi Hayford, received his Bachelor's degree in Electrical and Electronic Engineering at the Kwame Nkrumah University of Science and Technology (KNUST), Ghana, in 2023. His research interests include Renewable Energy and Power Systems.



Eliezer Owusu Boateng, received his Bachelor's degree in Electrical and Electronic Engineering at the Kwame Nkrumah University of Science and Technology (KNUST), Ghana, in 2023. His research interests include Renewable Energy and Power Systems.



Kelvin Worlanyo Tamakloe received his Bachelor's in Electrical and Electronic Engineering at Kwame Nkrumah University of science and technology (KNUST), Ghana in 2023. His research includes Developing innovative power converter topologies to optimize renewable energy integration, Electric Vehicle Propulsion systems, Advanced Motor Drive Control, Smart Grids and Microgrids.



Nana Maryam Abdul-Bassit Munagah received her Bachelor's in Electrical and Electronic Engineering at Kwame Nkrumah University of science and technology (KNUST), Ghana in 2022. Her research interests lie in leveraging AI and ML to optimize system performance, energy efficiency, and creating intelligent behaviors in automation in engineering. She is also keen on exploring edge computing for real-time data processing, creating autonomous systems, enhancing human-machine interaction, and building energy-efficient AI models.

Copyrights

© 2024 Licensee Shahid Chamran University of Ahvaz, Ahvaz, Iran. This article is an open-access article distributed under the terms and conditions of the Creative Commons Attribution –NonCommercial 4.0 International (CC BY-NC 4.0) License (<http://creativecommons.org/licenses/by-nc/4.0/>).





Shahid Chamran
University of Ahvaz



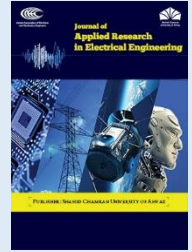
Iranian Association of
Electrical and Electronics
Engineers

Journal of Applied Research in Electrical Engineering

E-ISSN: 2783-2864

P-ISSN: 2717-414X

Homepage: <https://jaree.scu.ac.ir/>



Research Article

Efficient Responding to Demand and Robust Voltage Control of an Islanded DC Microgrid Under Variations in Load and Supply

Sajed Derakhshani Pour ^{1,2} , and Reza Eslami ^{2,*} 

¹ Department of Energy, Polytechnic University of Milan, Milan, Italy

² Department of Electrical Engineering, Sahand University of Technology, Tabriz, Iran

* Corresponding Author: eslami@sut.ac.ir

Abstract: In the last few years, there has been growing attention to isolated DC microgrids (MGs) with robust voltage control and efficient responding to demand in the face of fluctuating demands and supply amounts. This attention is due to significant voltage mismatches originating from the sudden transitions of the load demand and the active power of the supplies, such as photovoltaic (PV) systems. To address these goals, a novel nonlinear robust voltage control strategy with a cascaded design consisting of proportional-integral (PI) and sliding mode control (SMC) techniques is developed in this research for the battery energy storage system (BESS). Additionally, this research considers a fuel cell as another power supply in addition to a solar PV system. For maximum power point tracking (MPPT) of the PV system, a novel backstepping sliding mode control (BSMC) technique is developed as well. The effective functioning of the suggested cascaded control strategy is examined using MATLAB/Simulink. The outcomes of the simulation represent the effectiveness of the proposed approach in robustly regulating the voltage level of the DC link at 50 V with small deviations in tracking, and quick reaction to fluctuations in both demand and supply sides, as well as guaranteeing an even distribution of responses to demand fluctuations from the DC MG.

Keywords: DC microgrid, cascaded robust voltage control, maximum power point tracking, battery energy storage system, backstepping sliding mode control, renewable energy sources

Article history

Received 08 January 2024; Revised 29 March 2024; Accepted 18 April 2024; Published online October 9, 2024.

© 2024 Published by Shahid Chamran University of Ahvaz & Iranian Association of Electrical and Electronics Engineers (IAEEE)

How to cite this article

S. Derakhshani Pour, and R. Eslami, "Efficient responding to demand and robust voltage control of an islanded DC microgrid under variations in load and supply," *J. Appl. Res. Electr. Eng.*, vol. 3, no. 1, pp. 51-63, 2024.

DOI: [10.22055/jaree.2024.45776.1100](https://doi.org/10.22055/jaree.2024.45776.1100)



1. INTRODUCTION

1.1. Motivations

The global shift away from conventional energy sources, notably fossil fuels, and toward renewable energy sources (RESs) such as solar PV systems keeps on gaining traction. This trend is being motivated by growing awareness of the considerable disadvantages connected with the use of fossil fuels. These negatives include the discharge of greenhouse gases and contaminants, the gradual dwindling of limited resources, which leads to crises in the energy sector, financial obligations, and the deterioration of current energy systems' functionality. Deployment of RESs, notably PV systems, is a possible approach for reducing the environmental effect of conventional supplies of energy. Nevertheless, the intermittent characteristic of RESs must be addressed. Solar energy

generation, for example, is affected by the climate and sunlight accessibility. To tackle this constraint and provide a continuous and reliable energy supply, rising attention is being placed on combining RESs with BESSs within MG. The power balance between the generating and consumption sides is maintained by adding BESSs into MG. BESSs are critical in storing surplus energy created during maximum generation intervals and providing it during weak or zero power generation time frames. This coordination improves the MG's reliability by optimizing power dispatch. By effectively controlling the flow of power, the MG becomes healthier and stable, lowering the danger of disturbances. Furthermore, concerted attempts in power sharing among various domains enable greater RES use while mitigating the effect of their intermittent behavior. This implies that variations in renewable energy production, such as those induced by shifts in weather, can be minimized through concerted activities,

resulting in a more seamless integration of RES into the grid structure [1, 2]. As a fundamental configuration, energy communities (ECs) are defined as a collection of demands and supplies that exchange energy on a local distribution grid [3]. ECs are not considered as islanded MGs. MGs are responsive electric power systems that can be divided into DC and AC MGs. DC MGs have various benefits over AC MGs [4-6]. The absence of frequency and reactive power characteristics is a considerable benefit. Maintaining a constant frequency and regulating reactive power in AC systems are challenging and need extra control techniques. DC MGs eliminate the requirement for frequency synchronization and reactive power control by running on a consistent voltage range. Additionally, DC MGs provide improved and more precise system operation. The lack of frequency variations enables greater control over power flow and voltage values. This improved degree of control leads to a more robust and rapid energy delivery system, which is critical for managing current power grid needs [7]. The great reliability of DC MGs is a further significant benefit. The DC design's straightforwardness, with a fewer number of elements and less complexity, leads to better system reliability. This is especially beneficial in situations where grid resilience and robustness are required, such as critical facilities and distant sites. Furthermore, DC MGs enable greener solutions for preserving the environment. The removal of some power conversion procedures, as well as the intrinsic efficiency of DC transmission, decreases energy losses and has minimal effect on the ecosystem. This is consistent with the global quest for renewable and environmentally friendly energy options [8]. Fig. 1 represents the architectural framework of the suggested DC MG design. This arrangement is a simplified and effective structure that combines multiple components ideally to provide secure and renewable energy delivery. The PV system, a critical RES, sits at the heart of the entire framework. A DC-DC step-up converter appropriately connects the PV array to the DC link. This converter is an important component of the system because it allows for the effective transformation of the produced DC voltage from the PV array to the appropriate useful voltage of the DC bus. This procedure is critical for guaranteeing the energy generated by the solar panels is adequately absorbed and incorporated into the MG. Furthermore, a fuel cell is considered as the second power supply to help the PV system in properly meeting the load demand. This power supply source is linked to the DC bus through a unidirectional DC-DC converter which is managed by SMC. Finally, the proposed DC MG includes a BESS to improve versatility and robustness. A DC-DC bidirectional converter properly connects the BESS to the DC link. This reversible converter manages the two-way flow of power between the DC link and the BESS. The bidirectional converter facilitates the storing of surplus energy in the BESS during periods of extra production. When the energy request exceeds the immediate supplies of the PV system and fuel cell, the converter permits the transfer of stored energy from the BESS, assuring an uninterrupted and reliable power supply to the MG. The proposed layout has many benefits. The integration of the PV array, fuel cell and BESS via specialized DC-DC converters enables a more straightforward and regulated energy flow, reducing energy losses and improving overall system efficiency. Furthermore, the BESS-connected converter's bidirectional capabilities provide a layer of flexibility, allowing the MG to rapidly respond to changes in both consumption and supply sides, which lead to various voltage drops and spikes. These voltage mismatches are addressed and suppressed by the proposed control algorithm.

1.2. Literature Review

In recent years, the robust voltage control and equal responding to demand of isolated DC MGs including PV, BESS, and other power supplies have arisen as major focuses of academic inquiry. The necessity to overcome the issues provided by fluctuating loads and supply variations is driving growing curiosity in these areas. Isolated DC MGs, which are meant to function independently of the main utility grid, must deal with unpredictable and unexpected situations, necessitating complex control systems for maximum efficiency. Robust voltage control is an essential part of this solution. Voltage stability, an important feature of MG functioning, is critical to guaranteeing the MG system's steady and reliable performance, especially in the face of unpredictable variations in both demand and supply. As demand varies during the day, and RESs bring unpredictability into the supply combination, voltage stability becomes critical. Voltage stability refers to the MG's capability to preserve proper voltage levels within accepted boundaries, avoiding voltage spikes or under-voltages that could cause malfunctions or operational disturbances. In the face of shifting consumption patterns and intermittent renewable energy production, enhanced monitoring, control, and administration solutions are critical for dynamically altering voltage levels and optimizing performance to meet the MG's developing requirements. Researchers have been actively investigating novel regulation strategies for maintaining a steady voltage profile, hence improving the resilience of DC MG [9, 10]. At the same time, demand response is the process of regulating and altering customer usage of energy in reaction to evolving circumstances inside the MG. Finding a harmonic balance between generation and demand is critical for grid stability and avoiding instabilities that can contribute to power outages. Consequently, a broad range of control systems for MGs have been presented in the literature, including droop control, SMC, droop-SMC, fuzzy logic, artificial intelligence (AI), and model predictive control (MPC) strategies. An adaptive droop control technique for DC MG has been defined in [11], with the main goal of successfully handling voltage control issues and guaranteeing an equal flow of current within the DC MG structure. By dynamically adjusting droop characteristics, this approach enhances voltage stability and promotes a balanced flow of current, thereby optimizing the performance and reliability of DC microgrid systems. [12] introduces a unique converter control approach based on a configurable variable droop coefficient. The fundamental goal of this strategy is to maintain voltage stability when there are considerable and rapid variations in power inside the system. [13] makes a substantial addition by presenting a unique adaptive droop control approach specially developed to support an integral feed-forward SMC within the PV-BESS DC MG framework to considerably increase each BESS converter's voltage response speed. [14] suggests integrating universal droop control with SMC to provide distributed energy resource (DER) integration and power-sharing management for the DC MG, therefore solving the DC MG's power stability. [15] advances sustainable energy integration by utilizing SMC and PWM pulses to enhance PV power production while maintaining DC voltage stability in an integrated system comprised of PV, wind, and BESS. In order to indicate the operational advantage of DC MG, [16] develops an SMC with

an integrated design and compares it to a simple PI control method. This comparative study highlights the enhanced effectiveness of operation and performance benefits given by the SMC in DC MG structures. In [17], the contributors have proposed an adaptive SMC particularly designed for dc-dc step-up converters, which is systematically implemented within the framework of PV-Wind-BESS-EV DC MG that serves CPLs in order to guarantee the maintaining adequate stability margins, especially when encountered with significant and sudden changes in load demand. In [18], an important breakthrough in control methods is proposed by the introduction of an adaptive fuzzy integrated fractional order controller that is particularly developed for a DC MG consisting of a hybrid energy storage system (HESS) to improve DC link voltage regulation, addressing and eliminating imbalances between consumption and supply within the MG. The artificial neural networks (ANNs) control approach is presented in [19] as a particular type of Artificial Intelligence (AI) for a DC MG consisting of DERs and BESS in order to enable efficient control of power converters while preserving efficiency, thus enhancing the general adaptability of the system and ensuring that the DC link voltage continues to be inside the admitted boundaries, improving the system's stability and reliability. [20] entails a decentralized model predictive control (DMPC) structure aimed at preserving voltage stability and equal power dispatch within a DC MG characterized by constant power loads (CPLs). This approach contributes to improve system performance and reliability by dynamically controlling voltage levels and guaranteeing equal power sharing across the grid. [21] also compares a unique model predictive control (MPC) approach and linear control strategy in view of successfully managing the DC link voltage level of a DC-DC step-up converter while also preserving the stability of the DC MG in the face of dynamic load behavior.

1.2.1. Gaps and Contributions

Given the information presented thus far, it is undeniable that there are significant gaps in the existing corpus of literature. In [11-14] obtaining accurate control and proper power sharing in droop control schemes can be difficult, resulting in voltage error and unequal supply usage, particularly in systems with fluctuating loads and operating cases. Droop control techniques are also easily affected by modifications in system variables. The changes in such variables can have an impact on the precision of droop calculations. These solutions have generally been intended for unidirectional power flow, which may restrict their usefulness in bidirectional power flow structures, particularly those that incorporate RESs and BESSs. Finally, these systems may have response time restrictions, especially in circumstances requiring quick and exact modifications. Although using a single SMC technique in [15-17] provides robust and rapid functionality in the face of uncertainty, it suffers from chattering issues due to high-frequency fluctuations or fast switching of duty cycle near the sliding surface, which can cause probable steady-state challenges and undesired damage to the materials in physical structures. The fuzzy logic control strategy, which is used in [18], is based on cognitive principles and fuzzy logic sets, which leads to issues in the exact modeling of complicated system

characteristics. Precise fuzzy principles can be challenging to expand, especially in nonlinear systems that have time-dependent dynamics. These controllers may have difficulty adapting to abrupt alterations in system characteristics. They are built to cope with slowly shifting conditions and may show shortcomings in quickly shifting surroundings. More sophisticated control approaches may be necessary in some circumstances for successful control in extremely nonlinear or unpredictable cases. In [19], knowing the network's underlying functions and procedures for making decisions might be difficult, resulting in an absence of clarity. Furthermore, the network's functionality is heavily impacted by the type of training data. In cases when the data is restricted or prejudiced, the ANN might be unable to generalize effectively to previously encountered instances. As a result, ANNs may experience difficulties responding to fast-changing systems. MPC strategies in [20, 21] are computationally complicated and take a significant amount of computing time and money to implement due to the large uncertainties in the modeling of the system, which may restrict applications that operate in real-time, especially in systems that demand quick reactions. Additionally, MPC only depends on the precise model of the system for forecasting, and any differences between the model and the real system performance might result in poor functionality. As a result, MPC is affected by model uncertainty, variable changes, and disruptions.

According to the gaps found in the existing literature above, the following are the goals and contributions of this research:

- I. A novel nonlinear robust control strategy, which combines the advantages of PI control with SMC, is introduced for a PV-BESS-fuel cell DC MG with the primary goals of assuring robust DC link voltage regulation and providing evenly-distributed response to fluctuating load demands and solar exposures.
- II. A BSMC approach, whose basic concept is the utilization of MPPT to maximize peak power harvesting from solar PV systems, is used to improve the efficiency of solar output power extraction by continuously and automatically controlling the operating point of the PV system to coincide with the MPP.
- III. In comparison to other control approaches, the suggested method notably has lower DC link voltage oscillations, more robust functioning, more rapid dynamic responsiveness, and less chattering influences. These distinguishing traits contribute to the suggested control approach's effectiveness.

1.3. Paper Arrangement

The remainder of the paper is organized in the following order: The suggested DC MG concept is described in [Section 2](#). [Section 3](#) presents formulations of the suggested control technique. [Section 4](#) depicts simulation findings and scenarios. [Section 5](#) finally concludes the paper.

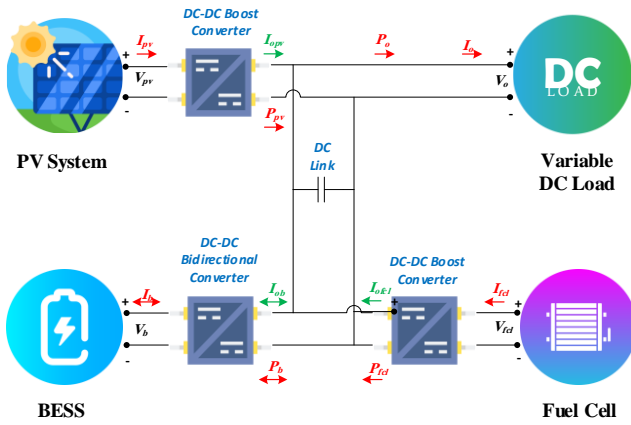


Fig. 1: DC MG structure.

2. MODEL DESCRIPTION

2.1. PV Array

Solar PV systems stand out as a superior alternative to standard DC MG power sources when it comes to power supply possibilities. The capability of PV systems to generate zero greenhouse gases contributes greatly to ecological sustainability while at the same time lowering power production costs. Solar irradiation and cell temperature are important parameters affecting the efficiency of PV systems since they directly affect the output power of the PV panels. A systematic strategy is used to maximize the system's performance. The solar array is smoothly incorporated into the DC link via a DC-DC step-up converter, which is an important component in guaranteeing an optimized power supply to satisfy the load needs. The requirement to run at the maximum power based on the P-V curve is an essential concept guiding the operation of solar PV arrays. This exact position on the curve ensures that the panels generate the highest amount of power feasible. The MPP-based BSMC is used to attain this level of accuracy in operation. This complex control system successfully tracks and adjusts for variations in the irradiation amount, ensuring that the PV array runs at its highest productivity point constantly. The PV module under discussion, the KC200GH-2P type, has 54 series-connected cells, each of which contributes to its total electrical properties. Table 1 provides a complete summary of the electrical characteristics, providing an in-depth look into the module's parameters and performance characteristics. These metrics include a variety of key data points, such as voltage, current, and power levels and provide a thorough insight of the module's behavior under varied situations.

Table 1: The electrical specifications of the PV panel.

Parameters	Values
MPP voltage V_{mpp}	26.6 [V]
MPP current I_{mpp}	7.55 [A]
Maximum power P_{mpp}	200 [W]
Short circuit current I_{sc}	8.21 [A]
Open circuit voltage V_{oc}	32.9 [V]
Temperature coefficient of SC current K_{sc}	0.00479
Diode ideality factor n	1.8
Cell temperature T	25 [°C]

2.2. Fuel Cell

A fuel cell, by incorporating an additional power source into the system, plays a supporting function in improving the ability to respond of the PV system to variable load demands. The fuel cell, which operates at a constant power output of 100 W, is purposefully utilized to offer an extra energy supply, guaranteeing a steady and reliable power supply to satisfy the dynamic demands of the load. A unidirectional DC-DC boost converter is the vital component developed for effectively carrying energy from the fuel cell to the system, facilitating the connection between the fuel cell and the DC link. SMC approach is used to regulate this converter, which is a robust and adaptive control method noted for its capability to tolerate inconsistencies and disturbances in the system. This adaptive control method enables accurate power output modification, guaranteeing that the fuel cell's extra energy instinctively supports the PV system's reaction to variable load demands. The integrated functioning of those parts not only improves the total reliability of the power production but also maximizes the use of RESs, demonstrating a comprehensive method for greener and responsive power systems.

2.3. Battery Energy Storage System

A BESS performs a crucial act in properly regulating the power imbalance that frequently occurs between supply and consumption inside a DC MG. A bidirectional DC-DC converter is used to provide a smooth link between the BESS and the DC link. This converter acts as an important interface, facilitating the regulated flow of electrical power between the BESS and the MG, as well as charging and discharging activities as necessary. The deployment of a PI-SMC strategy can be a complex and versatile control method designed to assure the DC MG's efficient and steady performance. This controller is critical in coordinating the BESS's charging and discharging operations, dynamically answering to changes in power demand and generation. This multidimensional strategy for BESS control not only tackles power discrepancy issues but also improves the overall reliability and efficiency of the DC MG, demonstrating the need for cutting-edge control tactics in present-day energy management. By synchronizing the power flow with the system's changing needs, the PI-SMC controller helps the DC MG's proper and balanced functioning by efficiently managing the following two operation phases:

Charging mode: The BESS plays a critical role during charging in effectively handling the extra power supplied by both the PV system and the fuel cell. This occurs when the needed output power to fulfill the demanded power is less than the total amount of power provided by the solar PV and the fuel cell. The BESS works as a repository for unused energy during this period, successfully gathering extra power that would otherwise go wasted. The energy storage system provides for the most efficient use of produced power, reducing waste and assuring a long-term solution to energy management. This mode is critical for system balance since it facilitates the storing of more energy during periods of ample supply, allowing the BESS to satisfy load demand effortlessly in later time frames when generation may be inadequate.

Discharging mode: In this phase, a scenario occurs in which one of the suppliers is unable to entirely match the

desired load power. In such cases, the system easily switches to utilizing the stored energy of the BESS, commencing a discharge operation to compensate for the shortage in total power generated by the PV array and the fuel cell. This mode is critical for providing an uninterrupted power supply, particularly when fluctuating solar irradiation or unanticipated changes in load demand influence the capability of the PV array and the fuel cell to produce adequate power on their own. The BESS acts as a dependable backup, delivering stored energy to meet the disparity between the total generation and the needed load power.

3. CONTROL STRATEGY FORMULATION

3.1. MPPT Control

A robust MPP-based BSMC control algorithm has been developed to enhance the productivity of the PV system. To guarantee maximum output power, the BSMC algorithm has two meticulously built control loops. The first control loop, dubbed the MPP block, takes advantage of both the PV voltage and the PV current. This block is in charge of determining the maximum point of the PV system and then creating the MPP voltage. In the second control loop, the MPP voltage acts as a critical reference value [22]. In the BSMC algorithm, the secondary control loop is in charge of producing the control signal that governs overall system behaviour. As shown in Fig. 2, this is accomplished by analyzing a variety of input values, comprising the voltage and current values of the PV, MPP reference voltage, inductor current, and output voltage. Each of these characteristics is critical in selecting the best operating conditions for the PV system. This dual-loop control technique enables meticulous and continuous performance improvement of the PV system. The system can adjust to shifting climatic circumstances and fluctuations in solar input by utilizing the MPP-based BSMC, guaranteeing that the PV system runs at the highest possible efficiency. The complicated interaction of these control loops and taking into account many factors result in the overall control system's resilient and adaptable behaviour, improving the PV system's reliability and output in the presence of various operating conditions.

$$I_{pv} = N_p \cdot I_{ph} - N_p \cdot I_{sat} \left[\exp\left(\frac{V_{pv}}{\alpha N_s}\right) - 1 \right] \quad (1)$$

where the quantity of cells linked in parallel and series are represented as N_p and N_s respectively. The cells arranged in parallel enhance current output, whereas the cells arranged in

series boost voltage potential. To obtain the necessary voltage and current rates, the PV arrays frequently use a mixture of parallel and series connections. Moreover, I_{pv} depicts the electric current produced by PV cells as a result of solar exposure that falls on them. Factors such as sun irradiation and cell temperature impact this number. Additionally, V_{pv} indicates the electrical potential differential between the solar cell terminals. The voltage produced is determined by the solar cell's properties as well as its operational circumstances. Finally γ shows a fixed value as the following equation:

$$\gamma = \frac{n \cdot T \cdot k_B}{q} \quad (2)$$

where $q = 1.6 \times 10^{-19}$ describes the amount of an electron's electrical charge, which is essential in comprehending electric currents and the functioning of semiconductor technologies. Also, n symbolizes the ideality factor of the P-N junction. This factor, also known as the diode ideality factor, is a metric that compensates for departures from a perfect operation of a diode. It takes into account recombination and other non-ideal phenomena. Furthermore, the Boltzmann constant is displayed as $k_B = 1.3805 \times 10^{-23}$, which is important in statistical mechanics and is utilized to connect the average kinetic energy of molecules in gas form to their temperature. Eventually T reflects the cell's temperature in absolute terms, which is a key variable in semiconductor physics because it affects the energy flow of charge transporters, which determines the general behavior of semiconductor technologies.

$$I_{sat} = I_{satr} \left(\frac{T}{T_r}\right)^3 \exp\left(\frac{E_g \cdot T}{\gamma} \left[\frac{1}{T_r} - \frac{1}{T}\right]\right) \quad (3)$$

where I_{sat} points out the cell's reverse bias saturation current, which quantifies the leakage current while the system is in reverse bias mode. In other words, it measures the movement of minority carriers throughout the dwindling zone. $E_g = 1.1$ reflects the semiconductor's energy gap which is the least amount of energy necessary for an electron to pass from the band known as the valence to the conduction region to transmit electricity. The reverse bias saturation current at the reference temperature T_r is indicated as I_{satr} which is given as the following equation[22]:

$$I_{satr} = \frac{I_{sc}}{\exp\left(\frac{V_{oc}}{\gamma \cdot N_s}\right) - 1} \quad (4)$$

where I_{sc} represents the short circuit current which is used to calculate the greatest amount of current that a circuit can supply when it is closed with no resistance. Also, V_{oc} exhibits the open circuit voltage which offers information on the potential gap across the circuit when no current is flowing. The photocurrent I_{ph} , which is the electric current produced by the capture of solar exposure in a PV cell, is dependent on the cell temperature and sun irradiances by the following expression [22]:

$$I_{ph} = 10^{-3} \cdot E [I_{sc} + K_{sc}(T - T_r)] \quad (5)$$

where E denotes the amount of solar exposure that comes from the sun per unit area. Solar exposure shifts which are impacted by factors like as geographic position, time of day, and climate, have a direct effect on the quantity of energy a

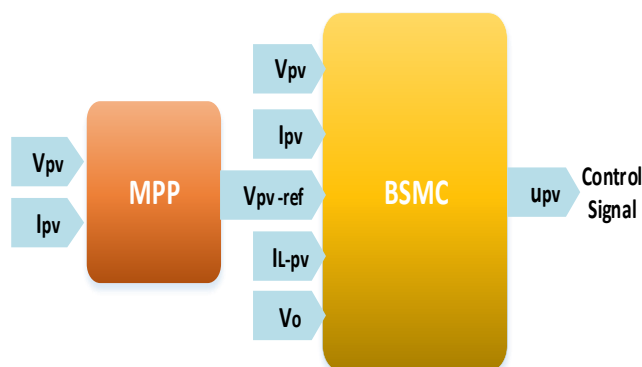


Fig. 2: MPP tracking strategy.

PV system can generate. Additionally, K_{sc} depicts the temperature coefficient of short circuit current which measures the effect of temperature fluctuations on a solar cell's short-circuit current. The solar cell functionality may suffer as temperatures increase, and short circuit current drops. Thus, PV output power P_{pv} can be obtained as follows by taking (1) into account:

$$P_{pv} = V_{pv} \cdot I_{pv} = V_{pv} \cdot N_p \left(I_{ph} - I_{sat} \left[\exp \left(\frac{V_{pv}}{\gamma \cdot N_s} \right) - 1 \right] \right) \quad (6)$$

Then, the PV array's unidirectional step-up converter formulations [22] are considered as follows:

$$\begin{cases} \frac{dV_{pv}}{dt} = \frac{I_{pv}}{C_1} - \frac{I_{L-pv}}{C_1} \\ \frac{dI_{L-pv}}{dt} = f_1(x) + g_1(x) \cdot u_{pv} \\ \frac{dV_o}{dt} = f_2(x) + g_2(x) \cdot u_{pv} \end{cases} \quad (7)$$

where,

$$\begin{cases} f_1(x) = \frac{1}{L_{pv}} \left[V_{pv} + V_D - \frac{R \cdot R_c}{R+R_c} I_{L-pv} - \left(\frac{R_c}{R+R_c} - 1 \right) V_o \right] \\ g_1(x) = \frac{1}{L_{pv}} \left[V_D + \frac{R \cdot R_c}{R+R_c} I_{L-pv} - \left(\frac{R_c}{R+R_c} - 1 \right) V_o \right] \\ f_2(x) = \frac{1}{C} \left[\frac{R}{R+R_c} I_{L-pv} + \frac{1}{R+R_c} V_o \right] \\ g_2(x) = -\frac{R}{C(R+R_c)} I_{L-pv} \end{cases} \quad (8)$$

According to the expressions above, the DC link output voltage of the DC MG and the current value of the PV inductor are displayed as V_o and I_{L-pv} respectively, L_{pv} is the value of PV inductor, C depicts the capacitor value of the DC bus, $V_D = 0.82$ defines the diode voltage in a PV module which is associated with the voltage drop across the bypass diode during reverse bias conditions especially in scenarios where shading or low-light conditions, R illustrates the value of the resistive load and R_c corresponds to 39.6Ω . To create the desired PV or MPP voltage, the MPP section is developed according to the subsequent form [22]:

$$\frac{dP_{pv}}{dI_{pv}} = \frac{d(V_{pv} \cdot I_{pv})}{dI_{pv}} = V_{pv} + I_{pv} \frac{dV_{pv}}{dI_{pv}} = 0 \quad (9)$$

Considering (9) in light of (1), the PV voltage V_{pv} is achieved as the following expression:

$$V_{pv} = \gamma \cdot N_s \cdot \log \left(\frac{I_{sat} + I_{ph} - I_{pv}}{I_{sat}} \right) \quad (10)$$

The derivation result of the PV voltage V_{pv} concerning the PV current I_{pv} is depicted as follows:

$$\frac{dV_{pv}}{dI_{pv}} = -\gamma \cdot N_s \left(\frac{1}{I_{sat} + I_{ph} - I_{pv}} \right) \quad (11)$$

Replacing (10) and (11) in (9), the subsequent expression is achieved [22]:

$$\log \left(\frac{I_{sat} + I_{ph} - I_{pv}}{I_{sat}} \right) = \frac{1}{I_{sat} + I_{ph} - I_{pv}} \quad (12)$$

The expression that follows represents a relationship between the intended peak power current I_P and the photocurrent I_{ph} . This mathematical equation is an important tool for analyzing and optimizing solar systems. Maximizing power production is a key aim in the field of solar energy production, and this formula gives insights into how to achieve the objective.

$$I_P = 0.91 \cdot I_{ph} \quad (13)$$

Eventually, the needed desired value of the PV or MPP voltage V_{pv-ref} is produced [22] by substituting I_P with I_{pv} in (9):

$$V_{pv-ref} = \gamma \cdot N_s \cdot \log \left(\frac{I_{sat} + 0.09 \cdot I_{ph}}{I_{sat}} \right) \quad (14)$$

As the main role of the BSMC algorithm, it must force the PV voltage V_{pv} to track and match the desired PV voltage level V_{pv-ref} to achieve the peak power. The errors in the tracking of the PV voltage [22] and inductor current are illustrated as the following equations:

$$\begin{cases} e_1 = V_{pv} - V_{pv-ref} \\ e_2 = I_{L-pv} - I_{L-pv-ref} \end{cases} \quad (15)$$

where $I_{L-pv-ref}$ exhibits the desired inductor current, which will be described thereafter. Firstly, the time derivation result of the PV voltage error e_1 concerning (7) is achieved as the following expression [22]:

$$\dot{e}_1 = \frac{I_{pv}}{C_1} - \frac{I_{L-pv}}{C_1} - \dot{V}_{pv-ref} \quad (16)$$

The equation above is revised as the following expression:

$$\dot{e}_1 = \frac{I_{pv}}{C_1} - \frac{e_2}{C_1} - \frac{I_{L-pv-ref}}{C_1} - \dot{V}_{pv-ref} \quad (17)$$

In order to stabilize (17), the subsequent control expression is suggested as:

$$I_{L-pv-ref} = C_1 \left(\frac{I_{pv}}{C_1} - \dot{V}_{pv-ref} - M_1 \cdot e_1 - M_{1sw} \cdot \text{sign}(e_1) \right) \quad (18)$$

where M_1 and M_{1sw} are positive values and define the gains of the controller. Then, by introducing the Lyapunov candidate as $V_1 = \frac{1}{2} e_1^2$, one can be found:

$$\begin{aligned} \dot{V}_1 &= e_1 \cdot \dot{e}_1 = e_1 \left(\frac{I_{pv}}{C_1} - \frac{e_2}{C_1} - \frac{I_{L-pv-ref}}{C_1} - \dot{V}_{pv-ref} \right) \\ &= e_1 \left(-\frac{e_2}{C_1} - M_1 \cdot e_1 - M_{1sw} \cdot \text{sign}(e_1) \right) \\ &= -\frac{e_1 \cdot e_2}{C_1} - M_1 \cdot e_1^2 - M_{1sw} \cdot |e_1| \end{aligned} \quad (19)$$

Secondly, by taking derivative of $e_2 = I_{L-pv} - I_{L-pv-ref}$, one can be achieved:

$$\begin{aligned} \dot{e}_2 &= \dot{I}_{L-pv} - \dot{I}_{L-pv-ref} \\ &= f_1(x) + g_1(x) \cdot u_{pv} - \dot{I}_{L-pv-ref} \end{aligned} \quad (20)$$

The Lyapunov candidate function is selected as the following expression in order to stabilize (20):

$$V_2 = V_1 + \frac{1}{2} \cdot e_2^2 \quad (21)$$

By taking time derivative of the equation above and applying (19), one finds:

$$\begin{aligned} \dot{V}_2 &= -\frac{e_1 \cdot e_2}{C_1} - M_1 \cdot e_1^2 - M_{1sw} \cdot |e_1| + e_2 \cdot \dot{e}_2 \\ &= -\frac{e_1 \cdot e_2}{C_1} - M_1 \cdot e_1^2 - M_{1sw} \cdot |e_1| \\ &\quad + e_2 (f_1(x) + g_1(x) \cdot u_{pv} - \dot{I}_{L-pv-ref}) \end{aligned} \quad (22)$$

Therefore, the subsequent regulation command is suggested:

$$u_{pv} = \frac{1}{g_1(x)} \left(-f_1(x) + \dot{I}_{L-pv-ref} + \frac{e_1}{C_1} - M_2 \cdot e_2 - M_{2sw} \cdot \text{sign}(e_2) \right) \quad (23)$$

where $M_2 > 0$ and $M_{2sw} > 0$ are the gains of the control method. The remainder of evidence is available in [23] for more detail.

3.2. SMC Current Control

The fuel cell as an additional power supply to help the PV system to properly meet the load demand is controlled by the SMC current controller. The sliding surface in the SMC strategy describes a situation in which the regulated current takes a specified path. The controller's goal is to drive actual current onto this sliding surface, guaranteeing that the fuel cell performs under the specified current level. The SMC strategy is robust against uncertainties, fluctuations in fuel cell properties, and disturbances from outside, making it suitable for practical uses characterized by changing and unforeseen circumstances. The proposed SMC current controller for regulating the fuel cell current is clearly illustrated in Fig. 3. Additionally, the SMC subsystem design is indicated as Fig. 4. Finally, the SMC parameters for this design are depicted in Table 2.

$$\frac{dI_{fcl}}{dt} = -(1 - u_{fcl}) \frac{1}{L_{fcl}} V_o + \frac{V_{fcl}}{L_{fcl}} + d_{fcl} \quad (24)$$

where I_{fcl} , V_{fcl} and L_{fcl} are the fuel cell's voltage, current and inductance respectively. Moreover, the u_{fcl} represent the current control signal and d_{fcl} indicates the lumped



Fig. 3: SMC current controller.

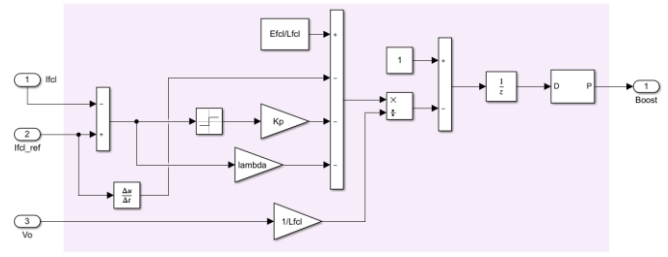


Fig. 4: SMC subsystem for fuel cell.

uncertainty term for the unknown diode current of the fuel cell I_{ofcl} which assumed to be confined to:

$$|d_{fcl}(t)| \leq \Delta_{fcl} \quad (25)$$

where Δ_{fcl} defines the known positive constant. The error of the fuel cell current e_{fcl} is defined as the following expression:

$$e_{fcl} = I_{fcl} - I_{fcl-ref} \quad (26)$$

where $I_{fcl-ref}$ indicates the desired fuel cell current. By taking derivative of (26) and replacing (24), the following expression can be obtained:

$$\begin{aligned} \dot{e}_{fcl} &= \dot{I}_{fcl} - \dot{I}_{fcl-ref} \\ &= -(1 - u_{fcl}) \frac{1}{L_{fcl}} V_o + \frac{V_{fcl}}{L_{fcl}} + d_{fcl}(t) - \dot{I}_{fcl-ref} \end{aligned} \quad (27)$$

The subsequent control rule is suggested to stabilize the existing error dynamics (27):

$$u_{fcl} = 1 - \frac{L_{fcl}}{V_o} \left(\frac{V_{fcl}}{L_{fcl}} - \dot{I}_{fcl-ref} + K_{fcl} \cdot e_{fcl} + K_{fcl-sg} \cdot \text{sgn}(e_{fcl}) \right) \quad (28)$$

where K_{fcl} and K_{fcl-sg} are the control and the sliding gains respectively.

3.3. PI-SMC Voltage Control

An advanced control method known as PI-SMC has been presented to guarantee stable voltage control and efficient response to demand inside the DC MG. The overall configuration of this enhanced control method is clearly displayed in Fig. 5, highlighting the critical role it performs in improving the stability and functionality of the DC MG. Moreover, the SMC subsystem for this configuration is designed as Fig. 6. The SMC subsystem parameters are also demonstrated in Table 2. The PI regulator creates the desired battery current I_{b-ref} for the SMC by acquiring the potential error between the reference DC link voltage $V_{(o-ref)}$ and its actual value V_o . Then, the SMC block gets the BESS current I_b , the DC link voltage V_o , and the desired BESS current $I_{(b-ref)}$ to maintain the DC link voltage V_o at the pre-defined voltage range, as well as manage the power sharing

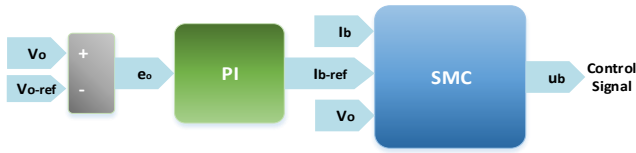


Fig. 5: PI-SMC voltage regulator.

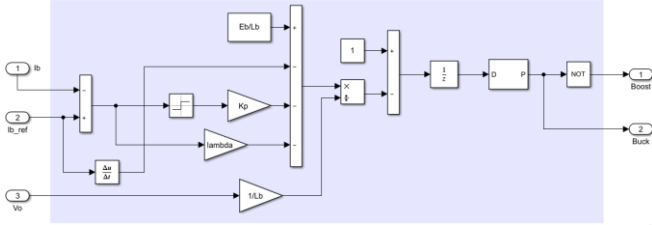


Fig. 6: SMC subsystem for BESS.

Table 2: SMC subsystem parameters.

Parameters	Values
Lithium-Ion battery nominal potential E_b	20 [V], 6.5 [Ah]
Fuel cell nominal voltage E_{fcl}	20[V]
Battery inductance L_b	3.3 [mH]
Fuel cell inductance L_{fcl}	3.3 [mH]
lambda	10
SMC constant K_p	100000

among the PV system, the fuel cell, and BESS to properly supply the fluctuating demanded power.

$$\begin{cases} \frac{dV_o}{dt} = \frac{1}{C}(1 - u_b)I_b + d_o(t) \\ \frac{dI_b}{dt} = -(1 - u_b)\frac{V_o}{L_b} + \frac{V_b}{L_b} + d_b(t) \end{cases} \quad (29)$$

where the BESS voltage is defined as V_b , the DC bus capacitance is indicated as C , and L_b shows the BESS inductor. Moreover, because the load current I_o and diode current of the BESS I_{ob} are not known, the lumped parametric uncertainty terms of the output and the BESS are displayed as $d_o(t) = \frac{1}{C}(I_{opv} + I_{ofcl} - I_o)$ and $d_b(t)$, which supposed to be confined to:

$$\begin{cases} |d_o(t)| \leq \Delta_0 \\ |d_b(t)| \leq \Delta_b \end{cases} \quad (30)$$

where the noted positive fixed values are represented as Δ_0 and Δ_b . Defining the voltage and current tracking errors as the following expressions:

$$\begin{cases} e_o = V_o - V_{o-ref} \\ e_b = I_b - I_{b-ref} \end{cases} \quad (31)$$

The subsequent expression of the PI control method is used to generate the desired BESS current for the SMC approach.

$$I_{b-ref} = K_p \cdot e_o + K_i \cdot \int e_o dt \quad (32)$$

where the proportional and integral gains are represented as K_p and K_i . The time derivation result of the BEES current error e_b is obtained as the following formula:

$$\begin{aligned} \dot{e}_b &= \dot{I}_b - \dot{I}_{b-ref} \\ &= -(1 - u_b)\frac{V_o}{L_b} + \frac{V_b}{L_b} + d_b(t) - \dot{I}_{b-ref} \end{aligned} \quad (33)$$

Eventually, the following SMC concept is suggested to produce the control signal or duty cycle of the voltage tracking u_b as the following equation [24]:

$$u_b = 1 - \frac{L_b}{V_o} \left(\frac{V_b}{L_b} - \dot{I}_{b-ref} + K_b \cdot e_b + K_{b-sg} \cdot \text{sgn}(e_b) \right) \quad (34)$$

where the control and sliding gains of the BESS are indicated as K_b and K_{b-sg} respectively.

3.4. Stability Authentication

Lyapunov stability analysis is whether a dynamic system identified by a group of differential equations will develop toward a stable state or demonstrate instability over time. Introducing the Lyapunov function as the following equation:

$$V_{total} = V_2 + V_{fcl} + V_b = \frac{1}{2} \cdot e_2^2 + \frac{1}{2} \cdot e_{fcl}^2 + \frac{1}{2} \cdot e_b^2 \quad (35)$$

The following expression is resulted by taking derivative of (35) as follows:

$$\begin{aligned} \dot{V}_{total} &= -e_2^2 - e_{fcl}^2 - e_b^2 - S \cdot \dot{S} \\ &\leq -e_2^2 - e_{fcl}^2 - e_b^2 - \delta \cdot S^2 - \beta \cdot |S| \end{aligned} \quad (36)$$

where $\dot{V}_{total} < 0$ as the result of positive δ and β . This specific derivative of the Lyapunov function assures that the system's paths go towards, instead of away from, the equilibrium point. This ensures that any fluctuation or disruption in the system will result in a return to stable condition.

4. SCENARIOS AND SIMULATION OUTCOMES

The proposed isolated DC MG and the proposed methodology are rigorously simulated in a software framework of MATLAB@R2020b/Simulink for result processing and to demonstrate the robust and effective functioning of the novel control structure. This simulation tool enabled comprehensive output analysis and verification of the control mechanism's effectiveness in a software-based setting. All simulations are performed on a 64-bit PC (Intel Core i5 CPU, 8G RAM, and Windows 7). Table 3 clearly summarizes the DC MG parameters, which are required for the simulation. This detailed simulation not only confirms the suggested control technique but also acts as a significant milestone in analyzing and assuring the most effective operation of the MG under different operating scenarios. The PI-SMC control technique is proposed for the DC-DC buck-boost converter to reach the robust regulation of the DC link voltage and ensure an evenly distributed and efficient response to demand and input variations. The operating flowchart of the proposed control strategy is indicated as Fig. 7, in which P_{pv} , P_{fcl} , P_b and P_o demonstrate the output power of PV, fuel cell, BESS and load respectively. As depicted in this figure, if the total output power of the PV and fuel cell is larger than the output load power, the BESS switches to charging mode and the surplus power is stored in the BESS

in order to maintain the balance between generation and consumption. Moreover, if the total supply of the PV and fuel cell is lower than the demanded output power, the BESS switches to discharging mode and the deficit supply power is provided by BESS. Finally, while the total generation amount meets the demanded load power, the BESS plays a pivotal role in offsetting losses within the MG. The proportional and integral parameters of the PI control method equal $K_p = 0.01$ and $K_i = 5$ respectively. A set of simulations containing shifts in both load demand and solar irradiation are undertaken to assess the effectiveness of the suggested controller, as depicted in Fig. 8 and, Fig. 9 respectively. These dynamic scenarios are intended to put the controller's capability to respond to changes in its operating conditions to the test. The output load varies inextricably with the needed load power, but variations in solar exposure have a direct influence on the generated PV power. To put it another way, the connection between the resistive load and asked load power is such that a rise in resistive load is equivalent to a drop in demanded load power. A reduction in the resistive load, on the other hand, indicates an increase in the requested power, establishing a direct relationship between load changes and the power requested by the system. In the meantime, changes in sun irradiation rates have an evident impact on the amount of PV production. As sun irradiance decreases, so does the output power of the PV system, resulting in a drop in produced PV power. All these changes on both the generation and consumption sides present dynamic difficulties to the system, increasing the tracking error of the DC MG output voltage e_o and threatening voltage stability. The interaction between variations in solar irradiance and load demand has an immediate effect on the DC link voltage balance, rendering it subject to swings that might jeopardize the whole system's stability. The suggested nonlinear robust controller's capability is well demonstrated in Fig. 10, displaying its extraordinary ability to preserve the DC link voltage at the desired level of 50 V in a variety of challenging scenarios, such as different load demands and sun exposure amounts, which lead to potential voltage drops and spikes. Significantly, the control unit has an outstanding capability to suppress voltage drops and spikes and retain the DC bus voltage with minimal fluctuations and at a high-speed rate. Additionally, the efficient demand response among the PV, fuel cell and BESS to supply the requested demand is fulfilled as indicated in Fig. 11 considering the subsequent scenarios. Fig. 12 and Fig. 13 also display the output load current and the output load power respectively, which are changed by the declared step variations.

4.1. Scenario 1: An Increase in Demand ($2 < t < 4$)

In this case, a decrease in resistive load to 6.25Ω is followed by a rise in necessary load power, which now reaches 400 W. As a result, the BESS must switch smoothly into discharging mode to augment total power production and satisfy the increased load power requirement. This operational adjustment is necessary because the total power produced by the PV system and the fuel cell is inadequate to meet the increased load power need. The BESS successfully provides more power to compensate for the shortage by discharging, guaranteeing the total delivered power corresponds with the increasing load demand.

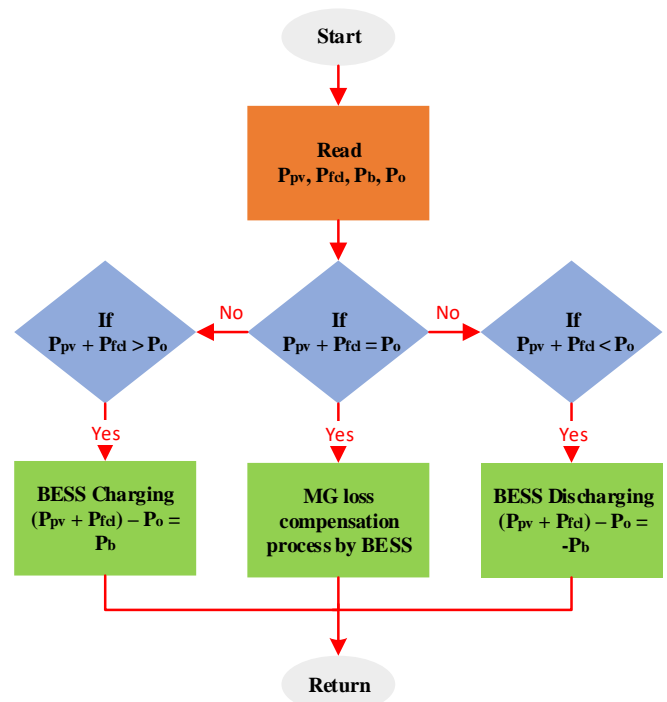


Fig. 7: Flowchart of BESS PI-SMC Controller.

4.2. Scenario 2: A Decrease in Demand ($6 < t < 8$)

In this scenario, a fall in required load power to 200 W is accompanied by a rise in resistive load to 12.5Ω . This modification causes a change in the power sharing approach, in which the generation units, which include the PV system and the fuel cell, successfully meet the required power demand. As a result, the excess power produced during this time is smartly routed to the BESS for storage. This crucial management guarantees that the power provided by the generation units meets the decreased load power demand and facilitates surplus energy storage in the BESS.

4.3. Scenario 3: No Change in Demand

Since the required output demand is exactly aligned with the total power generation of the PV system and the fuel cell, which equals 300 W, the BESS is not used for demand support. At a resistive load rating of 8.33Ω , this balance between demanded and produced power eliminates the need for BESS involvement in satisfying the load demand. Instead, the BESS is critical in meeting the MG losses, guaranteeing the whole system functions at peak efficiency and in balance.

4.4. Scenario 4: A Decrease in Irradiance ($10 < t < 12$)

The sun irradiation is reduced to $500 W/m^2$ during this specific time frame. As a result, the produced power from the

Table 3: DC MG parameters.

Parameters	Values
DC bus capacitance C	1000 [μ F]
PV capacitance C_1	1000 [μ F]
PV inductor L_{pv}	1.21 [mH]
Battery inductance L_b	3.3 [mH]
Fuel cell output power P_{fcl}	100 [W]
Switching frequency f_s	50 [kHz]
Load powers P_o	400, 300, 200 [W]
Variable resistive load values R_{Load}	6.25, 8.33, 12.5 [Ω]

PV system drops to around 100 W. In reaction to the decrease in PV power production, and in order to maintain an uninterrupted power supply to satisfy the requested load demand, the BESS quickly changes to discharging mode again. By switching to this mode, the BESS compensates for the reduced PV power by giving the required power to meet the load requirement. In addition to deal with voltage drops and spikes due to shifts in supply and demand, and preserve the DC link voltage at the reference voltage level, as the main goal of the research, to maintain the overall stability of the MG's system, the novel MPP-based BSMC technique is presented as a unique method for the DC-DC step-up converter in the PV system. The fundamental goal of this strategy is to effectively maximize the power production from the PV panels by tracking the MPP as effectively as possible. This critical work is depicted in Fig. 14, where it is clear that the suggested technique allows the PV output voltage V_{pv} to swiftly match its desired value or the MPP voltage V_{pv-ref} which equals 26.6 V. Moreover, the PV output current equals almost 7.55 A as indicated in Fig. 15. Thus, the derived peak power arrives at 200 W in solar exposure amount of 1000 W/m^2 and the cell temperature of 25°C as illustrated in Fig. 16. It's also worth noting that the suggested MPP-based BSMC method is intended to solve the unpredictable behavior of solar irradiation levels. In practice, the quantity of solar irradiation falling on the PV panels can vary fast, as illustrated by a change from 1000 W/m^2 to 500 W/m^2 at $10 < t < 12$ in Fig. 9. In reaction to such shift, the MPPT controller expertly modifies the PV array's operation point, allowing for maximum energy harvesting under variable irradiance circumstances. Fig. 17-Fig. 19 clearly point out the BESS voltage, output power and current respectively, in which the BESS charging and discharging modes are visible. As demonstrated in Fig. 19, the magnitude of the BESS current equals to 5 A. The sign of the current is positive and negative for BESS discharging and charging modes respectively. As a result, the multiplication of the BESS current and voltage represent the BESS discharging and charging output power as represented in Fig. 18. Finally, the output current and power of the fuel cell are indicated in Fig. 20 and Fig. 21, respectively.

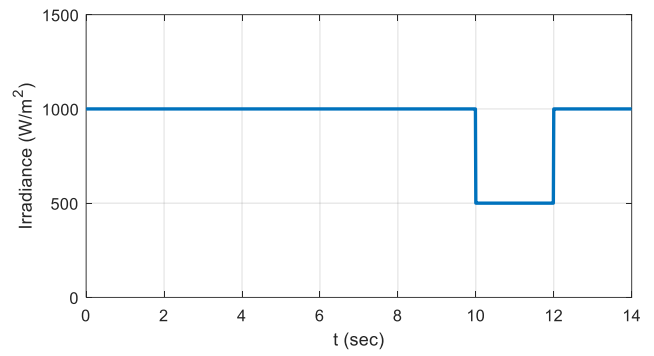


Fig. 9: Step change in solar irradiation.

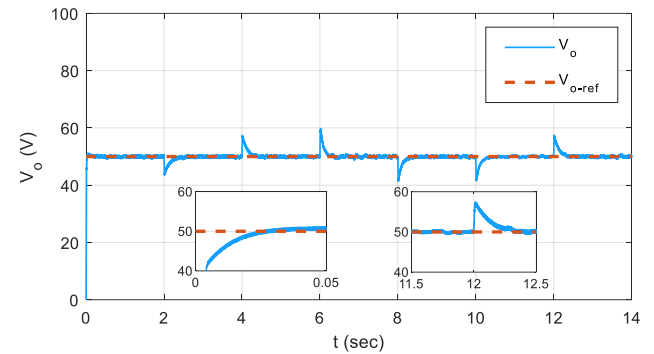


Fig. 10: DC bus voltage.

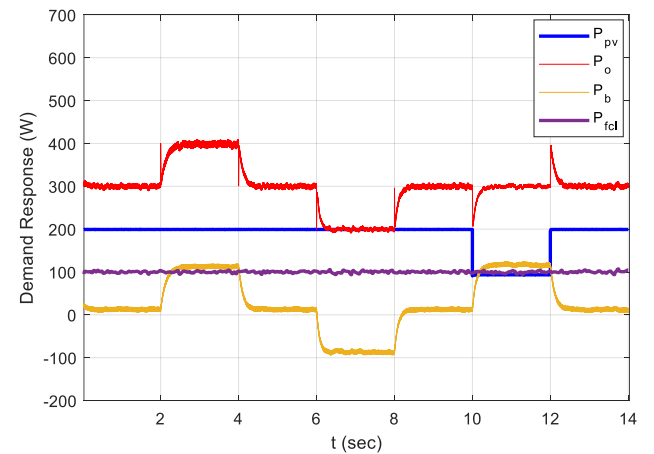


Fig. 11: Efficient balanced demand response.

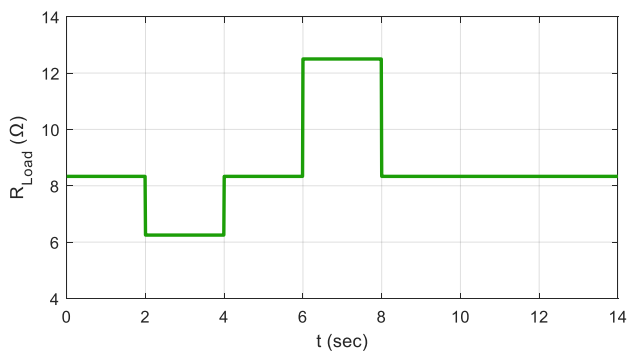


Fig. 8: Step changes in load.

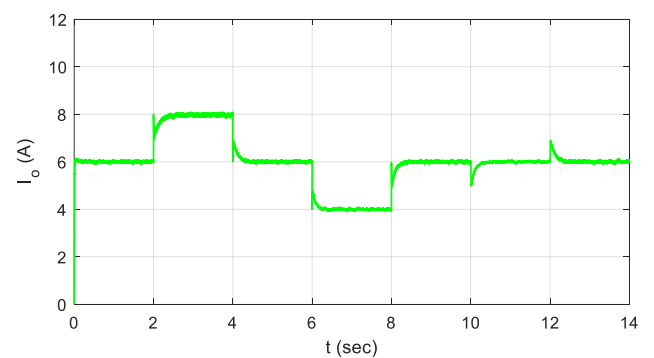


Fig. 12: Load current.

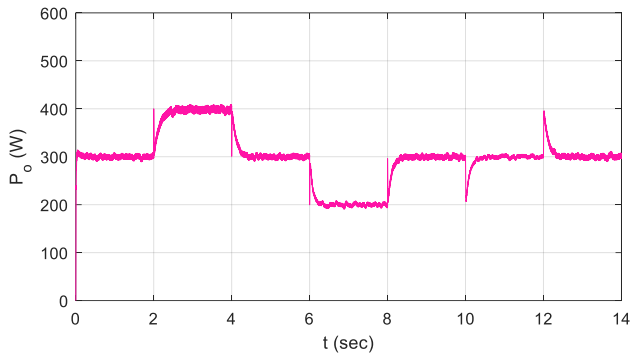


Fig. 13: Demand load power.

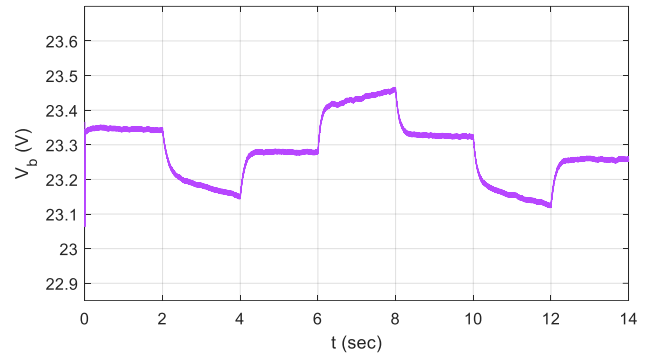


Fig. 17: BESS voltage.

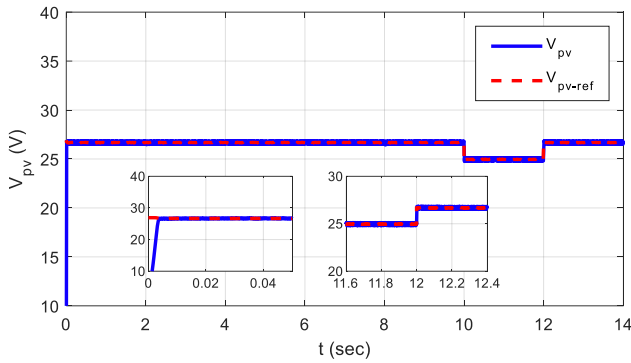


Fig. 14: PV voltage.

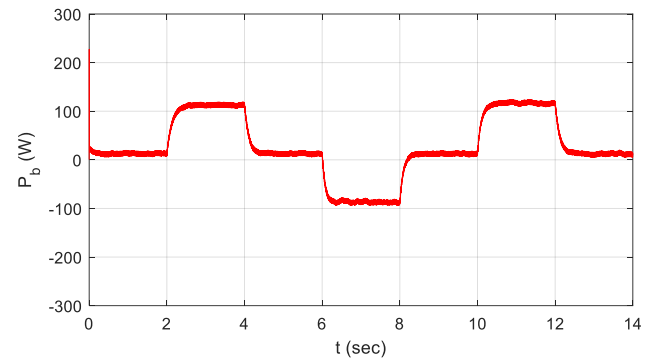


Fig. 18: BESS output power.

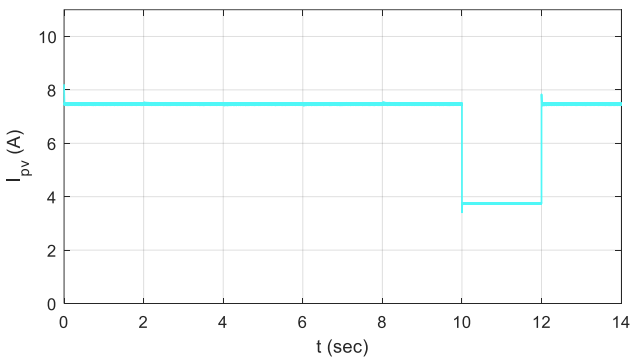


Fig. 15: PV current.

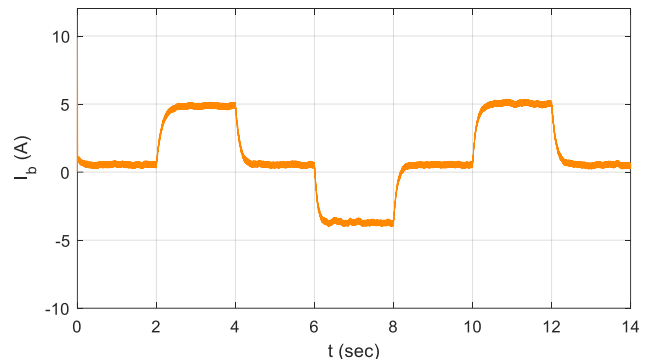


Fig. 19: BESS current.

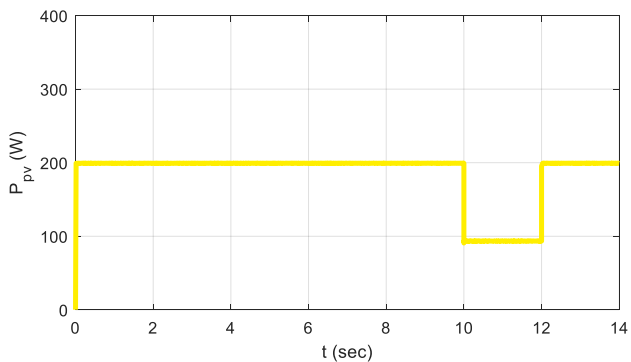


Fig. 16: PV output power.

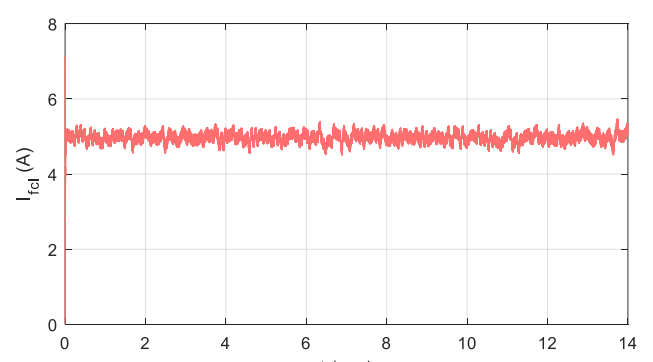


Fig. 20: Fuel cell current.

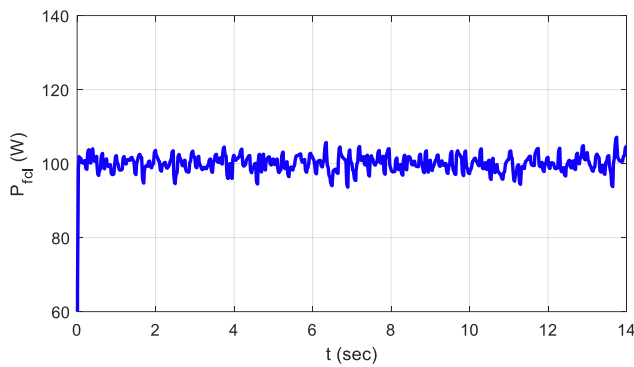


Fig. 21: Fuel cell output power.

5. CONCLUSION

In the face of fluctuating load and varying sun radiation exposures, this research developed a robust PI-SMC as a nonlinear cascaded controller for voltage control and efficient response to demand of a freestanding DC MG comprising of PV, BESS, and fuel cell. In order to successfully reach the MPP and extract the highest feasible output from the solar array, an MPP-based BSMC technique is additionally proposed and examined. Furthermore, BESS is becoming accessible to aid in the power distribution of the PV system and fuel cell. The suggested control approach fulfills the charging and discharging process of the BESS to react to the changing demanded power and save the extra power. The functionality of the proposed control method is demonstrated by modelling the DC MG under demand changes and varied solar irradiations. This technique ensures efficient and robust control of the DC link voltage with extremely tiny variations and rapid response. This model is also applicable over extended time frames and for consumers with larger demand through installing extra PV modules and taking into account the precise power sharing among the PV system, the BESS, and the fuel cell. Furthermore, the devised regulating approach is simple to adopt and ensures system stability. In regard to significance, this study contributes to the development of DC MG control approaches by providing a straightforward yet efficient and robust control method. Future studies could focus on numerical comparisons with current benchmark and as well as prior efforts to evaluate the proposed methodology's effectiveness.

CREDIT AUTHORSHIP CONTRIBUTION STATEMENT

Sajed Derakhshani Pour: Funding acquisition, Project administration, Supervision, Validation. **Reza Eslami:** Conceptualization, Data curation, Formal analysis, Investigation, Methodology, Resources, Software, Visualization, Writing - original draft, Writing - review & editing.

DECLARATION OF COMPETING INTEREST

The authors declare that they have no known competing financial interests or personal relationships that could have appeared to influence the work reported in this paper. The ethical issues; including plagiarism, informed consent, misconduct, data fabrication and/or falsification, double publication and/or submission, redundancy has been completely observed by the authors.

REFERENCES

- [1] P. Singh, and J. S. Lather, "Dynamic current sharing, voltage and SOC regulation for HESS based DC microgrid using CPISM technique," *Journal of Energy Storage*, vol. 30, p. 101509, 2020.
- [2] V. Suresh, N. Pachauri, and T. Vigneysh, "Decentralized control strategy for fuel cell/PV/BESS based microgrid using modified fractional order PI controller," *International Journal of Hydrogen Energy*, vol. 46, no. 5, pp. 4417-4436, 2021.
- [3] A. Dimovski, M. Moncecchi, and M. Merlo, "Impact of energy communities on the distribution network: An Italian case study," *Sustainable Energy, Grids and Networks*, vol. 35, p. 101148, 2023.
- [4] S. A. Mehraban, and R. Eslami, "Multi-microgrids energy management in power transmission mode considering different uncertainties," *Electric Power Systems Research*, vol. 216, p. 109071, 2023.
- [5] M. Tofighi-Milani, S. Fattaheian-Dehkordi, and M. Fotuhi-Firuzabad, "A new peer-to-peer energy trading model in an isolated multi-agent microgrid," *Journal of Applied Research in Electrical Engineering*, vol. 1, no. 1, pp. 33-41, 2022.
- [6] A. M. Dezfuli, M. Abasi, M. E. Hasanzadeh, and M. Joorabian, "Voltage and frequency control considering disturbance in input power of DG," *Journal of Applied Science in Electrical Engineering*, 2024.
- [7] B. Modu, M. P. Abdullah, M. A. Sanusi, and M. F. Hamza, "DC-based microgrid: Topologies, control schemes, and implementations," *Alexandria Engineering Journal*, vol. 70, pp. 61-92, 2023.
- [8] S. Vasantharaj, V. Indragandhi, V. Subramaniaswamy, Y. Teekaraman, R. Kuppasamy, and S. Nikolovski, "Efficient control of dc microgrid with hybrid PV—fuel cell and energy storage systems," *Energies*, vol. 14, no. 11, p. 3234, 2021.
- [9] M. Shirkhani *et al.*, "A review on microgrid decentralized energy/voltage control structures and methods," *Energy Reports*, vol. 10, pp. 368-380, 2023.
- [10] Z. Lu, L. Wang, and P. Wang, "Review of voltage control strategies for DC microgrids," *Energies*, vol. 16, no. 17, p. 6158, 2023.
- [11] R. Kumar, and M. K. Pathak, "Distributed droop control of dc microgrid for improved voltage regulation and current sharing," *IET Renewable Power Generation*, vol. 14, no. 13, pp. 2499-2506, 2020.
- [12] Y. Liu, W. Deng, P. Yang, Y. Teng, X. Zhang, Y. Yang, and W. Pei, "Dispatchable droop control strategy for DC microgrid," *Energy Reports*, vol. 9, pp. 98-102, 2023.
- [13] B. Li, C. Yu, X. Lu and F. Wang, "A novel adaptive droop control strategy for SoC balance in PV-based DC microgrids," *ISA Transactions*, vol. 141, pp. 351-364, 2023.

- [14] K. Ahmed, I. Hussain, M. Seyedmahmoudian, A. Stojcevski, and S. Mekhilef, "Voltage stability and power sharing control of distributed generation units in DC microgrids," *Energies*, vol. 16, no. 20, p. 7038, 2023.
- [15] N. G. and J. K., "Real-time implementation of sliding mode controller for standalone microgrid systems for voltage and frequency stabilization," *Energy Reports*, vol. 10, pp. 768-792, 2023.
- [16] D. Sattianadan, G. R. P. Kumar, R. Sridhar, K. V. Reddy, B. S. U. Reddy, and P. Mamatha, "Investigation of low voltage DC microgrid using sliding mode control," *International Journal of Power Electronics and Drive Systems*, vol. 11, no. 4, pp. 2030-2037, 2020.
- [17] S. Y. Rahme, S. Islam, S. M. Amrr, A. Iqbal, I. Khan, and M. Marzband, "Adaptive sliding mode control for instability compensation in DC microgrids due to EV charging infrastructure," *Sustainable Energy, Grids and Networks*, vol. 35, p. 101119, 2023.
- [18] S. Patel, A. Ghosh, and P. K. Ray, "Efficient power management and control of DC microgrid with supercapacitor-battery storage systems," *Journal of Energy Storage*, vol. 73, p. 109082, 2023.
- [19] A. N. Akpolat et al., "Sensorless Control of DC Microgrid Based on Artificial Intelligence," *IEEE Transactions on Energy Conversion*, vol. 36, no. 3, pp. 2319-2329, 2021.
- [20] Z. Karami, Q. Shafiee, Y. Khayat, M. Yaribeygi, T. Dragičević, and H. Bevrani, "Decentralized model predictive control of DC microgrids with constant power load," *IEEE Journal of Emerging and Selected Topics in Power Electronics*, vol. 9, no. 1, pp. 451-460, 2021.
- [21] Q. Guo, I. Bahri, D. Diallo, and E. Berthelot, "Model predictive control and linear control of DC-DC boost converter in low voltage DC microgrid: An experimental comparative study," *Control Engineering Practice*, vol. 131, p. 105387, 2023.
- [22] K. Dahech, M. Allouche, T. Damak, and F. Tadeo, "Backstepping sliding mode control for maximum power point tracking of a photovoltaic system," *Electric Power Systems Research*, vol. 143, pp. 182-188, 2017.
- [23] S. Shoja-Majidabad, and A. Yazdani, "Paralleled DC-DC converters control using master-slave adaptive fuzzy backstepping techniques," *Iranian Journal of Science and Technology, Transactions of Electrical Engineering*, vol. 45, pp. 1343-1367, 2021.
- [24] S. Shoja-Majidabad, and S. D. Pour, "Robust control of multi-phase interleaved boost converters in the presence of perturbations and open phase fault," *International Journal of Power Electronics*, vol. 16, no. 2, pp. 162-179, 2022.

BIOGRAPHY



Sajed Derakhshani Pour received the B.Sc. in Electrical Engineering from the Department of Electrical Engineering, University of Bonab, Bonab, Iran, in 2020, and he is currently studying M.Sc. in Sustainable Smart Grids for Energy Transition (R2E) at the Department of Energy, Polytechnic University of Milan, Milan, Italy, since 2022. His research interests oriented to renewable energy systems, energy storage systems and smart/micro grids.



Reza Eslami received the B.Sc., M.Sc. and Ph.D. degrees in Electrical and Electronics Engineering from the Department of Electrical Engineering, Amirkabir University of Technology, Tehran, Iran, in 2010, 2012 and 2017 respectively. He has also worked as an Associate Professor with the Department of Electrical Engineering, Sahand University of Technology, Tabriz, Iran, since 2017. His research interests are smart grids and power system protection.

Copyrights

© 2024 Licensee Shahid Chamran University of Ahvaz, Ahvaz, Iran. This article is an open-access article distributed under the terms and conditions of the Creative Commons Attribution –NonCommercial 4.0 International (CC BY-NC 4.0) License (<http://creativecommons.org/licenses/by-nc/4.0/>).





Shahid Chamran
University of Ahvaz



Iranian Association of
Electrical and Electronics
Engineers

Journal of Applied Research in Electrical Engineering

E-ISSN: 2783-2864

P-ISSN: 2717-414X

Homepage: <https://jaree.scu.ac.ir/>



Research Article

Conventional DC-DC Converters Through Duality Approach for Current-Based Applications

Zahra Gholami ¹, Rahim Ildarabadi ^{1,*}, and Hamed Heydari-Doostabad ²

¹ Department of Electrical Engineering, Faculty of Electrical and Computer Engineering, Hakim Sabzevari University, Savzevar, Iran

² School of Electrical-Electronic Engineering, University College Dublin, Ireland.

* Corresponding Author: r.ildar@hsu.ac.ir

Abstract: This paper discusses the application of the principle of duality to conventional voltage-based DC-DC converters, such as buck, boost, fly-back, cuk, sepic, and zeta topologies, in order to obtain their current-based DC-DC converters. The duality approach involves finding the dual of a circuit, which is a circuit equivalent to the original circuit but with certain parameters swapped. Therefore, this paper presents a comprehensive study on achieving the most commonly used topologies of DC-DC current converters by applying the duality approach to their DC-DC voltage converters. This approach serves as a solution for applications where a current source is available and there is a need for output current control. An application of these current converters is to power current-based loads, such as light-emitting diodes (LEDs), and to provide conversion for current sources, such as photovoltaics (PV). As an advantage, these converters do not require additional inductors at their input or output terminals. Additionally, the paper provides a detailed explanation of the principle of operation and mathematical analysis of the conversion ratio for the discussed current converters. The proposed current converters and their application as an interface between a PV and a high-power LED were simulated using MATLAB to verify the mathematical equations. Overall, this paper provides a useful study guideline for understanding the principle of duality and the application of DC-DC current converters for current-based loads and sources.

Keywords: Duality approach, DC-DC current converters, current-based loads, current source.

Article history

Received 03 October 2023; Revised 15 March 2024; Accepted 21 March 2024; Published online 23 October 2024.

© 2024 Published by Shahid Chamran University of Ahvaz & Iranian Association of Electrical and Electronics Engineers (IAEEE)

How to cite this article

Z. Gholami, R. Ildarabadi, and H. Heydari-Doostabad, "Conventional DC-DC converters through duality approach for current-based applications," *J. Appl. Res. Electr. Eng.*, vol. 3, no. 1, pp. 64-73, 2024.

DOI: [10.22055/jaree.2024.44925.1083](https://doi.org/10.22055/jaree.2024.44925.1083)



NOMENCLATURE

Symbol Variables	Description
D	Transistor ON duty cycle
T_s	Sampling period time
G	Current conversion ratio
TVS	Total voltage stress (V)
TCS	Total current stress (A)
V_{PV}	PV module voltage (V)
I_{PV}	PV module current (A)
r_d	Differential resistance (Ω)
C_j	Junction capacitance
C_{sc}	Space-charge capacitance
C_d	Diffusion capacitance

R_b	Series bonding resistance (Ω)
L_b	Series bonding inductance
C_b	Parallel bonding capacitance
Z_{LED}	Impedance of an LED
I_{ph}	Light current (A)
I_0	Diode reverse saturation current (A)
Q_d	Diode ideality factor
n_s	Number of cells in series
R_s	Series resistance (Ω)
R_p	Shunt resistance (Ω)
k	Boltzmann's constant
T_c	Cell temperature
q	Charge of an electron

1. INTRODUCTION

The classical switched-mode power converters (SMPCs) have been the dominant power converters for DC-DC power conversion in recent times [1-3]. Classical SMPCs typically use inductors and capacitors as energy storage components and are well-suited for providing DC power supplies and low-voltage DC drives [4, 5]. DC-DC converters with high-frequency switching devices are used to achieve the modulation or demodulation of output voltages at the same power levels [6, 7]. They are typically fed by a constant power source and can be divided into different types of structures [8-10]. These structures are obtained by making changes in the component configurations of basic converters, such as the buck and boost converters. Hence, new converter topologies have been developed, such as the fly-back, cuk, sepic, and zeta converters, which have different features and are suitable for different applications [11].

Another type of power converter has recently been introduced for current conversion applications. These converters are designed to control the output or load currents [12-21]. There are several methods to achieve the current converters, each coming with its own advantages and disadvantages, like those introduced in [17-21]. However, there is another way to access DC-DC current converters by making changes in DC-DC voltage converters. These changes are made by applying the principle of duality in the circuit of the voltage converters [12-16]. Some of the advantages of this method are its simplicity, applicability, and ease of implementation. Ref. [15] and [16] present a current DC-DC buck converter obtained by applying the principle of duality to the conventional voltage DC-DC buck converter. To conduct a comprehensive study and achieve conventional DC-DC current converters, this article was selected as the basis of our work. Furthermore, in addition to buck converter, other topologies of conventional DC-DC voltage converters were also examined. These DC-DC current converters are particularly well-suited for applications that require precise control of output current, such as powering current-based loads like light-emitting diodes (LEDs). The converters can also be used to convert current sources, such as photovoltaic (PV) cells, to produce multiple or fractional current outputs [22, 23]. Since the source and load currents that are connected to these DC-DC current converters are constant, so we need to obtain a constant current at the input and output terminals of the converters. However, the main difference between these proposed converters and other conventional current converters is that it does not need to use some equipment, such as inductors, at their input and output terminals to filter the current ripple. Actually, these proposed DC-DC current converters perform current filtering in their internal structure, and there is no need to use additional elements,

Table 1: Duality relationship between components and wiring system.

Components/terms in the original circuit	Their Dual
Voltage source	Current source
Current source	Voltage source
Resistance	Conductance
Conductance	Resistance
Inductance	Capacitance
Capacitance	Inductance
Transistor	Transistor
Diode	Diode
Star wiring system	Delta wiring system
Delta wiring system	Star wiring system
Volt second balance of the inductors	Ampere second balance of the capacitors
Ampere second balance of the capacitors	Volt second balance of the inductors
Series connection	Parallel Connection
Parallel Connection	Series connection
Mesh	Node
Node	Mesh

which is their main advantage over other current converters.

In this paper, Section 2 first introduces the duality principle. Then, the structures of the conventional DC-DC current converters, including the buck, boost, fly-back, cuk, sepic, and zeta converters are proposed, and their semiconductor ratings are calculated. Also, the circuit models of a photovoltaic (PV) system and a high-power LED as examples of current sources and loads, respectively, which can be used with the proposed DC-DC current converters, are described. Section 3 verifies the feasibility of the proposed new type DC-DC current converters and the principle of duality by using simulation results obtained from MATLAB. Eventually, Section 4 presents the conclusions.

2. METHODOLOGY

2.1. Duality Principle

The principle of duality is a fundamental concept that states the existence of a correspondence between different circuit elements and variables. This principle allows for the transformation of a given circuit into an equivalent dual circuit by interchanging certain elements and variables while maintaining the same overall behavior and functionality. One common application of the principle of duality is in circuit analysis in which voltage and current sources are interchanged and elements and wiring connections are replaced with their dual counterparts. This dual circuit exhibits the same behavior and response as the original circuit but with different element configurations. Furthermore, the characterizing equations, e.g., Kirchhoff's laws and Ohm's law, remain the same in both circuits, but the roles of voltage and current are interchanged. Table 1 presents the duality relationships between components and wiring connections in electrical circuits.

By applying the principle of duality, the circuit analysis and design can be simplified. Complex circuits can be transformed into more manageable dual circuits, which may exhibit similar characteristics but in a different configuration. This enables researchers to leverage their understanding of circuit properties and behavior in one domain to analyze and solve problems in the corresponding dual domain.

2.2. Proposed Current-Type Converters

In DC-DC current converters, capacitor C is used to regulate the current conversion ratio, while inductor L is used as a filter for the output terminal. Unlike voltage-type converters, which operate based on volt-second balance, current-type converters operate based on the ampere-second balance of capacitor C. This means that to maintain a steady state, the quantity of charge flowing into capacitor C during one switching cycle should be equal to that flowing out of it. Or, the current integration of capacitor C should be equal to zero during one switching cycle.

Hence, the mentioned DC-DC current converters are proposed as follows, respectively.

2.2.1. Current DC-DC buck converter

By applying the principle of duality to the conventional voltage buck converter (Fig. 1), the proposed current buck converter is derived as depicted in Fig. 2. The proposed current buck converter operates in the following two modes, depending on whether switch S is ON or OFF:

State 1 [$0 \leq t \leq DT_s$]: As shown in Fig. 3(a), in this interval, S is turned ON, and diode D is in reversed bias. Thus, capacitor C is discharged through inductor and load. The current flowing through inductor and load is equal and increases linearly.

State 2 [$DT_s \leq t \leq T_s$]: According to Fig. 3(b), in this state, switch S is turned OFF when diode D is in forward bias. Hence, the current source charges capacitor C, and inductor L releases its energy into the output load.

By applying the ampere-second balance on C, we have:

$$DT_s(-I_{out}) + (1 - D)T_s(I_{in} - I_{out}) = 0 \quad (1)$$

Hence, the current conversion ratio of the proposed converter is:

$$G_{Buck} = \frac{I_{out}}{I_{in}} = 1 - D \quad (2)$$

2.2.2. Current DC-DC Boost converter

Fig. 4 depicts the conventional voltage boost converter. By applying the duality principle to it, the proposed current boost converter is obtained as shown in Fig. 5. And its operation modes are as below:

State 1 [$0 \leq t \leq DT_s$]: Based on Fig. 6(a), in this mode, S is turned ON and D is in reversed bias. Therefore, L is charged through the input current source and C.

State 2 [$DT_s \leq t \leq T_s$]: As shown in Fig. 6(b), S is turned OFF where D is in forward bias. Thus, the input current source charges C, and L releases its energy into the output load.

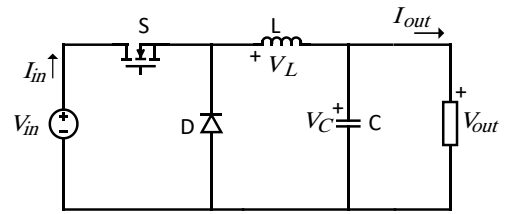


Fig. 1: The conventional voltage buck converter.

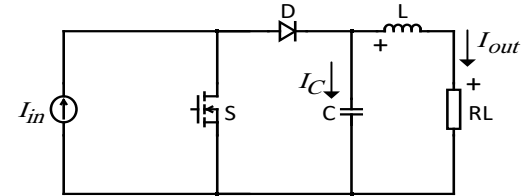


Fig. 2: The proposed current buck converter.

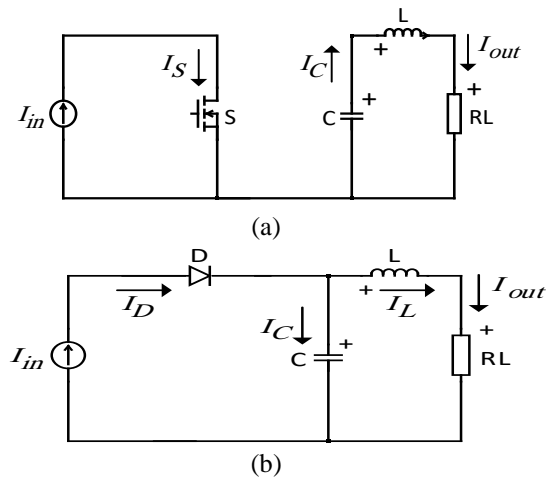


Fig. 3: The equivalent circuits of the proposed current buck converter: (a) ON state and (b) OFF state.

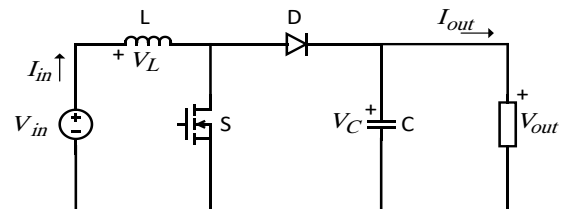


Fig. 4: The conventional voltage boost converter.

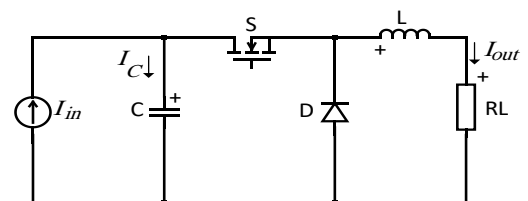


Fig. 5: The proposed current boost converter.

By applying the ampere-second balance on C, we have:

$$DT_s(I_{in} - I_{out}) + (1 - D)T_s(I_{in}) = 0 \quad (3)$$

Thus, the current conversion ratio is obtained as:

$$G_{Boost} = \frac{I_{out}}{I_{in}} = \frac{1}{D} \quad (4)$$

2.2.3. Current DC-DC Fly-back converter

The principle of duality is applied to the conventional

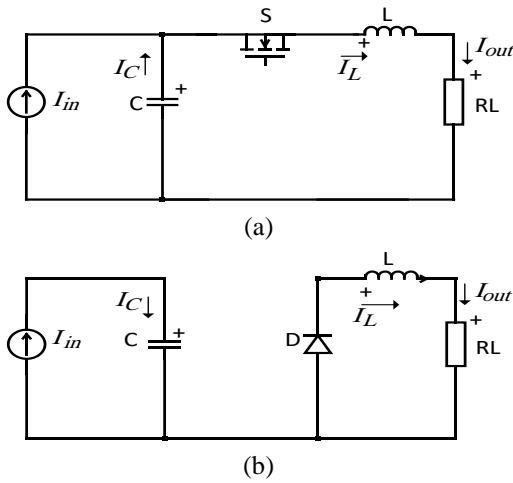


Fig. 6: The equivalent circuits of the proposed current boost converter: (a) ON state and (b) OFF state.

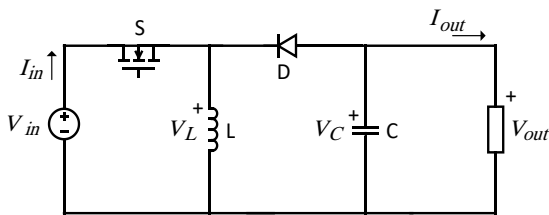


Fig. 7: The conventional voltage fly-back converter.

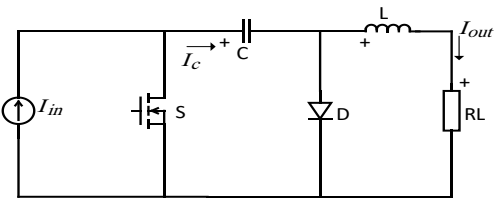


Fig. 8: The proposed current fly-back converter.

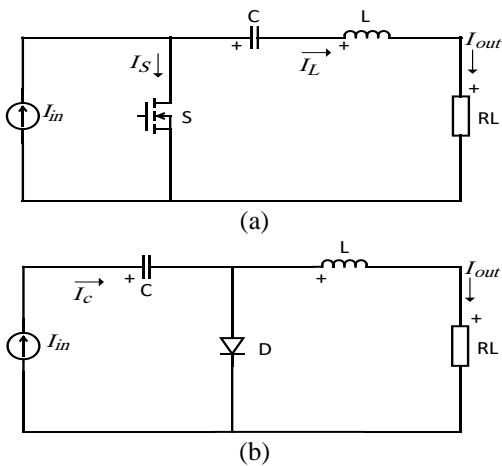


Fig. 9: The equivalent circuits of the proposed current fly-back converter: (a) ON state and (b) OFF state.

Voltage fly-back converter (Shown in Fig. 7). Hence, the proposed current fly-back converter is derived as exhibited in Fig. 8. Its two operation modes are as follows:

State 1 [$0 \leq t \leq DT_s$]: In this state, switch S is turned ON, and D is in reversed bias, according to Fig. 9(a). Thus,

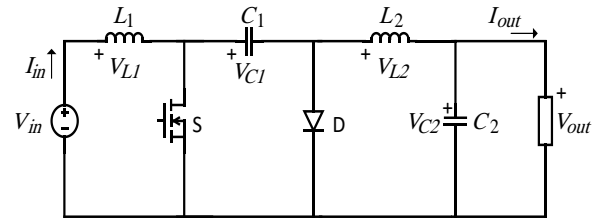


Fig. 10: The conventional voltage cuk converter.

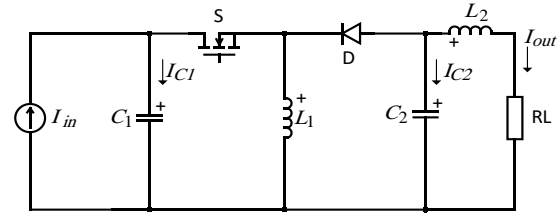


Fig. 11: The proposed current cuk converter.

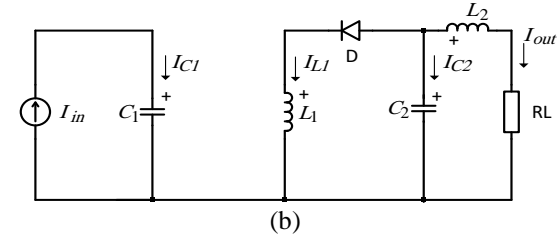
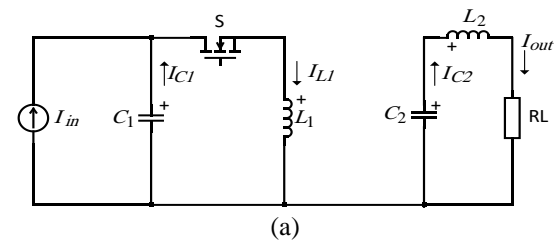


Fig. 12: The equivalent circuits of the proposed current cuk converter: (a) ON state and (b) OFF state.

The input current source and C are charging inductor L and output load in series.

State 2 [$DT_s \leq t \leq T_s$]: Fig. 9(b) shows this interval. So, S is turned OFF and D is in forward bias. The input current source charges capacitor C.

To obtain the current conversion ratio, the ampere-second balance on C is applied as:

$$DT_s(I_{out}) + (1 - D)T_s(I_{in}) = 0 \quad (5)$$

Hence, the current conversion ratio is:

$$G_{Fly-back} = \frac{I_{out}}{I_{in}} = -\frac{1-D}{D} \quad (6)$$

2.2.4. Current DC-DC Cuk converter

Fig. 10 shows the conventional voltage cuk converter. By applying the principle of duality to it, the proposed current cuk converter is derived (Fig. 11) whose ON and OFF operation modes are as follows:

State 1 [$0 \leq t \leq DT_s$]: In this interval, S in ON and D is in reversed bias as shown in Fig. 12(a). Hence, C_1 charges L_1 , and C_2 charges L_2 , which is in series with the output load. So, the currents of all inductors increase linearly.

State 2 [$DT_s \leq t \leq T_s$]: Based on Fig. 12(b), in this operation mode, switch S is turned OFF and diode D is in

forward bias. Thus, the input current source charges C_1 and the inductors release their energy into C_2 .

By applying the ampere-second balance on C_1, C_2 , we have:

$$\begin{cases} DT_s(I_{in} - I_{L1}) + (1 - D)T_s(I_{in}) = 0 \\ DT_s(-I_{out}) + (1 - D)T_s(-I_{L1} - I_{out}) = 0 \end{cases} \quad (7)$$

Thus, the average current across L_1 is determined as:

$$I_{L1} = \frac{1}{D} I_{in} \quad (8)$$

and, the current conversion ratio is obtained as:

$$G_{Cuk} = \frac{I_{out}}{I_{in}} = -\frac{1-D}{D} \quad (9)$$

2.2.5. Current DC-DC Sepic converter

The principle of duality is applied to the conventional voltage sepic converter as shown in Fig. 13. Then, the proposed current sepic converter is obtained as displayed in Fig. 14. The operation modes of the proposed circuit are as below:

State 1 $[0 \leq t \leq DT_s]$: As shown in Fig. 15(a), in this mode, S is turned ON, and D is in reversed bias. Therefore, L_1 and L_2 are charged by C_1 and C_2 , respectively, where the output load is in series with L_2 .

State 2 $[DT_s \leq t \leq T_s]$: S is turned OFF, and D is in forward bias, according to Fig. 15(b). Hence, the input current source charges C_1 , and C_2 is fed by L_1 .

If the amp-second balance is applied on C_1 and C_2 , we will have:

$$\begin{cases} DT_s(I_{out}) + (1 - D)T_s(-I_{L1}) = 0 \\ DT_s(I_{in} - I_{L1} - I_{out}) + (1 - D)T_s(I_{in}) = 0 \end{cases} \quad (10)$$

Hence, the current across L_1 is calculated as:

$$I_{L1} = \frac{D}{1-D} I_{out} \quad (11)$$

Therefore, the current conversion ratio of the proposed converter is as follows:

$$G_{Sepic} = \frac{I_{out}}{I_{in}} = \frac{1-D}{D} \quad (12)$$

2.2.6. Current DC-DC Zeta converter

By applying the principle of duality to the conventional voltage zeta converter which is shown in Fig. 16, the proposed current zeta converter is derived as shown in Fig. 17. Its two states of operation modes are described as follows:

State 1 $[0 \leq t \leq DT_s]$: According to Fig. 18(a), in this operation mode, S is turned ON, and D is in reversed bias. Subsequently, C_1 charges L_1 , and L_2 , which is in series combination with the output load, is fed by C_2 .

State 2 $[DT_s \leq t \leq T_s]$: As the circuitry of this state is shown in Fig. 18(b), switch S is turned OFF, and D is in forward bias. Thus, the input current source charges C_1 , and inductor L_1 is discharged into C_2 .

Similarly, by applying the ampere-second balance on C_1 and C_2 , we have:

$$\begin{cases} DT_s(I_{L1}) + (1 - D)T_s(I_{in}) = 0 \\ DT_s(-I_{out}) + (1 - D)T_s(I_{in} - I_{L1} - I_{out}) = 0 \end{cases} \quad (13)$$

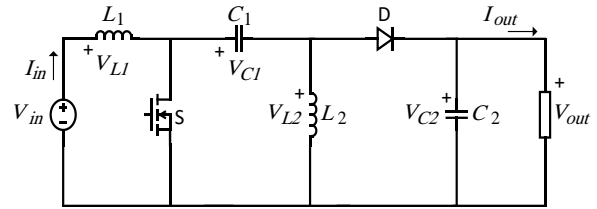


Fig. 13: The conventional voltage sepic converter.

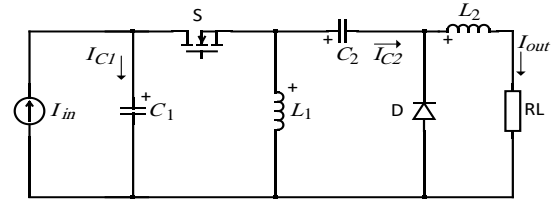
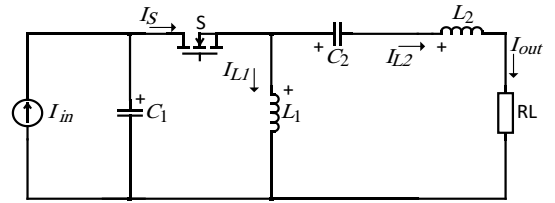
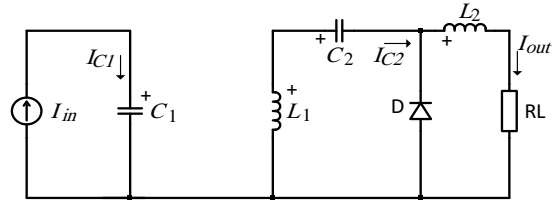


Fig. 14: The proposed current sepic converter.



(a)



(b)

Fig. 15: The equivalent circuits of the proposed current sepic converter: (a) ON state and (b) OFF state.

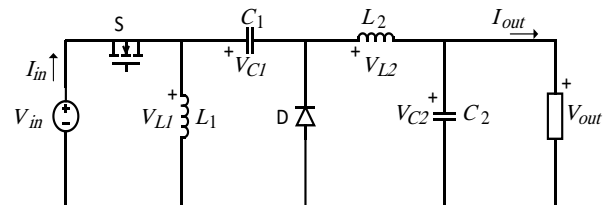


Fig. 16: The conventional voltage zeta converter.

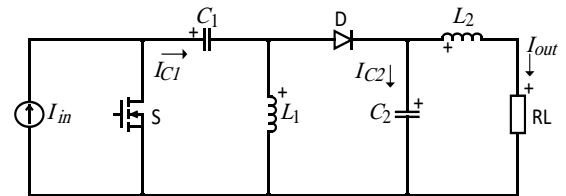


Fig. 17: The proposed current zeta converter.

And, the average current across L_1 is:

$$I_{L1} = -\frac{1-D}{D} I_{in} \quad (14)$$

Hence, the current conversion ratio is obtained as:

$$G_{Zeta} = \frac{I_{out}}{I_{in}} = \frac{1-D}{D} \quad (15)$$

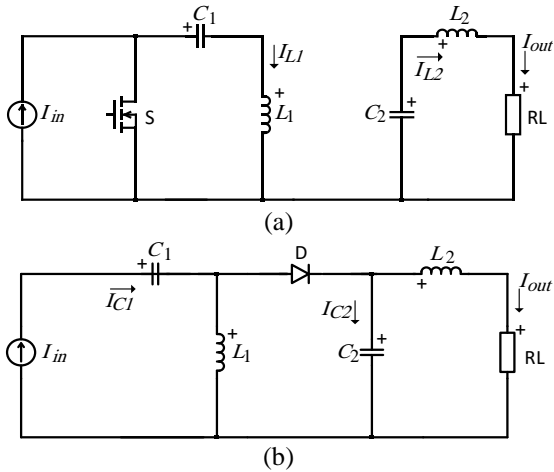


Fig. 18: Equivalent circuits of proposed Current Zeta converter: (a) ON state and (b) OFF state.

2.3. Semiconductor Rating

The expressions for the average ON-state current and the average OFF-state voltage across the switch and diode for each of the proposed current converters are as follows:

$$\text{Boost structure: } \begin{cases} V_S = V_{in} \\ I_S = \frac{3-2D}{D} I_{in} \end{cases} \quad (16)$$

$$\text{Buck and fly-back structures: } \begin{cases} V_S = \frac{1}{1-D} V_{in} \\ I_S = \frac{1}{D} I_{in} \end{cases} \quad (17)$$

$$\text{Cuk, sepic, and zeta structures: } \begin{cases} V_S = \frac{1}{1-D} V_{in} \\ I_S = \frac{1}{D^2} I_{in} \end{cases} \quad (18)$$

Therefore, the values of the total current stress (TCS) and total voltage stress (TVS) of each current DC-DC converter semiconductor device are listed in Table 2.

2.4. Equivalent Circuit Model of Photovoltaic (PV)

The simple equivalent circuit model for a PV cell includes a real diode in parallel with an ideal current source. The diode represents the non-linear I-V characteristic of the cell, where the current is proportional to the solar flux, and the voltage is limited by the built-in potential of the cell. However, in the case of shading, the simple model is not sufficient to accurately predict the behavior of the PV cell. To account for this issue, a more complex equivalent circuit model is required, which includes resistive elements such as the parallel leakage resistance R_p and series resistance R_s [24]. Such a circuit is depicted in Fig. 19. By applying the current balance equation with the Shockley diode equation to a point to the left of R_s , we can obtain an equation that relates the current through the diode and the current through the resistor as:

$$I_{PV} = I_{ph} - I_d - I_p = I_{ph} - I_0 \left(e^{\frac{V_{PV} + R_s I_{PV}}{n_s V_t Q_d}} - 1 \right) - \frac{V_{PV} + R_s I_{PV}}{R_p} \quad (19)$$

Table 2: The value of the total voltage and current stress.

Current DC-DC Converter	TVS	TCS
Buck	$V_{in} / (1 - D)$	I_{in} / D
Boost	V_{in}	$(3 - 2D) I_{in} / D$
Fly-back	$V_{in} / (1 - D)$	I_{in} / D
Cuk	$V_{in} / (1 - D)$	I_{in} / D^2
SePIC	$V_{in} / (1 - D)$	I_{in} / D^2
Zeta	$V_{in} / (1 - D)$	I_{in} / D^2

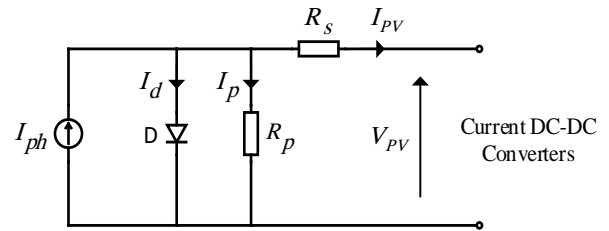


Fig. 19: The single-diode electrical PV module equivalent circuit.

where

$$V_t = kT_c / q \quad (20)$$

While a single PV cell may not produce enough voltage to power most household appliances or electronic devices, multiple cells can be connected in series to produce a higher voltage. A module consisting of several prewired cells connected in series is commonly used as the basic building block for PV applications. So, one of the most important considerations in PV system design is the configuration of the PV modules, specifically how many modules should be connected in series and how many in parallel to meet the energy requirements of the system. [25].

2.5. Equivalent Circuit Model of High-power LED

Packaging is an important consideration for high-power LEDs with large areas to ensure good heat dissipation and a longer lifetime. One important component in LED packaging is the electrostatic discharge (ESD) protection diode. The ESD protection diode, typically a Zener diode, is used to shunt the ESD current away from the LED chip and prevent damage [26]. In LED packaging, the ESD protection diode is often modeled as a single capacitor for simplicity, even though its accurate model cannot be obtained due to its integration into the package. Fig. 20 shows the equivalent circuit for high-power LEDs [27]. The impedance of an LED can be expressed as below:

$$Z_{LED} = R_b + j\omega L_b + \frac{1}{j\omega C_b} // (R_s + \frac{1}{j\omega C_j} // r_d) \quad (21)$$

in which $C_j = C_{sc} + C_d$ is the junction capacitance.

3. TEST RESULTS

Fig. 21 provides the input and output current waveforms

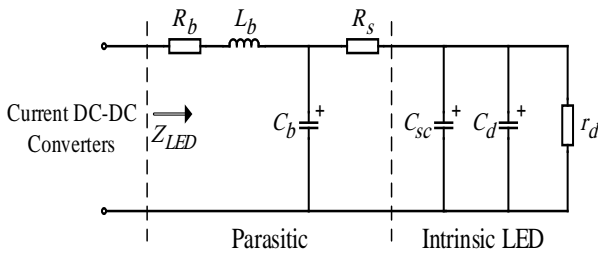


Fig. 20: The equivalent circuit model for the high-power LED.

of all proposed DC-DC current converters used as an interface between a PV cell and a high-power LED.

The simulation parameters for the PV system, high-power LED, and proposed DC-DC current converters are consistent, except for some, which have been listed below: In order to produce the required electrical output power in the PV system, the module has 36 cells in series, except for the fly-back topology whose module requires 50 cells in series. Another PV parameter is $I_{ph} = 5 A$ for all topologies, except for the fly-back and zeta structures which is $I_{ph} = 7 A$. Also, $R_p = 1000 \Omega$ and $R_{s_{PV}} = 0.3 \Omega$.

A 50-W and approximately 18-V high-power LED is considered the load and its parameters are $R_b = 0.27 \Omega$, $R_{s_{LED}} = 2.61 \Omega$, $R_d = 7.07 \Omega$, $L_b = 2.45 nH$, $C_b = 14.4 nF$, and $C_j = 0.2 mF$.

The parameters for the proposed DC-DC current converters are $L = L_2 = 1 mH$, $L_1 = 0.04 mH$, $C = C_2 = 50 \mu F$, $f_s = 10 KHz$, and $C_1 = 10 \mu F$, except for the zeta topology in which we have $C_1 = 6 \mu F$. Besides, in order to implement the control system on these current converters, the PWM method is used by applying specific pulse signals with defined amplitudes to the switches. So, its details are as follows: the ON time duty cycle is considered 40% for all topologies, except for the boost and fly-back topologies, in which it is considered 90% and 70% to avoid working at DCM mode, respectively.

According to Figs. 21(c) and 21(d), the fly-back and cuk converters have equal negative output currents as their equal negative current conversion ratio are calculated by Eq. (6) and (9), respectively. Furthermore, based on Eq. (12) and Fig. 21(e), the sepic topology has the same current conversion ratio and output current as the fly-back and cuk topologies but in a reversed direction.

Also, based on Eq. (12) and (15) and Figs. 21(e) and 21(f), respectively, the sepic and zeta topologies have the same current conversion ratio and output currents.

To show the stability of the new topologies in a wide range of operations, there are some other results about input voltages of the proposed DC-DC current converters, which are shown in Fig. 22.

Furthermore, the graph of the proposed converters' current gain versus their OFF time duty cycle is depicted in Fig. 23. It is shown that the buck topology has a positive

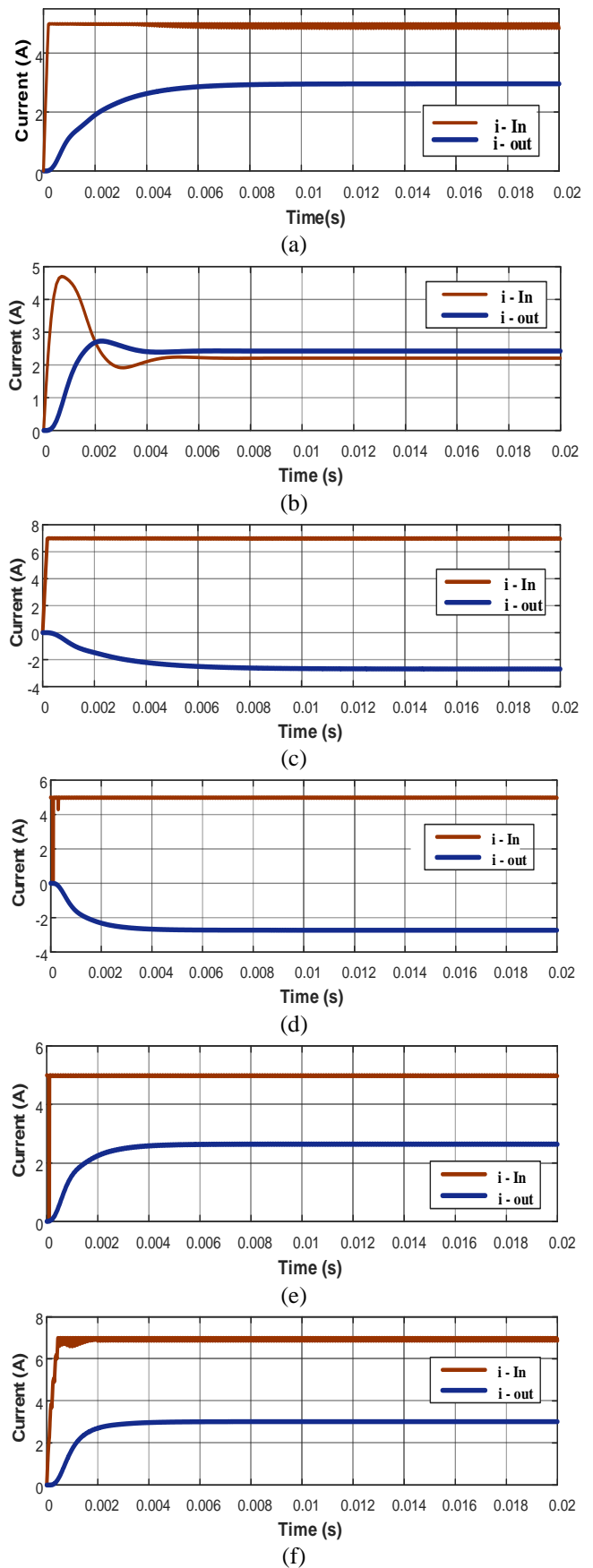


Fig. 21: The input and output currents of the proposed current DC-DC converters: (a) buck, (b) boost, (c) fly-back, (d) cuk, (e) sepic, and (f) zeta.

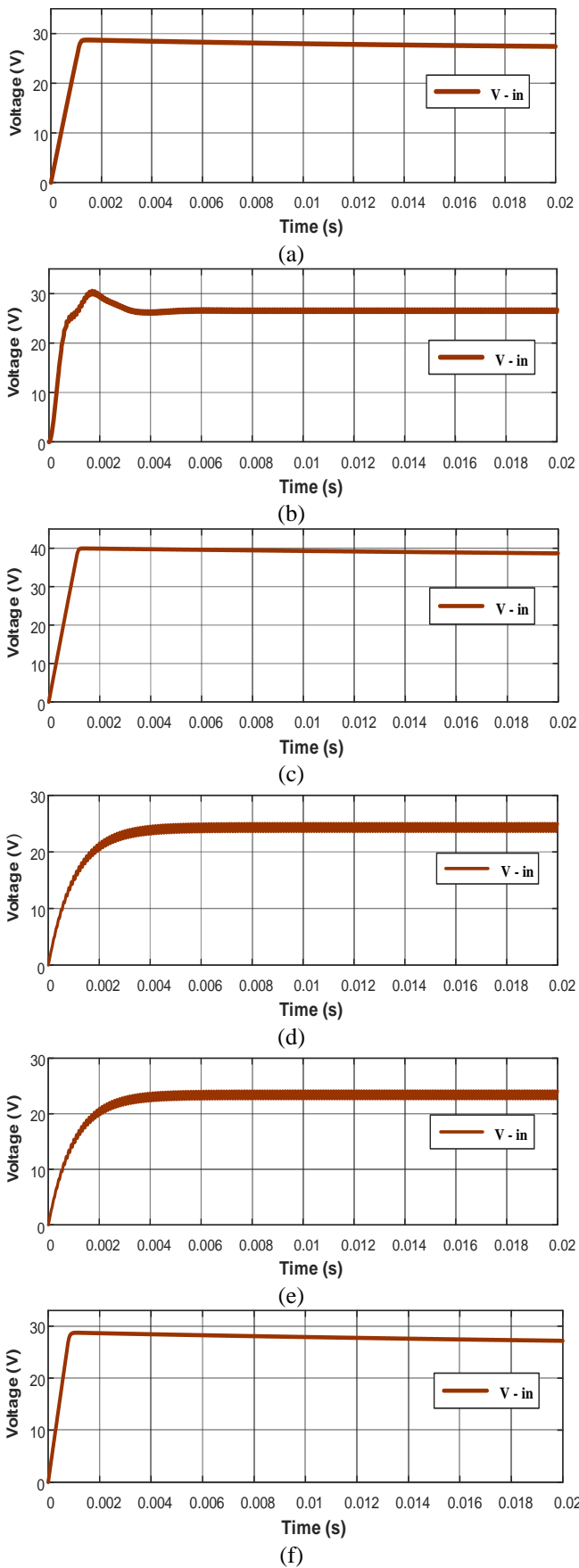


Fig. 22: The input voltages of the proposed DC-DC current converters: (a) buck, (b) boost, (c) fly-back, (d) cuk, (e) sepic, and (f) zeta.

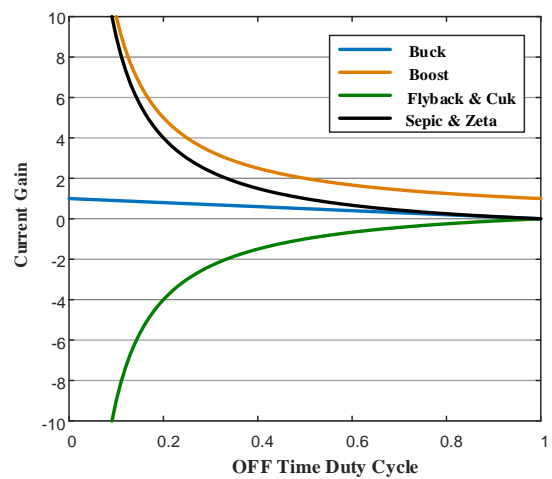


Fig. 23: The graph of the current gain versus duty cycle.

limited current gain, the boost, sepic, and zeta topologies have positive unlimited current gains, and the fly-back and cuk topologies have negative unlimited current gains. However, it is notable that these results are obtained theoretically based on their calculated current gain equations.

4. CONCLUSIONS

This paper explained several current-based DC-DC converters, including buck, boost, flyback, cuk, sepic, and zeta topologies, as viable solutions for applications that require current control. The proposed converters were derived using the principle of duality, which allows for the conversion of a voltage-based circuit into a current-based circuit. A detailed analysis of the circuit configurations and operation principles of the proposed current conversion circuits, and also mathematical equations for the proposed converters were presented. Besides, the semiconductor rating and the values of the total current stress (TCS) and the total voltage stress (TVS) were calculated for each current DC-DC converter's semiconductor device. In addition, the paper described a practical case study in which the proposed current converters were applied to a photovoltaic system and a high-power LED load. The circuit models of the PV system and LED load were described in detail, and simulations were provided in MATLAB to demonstrate the feasibility of the proposed converters in this application and the principle of duality and to verify the mathematical equations of the proposed DC-DC current converters.

CREDIT AUTHORSHIP CONTRIBUTION STATEMENT

Zahra Gholami: Data curation, Formal analysis, Investigation, Methodology, Project administration, Resources, Writing - original draft, Writing - review & editing. **Rahim Ildarabadi:** Conceptualization, Data curation, Formal analysis, Funding acquisition, Methodology, Supervision, Validation, Visualization, Writing - review & editing. **Hamed Heydari-Doostabad:** Validation, Visualization, Writing - review & editing.

DECLARATION OF COMPETING INTEREST

The authors declare that they have no known competing financial interests or personal relationships that could have appeared to influence the work reported in this paper. The ethical issues; including plagiarism, informed consent, misconduct, data fabrication and/or falsification, double publication and/or submission, redundancy has been completely observed by the authors.

REFERENCES

- [1] S. Cuk, R. D. Middlebrook, "Advances in switched-mode power conversion part II," *IEEE Transactions on Industrial Electronics*, vol. IE-30, no.1, p.p. 19–29, 1983.
- [2] A Abramovitz , "An approach to average modelling and simulation of switch-mode systems," *IEEE Transactions on Education* ,vol. 54, no.3 , p.p. 509–517, 2011.
- [3] M. C. Di Piazza and G. Vitale, *Photovoltaic Sources: Modeling and Emulation*, Green Energy and Technology. London, U.K.: Springer, 2012.
- [4] H. Plesko, J. Biela, J. Luomi, and J. W. Kolar, "Novel concept for integrating the electrical drive and auxiliary DC-DC converter for hybrid vehicles," *IEEE Transactions on Power Electronics*, vol. 23, no. 6, pp. 3025–3034, 2008.
- [5] G. Ch. Ioannidis *et al.*, "AC-DC & DC-DC converters for DC motor drives," in *Proc. Int. Conf. Electronics and Communication Systems (ICECS)*, 2013.
- [6] K. W. E. Cheng, "Overview of the DC power conversion and distribution," *Asian Power Electronic*, vol. 2, no. 2, p.p. 75–82, 2008.
- [7] M. S. Bhaskar, P. K. Maroti, and D. K. Prabhakar, "Novel topological derivations for DC-DC converters," *International Journal of Computational Engineering & Management*, vol. 16, no. 6, 2013.
- [8] A. Bubovich, "The comparison of different types of DC-DC converters in terms of low-voltage implementation," in *Proc. 5th IEEE Workshop AIEEE*, 2018.
- [9] S. A. Gorji *et al.*, "Topologies and control schemes of bidirectional DC–DC power converters: An overview," *IEEE Access*, vol. 7, pp. 117997–118019, 2019.
- [10] N. Siddharthan and B. Balasubramanian, "Performance evaluation of SEPIC, Luo and ZETA converter," *International Journal of Power Electronics and Drive Systems*, vol. 10, no. 1, pp. 374–380, 2019.
- [11] L. J. Jeremy, C. A. Ooi, and J. Teh, "Non-isolated conventional DC-DC converter comparison for a photovoltaic system: A review," *Journal of Renewable and Sustainable Energy*, vol. 12, 2020.
- [12] K. T. Mok *et al.*, "Synthesis of two-state ladder-structured DC-DC power converters by duality principle," in *Proc. IEEE Industrial Electronics Society (IECON)*, 2012.
- [13] K. W. E. Cheng and Y.-M. Ye, "Duality approach to the study of switched-inductor power converters and its higher order variations," *IET Power Electronics*, vol. 8, no. 4, pp. 479–489, 2015.
- [14] M. Samie *et al.*, "Developing prognostic models using duality principles for DC to DC converters," *IEEE Transactions on Power Electronics*, vol. 30, no. 5, pp. 2872–2884, 2015.
- [15] M. S. Bhaskar *et al.*, "DC-DC buck converter through duality approach for current-based loads," in *Proc. International Conference on Electrical, Electronics, and Optimization Techniques (ICEEOT)*, 2016.
- [16] M. S. Bhaskar *et al.*, "DC-DC buck converter through duality approach and its DC transformer modelling for current-based loads," in *Proc. International Conference on Circuit, Power and Computing Technologies (ICCPCT)*, 2016.
- [17] A. K. Rathore, "Current-fed DC-DC converters for high voltage gain and low voltage high current applications," in *Proc. IEEE International Conference on Power Electronics, Drives and Energy Systems (PEDES)*, 2016.
- [18] N. E. Zakzouk *et al.*, "Continuous-input continuous-output current buck-boost DC/DC converters for renewable energy applications: Modelling and performance assessment," *Energies*, vol. 12, no. 11, 2019.
- [19] J. H. Sun, and K. W. E. Cheng, "Current-source mode switched-capacitor power converters with improved current gain capability," *IET Power Electronics*, vol. 13, no. 1, pp. 116–126, 2020.
- [20] B. Zhu, H. Wang, Y. Zhang, and S. Chen, "Buck-Based Active-Clamp Circuit for Current-Fed Isolated DC–DC Converters," *IEEE Transactions on Power Electronics*, vol. 37, no. 4, 2022.
- [21] M. Afkar, P. Karimi, R. Gavagsaz-Ghoachani, M. Phattanasak, and S. Pierfederici, "Effect of changes in the parameters of a modular converter in its controllability range in fuel cell applications," *Journal of Applied Research in Electrical Engineering*, vol. 2, no. 1, pp. 54-61, 2023.
- [22] A. Cid-Pastor, L. Martinez-Salamero, R. Leyva, R. Calvente, and J. Giral, "Design of photovoltaic-based current sources for maximum power transfer by means of power gyrators," *IET Power Electronics*, vol. 4, no. 6, pp. 674–682, 2011.
- [23] M.-T. Wu, C.-L. Lin, C.-C. Lin, and L.-P. Chung, "Stabilising current driver for high-voltage light-emitting diodes," *IET Power Electronics*, vol. 7, no. 4, p. 1024, 2014.
- [24] M. Rosa-Clot, and G. M. Tina, *Submerged and Floating Photovoltaic Systems, Modelling, Design and Case Studies*, Chapter 3, Academic Press, 2018.
- [25] P. Acharya, M. N. Shaikh, S. K. Jha, and A. P. Papadakis, "Electrical Modelling Of a Photovoltaic Module," in *Engineering and Industry Series Volume Power Systems*, 2016.

- [26] E. F. Schubert, *Light-emitting diodes*, 2nd ed., Springer, 2018.
- [27] X. Li, Z. Ghassemlooy, S. Zvanovec, M. Zhang, and A. Burton, "Equivalent Circuit Model of High Power LEDs for VLC Systems," in *proc. 2nd West Asian Colloquium on Optical Wireless Communications (WACOWC)*, 2019.

Biography



Zahra Gholami received the M.S. degree in electrical engineering from the Hakim Sabzevari University, Iran, in 2023. Her research interests include power electronics, especially dc-dc power converters, inverters, drives, electric vehicles, and renewable power systems.



Rahim Ildarabadi was born in Sabzevar, Iran in 1975. He received the PhD degree from Ferdowsi University of Mashhad in 2010. He is a full-time faculty member at Sabzevar, Hakim Sabzevari University. His main area of interests is automation system, electrical machine drive, renewable energy, instruments and measurement. He is currently an Associate Professor of electrical engineering at Hakim Sabzevari University.



Hamed Heydari-Doostabad (Member, IEEE) received the Ph.D. (Hons.) degree in electrical engineering from the Ferdowsi University of Mashhad, Mashhad, Iran, in 2018. He is currently a Postdoctoral Senior Power System Researcher with the School of Electrical and Electronic Engineering, University College Dublin (UCD), Dublin, Ireland. His research interests include power electronics, especially grid-feeding-forming inverters, distributed energy resources, photovoltaic inverters, dc converters, power quality, and control systems.

Copyrights

© 2024 Licensee Shahid Chamran University of Ahvaz, Ahvaz, Iran. This article is an open-access article distributed under the terms and conditions of the Creative Commons Attribution –NonCommercial 4.0 International (CC BY-NC 4.0) License (<http://creativecommons.org/licenses/by-nc/4.0/>).





Iranian Association of
Electrical and Electronics
Engineers

Journal of Applied Research in Electrical Engineering

E-ISSN: 2783-2864

P-ISSN: 2717-414X

Homepage: <https://jaree.scu.ac.ir/>



Research Article

Consensus-Based Algorithm for Distributed Continuous-Time Convex Optimization Over Undirected and Directed Networks

Ehsan Nazemorroaya¹, Mohsen Shafieirad^{1,*}, Mahdi Majidi¹, and Mahdiah Adeli²

¹ Department of Electrical and Computer Engineering, University of Kashan, Kashan, Iran

² Electrical Engineering Department, Kermanshah University of Technology, Kermanshah, Iran

* Corresponding Author: m.shafieirad@kashanu.ac.ir

Abstract: In this article, the distributed continuous-time convex Optimization Problem (OP) is investigated over undirected and balanced directed graphs. The cost function of the distributed convex OP is determined as the sum of local convex functions where each of them is known only for one agent. The proposed algorithm consists of two main steps. The first step is a consensus-based scheme which is in combination with the gradient descent method. Employing the Lyapunov theory and LaSalle's invariance principle, the convergence to the Optimal Solution (OS) is analyzed. Moreover, inspired by the average consensus, in the second step the Optimal Value (OV) of the distributed convex OP is calculated. Using consensus concepts converges to the OV is substantiated in the second step. Therefore, the offered algorithm can calculate the OS and the OV of the distributed convex OP with no need for the strong convexity assumption. Beyond the theoretical findings, the results from simulations are also showcased to demonstrate the efficiency and accuracy of the proposed algorithm.

Keywords: Distributed convex optimization, multi-agent system, consensus, convergence analysis, gradient descent method.

Article history (Please do not write in this space)

Received 16 March 2024; Revised 19 July 2024; Accepted 13 October 2024; Published online 23 October 2024.

© 20xx Published by Shahid Chamran University of Ahvaz & Iranian Association of Electrical and Electronics Engineers (IAEEE)

How to cite this article

E. Nazemorroaya, M. Shafieirad, M. Majidi, and M. Adeli, "Consensus-based algorithm for distributed continuous-time convex optimization over undirected and directed networks," *J. Appl. Res. Electr. Eng.*, vol. 3, no. 1, pp. 74-82, 2024. DOI: [10.22055/jaree.2024.46401.1113](https://doi.org/10.22055/jaree.2024.46401.1113)



1. INTRODUCTION

Over the last few years, a lot of research has been done on Multi-Agent Systems (MASs) [1-4]. Researchers have shown a keen interest in MASs due to the agents' ability to reach consensus on a value through their mutual interactions [5]. It should be mentioned that this value, named consensus value, is the mean of the initial conditions of agents.

Due to the extensive application of MASs, the design and analysis of distributed algorithms have emerged as a significant area of research [6]. Distributed algorithms achieve the specified objectives by relying solely on local calculations and the exchange of information between each agent and its neighbors the distributed algorithms based on consensus are the predominant ones. The complexities of distributed consensus algorithms are enormous. Therefore, designing an appropriate distributed consensus algorithm is a critical and challenging problem [7]. Algorithms that utilize

distributed consensus are widely implemented to solve the distributed Optimization Problem (OP). The objective of the distributed OP is to determine the Optimal Solution (OS) for the cost function through the application of distributed algorithms. It should be noted that the distributed optimization does not need a long-distance communication system and a data fusion center; thus, the load balance for the network becomes better [8]. Also, due to the time-varying communication topology, energy constraints, the large size of the network and privacy problems, distributed optimization methods have received much attention [8-10]. The distributed OP has been used in distributed estimation [8], power distribution systems [11], economic dispatch in power systems [12, 13], federated learning [14] and formation control [15].

In general, the OPs are divided into constrained OP [16, 17] and unconstrained OP [16, 18]. It should be pointed out that the unconstrained OP is discussed in this article. An

unconstrained OP is convex if and only if the cost function is convex. The cost function in the distributed convex OP consists of the sum of local convex functions, each of them is known only for one agent. It is worth mentioning that the goal of the distributed convex OP is to minimize the total cost function by using local information and computation.

Subgradient-based approaches are commonly employed to solve the distributed convex OP [19]. In [20], the distributed convex OP under non-smooth and smooth cost functions has been investigated. In the mentioned reference, the communication network has been considered to be undirected. By combining the gradient algorithm and consensus algorithm, a novel distributed algorithm for the distributed convex optimization over the directed graph has been designed in [21]. The designed algorithm has been named as push-pull gradient algorithm because all agents push and pull information (gradient information and the optimization variables) through the communication network. For the distributed convex OP, an asynchronous algorithm has been designed by Zhang and You [22]. In the asynchronous algorithm, each agent iteratively calculates the OS by using the currently available local information, but in the synchronous algorithm, each agent waits for information updates from other agents and then goes to the next iteration of the algorithm. It should be noted that asynchrony causes difficulties in optimization algorithm design. In all the above-mentioned studies, the distributed discrete-time OP has been investigated. On the other hand, the studies about the distributed continuous-time OP are discussed in the next paragraph. It should be mentioned that for solving the distributed continuous-time OP, an algorithm is often designed using control theory such as Lyapunov theory and LaSalle's invariance principle.

In [23], a novel consensus-based algorithm has been designed for the distributed convex OP. In the mentioned reference, the convergence of the designed algorithm to the OS has been guaranteed over the weight-balanced directed graph, by using the Lyapunov theory. For undirected graphs, the distributed convex OP has been studied by Li *et al.* [24]. Therefore, an event-triggered controller has been designed to solve the OP. It should be noted that the linear MAS with heterogeneous dynamics has been studied in the mentioned reference. In heterogeneous MASs, unlike homogeneous MASs, the agents do not have the same dynamics. Based on the event-triggered mechanism, a distributed optimization algorithm has been designed by Shi *et al.* [25]. The major advantage of this algorithm is communication resource saving. Inspired by second-order consensus, a novel subgradient-based algorithm for distributed convex OP is presented in [26]. The proposed algorithm can only calculate the OS of the distributed convex OP. In [27], a proposed algorithm addresses the distributed convex OP, and the communication network is assumed to be undirected. Furthermore, by applying the Lyapunov theory, the exponential convergence of the suggested algorithm has been proved with no need for the strong convexity assumption.

The calculation of the Optimal Value (OV) has not been investigated in any of the above-mentioned studies. It should be emphasized that the design of the distributed algorithm for calculating the OV is an important problem with complexity because each agent has access to only a part of the total cost

function. Based on the explanations provided, this paper presents an algorithm that integrates the gradient method with the consensus algorithm of the MAS. Two theorems for the convergence of the offered algorithm to the OS and the OV are presented and by application of mathematical tools from control theory and convex optimization they are proved.

The main contribution to the article is listed as follows:

- Achieving higher accuracy than similar algorithms;
- Efficiency of the algorithm for balanced directed graphs;
- Calculating both the OS and the OV.

The subsequent sections of the paper are organized as follows. Section 2 introduces the graph of the MAS and the distributed OP along with several beneficial assumptions and lemmas. Section 3 presents the proposed algorithm and examines its convergence to the OS and OV, utilizing the Lyapunov theory and the consensus concepts. Then, in Section 4, the simulation results are given to show the optimization ability of the offered algorithm. In the end, Section 5 concludes the article.

Notations. \mathbb{R}^+ and \mathbb{R} denote the positive real numbers set and the real numbers set \mathbb{R}^+ and \mathbb{R} , respectively. The Euclidean norm and the Kronecker product are represented by $\|\cdot\|$ and \otimes , respectively.

2. BASIC CONCEPTS AND PROBLEM STATEMENT

This section begins by presenting the communication network model and the required concepts and assumptions for the communication network are stated. Then, the OP is presented and the necessary concepts pertaining to the convex optimization are outlined.

2.1. Communication Network

In this article, to model the communication network, the principles of the MAS and graph theory are employed. To do that, a graph is used to model the communication between the agents. It is assumed that the graph of the MAS is undirected and balanced directed. Thus, $\mathcal{G} = (\mathcal{V}, \mathcal{E}, \mathcal{A})$ is defined as a graph that includes the set of nodes $\mathcal{V} = [\mathcal{V}_1, \mathcal{V}_2, \dots, \mathcal{V}_n]$, the set of edges $\mathcal{E} \subset \mathcal{V} \times \mathcal{V}$ and the adjacency matrix $\mathcal{A} = \{a_{ij}\}_{i,j=1,\dots,n} \in \mathbb{R}^{n \times n}$ where n is the number of agents. If the agent i is capable of receiving the data sent by the agent j , then $a_{ij} > 0$, otherwise $a_{ij} = 0$.

Definition 1 [28]. A path is defined as a series of nodes connected in such a way that each pair of adjacent nodes is linked by an edge. In graph theory, the path can be directed or undirected.

Definition 2 [28]. An undirected graph is called connected when there is an undirected path between any two distinct nodes.

Definition 3 [28]. In directed graphs, if there is a directed path between any two arbitrary nodes; then, the graph is called to be strongly connected.

An indispensable condition for the consensus of MAS is that the graph is connected or strongly connected [28]. Hence, Assumptions 1 and 2 are presented.

Assumption 1. The graph \mathcal{G} is undirected and connected.

Assumption 2. The graph \mathcal{G} is assumed to be directed and strongly connected.

The definition of the Laplacian matrix corresponding to graph \mathcal{G} is as follows:

$$\mathcal{L} = \{\ell_{i,j}\}_{i,j=1,\dots,n} \in \mathbb{R}^{n \times n},$$

$$\ell_{i,j} = \begin{cases} -a_{ij}, & \text{if } i \neq j \\ \sum_{j=1}^n a_{ij}, & \text{if } i = j \end{cases} \quad (1)$$

It is apparent that $\mathbf{1}_n = [1,1,\dots,1]^T \in \mathbb{R}^n$ serves as a right eigenvector of the Laplacian matrix; thus, one has $\mathcal{L}\mathbf{1}_n = 0$.

Definition 4 [28]. The graph is termed balanced if $d_{in}(\mathcal{V}_i) = d_{out}(\mathcal{V}_i)$ holds for all nodes where $d_{in}(\mathcal{V}_i) = \sum_{j=1}^n a_{ij}$ and $d_{out}(\mathcal{V}_i) = \sum_{j=1}^n a_{ji}$.

Assumption 3 [29]. The graph \mathcal{G} is supposed to be balanced.

2.2. Distributed OP Formulation

In this article, the distributed unconstrained OP is investigated. Therefore, the OP is defined as the following equation.

$$\min_{x \in \mathbb{R}^N} f(x) = \sum_{i=1}^n f_i(x) \quad (2)$$

where $f(x): \mathbb{R}^N \rightarrow \mathbb{R}$ is the total cost function, $x \in \mathbb{R}^N$ is the optimization variable and $f_i(x): \mathbb{R}^N \rightarrow \mathbb{R}$ is the local cost function. Every local cost function is both convex and differentiable. Each local cost function is exclusively known to a single agent. It seems obvious that the total cost function is convex because it consists of the sum of convex functions.

The vector $x^* \in \mathbb{R}^N$ and the scalar $f^* = f(x^*)$ represent the OS and the OV of the OP in (2), respectively.

Two lemmas are given in the following which will be used in Section 3 in the design and convergence analysis of the offered algorithm.

Lemma 1 [30]. If the following inequality holds for every $x \in \mathbb{R}^N$ and $y \in \mathbb{R}^N$, then the function $f(x): \mathbb{R}^N \rightarrow \mathbb{R}$ is convex.

$$(\nabla f(x))^T (y - x) \leq f(y) - f(x) \quad (3)$$

where $\nabla f(x): \mathbb{R}^N \rightarrow \mathbb{R}^N$ denotes the gradient of the function $f(x)$.

Lemma 2 [30]. For each convex function $f(x): \mathbb{R}^N \rightarrow \mathbb{R}$ and for each $x, y \in \mathbb{R}^N$, the subsequent inequality holds.

$$(\nabla f(x) - \nabla f(y))^T (x - y) \geq 0 \quad (4)$$

Remark 1. If $f(x) - \frac{m}{2} \|x\|_2^2$ is convex, then $f(x)$ is termed strongly convex [20]. In [8, 20, 24, 25], for the design of the optimization algorithm, it has been assumed that the

cost function is strongly convex. Unlike the mentioned references, the strong convexity assumption is not required for the convergence of the offered algorithm in this article.

3. DESIGN AND ANALYSIS OF THE DISTRIBUTED OPTIMIZATION ALGORITHM

In this section, an innovative two-step consensus-based algorithm is introduced that combines calculating OS and OV. Then, the convergence analysis of this algorithm is performed using the concepts of MAS and consensus. First, based on the concept of consensus, the OS is calculated, and the convergence is investigated using the Lyapunov theory. Then, another consensus-based scheme is proposed to calculate the OV and the convergence analysis of this step is performed using the concepts of the MAS and consensus. At the end of this section, the algorithm resulting from the combination of these two steps is fully introduced, and its features are stated. Fig. 1 shows the general scheme of the algorithm.

Step 1: Computing OS

Based on the concept of average consensus, for a MAS with n agents, where the optimization variable of each agent is called $x_i, i = 1, \dots, n$, the following relations is used to compute the OS.

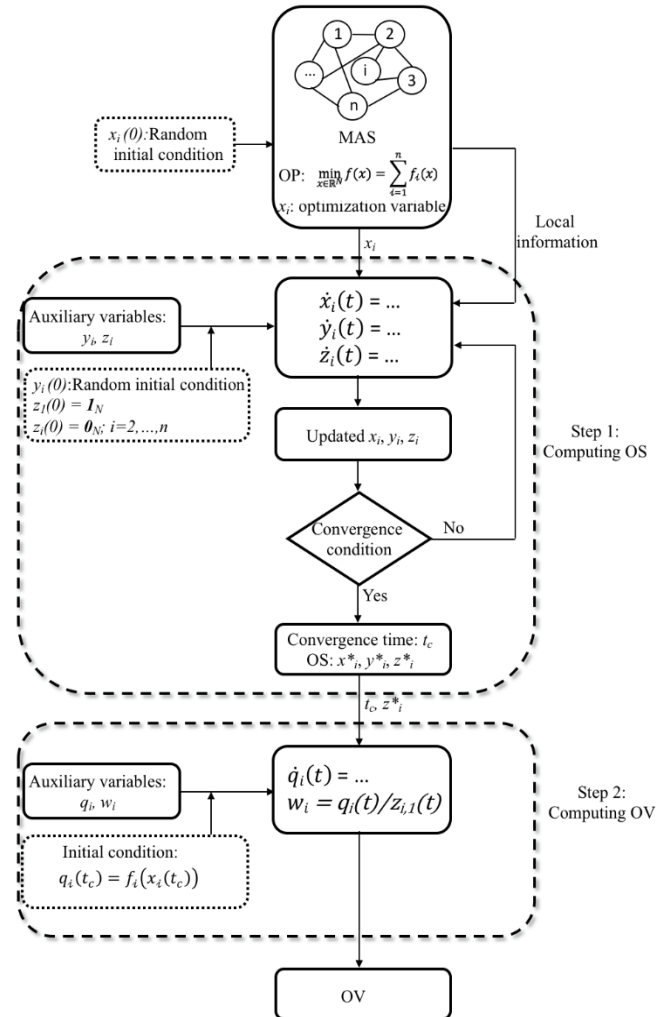


Fig. 1: The method overview.

$$\dot{x}_i(t) = \sum_{j=1}^n a_{ij} (x_j(t) - x_i(t)) \quad (5)$$

$$+ \varpi \sum_{j=1}^n a_{ij} (y_j(t) - y_i(t)) - \rho g_i(x_i(t))$$

$$\dot{y}_i(t) = \varpi x_i(t) \quad (6)$$

$$\dot{z}_i(t) = \sum_{j=1}^n a_{ij} (z_j(t) - z_i(t)) \quad (7)$$

Parameters $\varpi \in R$ and $\rho \in R^+$ are constant and $g_i(x_i(t))$ is the gradient of the function $f_i(x)$ at $x_i(t)$. The initial conditions for the variables $x_i(t) = [x_{i,1}(t), x_{i,2}(t), \dots, x_{i,N}(t)]^T \in \mathbb{R}^N$ and $y_i(t) = [y_{i,1}(t), y_{i,2}(t), \dots, y_{i,N}(t)]^T \in \mathbb{R}^N$ are chosen randomly and the initial conditions for the variable $z_i(t) = [z_{i,1}(t), z_{i,2}(t), \dots, z_{i,N}(t)]^T \in \mathbb{R}^N$ are selected as $z_1(0) = \mathbf{1}_N, z_2(0) = \mathbf{0}_N, \dots, z_n(0) = \mathbf{0}_N$, where $\mathbf{1}_N = [1 \dots 1]_{1 \times N}^T$ and $\mathbf{0}_N = [0 \dots 0]_{1 \times N}^T$.

Remark 2. The variable $z_i(t)$ has no relationship to the variables $x_i(t)$ and $y_i(t)$ because (7) is a first-order consensus for the variable $z_i(t)$. It should be pointed out that in the step 2, the consensus values of variable $z_i(t)$ will be used. Therefore, the variable $z_i(t)$ should be defined in the first step so that it has converged to the consensus values before executing the second step.

Considering (5) and (6) for all agents and using the matrix form, step 1 is written as follows:

$$\dot{X}(t) = -\mathcal{L}_1 X(t) - \varpi \mathcal{L}_1 Y(t) - \rho G(X(t)) \quad (8)$$

$$\dot{Y}(t) = \varpi X(t) \quad (9)$$

where $X(t) = [x_1^T(t), \dots, x_n^T(t)]^T$, $Y(t) = [y_1^T(t), \dots, y_n^T(t)]^T$, $G(X(t)) = [g_1^T(x_1(t)), \dots, g_n^T(x_n(t))]^T$ and $\mathcal{L}_1 = \mathcal{L} \otimes I_N$.

On the other hand, for the OSs $X^* \in \mathbb{R}^{Nn}$ and $Y^* \in \mathbb{R}^{Nn}$ the following equations can be written. It should be noted that the OS of all agents is collected in the vector X^* which is defined as $X^* = \mathbf{1}_n \otimes x^*$.

$$\dot{X}^* = -\mathcal{L}_1 X^* - \varpi \mathcal{L}_1 Y^* - \rho G(X^*) \quad (10)$$

$$\dot{Y}^* = \varpi X^* \quad (11)$$

According to the property $(A \otimes B)(C \otimes D) = (AC) \otimes (BD)$, one has

$$\begin{aligned} \mathcal{L}_1 X^* &= (\mathcal{L} \otimes I_N)(\mathbf{1}_n \otimes x^*) \\ &= (\mathcal{L} \mathbf{1}_n) \otimes (I_N x^*) \\ &= \mathbf{0}_{Nn} \end{aligned} \quad (12)$$

$$\text{where } \mathbf{0}_{Nn} = \begin{bmatrix} 0 & \dots & 0 \\ \vdots & \ddots & \vdots \\ 0 & \dots & 0 \end{bmatrix}_{N \times n}$$

Finally, according to (8)-(12), the convergence error of the variables is given by:

$$\dot{e}_x(t) = -\mathcal{L}_1 e_x(t) - \varpi \mathcal{L}_1 e_y(t) \quad (13)$$

$$- \rho (G(X(t)) - G(X^*))$$

$$\dot{e}_y(t) = \varpi e_x(t) \quad (14)$$

Theorem 1 [26]. Under Assumption 1, and according to Lemma 1 and 2, the convergence of the algorithm defined in (5) and (6) to the OS of the distributed unconstrained OP defined in (2) is guaranteed.

The proof can be followed by [26]. ■

Step 2: Computing OV

For calculating the OV, the following relations are introduced:

$$\dot{q}_i(t) = \sum_{j=1}^n a_{ij} (q_j(t) - q_i(t)), \quad \text{for } t \geq t_c \quad (15)$$

$$w_i(t) = \frac{q_i(t)}{z_{i,1}(t)}, \quad \text{for } t \geq t_c \quad (16)$$

where $q_i \in \mathbb{R}$, $w_i \in \mathbb{R}$ and t_c is the time that all agents converge to OS x^* . In this algorithm, initial conditions for variables $q_i(t)$ are chosen as $q_i(t_c) = f_i(x_i(t_c))$. It should be mentioned that $f_i(x_i(t_c)) = f_i(x^*)$.

It is important to define a method for each agent to calculate the time t_c based on the local information. For each agent, this method is defined as follows:

$$\text{if } \begin{cases} \sum_{j=1}^n a_{ij} (x_j(t_k) - x_i(t_k)) \leq \varepsilon \\ \& \\ x_i(t_k) - x_i(t_{k-1}) \leq \varepsilon \end{cases} \Rightarrow t_k = t_c \quad (17)$$

where ε is a very small positive constant.

Remark 3. It should be noted that at time t_c the differences between the variable $x_i(t)$ and the optimization variable of its neighbors are zero and the value of the variable $x_i(t)$ does not change because it has been converged to the OS. Therefore, in (17), the value of constant ε should be considered zero and inequalities should be replaced by equalities, but due to the computational errors in the simulation software and the communication noise in the practical implementation, the parameter ε is assumed to be a very small positive constant. If the constant ε is selected smaller, then the proposed algorithm has a higher accuracy. For example, $\varepsilon = 10^{-5}$ is a good choice for the simulation.

Theorem 2. Under Assumption 1, the optimization algorithm defined in (15) and (16) converges to the OV of the problem defined in (2).

Proof. Based on the first-order consensus algorithm and according to [28], all agents reach the consensus in the second algorithm and $q_i(t)$ for $i = 1, 2, \dots, n$ converges to $\frac{1}{n} \sum_{i=1}^n q_i(t_c)$. As mentioned before, the initial conditions are selected as $q_i(t_c) = f_i(x^*)$. Thus, the consensus value of variables $q_i(t)$ for $i = 1, 2, \dots, n$ is $\frac{1}{n} \sum_{i=1}^n f_i(x^*)$. On the other hand, according to (7), $z_i(t)$ for $i = 1, 2, \dots, n$ reach the consensus with the consensus vector $\frac{1}{n} \sum_{i=1}^n z_i(0)$ where in the first algorithm, initial conditions are chosen as $z_1(0) =$

$\mathbf{1}_N, z_2(0) = \mathbf{0}_N, \dots, z_n(0) = \mathbf{0}_N$. Therefore, $z_i(t)$ for $i = 1, 2, \dots, n$ converges to $\frac{1}{n} \times \mathbf{1}_N$ or in other words, the consensus value for $z_{i,1}(t)$ is $\frac{1}{n}$. Finally, according to (16), parameters $w_i(t)$ for $i = 1, 2, \dots, n$ converges to $\sum_{i=1}^n f_i(x^*)$. Hence, it is proved that in the second algorithm, all agents reach the OV.

Remark 4. Inspired by [23], by changing the coordinate, Theorem 1 can be proved for balanced directed networks. In addition, the proof of Theorem 2 is also true for balanced directed networks. Therefore, under Assumptions 2 and 3, the algorithm presented in this article is effective for directed networks and the simulation outcomes of Example 2 in Section 4 indicate the correctness of this claim.

Remark 5. In [23, 27], the distributed continuous-time OP has been investigated over the undirected graph and the balanced directed graph. The algorithm presented in the mentioned references is the same, but different methods have been used to analyze the convergence of the algorithm. It should be emphasized that the algorithm designed in the mentioned references only calculates the OS, while the offered algorithm in this article has the ability to calculate the OV, too. Therefore, the proposed algorithm in this article has an advantage over the algorithm designed in [23, 27].

Remark 6. In [8], the distributed discrete-time OP has been studied on undirected networks and an algorithm has been presented for calculating the OS and OV. It should be noted that in [8], the OP has been considered as $\min_{x \in \mathbb{R}^N} f(x) = \frac{1}{n} \sum_{i=1}^n f_i(x)$. According to (2), it is clear that the OP considered in this article is more comprehensive.

At the end of this section, a new algorithm is presented in the following (Algorithm 1) by combining the two mentioned algorithms. This algorithm has the ability to calculate the OS and OV.

Algorithm 1. The offered optimization algorithm

1. Each agent initializes the variables $x_i(t)$, $y_i(t)$ and $z_i(t)$.
2. Each agent updates the optimization variable $x_i(t)$ by (5).
3. Each agent updates the variable $y_i(t)$ by (6).
4. Each agent updates the variable $z_i(t)$ by (7).
5. Each agent evaluates the condition (17)1 until this condition is satisfied.
6. **if** $t \geq t_c$, **then**
7. Each agent updates the variable $q_i(t)$ by (15).
8. Each agent calculates the variable $w_i(t)$ by (16).
9. **end if.**

4. NUMERICAL SIMULATION

In this section, two numerical examples are simulated by MATLAB software and the outcomes of simulation are given to show the ability of the offered algorithm in the distributed

continuous-time convex optimization on undirected and balanced directed graphs.

Example 1. For wireless-sensor networks, a distributed parameter estimation problem is considered as a numerical example. For a sensor network, the parameter estimation problem is defined as [8]

$$\min_{x \in \mathbb{R}} f(x) = \sum_{i=1}^{10} \frac{|x - v_i|^2}{10} \quad (18)$$

where $v = [0.1, 0.2, \dots, 1]$. In this example, the OS is $x^* = 0.55$ and the OV is $f^* = 0.0825$. The algorithm parameters are selected as

$$\varpi = 2, \quad \varrho = 4, \quad \varepsilon = 10^{-5} \quad (19)$$

The adjacency matrix is determined as follows:

$$\mathcal{A} = \begin{bmatrix} 0 & 2 & 0 & 0 & 0 & 0 & 0 & 0 & 0 & 0 \\ 2 & 0 & 1 & 0 & 0 & 0 & 0 & 0 & 0 & 0 \\ 0 & 1 & 0 & 3 & 0 & 0 & 0 & 0 & 0 & 0 \\ 0 & 0 & 3 & 0 & 1 & 0 & 0 & 0 & 0 & 0 \\ 0 & 0 & 0 & 1 & 0 & 5 & 0 & 0 & 0 & 0 \\ 0 & 0 & 0 & 0 & 5 & 0 & 1 & 0 & 0 & 0 \\ 0 & 0 & 0 & 0 & 0 & 1 & 0 & 2 & 0 & 0 \\ 0 & 0 & 0 & 0 & 0 & 0 & 2 & 0 & 6 & 0 \\ 0 & 0 & 0 & 0 & 0 & 0 & 0 & 6 & 0 & 1 \\ 0 & 0 & 0 & 0 & 0 & 0 & 0 & 0 & 1 & 0 \end{bmatrix} \quad (20)$$

The simulation outcomes of this example are shown in Figs. 2-4. The variable $x_i(t)$ for all agents is shown in Fig. 2 and the absolute value of convergence errors are shown in Fig. 3. According to Figs. 2 and 3, it is clear that the optimization variable $x_i(t)$ for all agents has been converged to $x^* = 0.55$.

In order to evaluate the offered algorithm, this example is also simulated using the algorithm presented in [27]. Thus, the outcomes of simulation related to the algorithm designed in [27] are shown in Figs. 5 and 6. First of all, it should be noted that the calculation of the OV has not been studied in [27]. Therefore, our offered algorithm has an advantage due to the calculation of the OV. On the other hand, by comparing Figs. 2 and 5, it can be seen that the offered algorithm has a faster rate of convergence than the algorithm designed in [27].

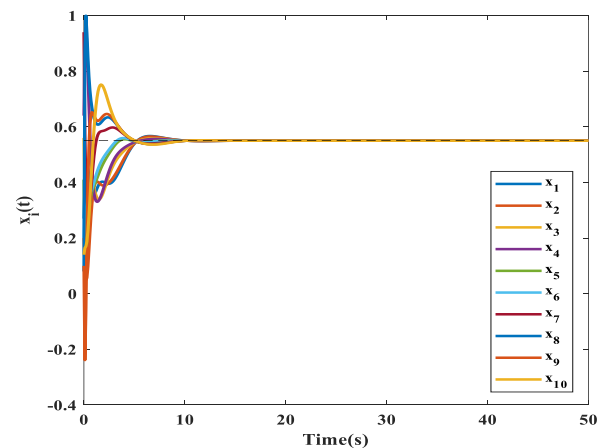


Fig. 2: Trajectories of variable $x_i(t)$.

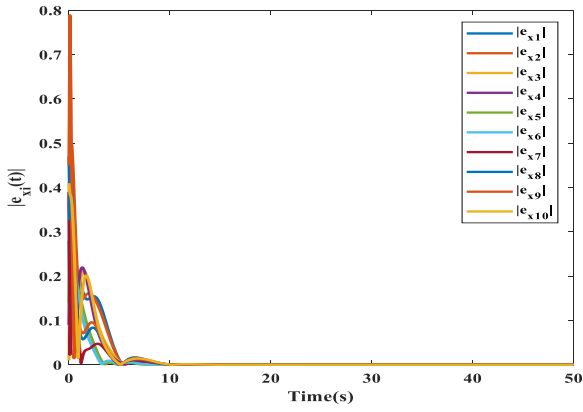


Fig. 3: Convergence errors using the offered algorithm.

In Fig. 4, the OV is shown by the dashed line. As shown in Fig. 4, all the agents have reached a consensus on the OV.

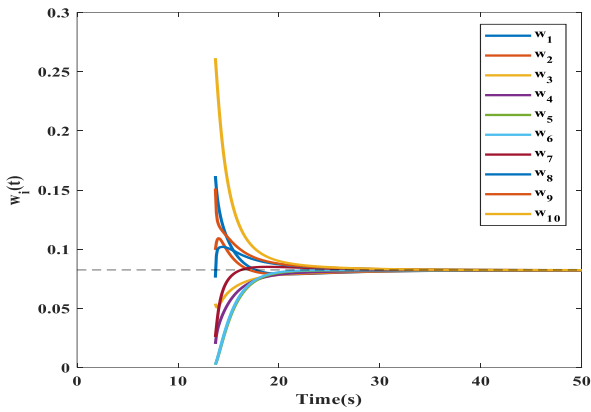


Fig. 4: Trajectories of variable $w_i(t)$.

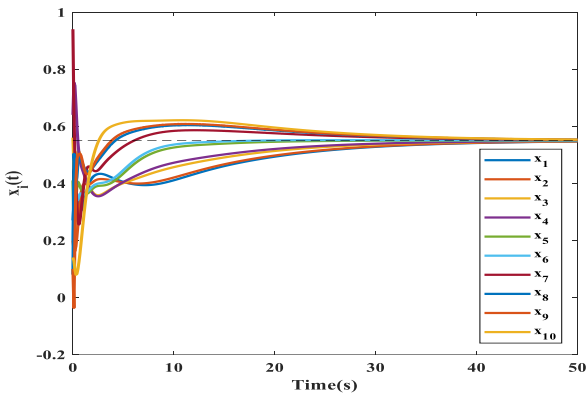


Fig. 5: Trajectories of variable $x_i(t)$ [27].

Example 2. The distributed OP is defined as

$$\min_{x \in \mathbb{R}^N} f(x) = \sum_{i=1}^5 f_i(x) \tag{21}$$

where $f_i(x)$ for $i = 1, 2, \dots, 5$ are given by

$$\begin{aligned} f_1(x) &= x - 2, & f_2(x) &= x^2 + 2, \\ f_3(x) &= (x + 1)^2, & f_4(x) &= 4x^4, \\ f_5(x) &= e^{x-1} \end{aligned} \tag{22}$$

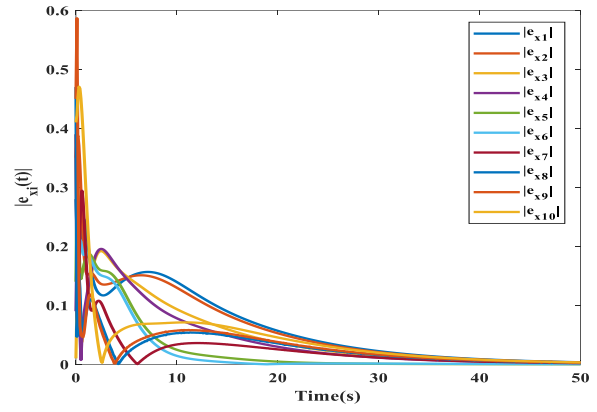


Fig. 6: Convergence errors using the algorithm presented in [27].

The OS and the OV are $x^* = -0.4483$ and $f^* = 0.4536$, respectively. The algorithm parameters are chosen as $\varpi = 3$, $\rho = 2$ and $\varepsilon = 10^{-5}$.

The communication network model is shown in Fig. 7. In Figs. 8-10, the simulation outcomes of this example are shown. In Fig. 8, the optimization variable $x_i(t)$ for all agents is shown and the dashed line shows the OS.

As shown in Fig. 9, the convergence errors for all agents have been converged to zero. In Fig. 10, the variable $w_i(t)$ is shown. It should be noted that the OV is shown by the dashed line in Fig. 10. In Fig. 10, the variable $w_i(t)$ for all agents has been converged to the OV $f^* = 0.4536$.

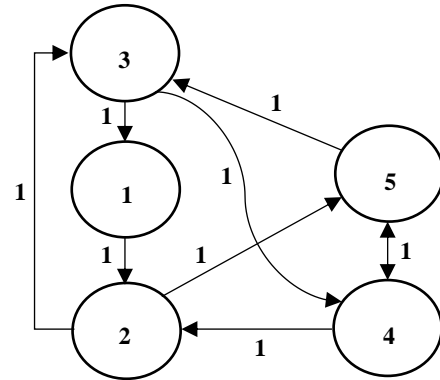


Fig. 7: Communication network model.

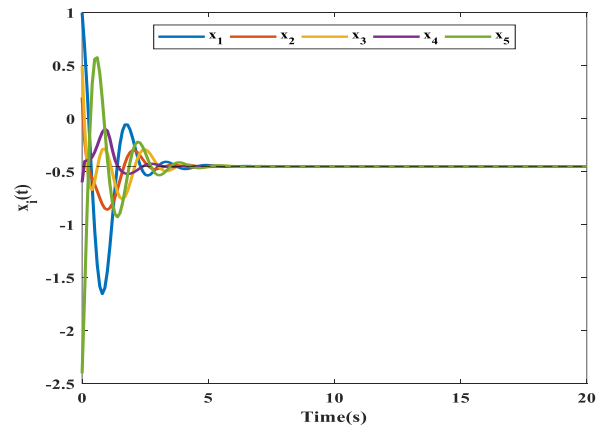


Fig. 8: Trajectories of variable $x_i(t)$.

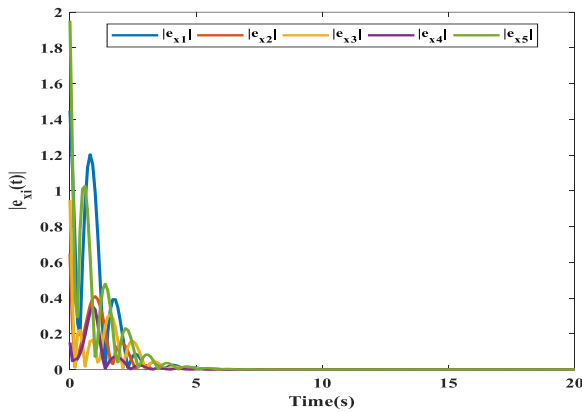


Fig. 9: Convergence errors.

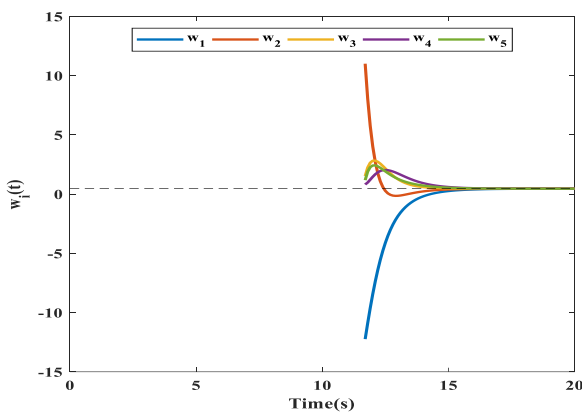


Fig. 10: Trajectories of variable $w_i(t)$.

5. CONCLUSION

The distributed continuous-time convex OP for undirected and directed balanced networks is the main focus of research in this article. Unlike other references, this article tries to address the calculation of OV in the distributed convex OP. By using the concepts of consensus and gradient descent method, a novel algorithm has been proposed to calculate the OS and the OV. The convergence of the offered algorithm to the OS and the OV has been ensured using the Lyapunov theory, LaSalle's invariance principle and average consensus concepts. Compared to the presented results in [27] where OV is not calculated, the offered algorithm has faster convergence for the same example. The convergence time in [27] is 50 seconds and the convergence time of the offered algorithm is about 10 seconds. Eventually, the offered algorithm provides a new perspective for researchers in solving distributed continuous-time convex OPs.

CREDIT AUTHORSHIP CONTRIBUTION STATEMENT

Ehsan Nazemorroaya: Conceptualization, Formal analysis, Investigation, Methodology, Resources, Software, Validation, Visualization, Writing - original draft, Writing - review & editing. **Mohsen Shafieirad:** Methodology, Project administration, Supervision, Validation, Roles/Writing - original draft, Writing - review & editing. **Mahdi Majidi:** Methodology, Project administration, Supervision, Validation, Roles/Writing - original draft, Writing - review & editing. **Mahdieh Adeli:** Methodology, Supervision, Roles/Writing - original draft, Writing - review & editing.

DECLARATION OF COMPETING INTEREST

The authors declare that they have no known competing financial interests or personal relationships that could have appeared to influence the work reported in this paper. The ethical issues; including plagiarism, informed consent, misconduct, data fabrication and/or falsification, double publication and/or submission, redundancy has been completely observed by the authors.

REFERENCES

- [1] E. Nazemorroaya, and M. Hashemi, "Adaptive sliding mode controller design for the bipartite consensus tracking of multi-agent systems with actuator faults and disturbances," *International Journal of Automation and Control*, vol. 16, no. 3-4, pp. 288-302, 2022.
- [2] E. Nazemorroaya, M. Shafieirad, and S. A. Zahiripour, "Mean square consensus of heterogeneous multi-agent systems in the presence of actuator faults," *Transactions of the Institute of Measurement and Control*, vol. 45, no. 6, pp. 1158-1168, 2023.
- [3] A. H. A. Mehra, M. Shafieirad, and I. Zamani, "Leader-following consensus considering effects of agents on each other via impulsive control: A topology dependent average dwell time approach," *Journal of the Franklin Institute*, vol. 359, no. 16, pp. 8639-8668, 2022.
- [4] F. Azadmanesh, and R. Ghasemi, "Different Types of Distributed Optimal Leader-Follower Consensus Protocol Design for a Class of High-Order Multi-Agent Systems," *Journal of Applied Research in Electrical Engineering*, 2023.
- [5] R. Olfati-Saber, J. A. Fax, and R. M. Murray, "Consensus and cooperation in networked multi-agent systems," *Proceedings of the IEEE*, vol. 95, no. 1, pp. 215-233, 2007.
- [6] M. Adeli, M. Hajatipour, M. J. Yazdanpanah, M. Shafieirad, and H. Hashemi Dezaki, "Distributed trust-based unscented Kalman filter for non-linear state estimation under cyber-attacks: The application of manoeuvring target tracking over wireless sensor networks," *IET Control Theory & Applications*, vol. 15, no. 15, pp. 1987-1998, 2021.
- [7] W. Zou, Z. Xiang, and C. K. Ahn, "Mean square leader-following consensus of second-order nonlinear multiagent systems with noises and unmodeled dynamics," *IEEE Transactions on Systems, Man, and Cybernetics: Systems*, vol. 49, no. 12, pp. 2478-2486, 2018.
- [8] H. Li, H. Zhang, Z. Wang, Y. Zhu, and Q. Han, "Distributed consensus-based multi-agent convex optimization via gradient tracking technique," *Journal of the Franklin Institute*, vol. 356, no. 6, pp. 3733-3761, 2019.
- [9] A. Nedić and A. Olshevsky, "Distributed optimization over time-varying directed graphs," *IEEE Transactions on Automatic Control*, vol. 60, no. 3, pp. 601-615, 2014.
- [10] G. Qu and N. Li, "Harnessing smoothness to accelerate distributed optimization," *IEEE Transactions on*

- Control of Network Systems*, vol. 5, no. 3, pp. 1245-1260, 2017.
- [11] M. Al-Saffar, and P. Musilek, "Distributed optimization for distribution grids with stochastic der using multi-agent deep reinforcement learning," *IEEE Access*, vol. 9, pp. 63059-63072, 2021.
- [12] X. Chang, Y. Xu, H. Sun, and I. Khan, "A distributed robust optimization approach for the economic dispatch of flexible resources," *International Journal of Electrical Power & Energy Systems*, vol. 124, p. 106360, 2021.
- [13] N. Mezhoud, and M. Amarouyache, "Multi-Objective optimal power flow based combined non-convex economic dispatch with valve-point effects and emission using gravitation search algorithm," *Journal of Applied Research in Electrical Engineering*, vol. 2, no. 1, pp. 26-36, 2023.
- [14] S. Samarakoon, M. Bennis, W. Saad, and M. Debbah, "Distributed federated learning for ultra-reliable low-latency vehicular communications," *IEEE Transactions on Communications*, vol. 68, no. 2, pp. 1146-1159, 2019.
- [15] L. Liu and J. Shan, "Distributed formation control of networked Euler-Lagrange systems with fault diagnosis," *Journal of the Franklin Institute*, vol. 352, no. 3, pp. 952-973, 2015.
- [16] E. Twumasi, Y. S. Abdul-Fatawu, and E. A. Frimpong, "Optimal sizing and placement of series capacitors in distribution networks using modified elephant herding optimization algorithm," *Journal of Applied Research in Electrical Engineering*, 2023.
- [17] N. Song *et al.*, "Design and optimization of halbach permanent magnet array with rectangle section and trapezoid section," *International Journal of Engineering*, vol. 34, no. 11, pp. 2379-2386, 2021.
- [18] P. Maghzi, M. Mohammadi, S. Pasandideh, and B. Naderi, "Operating room scheduling optimization based on a fuzzy uncertainty approach and metaheuristic algorithms," *International Journal of Engineering*, vol. 35, no. 2, pp. 258-275, 2022.
- [19] C. Gu, L. Jiang, J. Li, and Z. Wu, "Privacy-Preserving dual stochastic push-sum algorithm for distributed constrained optimization," *Journal of Optimization Theory and Applications*, vol. 197, no. 1, pp. 22-50, 2023.
- [20] K. Scaman, F. Bach, S. Bubeck, Y. T. Lee, and L. Massoulié, "Optimal convergence rates for convex distributed optimization in networks," *Journal of Machine Learning Research*, vol. 20, pp. 1-31, 2019.
- [21] S. Pu, W. Shi, J. Xu, and A. Nedić, "Push-pull gradient methods for distributed optimization in networks," *IEEE Transactions on Automatic Control*, vol. 66, no. 1, pp. 1-16, 2020.
- [22] J. Zhang and K. You, "AsySPA: An exact asynchronous algorithm for convex optimization over digraphs," *IEEE Transactions on Automatic Control*, vol. 65, no. 6, pp. 2494-2509, 2019.
- [23] B. Gharesifard and J. Cortés, "Distributed continuous-time convex optimization on weight-balanced digraphs," *IEEE Transactions on Automatic Control*, vol. 59, no. 3, pp. 781-786, 2013.
- [24] Z. Li, Z. Wu, Z. Li, and Z. Ding, "Distributed optimal coordination for heterogeneous linear multiagent systems with event-triggered mechanisms," *IEEE Transactions on Automatic Control*, vol. 65, no. 4, pp. 1763-1770, 2019.
- [25] X. Shi, Z. Lin, R. Zheng, and X. Wang, "Distributed dynamic event-triggered algorithm with positive minimum inter-event time for convex optimisation problem," *International Journal of Control*, vol. 95, no. 5, pp. 1363-1370, 2022.
- [26] E. Nazemorroaya, M. Shafieirad, and M. Majidi, "Consensus-based algorithm for distributed convex optimization," in *Proc. 4th Conference on Computational Algebra, Computational Number Theory and Applications*, 2023.
- [27] S. Liang and G. Yin, "Exponential convergence of distributed primal-dual convex optimization algorithm without strong convexity," *Automatica*, vol. 105, pp. 298-306, 2019.
- [28] F. L. Lewis, H. Zhang, K. Hengster-Movric, and A. Das, *Cooperative control of multi-agent systems: optimal and adaptive design approaches*. Springer Science & Business Media, 2013.
- [29] X. Meng and Q. Liu, "A consensus algorithm based on multi-agent system with state noise and gradient disturbance for distributed convex optimization," *Neurocomputing*, vol. 519, pp. 148-157, 2023.
- [30] S. P. Boyd and L. Vandenberghe, *Convex optimization*. Cambridge University Press, 2004.

BIOGRAPHY



Ehsan Nazemorroaya was born in Isfahan, Iran, in 1996. He received the B.Sc degree in Electrical Engineering from the Department of Electrical Engineering, Arak University of Technology, Arak, Iran, in 2018. Also, he received the M.Sc. degree in Electrical Engineering from the Department of Electrical Engineering, Islamic Azad University, Najafabad Branch, Najafabad, Iran, in 2020. Currently, he is a Ph.D. candidate in Electrical Engineering at University of Kashan, Iran. His research interests include multi-agent systems, optimization, fractional-order systems, adaptive control, and stochastic systems. (Email: ehsan.nzm74@gmail.com)



Mohsen Shafieirad received a B.Sc. degree in control engineering from Isfahan University of Technology, Iran, in 2005. Also, he received the M.S. and Ph.D. degrees in control engineering from Amirkabir University of Technology, Iran, in 2007 and 2013, respectively. He is currently an assistant professor of Control at the University of Kashan,

Iran. M.Shafieirad overall research output has culminated in more than 50 publications. His research interests include multi-agent systems, biological systems, system identification, ad-hoc/sensor networks, and multi-dimensional systems. (Email: m.shafieirad@kashanu.ac.ir)



Mahdi Majidi received the B.Sc. degree in electrical engineering from Isfahan University of Technology, Isfahan, Iran, in 2004, and the M.S. and Ph.D. degrees in electrical engineering from Amirkabir University of Technology (Tehran Polytechnic), Tehran, Iran, in 2007 and 2014, respectively. In 2012, he joined the Communications and Networks

Laboratory, Department of Electrical and Computer

Engineering, National University of Singapore (NUS), Singapore, as a Visiting Ph.D. Student. In 2015, he worked as a researcher at the Iran Telecommunication Research Center (ITRC). Since 2016, he is an assistant professor of the Department of Electrical and Computer Engineering, University of Kashan, Iran. Also, since 2023, he works as a senior communication system designer for the Qualinx BV in Netherlands. His research interests include numerical and analytical optimization methods, Intelligent reflecting surfaces, machine learning, wireless transceiver design, LPWAN, and GNSS. (Email: m.majidi@kashanu.ac.ir)



Mahdiah Adeli received the B.Sc. and M.S. degrees in control engineering from Imam Khomeini International University, Iran, in 2008 and 2012, respectively. Also, she received a Ph.D. degree in control engineering from Kashan University, Iran, in 2022. She is currently an assistant professor of Control at the Kermanshah University of

Technology, Iran. Her research interests include optimization, cyber-physical systems, and distributed estimation. (Email: m.adeli@kut.ac.ir)

Copyrights

© 2024 Licensee Shahid Chamran University of Ahvaz, Ahvaz, Iran. This article is an open-access article distributed under the terms and conditions of the Creative Commons Attribution –NonCommercial 4.0 International (CC BY-NC 4.0) License (<http://creativecommons.org/licenses/by-nc/4.0/>).

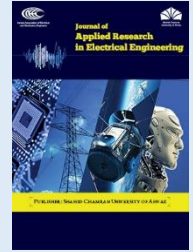


Shahid Chamran
University of AhvazIranian Association of
Electrical and Electronics
Engineers

Journal of Applied Research in Electrical Engineering

E-ISSN: 2783-2864

P-ISSN: 2717-414X

Homepage: <https://jaree.scu.ac.ir/>

Research Article

Improvement of IBC-SHJ Solar Cell Efficiency Based on Back Contacts Geometry Engineering

Pegah Paknazar, Maryam Shakiba^{*}, and Gholamreza Shaloo

Department of Electrical and Computer Engineering, Jundi-Shapur University of Technology, Dezful, Iran

* Corresponding Author: shakiba@jsu.ac.ir

Abstract: In this study, the effect of the width of the n- and p-strips and gap between the electrodes on output characteristics of the IBC-SHJ solar cell, including short-circuit current density, open-circuit voltage, fill factor, and efficiency, was investigated using Silvaco ATHENA and ATLAS simulation software. In this regard, the efficiency of the IBC-SHJ solar cell was improved by developing the geometry of the back contacts. The values for the short-circuit current density, open-circuit voltage, fill factor, and efficiency of the solar cell were analysed using physical phenomena and the distribution of the electric field and electric potential for the aforementioned parameters. The results have shown that the width of the n- and p-strips is one of the most effective parameters for improving the efficiency. Moreover, a maximum efficiency of 23.52% was achieved for IBC-SHJ with improved solar cell parameters, focusing on the elimination of additional ARCs and greater structural periodicity. Thus, a simple structure with no complexity in the fabrication process is proposed. The results show that the best width of the p-strip, n-strip, and gap between the electrodes is 400 μm , 80 μm , and 30 μm , respectively, to achieve improved efficiency.

Keywords: Back contacts geometry engineering, p-strip width, n-strip width, gap width, IBC-SHJ solar cell, cell efficiency

Article history

Received 14 April 2024; Revised 22 August 2024; Accepted 06 September 2024; Published online 23 October 2024.

© 2024 Published by Shahid Chamran University of Ahvaz & Iranian Association of Electrical and Electronics Engineers (IAEEE)

How to cite this article

P. Paknazar, M. Shakiba, and G. Shaloo, "Improvement of IBC-SHJ solar cell efficiency based on back contacts geometry engineering," *J. Appl. Res. Electr. Eng.*, vol. 3, no. 1, pp. 83-89, 2024.

DOI: [10.22055/jaree.2024.46609.1115](https://doi.org/10.22055/jaree.2024.46609.1115)



1. INTRODUCTION

The main renewable energy sources such as wind and solar energy are not only abundant and affordable, but are also considered a suitable alternative to fossil fuels. Among the renewable energy sources, solar energy has a high potential to be converted into other types of energy [1-3]. So far, much research has been done to increase the efficiency of silicon solar cells with the common finger contact structure [4-5]. In recent years, the design of the contact geometry of the cell has been one of the areas of interest for researchers to achieve optimal efficiency [6-7]. One of the most important structures presented in this field is the silicon heterojunction solar cell with interdigitated back contacts [7]. The fact that all contacts are arranged behind the cell eliminates the shadow effect and increases the short-circuit current [8]. In addition, the use of the heterojunction structure leads to an increase in the open circuit voltage due to the use of the intrinsic hydrogenated a-Si buffer layer [8]. Over the past 10 years, research has been conducted to increase the efficiency of IBC-SHJ cells. In 2013, Silvaco presented the IBC-SHJ cell with an efficiency

of 20.43% [8]. In 2016, M. Belarbi et. al. achieved an efficiency of 23.20% by improving the cell deposition parameters [9]. Taking into account a periodicity of the IBC-SHJ structure and simultaneously adding further layers and anti-reflective coatings with textured structures on the front side as well as the use of TCO layers in the rear part of the cell, an efficiency of 27.41% was achieved by J. Bao et. al. in 2020 [10]. The removal of the amorphous silicon layers and the use of a silver contact in addition to the aluminium contact for increase the cell current, modelling two samples of IBC solar cells including planar and pyramidal textured ones, with a focus on optimizing the texturing of the front surface. In [11], A. R. M. Rais et. al. reported that the efficiency of planar and pyramidal textured solar cells were 22.36% and 23.31%, respectively [11]. However, it should be noted that the increase in efficiency in the studies [10] and [11] requires an increase in the complexity of the structure, the manufacturing cost due to the use of silver contacts and thus an increase in the challenges of the manufacturing process. In this research work, the aim is to design and simulate an improved silicon heterojunction solar cell with

interdigitated back contacts, which has the simplest structure compared to other research works and also has the least fabrication challenges. In fact, the efficiency of the IBC-SHJ solar cells have been improved by developing the geometry of the back contacts. In this regard, the effect of the width of the n- and p-strip and gap between the electrodes on the output characteristics of the IBC-SHJ solar cell including J_{sc} , V_{oc} , FF and E_{ff} have been investigated. To model the IBC-SHJ solar cell, ATHENA and ATLAS toolboxes have been used, respectively, to deposit different layers of the cell and simulate its electrical behavior in Silvaco software. To increase the accuracy of the simulation of the structure, the trap levels of the amorphous silicon layers have been modelled. MATLAB software was also used to draw the diagrams as accurately as possible. In the second part of this research, the analysis of the electric field distribution and its effect on the charge carrier transport in the IBC-SHJ cell is presented. In the third part, the mathematical relationships that determine the density of states (DOS) model and the particle transport have been investigated. In the fourth part, the effect of the width of the n- and p-strip and gap between the electrodes on the output characteristics of the IBC-SHJ solar cell including J_{sc} , V_{oc} , FF and E_{ff} have been investigated. In addition, the results were compared with those of previous studies. In the fifth section, the main results of the proposed IBC-SHJ cell structure are presented.

2. ANALYSIS OF ELECTRIC FIELD DISTRIBUTION AND ITS EFFECT ON CARRIER TRANSPORT

To create anode and cathode electrodes, a structure of n-type and p-type layers of hydrogenated a-Si is deposited on the back side of the IBC-SHJ cell so that the layers are one in between. Depending on the doping concentration of the c-Si substrate, these n- and p-type layers play the role of the emitter or the back surface field (BSF). As shown in Figure 1, the width of the elementary structure (pitch) of the cell is equal to the distance between the opposing electrodes, taking into account the gap between them. It is possible to create the periodicity in more complex structures, which of course poses more challenges in fabrication. In this research, the dimensions and the type of materials used in the different layers have been selected according to the criterion of reproducibility, so that the simulation results can contribute to the improvement of the fabrication process [12].

It is worth noting that in Fig. 1, the thickness of SiN_x , n-type c-Si, defective c-Si, i-a-Si, emitter/a-Si, BSF/a-Si, and electrode/Al layers are 75 nm, 150 μm , 1 nm, 6 nm, 20 nm, 20 nm, 0.2 μm , respectively. Moreover, the optimal doping concentration of the emitter and BSF regions is $2 \times 10^{19} \text{ cm}^{-3}$ and $4.3 \times 10^{18} \text{ cm}^{-3}$, respectively. The substrate used to improve deposition parameters is an n-type c-Si wafer with a thickness of 300 μm and a width of 1750 μm , which is equivalent to one cell pitch. The resistivity of the substrate is equal to 2 $\Omega \cdot cm$.

Also, using n-type c-Si substrate will lead to an increase in V_{oc} as a result of increasing efficiency [13, 14]. On the front surface of the cell, a SiN_x layer with a thickness of 75 nm has been used as an anti-reflection coating, for this purpose, the physical model of concentration mobility (CONMOB) has been used in the simulation [15-17]. Therefore, due to not

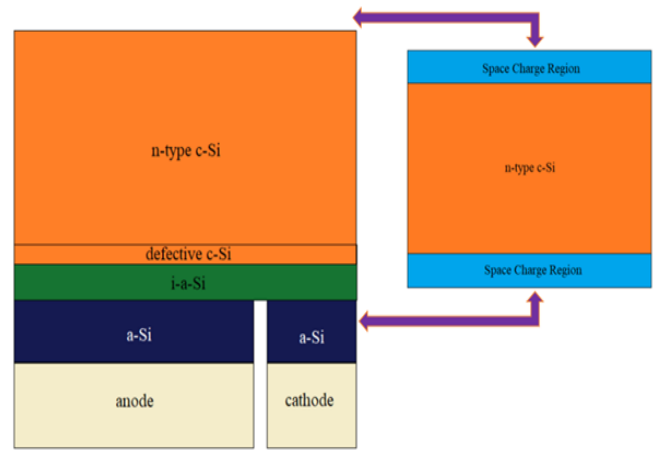


Fig. 1: Schematic of the simulated IBC-SHJ structure along with the approximated regions of space charge in the upper and lower areas of the cell .

choosing the same type of impurity for ARC layers and c-Si substrate, the existence of an electric field on the top of the cell that leads to more drift of the photocarriers and prevents their recombination will be inevitable. According to Figure 1, the presence of anti-reflection coating with the opposite doping concentration of the substrate leads to the creation of a space charge region in the front part of the cell. The internal electric field created in this space charge region will prevent the recombination of the generated photocarriers and move them towards the back contacts of the cell. Also, near the back contacts, due to the presence of the back p-n junction, another space charge region is created, which facilitates the drift of the electron and hole carriers towards the electrode of the same name, and by preventing the recombination of photocarriers, it will increase the photocurrent of the cell.

As shown in Fig. 2, the distribution of electric field and potential at the rear of back contact prevent the recombination of photocarriers. In fact, the design of two space charge areas in the upper and lower parts of the cell, in addition to preventing the recombination of photocarriers, leads to drift them towards the interdigitated back contacts.

Consideration of electric field distribution of IBC-SHJ solar cell structure is so important. In the front part of the cell where there is the maximum photo generation rate, the electric field increases so that the photocarriers are separated and reach the back contacts with the lowest recombination rate. Also, the electric field reaches its maximum value near the back contacts; because in this part of the structure, the amount of carrier collection in metal contacts must reach its highest value. Therefore, the electric field must be large enough to collect more photocarriers at the metal contacts by separating them as much as possible.

3. PHYSICAL MODELS AND EQUATIONS USED IN SIMULATION

3.1. Physical Models

In order to match the numerical modelling and experimental results as much as possible, in this research, we have tried to use accurate physical models to describe the behaviour of IBC-SHJ cells. In this regard, the band gap

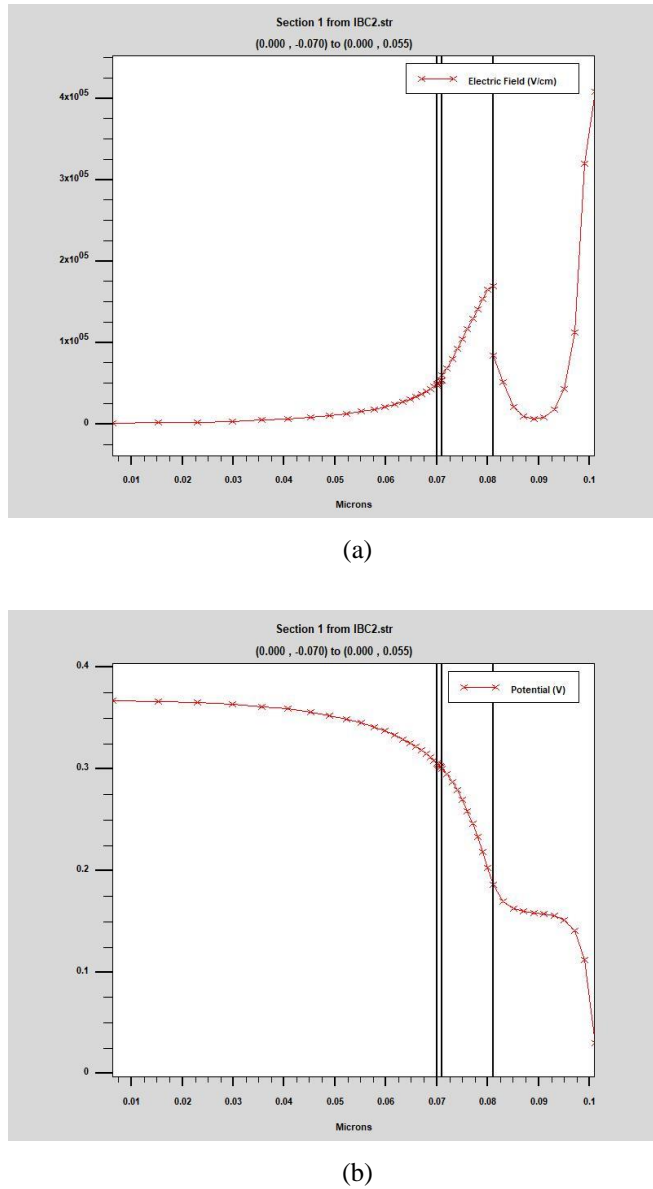


Fig. 2: (a) Electric field distribution, and (b) Electric potential distribution of space charge region at the rear of back contacts.

narrowing (BGN) model has been used to reduce the energy gap [8]. In fact, the narrowing of the band gap shows how applying a high doping concentration (greater than 10^{18} cm^{-3}) changes the band gap by reducing the energy of the conduction band and increasing the energy of the valence band [8]. On the other hand, in order to model different recombination mechanisms, Fermi, Shockley-Read-Hall (SRH), Auger and surface recombination models are also included in the simulation. Meanwhile, carrier recombination is also modelled as a function of doping concentration via SRH and Auger mechanisms [18-20].

Disordered materials such as amorphous silicon contain a large amount of defect states in their energy band gap. Therefore, the density of state (DOS) model in the energy bandgap is used to model amorphous silicon devices. The density model of the defect states is described as a combination of the tail of the band using the exponential decay function and the mid of the band using the Gaussian distribution function. It is assumed that the total density of states, $g(E)$, is composed of four bands: two tail bands (a

donor-like valence band and an acceptor-like conduction band) and two deep level bands (one acceptor-like and the other donor-like) which are modelled using a Gaussian distribution. $g(E)$ is modeled according to (1) [8]:

$$g(E) = g_{TA}(E) + g_{TD}(E) + g_{GA}(E) + g_{GD}(E) \quad (1)$$

In (1), E is the trap energy, E_C is the conduction band energy, E_V is the valence band energy and the subscripts (T, G, A, D) stand for tail, Gaussian (deep level), acceptor and donor states respectively. The components of $g(E)$ are defined as follows [15]:

$$g_{TA}(E) = N_{TA} \exp\left[\frac{E-E_C}{W_{TA}}\right] \quad (2)$$

$$g_{TD}(E) = N_{TD} \exp\left[\frac{E_V-E}{W_{TD}}\right] \quad (3)$$

$$g_{GA}(E) = N_{GA} \exp\left[-\left[\frac{E_{GA}-E}{W_{GA}}\right]^2\right] \quad (4)$$

$$g_{GD}(E) = N_{GD} \exp\left[-\left[\frac{E-E_{GD}}{W_{GD}}\right]^2\right] \quad (5)$$

For an exponential tail distribution, the DOS is described by its conduction and valence band edge intercept densities (N_{TA} and N_{TD}), and by its characteristic decay energy (W_{TA} and W_{TD}). For Gaussian distributions, the DOS is described by its total density of states (N_{GA} and N_{GD}), its characteristic decay energy (W_{GA} and W_{GD}), and its peak energy distribution (E_{GA} and E_{GD}). The energy distribution of exponential band tail and Gaussian distribution of trap states in the middle of the energy gap are key parameters for high accuracy simulation.

For the c-Si/a-Si interface on the back surface, the thermionic emission model has been used, in which the distribution function of the defect states at the interface of two layers, one for holes and the other for electrons, is modeled. In order to model the interface between the defects-free crystalline silicon layer and the amorphous silicon layer as much as possible, a defective c-Si thin layer has been used between the two layers [15]. The Sopra database is also used for the refractive index of a-Si layers [21, 22]. AM1.5G solar spectrum has been used to simulate sunlight in standard conditions with a light intensity of 1000 W/m^2 and a temperature of 26°C .

3.2. Equations of Carrier Transport

The specialized software used in this research to design and simulation the IBC-SHJ solar cell is Silvaco software. The Athena tool in this software models and simulates the fabrication process in the Monte Carlo method and in conditions very similar to the new technologies presented in the field of semiconductor devices fabrication. In addition, the Atlas tool simulates the electrical behaviour of cell designed in Athena. It uses the drift-diffusion model based on the discretization of differential equations and solving equations using numerical solutions such as Gumel, Newton-Raphson and Block methods. Output characteristics extracted from Atlas tool are Fill Factor (FF) and Efficiency (η) obtained from (6) and (7), respectively [15, 19]:

$$FF = \frac{V_{mpp} I_{mpp}}{V_{oc} I_{sc}} \quad (6)$$

$$\eta = \frac{P_{out}}{P_{in}} = \frac{V_{oc} I_{sc} FF}{P_{light}} \quad (7)$$

In (6), V_{mpp} and I_{mpp} represent the voltage and current at the maximum power point, respectively.

Three sets of basic equations are used to simulate the solar cell in the Silvaco software based on the drift-diffusion model. These equations are: Poisson's equation, carrier's continuity equations and transport (current) equations. Poisson's equation specifies the relationship between electrostatic potential (ψ) and the space charge density (ρ) and is expressed as follows [19]:

$$\text{div}(\epsilon \nabla \psi) = -\rho \quad (8)$$

In (8), ϵ is the permeability coefficient of the environment. The local space charge density represents carriers (electrons and holes) and ionized impurities. On the other hand, carriers continuity equations specify the gradient of electron and hole carriers in terms of time and are defined as follows [8]:

$$\frac{\partial n}{\partial t} = \frac{1}{q} \text{div} \vec{J}_n + G_n - R_n \quad (9)$$

$$\frac{\partial p}{\partial t} = -\frac{1}{q} \text{div} \vec{J}_p + G_p - R_p \quad (10)$$

In (9) and (10), n and p are electrons and holes concentration respectively. J Indicates the current density, G indicates the photo generation rate and R indicates the recombination rate for the respective carriers. Electric charge is also represented by q . Also, the transport equations that determine the gradient of electron and hole carriers in terms of location and are defined as follows [15]:

$$\vec{J}_n = q\mu_n nE + qD_n \nabla n(x) \quad (11)$$

$$\vec{J}_p = q\mu_p pE - qD_p \nabla p(x) \quad (12)$$

In (11) and (12), μ_n and μ_p are electron and hole mobilities, respectively, E is electric field and D_n and D_p are electrons and holes diffusion coefficients, respectively.

3.3. Ray Tracing

Ray tracing is one of the simplest models of optical simulation. In this study, the ray tracing optical model has also been employed. This optical model primarily disregards the wave nature of light and traces direct paths towards rays passing through boundaries. Reflected and transmitted components are calculated based on the Fresnel equations, and incoming rays at each boundary are divided into two parts. Following these steps, the system traces the trajectories of both these rays. The simplified Fresnel equations with Snell's laws are as follows:

$$r_p = -\frac{\tan(\theta_i - \theta_t)}{\tan(\theta_i + \theta_t)} \quad (13)$$

$$t_p = \frac{2 \sin \theta_t \cos \theta_i}{\sin(\theta_i + \theta_t) \cos(\theta_i - \theta_t)} \quad (14)$$

$$r_s = -\frac{\sin(\theta_i - \theta_t)}{\sin(\theta_i + \theta_t)} \quad (15)$$

$$t_s = \frac{2 \sin \theta_t \cos \theta_i}{\sin(\theta_i + \theta_t)} \quad (16)$$

In the equations for r_p and r_s , representing the reflection of p- and s-polarized rays, t_p and t_s indicate the transmission of p- and s-polarized rays, respectively. θ_i and θ_t denote the angles of incidence and transmission with respect to the surface normal vector. Also, reflecting and refracting rays each present at their respective angles relative to the surface

normal vector. The incident angles are also specified in the equations in this illustration. The refractive index of the upper medium (n_1 , smaller than the refractive index of the lower medium n_2), is such that the refracted ray approaches the normal vector of the boundary.

4. RESULTS AND DISCUSSION

In this research, in order to improve the characteristics of the IBC-SHJ cell, one of the most effective parameter as the width of the n- and p-strip and the gap width between electrodes are improved.

In the following, the influence of the mentioned parameters on the output characteristics of J_{sc} , V_{oc} , FF and Eff is investigated to improve the efficiency of the IBC-SHJ solar cell. It should be noted that to investigate the effect of each parameter, other parameters of the cell are considered constant.

4.1. Effect of p-Strip Width

The J_{sc} , V_{oc} , FF and Eff graphs considered with the change of p-strip width are presented in Fig. 3.

Increasing the width of p-strip, increases the current. But at the same time, it does not have much effect on the voltage. As can be seen in Fig. 3, J_{sc} increases with increasing the p-strip width. Because the width of metal contact is equal to the p-strip. On the other hand increasing the width of metal contact decreases the cell series resistance and thus, increases the cell current. Generally, in the IBC-SHJ structure, the p-strip width is set to be larger than the n-strip width. Holes are the minority carriers of the substrate. By choosing a larger width for the p-strip region, it will be possible to collect more minority carriers in the metal contacts. It significantly reduces the possibility of recombination in the substrate and this leads to an increase the cell current. Meanwhile, V_{oc} increases with increasing the p-strip width. But the voltage increase is very small and insignificant. Increasing the width of p-strip does not have much effect on the voltage. On the other hand, the FF decreases as the p-strip width increases. Because, increasing the width of p-strip, increases I_{sc} . Therefore, according to (6), FF decreases. Also, the efficiency of the cell decreases with the increase of the p-strip width. Considering the simulation, the most optimal value for p-strip width is equal to 400 μm .

4.2. Effect of Gap Width between Electrodes

The width of the gap between the electrodes is one of the key parameters in controlling the current of the cell. Because it can lead to shunting the electrodes if it not adjusted accurately. On the other hand, its excessive increase reduces the photocurrent by reducing the optimal value of the n- and p-strip width and increasing the cell series resistance. Next, the J_{sc} , V_{oc} , FF and Eff graphs considering the change of gap width between the electrodes are presented in Fig. 4. Increasing the gap width between the electrodes leads to decrease the current but does not have a great effect on the voltage. As shown in Fig. 4, J_{sc} decreases with increasing gap width. In fact, the gap region between the electrodes has an important effect on the photocurrent of the cell by influencing the n- and p-strip width. On the other hand, due to the increase in cell resistance, V_{oc} increases with a low slope.

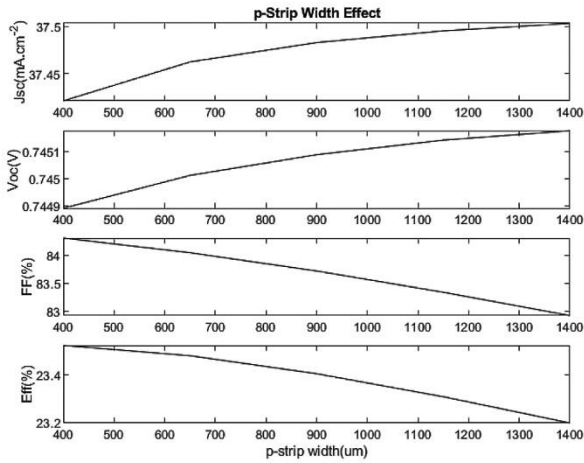


Fig. 3: Effect of p-strip width on J_{sc} , V_{oc} , FF and Eff , the doping concentration of Emitter and BSF regions is equal to $2 \times 10^{19} \text{ cm}^{-3}$ and $4.3 \times 10^{18} \text{ cm}^{-3}$, respectively.

According to Fig. 4, as the gap width increases, I_{sc} increases and thus, FF decreases. Also, cell efficiency decreases. Because the recombination of the minority carriers between the p- and the n-strip increases due to the increase in the lateral distance travelled. In other words, the increase of the gap width corresponds to an additional lateral distance for the minority photocarriers generated in the c-Si substrate and in the upper part of the n-strip. This extra distance increases the probability of recombination before reaching the p-strip. In addition, by increasing the width of the gap between the electrodes, the possibility of recombination at the interface between the c-Si substrate and the gap region increases. Therefore, according to all reasons mentioned above, the gap width should be set as low as possible to obtain the optimal value for cell efficiency. As a result, the most optimal value for the gap width equal to $30 \mu\text{m}$ is obtained.

4.3. Effect of n-Strip Width

The J_{sc} , V_{oc} , FF and Eff graphs with changing the n-strip width are presented in Fig. 5. Increasing the n-strip width increases the cell current. But it has little effect on the voltage. In this situation, due to the increase of the average lateral distance that the minority carriers must travel to reach the p-strip, J_{sc} decreases and increases the probability of carrier recombination and decreases the cell current. According to the V_{oc} graph, V_{oc} decreases with a small slope. As the n-strip width increases to $580 \mu\text{m}$, FF increases and then decreases. Because its increase up to $580 \mu\text{m}$, increases the I_{mpp} and for more than $580 \mu\text{m}$, J_{sc} increases. Therefore, according to (6), it can be seen that FF increases until reaching a width of $580 \mu\text{m}$ and then decreases from this value. On the other hand, the efficiency decreases with the decrease of J_{sc} . Therefore, the n-strip should be set as low as possible to obtain the best J_{sc} values. In fact, a larger width leads to an increase in series resistance against with the current of majority carriers (electrons). As a result, the most optimal value for the n-strip width is equal to $80 \mu\text{m}$. Therefore, in the proposed IBC-SHJ solar cell, the most improved value for the width of p-strip, gap and n-strip is equal to $400 \mu\text{m}$, $30 \mu\text{m}$ and $80 \mu\text{m}$ respectively. Proposed values of IBC-SHJ cell efficiency at different p-strip, gap, and n-strip widths are given in Tables 1, 2 and 3, respectively. Also in Table 4, the width of p-strip,

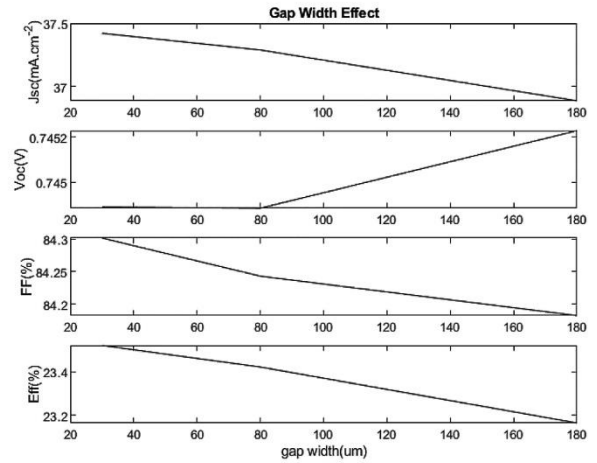


Fig. 4: Effect of gap width on J_{sc} , V_{oc} , FF and Eff , doping concentration of Emitter and BSF regions is equal to $2 \times 10^{19} \text{ cm}^{-3}$ and $4.3 \times 10^{18} \text{ cm}^{-3}$, respectively.

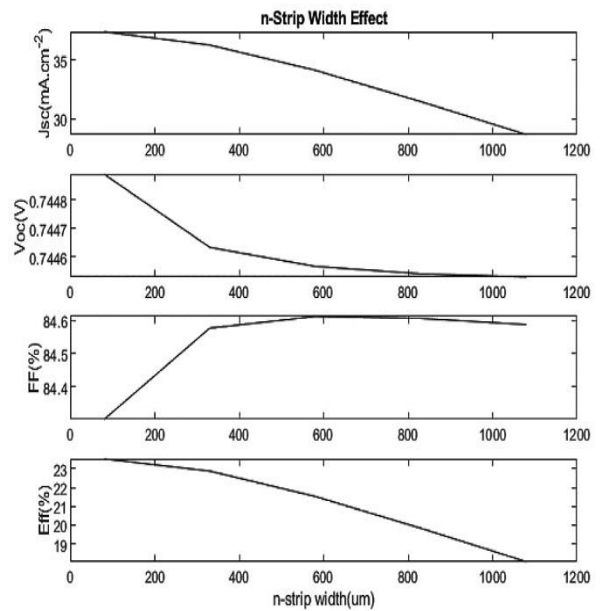


Fig. 5: Effect of n-strip width on J_{sc} , V_{oc} , FF and Eff , doping concentration of Emitter and BSF regions is equal to $2 \times 10^{19} \text{ cm}^{-3}$ and $4.3 \times 10^{18} \text{ cm}^{-3}$, respectively.

gap and n-strip and Efficiency of the proposed IBC-SHJ solar cell compared to previous research.

As mentioned preview and as shown in Table 4, in the proposed IBC-SHJ solar cell, the most improved value for the width of p-strip, gap and n-strip is equal to $400 \mu\text{m}$, $30 \mu\text{m}$ and $80 \mu\text{m}$ respectively. Generally, in the IBC-SHJ structure, the p-strip width is set to be larger than the n-strip width. Because holes are the minority carriers of the substrate then by choosing a larger width for the p-strip region, it will be possible to collect more minority carriers in the metal contacts. It significantly reduces the possibility of recombination in the substrate and this leads to an increase the cell current and cell efficiency. On the other hand, the gap region between the electrodes has an important effect on the photocurrent of the cell by influencing the n- and p-strip width. Because the recombination of the minority carriers

Table 1: IBC-SHJ cell efficiency at different p-strip width.

p-strip width (μm)	Efficiency (%)
400	23.52
650	23.48
900	23.40
1150	23.31
1400	23.20

Table 2: IBC-SHJ cell efficiency at different gap width.

Gap width (μm)	Efficiency (%)
30	23.52
80	23.42
180	23.16

Table 3: IBC-SHJ cell efficiency at different n-strip width.

n-strip width (μm)	Efficiency (%)
80	23.52
330	22.88
580	21.53
830	19.83
1080	18.05

Table 4: The width of p-strip, gap and n-strip and efficiency of the proposed IBC-SHJ solar cell compared with previous structures.

Ref.	Parameters			Efficiency (%)
	p-Strip width (μm)	Gap width (μm)	n-Strip width (μm)	
[8]	1200	50	500	20.43
[9]	950	50	180	23.20
Proposed structure	400	30	80	23.52

between the p- and the n-strip increases due to the increase in the lateral distance travelled. In other words, the increase of the gap width corresponds to an additional lateral distance for the minority photocarriers generated in the c-Si substrate and in the upper part of the n-strip. Finally, increasing the n-strip width, due to the increase of the average lateral distance that the minority carriers must travel to reach the p-strip, J_{sc} decreases and increases the probability of carrier recombination and decreases the cell current. Therefore, the n-strip should be set as low as possible to obtain the best J_{sc} values.

5. CONCLUSION

In this research, one of the most effective parameters for the efficiency of the IBC-SHJ cell was investigated, namely the width of the n- and p-strip and the gap width between the electrodes. Our improved IBC-SHJ solar cell yields a short-circuit current density of 37.42 mA/cm² and an open-circuit voltage of 745 mV with a cell efficiency of 23.52% and a fill factor of 84.30 under AM1.5G without additional ARCs and more structural periodicity. Thus, a simple structure with improved conversion efficiency is proposed. The simulation shows that the efficiency of the cell depends on the width of the p-strip, gap and n-strip, so these parameters can be

improved accordingly. The results show that the optimum width of the p-strip, the gap between the electrodes and the n-strip is 400 μm , 30 μm and 80 μm respectively. The presence of an antireflective coating with the opposite concentration of the substrate, by creating a space charge region and its electric field in the front part of the cell, prevents the photocarriers from recombining and drifts them to the rear contacts of the cell, so that they are collected in the rear contact of the same name due to the existence of the rear p-n junction and the resulting electric field.

CREDIT AUTHORSHIP CONTRIBUTION STATEMENT

Pegah Paknazar: Data curation, Formal analysis, Investigation, Project administration, Resources, Software, Validation, Visualization, Roles/Writing - original draft.
Maryam Shakiba: Conceptualization, Investigation, Methodology, Supervision, Writing - review & editing.
Gholamreza Shaloo: Data curation, Formal analysis, Software, Validation, Visualization.

DECLARATION OF COMPETING INTEREST

The authors declare that they have no known competing financial interests or personal relationships that could have appeared to influence the work reported in this paper. The ethical issues; including plagiarism, informed consent, misconduct, data fabrication and/or falsification, double publication and/or submission, redundancy has been completely observed by the authors. This paper is an extension of the authors' previous work which was presented in the 2024 4th National Conference on Applied Research in Electrical Engineering (AREE2024), and selected as a top paper to be printed in this journal with some extensions.

REFERENCES

- [1] T. Allen, J. Bullock, X. Yang, A. Javey, and S. De Wolf, "Passivating contacts for crystalline silicon solar cells", *Nature Energy*, vol. 4, pp. 914-928, 2019.
- [2] C. N. Kruse *et al.*, "Simulation-based roadmap for the intergration of poly-silicon on oxide contacts into screen-printed crystalline silicon solar cells", *Nature Research*, vol. 11, pp. 996, 2021.
- [3] M. Shakiba, and M. Shakiba, "Role of critical processing parameters on fundamental phenomena and characterizations of DC argon glow discharge", *Optoelectronic Nanostructures*, vol. 7, pp. 67-91, 2022.
- [4] Y. Menni, A. Azzi, and A. J. Chamkha, "A review of solar energy collectors: Models and applications", *Journal of Applied and Computational Mechanics*, vol. 4, no.4, pp. 375-401, 2018.
- [5] V. Giglia, R. Varache, J. Veirman, and E. Fourmond, "Influence of cell edges on the performance of silicon heterojunction solar cells", *Solar Energy Materials and Solar Cells*, vol. 238, article 111605, 2022.
- [6] M. Shakiba, A. Kosarian, and E. Farshidi, "Effects of processing parameters on crystalline structure and optoelectronic behavior of DC sputtered ITO thin film", *Journal of Materials Science: Materials in Electronics*, vol. 28, pp. 787-797, 2016.

- [7] A. Pavlovic, C. Fragassa, M. Bertoldi, and V. Mikhnych, "Thermal behavior of monocrystalline silicon solar cells: A numerical and experimental investigation on the module encapsulation materials", *Journal of Applied and Computational Mechanics*, vol. 7, no. 3, pp. 1847-1855, 2021.
- [8] 2D IBC-SHJ solar cell simulation and optimization, (July 01, 2013). [Online], Available: https://silvaco.com/dynamicweb/jsp/downloads/DownloadDocStepsAction.do?req=download&nm=simstd_Q3_2013_a2.pdf
- [9] M. Belarbi, M. Beghdad, and A. Mekemeche, "Simulation and optimization of n-type interdigitated back contact silicon heterojunction (IBC-SiHJ) solar cell structure using Silvaco Tcad Atlas", *Solar Energy*, vol. 127, pp. 206-215, 2016.
- [10] J. Bao, A. Liu, Y. Lin, and Y. Zhou, "An insight into effect of front surface field on the performance of interdigitated back contact silicon heterojunction solar cells", *Materials Chemistry and Physics*, vol. 255, pp. 123625, 2020.
- [11] A. R. M Rais et al., "Photo-generation profiles in deeply-etched, two-dimensional patterns in interdigitated back contact solar cells", *Journal of Ovonic Research*, vol. 17, pp. 283-289, 2021.
- [12] C. Hollemann et al., "Separating the two polarities of the POLO contacts of an 26.1%-efficient IBC solar cell", *Nature Research*, vol. 10, pp. 658, 2020.
- [13] P. Procel, G. Yang, O. Isabella, and M. Zeman, "Theoretical evaluation of contact stack for high efficiency IBC-SHJ solar cells", *Solar Energy Materials and Solar Cells*, vol. 186, pp. 66-77, 2018.
- [14] A. Kosarian, M. Shakiba, and E. Farshidi. "Role of hydrogen treatment on microstructural and opto-electrical properties of amorphous ITO thin films deposited by reactive gas-timing DC magnetron sputtering". *Journal of Materials Science: Materials in Electronics*, vol. 28, pp. 10525–10534, 2017.
- [15] M. Aurientis, "Interdigitated back contact n-type solar cell with black silicon anti-reflecting layer: simulations and experiments," M.Sc. Thesis, Aalto University, 2014.
- [16] A. Kosarian, M. Shakiba, and E. Farshidi. "Role of sputtering power on the microstructural and electro-optical properties of ITO thin films deposited using DC sputtering technique," *IEEJ Transaction on Electrical and Electronic Engineering*, vol. 13, pp. 27–31, 2018.
- [17] M. Makvandi, M. Javad Maleki, and M. Soroosh, "Compact all-optical encoder based on silicon photonic crystal structure", *Journal of Applied Research in Electrical Engineering*, vol.1, no.1, pp. 1-7, 2022.
- [18] Z. Ahangari, "Performance analysis of a steep-slope bi-channel GaSb-GaAs extended source tunnel field effect transistor with enhanced band-to-band tunneling current", *Journal of Applied Research in Electrical Engineering*, vol. 2, no. 2, pp. 206-213, 2023.
- [19] M. Lu, S. Bowden, and R. Birkmire, "Two dimensional modeling of interdigitated back contact silicon heterojunction solar cells," in *Proc. 2007 International Conference on Numerical Simulation of Optoelectronic Devices*, Newark, USA, 2007, pp. 55-56.
- [20] T. Sawada et al. , "High-efficiency a-Si/c-Si heterojunction solar cell", in *Proc. 1994 IEEE 1st World Conference on Photovoltaic Energy Conversion*, Waikoloa, USA, 1994, pp. 1219–1226.
- [21] K. Yoshikawa et al. , "Silicon heterojunction solar cell with interdigitated back contacts for a photoconversion efficiency", *Nature Energy*, vol. 2, pp. 17032, 2017.
- [22] D. Diouf, J. P Kleider, and C. Longeaud, "Two-dimensional simulations of interdigitated ack contact silicon heterojunctions solar cells", in *Physics and Technology of Amorphous-Crystalline Silicon Heterostructure Solar Cells*, Springer. pp. 483-519, 2011.

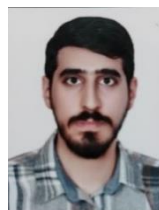
BIOGRAPHY



Pegah Paknazar was born in Dezful, Khuzestan, Iran. She received the master degree in Electrical and electronic engineering with a focus on the field of semiconductor devices from the Jundi-Shapur University of Technology, Dezful, Iran in 2022. Her studies in the master thesis were done on the subject of increasing the efficiency of silicon heterojunction solar cell by designing and adjusting interdigitated back contacts and some of the results obtained in the studies were presented in this paper.



Maryam Shakiba was born in Dezful, Khuzestan, Iran. She received the Ph.D. degree in electronic engineering from the Shahid Chamran University of Ahvaz, in 2015. She is presently an Assistant Professor in electronic engineering in Jundi-Shapur University of Technology, Dezful, Iran. Her research interests include semiconductor electronics, especially amorphous silicon solar cells, intelligent system and analog integrated circuit.

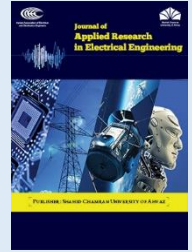


Gholamreza Shaloo was born in Abadan, Iran. He completed his undergraduate education at Isfahan University in Iran in 2020 and his postgraduate education at Jundi-Shapur University of Technology, Dezful, Iran in 2024. His field of study at the graduate level was using intelligent system for modelling semiconductor device. The title of his thesis was modelling of IBC silicon solar cell based on artificial neural network.

Copyrights

© 2024 Licensee Shahid Chamran University of Ahvaz, Ahvaz, Iran. This article is an open-access article distributed under the terms and conditions of the Creative Commons Attribution –NonCommercial 4.0 International (CC BY-NC 4.0) License (<http://creativecommons.org/licenses/by-nc/4.0/>).





Research Article

Demand Response Design for Healthy Operation of Transformers in Heavy-Load and High-Temperature Conditions

Arash Moghadami ¹, Davood Azizian ^{2,*}, and Amin Karimi ¹

¹ Electrical Engineering Department, Sanandaj Branch, Islamic Azad University, Sanandaj, Iran

² Electrical Engineering Department, Abhar Branch, Islamic Azad University, Abhar, Iran

* Corresponding Author: d.azizian@abhariau.ac.ir

Abstract: The healthy operation of high-power transformers plays a crucial role in the reliability of power systems. Given the thermal model of transformers under heavy-load and high-temperature conditions, the hot spot temperature exceeding the maximum allowable value may result in oil dissolution and cascading. This paper uses a thermal model of transformers to analyze the hot spot temperature load level under predicted ambient temperature, which may cross the healthy conditions. Then, an Incentive-Based Demand Response (IBDR) and a thermal model of transformers are used to determine optimal load curtailment. On the other hand, as the paper uses the demand response (DR) for security reasons, the risk of load participation in IBDR programs should be minimized. Hence, a Response Fatigue Index (RFI) is employed to maintain the comfort level of demands participated in DR. Also, the feasible solution area for multi-objective optimization is determined, given costs and RFI, using the sequential solution of a single-objective problem with cost reduction as the objective and RFI as the constraint with different levels of maximum acceptable RFI. The developed model was applied to a real substation in Iran as a test case. The results show that DR can enhance the reliability and life expectancy of the transformer while keeping the comfort level of loads as high as possible.

Keywords: Demand response, hot spot temperature, response fatigue index, transformer thermal model.

Article history

Received 24 January 2024; Revised 12 April 2024; Accepted 03 May 2024; Published online 23 October 2024.

© 2024 Published by Shahid Chamran University of Ahvaz & Iranian Association of Electrical and Electronics Engineers (IAEEE)

How to cite this article

A. Moghadami, D. Azizian, and A. Karimi, "Demand response design for healthy operation of transformers in heavy-load and high-temperature conditions," *J. Appl. Res. Electr. Eng.*, vol. 3, no. 1, pp. 90-98, 2024.

DOI: [10.22055/jaree.2024.45826.1101](https://doi.org/10.22055/jaree.2024.45826.1101)



NOMENCLATURE

Subscripts

<i>Cntrl</i>	Controllable loads
<i>Crit</i>	Critical demand
<i>Degr</i>	Transformer degradation
<i>dissat</i>	Dissatisfaction
<i>WODR</i>	Without DR
<i>Rated</i>	Rated load
<i>amb</i>	Ambient

Indices

<i>i</i>	Controllable loads
<i>T (T)</i>	Time

Variables and parameters

$Cost^{cap}$	Transformer capital cost
--------------	--------------------------

C^d	Transformer degradation cost
Inc	Incentive paid to the load for curtailment
L^T	Transformers' useful life
P	Power
DRF	Demand response fatigue
s	Binary variable of the demand participated in DR
U	Utility function
v	Load insistence parameter
V	Customer's displeasure value
θ	Temperature
θ_o	The increase in top oil temperature compared to the ambient temperature

θ_{ft}	The increase in top oil temperature compared to the ambient temperature at the nominal load
θ_u	The maximum temperature rise of top oil at load K
θ_i	The initial value of temperature rise of top oil at $t = 0$
θ_{amb}	Ambient temperature
T_o	Time constant of transformer oil at rated load
P_{ft}	Total loss at rated load
C	Heat capacity of the transformer
n	Oil exponent
K	Loading ratio
R	The ratio of load losses to no-load losses at rated load

1. INTRODUCTION

1.1. Problem Statement

Power transformers are often the most expensive components in a power distribution system. Their lifetime depends on the conditions of the paper insulation, which deteriorates due to heat loss, and the loss depends on the load speed of the transformer. In unexpected situations, overloads occur in healthy transformers of substations. The acceptable overloads defined by standards [1, 2] are at the expense of the transformer's life. In a heavily used system, contingencies with the overload time are severe, resulting in significant wear and tear of the transformers. Therefore, it is necessary to reduce the overload of transformers to extend their life.

Also, slight Load Factor (LF) and redundancy requirements impair the efficiency of transformers. In fact, transformers are generally designed and operated with a 40-60% nominal load to maintain system reliability at a desired level [3]. Almost one-quarter of distribution system equipment in the United States is operated for only 440 hours at peak loads [4]. Also, as the load increases, it is necessary to upgrade the transformers. The conventional method of system amplification for growing loads has high capital costs [5]. Therefore, applications tend to increase the LF of existing equipment [3]. Based on [6], it can be said that a distribution transformer loses 12-15% due to aging and overload. Therefore, it is necessary to check the basic and essential factors affecting the load, lifetime, and operation of transformers with new methods of monitoring the state of transformers so that by using them, we can use the capacity of network equipment in the best possible way.

1.2. Literature Review

A solution based on fuzzy logic is proposed in [6] to increase the life of distribution transformers. This solution tries to provide a good prediction for transformer loading. Some factors, such as reverse power currents, increase in ambient temperature, and voltage distortion, increase the temperature of the transformer coils, thereby impairing the transformer's performance.

A solution to increase transformers' life is the Demand Response (DR) [7], which is used by changing the load in

smart networks and shows the best performance when the load reaches its maximum. With this method, the efficiency of the transformer increases, and it also saves money in terms of amplifiers. Therefore, the idea of the DR method to extend transformers' life is implemented in the worst conditions by applying maximum heat to the transformer windings before the temperature of the transformer windings rises too high. However, this method is unsuitable for oil temperature and the effects on the transformer. On the other hand, it does not provide a solution for the transformer's life. Smart meters use DR methods to prevent customers' excessive energy demand and reduce the effect of the load on the transformer. These methods provide their management programs based on the clustered data of the smart meters [8].

This method does not provide an idea for changes in ambient temperature, excessive effects caused by overloading, and failure rates. In [9], the researchers conducted various studies of the DR method on the transformer's life, one of which was the hot spot, which was considered a desirable method. However, they did not provide an optimal type of DR. Furthermore, this method fails to track the rise in the failure rate. In fact, the failure rate is important in the reliability assessment of power systems, and a fixed value is currently considered for it. Therefore, this investigation gave acceptable results, but it did not positively affect the accuracy of the failure rate because it did not consider the heterogeneity in the component population. In [10], a risk-based model was investigated, in which the risk caused by different measurements was evaluated to obtain the failure rate in the population. So, 12 power transformers were applied, and the failure rate obtained showed the maintenance performance. These transformers usually had a higher failure rate over a longer period.

Online monitoring, as well as the continuous removal of damage from oil, was used in [11] to increase the transformer's life and efficiency in charging electric vehicles. Transformers, including both medium-pressure and low-pressure ones, have been analyzed by many researchers [12]. In [13], the authors proposed a model to improve the use of transformers by keeping the HST under certain limits using DR.

In [14], the numerical health index of a transformer was calculated based on six components, including insulation resistance, the amount of water, $\tan \delta$, and dissolved gases. These components were combined using a neural network. The results revealed that these six components accurately showed the health status of the transformer. This study did not consider the transformer failure rate index, which is the main reason for replacing the transformer. The authors in [15] presented the health index of the studied 69-kV transformers with the help of gas measurements in oil, oil analysis, and aldehyde analysis in oil. Finally, due to the existing uncertainties, the fuzzy method was used for evaluation, and the calculated index was also fuzzy. In [16], a health index method was provided for transformers using equipment life criteria, equipment loading pattern during its lifetime, periodic service and repairs, internal errors occurring in the equipment history, substation location, transformer manufacturer, winding insulation test, the amount of water in the oil, insulating strength, analysis of gases in the oil, the resistance of the coils, and the power factor of the coil.

In [17], indicators such as insulation resistance, inspection and routine testing of power transformers, thermographic analyses, oil quality, analysis of undissolved gases in the oil, periodic testing and inspection of tap changer, $\tan \delta$, excitation current, coil resistance, and partial failure were used to determine the remaining life or relative health of the transformer. In [18], a method was provided for calculating the specific failure rate for each transformer based on its failure history, reliability measurements, undissolved gases, and furfuraldehyde. This study was conducted on 30 transformers, and the new index was compared with previous indices and asset management methods. In [19], a method was presented for ranking equipment based on the need for preventive maintenance. This rating took the initial condition of the equipment (after the previous overhaul), operating conditions, and environmental conditions during its operation into account.

The researchers in [20] evaluated the effect of lifetime, environmental conditions, and preventive and corrective repairs on the failure rate of transformers with the help of transformer failure and repair history information. Also, Ref. [21] used past information on the failure rate of transformers to evaluate their reliability for the current conditions. However, the transformer conditions were not considered. In summary, Table 1 provides a good comparison between some references and the research reported in this article.

1.3. Innovation and Research Contributions

So far, no research has studied the effect of DR on reducing the unreliability arising from transformers at unexpected times in the case of overload. Two important points considered in this article to accurately evaluate the failure rate include:

Table 1: The comparison of references

Ref. No.	Oil impurity	Thermal model	Loading	Demand response
[8,9]	-	-	-	✓
[10]	-	-	✓	-
[11]	✓	-	✓	-
[12]	✓	-	✓	-
[13]	-	-	-	✓
[14]	✓	-	-	-
[15]	✓	-	-	-
[16]	✓	-	✓	-
[17]	✓	-	-	-
[18]	✓	-	-	-
[19]	-	-	✓	-
[20]	-	✓	✓	-
[21]	-	✓	✓	-
Proposed	-	✓	✓	✓

1- The effect of loading on failure rate

2- The effect of special operating conditions

In this situation, the temperature of the hot spot exceeds the permissible limit and negatively affects the failure rate of the transformer. These two cases are clearly the main research contributions compared to other studies, as they have not been considered in any of the references.

1.4. Research Purposes

This paper proposes the direct effects of DR on the transformer using the transformer’s thermal model to determine the accurate time of load curtailment. The dynamic thermal model is developed based on existing standards. Online condition evaluation is then done using the loading and ambient temperature data, and the reliability cost is analyzed for optimal determination of load curtailment considering load response fatigue and demand dissatisfaction to keep load motivation for participation in DRPs.

The contributions of this paper can be itemized as follows:

- Employing a thermal model in studying transformer operation considering DR
- Proposing a new method for monitoring transformer status and load response
- Reducing the DR risk using the Response Fatigue Index (RFI)
- Using sequential single-objective optimization with different RFI to find the Pareto front of the solution

2. DEVELOPED MODELLING

In the developed model, the direct effects of DR on the transformer’s loading level must be considered. The mathematical model consists of an optimization problem to model transformer operation incorporating DR. Then, a thermal model of the transformer is developed based on available standards. Finally, the transformer’s degradation cost due to unhealthy conditions (i.e., heavy load or high ambient temperature) is expressed using a short-term virtual model for the failure rate of transformers, which is a function of thermal conditions.

2.1. Optimization Problem

The objective functions are the transformer degradation cost, incentives paid to responsive loads, and the cost of dissatisfaction for DRs, as expressed in (1) [24]:

$$OF = \sum_{t=1}^T \{ Cost_t^{Degr} + Inct_t(\Delta P_t^{DR}) + V_t \} \tag{1}$$

where the first term expresses the transformer’s degradation cost caused by the high-temperature operation, which is given in (2) [14].

$$Cost_t^{Degr} = (\xi_t^{Degr}) C^d, \forall t \tag{2}$$

where $Cost_t^{Degr}$ is the degradation cost due to operation in unhealthy conditions. The term ξ_t^{Degr} is the loss of life, which is explained in the next section. C^d is the transformer’s wear-out cost and can be calculated by (3) [25].

$$C^d = Cost^{inv} / L^T \tag{3}$$

where $Cost^{inv}$ is the investment cost of the transformer, and L^T is the useful lifetime of the transformer. Also,

$Inct_t(\Delta P_t^{DR})$ represents the incentive paid to the loads participating in an incentive-based program. Lastly, V_t represents the load dissatisfaction due to shifting from the desired consumption time modeled by (4). Note that the term in parenthesis represents ΔP_t^{DR} [24].

$$V_t = \sum_i v_i^{DR} (P_{i,t}^{WODR} - P_{i,t}^{DR}) \quad (4)$$

where $v_i^{DR} > 0$ is defined as the load's inelasticity parameter [14]. The higher amounts of v_i^{DR} indicate that the consumer insists on consuming load i at the initial time. Equation (5) gives demand response fatigue (DRF) based on [25].

$$DRF = \sum_{\omega} \pi_{\omega} \left(\frac{\sum_i v_i^{DR} \tau_i^{dissat}}{T \sum_i v_i^{DR}} \right) \times 100\% \quad (5)$$

where τ_i^{dissat} is the duration of the customer dissatisfaction due to the shifting of appliance i from the most convenient time, T_i^{ini} in a DRP. Equation (6) limits DRF to the given amount of DRF^{max} [25].

$$DRF \leq DRF^{max} \quad (6)$$

2.2. Thermal Model

According to the IEEE standard [26], the temperature rise of oil over the ambient temperature can be expressed by (7):

$$T_o \frac{d\theta_o}{dt} = -\theta_o + \theta_u, \theta_o(0) = \theta_i \quad (7)$$

By solving this equation, we get (8) [14]:

$$\theta_o = (\theta_u - \theta_i)(1 - e^{-(t/T_o)}) + \theta_i \quad (8)$$

where θ_u is the maximum top oil temperature at load factor K , which is determined by (9) and (10) [27].

$$\theta_u = \theta_{fl} \left(\frac{K^2 \times R + 1}{R + 1} \right)^n \quad (9)$$

$$K = \frac{I}{I_{rated}} \quad (10)$$

and T_o is the time constant of transformer oil at a rated load as shown by (11) [27].

$$T_o = \frac{C\theta_{fl}}{P_{fl}} \quad (11)$$

According to the above information, the oil temperature above the trans is obtained from (12) [22,31]:

$$\theta_{top} = (\theta_o + \theta_{amb}) = (\theta_u - \theta_i)(1 - e^{-(t/T_o)}) + \theta_i + \theta_{amb} \quad (12)$$

For practical use to predict and make an estimation, the above parameters in (12) are discretized using the Euler method as shown in (13) [17]:

$$\frac{d\theta_o[k]}{dt} \approx \frac{\theta_o[k] - \theta_o[k-1]}{\Delta t_1} \quad (13)$$

where Δt is the sampling period. Equation (13) can be written as (14) [23]:

$$\theta_o[k] = \frac{T_o}{T_o + \Delta t} \theta_o[k-1] + \frac{\Delta t \theta_{fl}}{T_o + \Delta t} \left(\frac{\left(\frac{I[k]}{I_{rated}} \right)^2 R + 1}{R + 1} \right)^n \quad (14)$$

If the load is close to the nominal load or more precisely, $R > 1$, (15) and (16) can be used [23].

$$\theta_u \approx \theta_{fl} \left(\frac{I}{I_{rated}} \right)^{2n} \quad (15)$$

$$\theta_u[k] \approx \theta_{fl} \left(\frac{I[k]}{I_{rated}} \right)^{2n} \quad (16)$$

Using the above equations, the following model can be extracted by (17) [23]:

$$\theta_o[k] = \frac{T_o}{T_o + \Delta t} \theta_o[k-1] + \frac{\Delta t \theta_{fl}}{T_o + \Delta t} \left(\frac{I[k]}{I_{rated}} \right)^{2n} = K_1 \theta_o[k-1] + K_2 I[k]^{2n} \quad (17)$$

To use the above equation, we must estimate parameters K_1 and K_2 and, subsequently, T_o and θ_{fl} . For this, since K_1 and K_2 seem to be linear, the least squares method can be used ($n=1$). In fact, state $n=1$ corresponds to the Oil Forced Air Forced (OFAF) cooling system. According to the definition of θ_o , the top oil temperature can be expressed as (18) [25]:

$$\theta_{top} = \theta_o + \theta_{amb} \quad (18)$$

According to (17) and (18), the top oil temperature can be written as (19) [25]:

$$\theta_{top}[k] = K_2(\theta_{top}[k-1] - \theta_{amb}[k-1]) + K_1 I[k]^{2n} + \theta_{amb}[k] \quad (19)$$

2.2.1. Improved model

Since the model cannot follow the dynamics of the ambient temperature, the relationships must be modified. There are lots of modified models to include dynamic thermal models in the literature, but there are no easy-to-use correction factors, e.g., the effect of the coolers' thermal resistance and top-oil and hot-spot gradients. For example, the authors in [28, 29] have proposed a simple model for the thermal monitoring of Oil-Directed Air Forced (ODAF) transformers. In this paper, (18) replaces (7), and (20) is obtained for dynamic condition consideration [26].

$$T_o \frac{d\theta_{top}}{dt} = -\theta_{top} + \theta_{amb} + \theta_u \quad (20)$$

whose parameters are similar to (7). When this equation is solved, it results in (21) [30]:

$$\theta_{top} = (\theta_u + \theta_{amb} - \theta_{top,i})(1 - e^{-(t/T_o)}) + \theta_{top,i} \quad (21)$$

The discrete form of (21) can be expressed as (22) [26] in which R , T_o , and θ_{fl} are defined by (23), (24), and (25), respectively [26]:

$$R = \frac{K_1}{K_3} \quad (23)$$

$$T_o = \frac{K_2 \Delta t}{1 - K_2} \quad (24)$$

$$\theta_{fl} = \frac{T_o(K_1 + K_3)}{K_2 \Delta t} \quad (25)$$

2.3. Variable Failure Rate Depending on the Temperature

According to the estimated models, the hot-spot temperature can be obtained and used to extract the duration of occurrences of unauthorized temperature in the hot spot during the equipment's lifetime. In this way, a model for the transformer failure rate is presented in this study by (26) [26].

$$\lambda_t = \left(1 + \frac{DU}{DU_{max}} \right) \lambda_{ini} \quad (26)$$

2.4. Degradation Cost

The term ξ_t^{Degr} in (2) represents the degradation coefficient, which is related to the transformer's failure rate as (27) [18]:

$$\xi_t^{Degr} = \eta + (1 - \eta) \left(\frac{\lambda_{ini}}{\lambda_t} \right) \quad (27)$$

According to (27) and (2), the value of a transformer falls to η times its annualized cost as the failure rate equals zero. On the other hand, it decreases with the growth of λ_t . Using the results of the previous parts, an algorithm can be obtained for the optimal loading of the transformer. The lost lifetime index (LOL) is one of the important indices in evaluating the results of such modeling, which is defined according to (28) [32].

$$LOL\% = \sum_{i=1}^T \frac{F_{AA,i}}{NIL} \times 100 \quad (28)$$

where F_{AA} is the definition called the aging intensity factor and is defined as (29), and θ_H is the temperature of the trans hot spot. Also, NIL is the transformer's normal insulation lifetime provided by its manufacturer [32].

$$F_{AA} = \exp \left(\left[\frac{NIL}{383} \right] - \left[\frac{NIL}{\theta_H + 273} \right] \right) \quad (29)$$

$$\theta_{top} = \frac{T_o}{T_o + \Delta t} \theta_{top}[k - 1] + \frac{\Delta t}{T_o + \Delta t} \theta_{amb}[k] + \frac{\Delta t \theta_{fl} R}{(T_o + \Delta t)(R + 1)} \left(\frac{I[k]}{I_{rated}} \right)^2 + \frac{\Delta t \epsilon^2 \theta_{fl}}{(T_o + \Delta t)(R + 1)} = K_1 I[k]^2 + (1 - K_2) \theta_{amb}[k] + K_2 \theta_{top}[k - 1] + K_3 \quad (22)$$

We assume that the load curve and ambient temperature are known. The goal is to find the maximum coefficient that, if multiplied by the load curve, the oil temperature and the temperature of the hot spots, as well as the amount of lost life of the transformer, do not exceed the permissible limits.

Using the results, we can propose an algorithm to calculate the productivity, which is specified in Fig. 1. The algorithm should determine the maximum delivered peak load (maximum load factor) of the transformer according to the limitations. It should also calculate the temperature of the oil above the transformer, the temperature of the hot spots, and the amount of lost life of the transformer hour by hour. The inputs of this algorithm are as follows:

- 1- Load and temperature curves and thermal limitations and the maximum allowable life that is lost
- 2- The coefficients of the model obtained from the loading data in the previous days

The output is as follows:

- 1- Displaying the maximum load factor (F) and the maximum load that can be delivered by the transformer;
- 2- Calculating oil temperature and temperature of hot

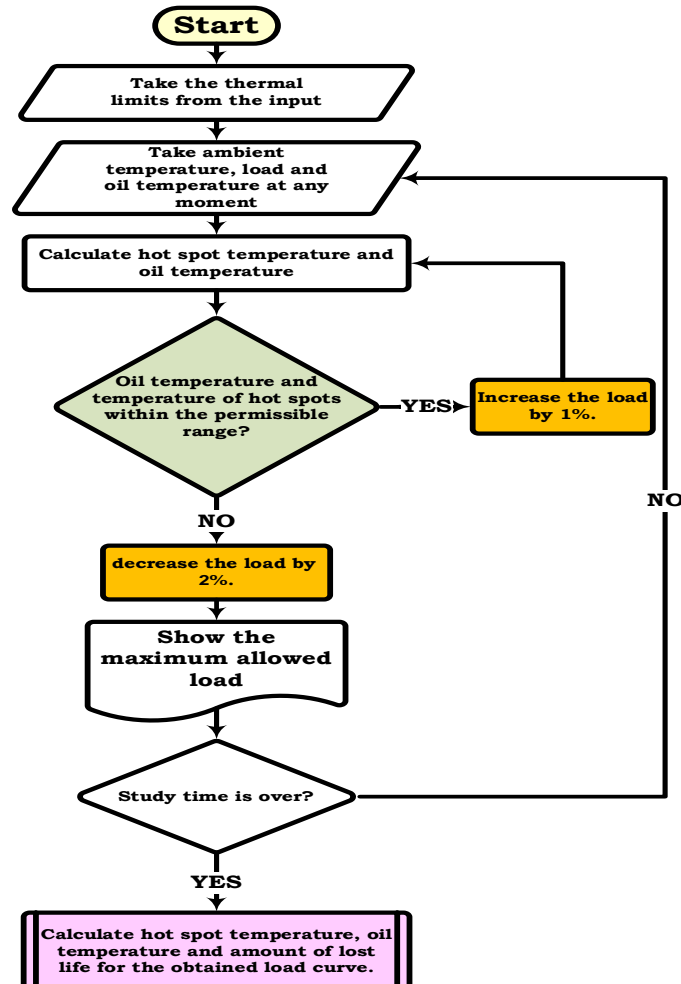


Fig. 1: Prediction flowchart of the maximum transferable load of the transformer.

spots and the amount of the lost life of the transformer according to the obtained load factor;

For a better understanding of the issue, Fig. 1 displays the flowchart of the algorithm for predicting the maximum load that can be delivered by the transformer.

3. NUMERICAL STUDIES

The numerical studies consist of two main parts: testing the prediction model to prove the proposed thermal model and conducting case studies for DR analysis and optimal solution area for two objective functions.

3.1. Prediction of Top Oil Temperature

There are several models for predicting the temperature of transformers, which can be used according to the coefficients given by the transformer manufacturer and the information that is measured. However, most of these models require measurements that are not usually done, or the information is unavailable. As a result, they cannot be used in practice. Variables that are typically measured are ambient temperature, transformer top oil temperature, and load. In this section, using these data, we obtained a model for predicting the oil temperature in the next moments. Then, using the model obtained, we predicted the temperature of the hot spots for the next moments. To evaluate the model, we used the load and temperature data of a 180-MVA, 230/63-kV transformer with OFAF cooling made by Toshiba located in Ghorkhane Station between July and March 2013. The capital cost of this transformer was considered 8 M\$, and the parameter η was considered 0.5 while λ_{ini} was considered 1.

These data are manually recorded hour by hour in offices. The data was transferred to MATLAB software, and these data were processed. An example of data for 1000 hours of loading in the time interval from July 26 to March 4 is shown in Fig. 2.

The simulation results and the measured values with the improved model are shown in Fig. 3. It can be seen that, in this case, the model could respond to the variation of ambient temperature and load. The error values of RMSE=1.36, and the maximum error is Max Error = 3.5°C.

As can be seen in Fig. 3, the transformer thermal modeling method used in this paper was able to predict the temperature of the transformer oil well. In Fig. 3, the predicted temperature from the proposed thermal model is shown in red color. It can also be seen that the blue lines, which are the actual temperature of the transformer oil, have a slight difference from the red lines, and as the yellow lines show, this difference is a value of zero. Finally, all these comparisons express the accuracy and efficiency of the thermal model proposed for the transformer in this article.

3.2. Case Studies

The hypothetical loading profile and ambient temperature for the horizon of 760 hours for the current problem were considered as depicted in Fig. 4. Two case studies are presented in this section to show the effect of DR on the transformer operation as follows:

- Case1: Operation without DR
- Case2: Operation with DR

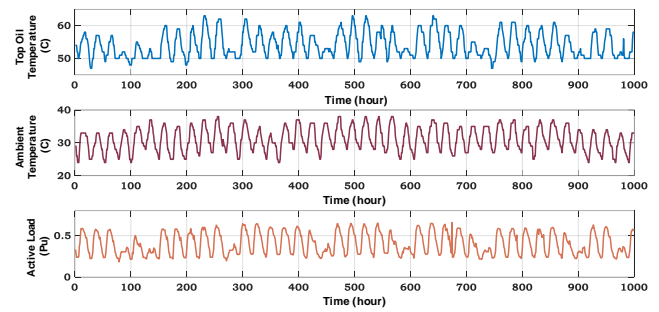


Fig. 2: Data for 1000 hours of loading in the time interval.

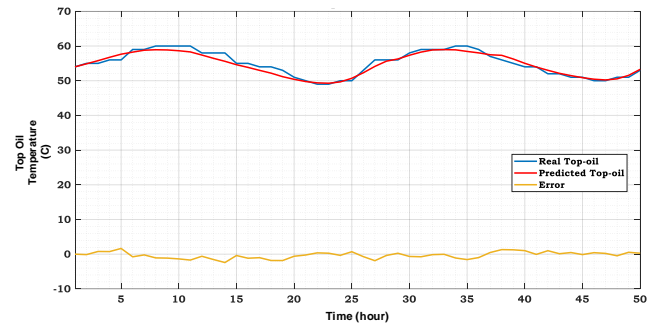


Fig. 3: Prediction with the improved model.

3.2.1. Case1

Fig. 5 depicts the predicted oil temperature, while the horizontal line is the limit of allowable temperature. As can be seen in this figure, the permissible temperature of transformer oil during the 760-hour period under investigation was higher than the threshold of 90°C in most of the hours, which is shown by the black horizontal line in Fig. 5. The reason for this issue is that the transformer is not used optimally, and the transformer loading is considered in the first case when the DR program has not yet been implemented. Also, as the results of Table 2 show, the cost of transformer failure is 0.0143 million dollars, which is obtained because the transformer is operated in suboptimal conditions. Therefore, if it is possible to optimize the operating conditions by using DR programs, this cost can be reduced. In the next case, the effect of the DR program has been examined.

3.2.2. Case 2

The result of changes in the objective function in terms of the maximum value of the acceptable load response fatigue constraint is drawn in Fig. 6. From Fig. 6, it can be concluded that if the maximum response fatigue index exceeds about 5.5, no improvement in the cost objective is achieved. Hence, the Pareto solution area for the problem is the area in the depicted rectangle. As the cost function is the main objective, the maximum optimal value for $RFI^{max} = 5.5$ is selected in this case study. In this case, 0.18 \$/MWh is considered the incentive for 20% of loads participated in DRP. The results of Case 2 are presented in Table 3. As can be seen in Table 3, the degradation cost of the transformer decreased to 0.0090 million dollars. The reason for this reduction was the implementation of the DR program, which optimized transformer loading. Of course, this work was done by paying a 0.000414-dollar incentive to the subscribers participating in the DR program and paying a 0.000054 dissatisfaction fee to the subscribers who did not participate in the plan. The total

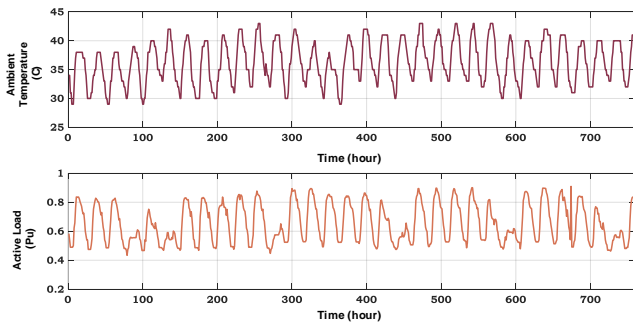


Fig. 4: Hypothetical loading profile and ambient temperature for the horizon of 760 hours.

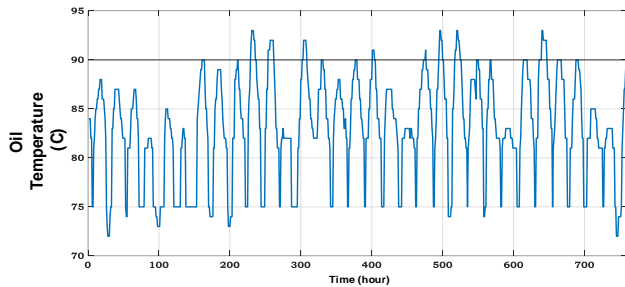


Fig. 5: Oil temperature by prediction for Case 1.

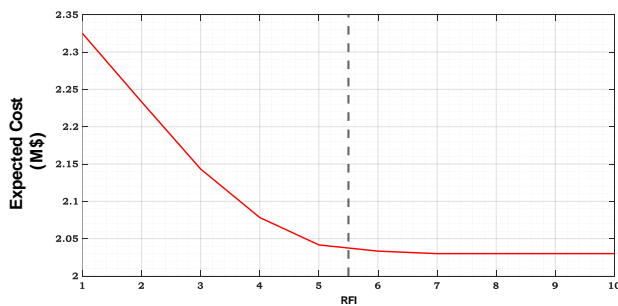


Fig. 6: The cost objective function value relative to the maximum value of the load response fatigue constraint.

Table 2: The costs for Case 1(M\$).

Degradation cost of transformers	0.0143
Incentive paid to responsive load	0
Dissatisfaction cost	0
Total cost	0.0143

Table 3: The costs for Case 2 (M\$).

Degradation cost of transformers	0.0090
Incentive paid to responsive load	0.000414
Dissatisfaction cost	0.000054
Total cost	0.0095

cost, as seen in Table 3, is \$0.0095 million. This cost is significantly lower than that in Case 1 due to the implementation of the DR program. The results in Table 3 versus Table 2 revealed that with very low cost paid as the incentive, a great operation cost reduction can be obtained as degradation cost. Fig. 7 depicts the predicted oil temperature with DR. As shown in Fig. 7, unlike Fig. 5, the amount of transformer temperature fluctuations in all 760 hours studied is below the threshold limit of 90°C. This reduction is due to the implementation of optimal operation of the transformer

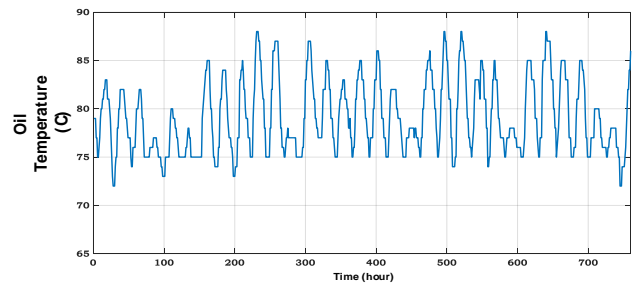


Fig. 7: Oil temperature by prediction for Case 2.

and the management of the transformer load during operation. In order to check the validity of the results of this article, they were qualitatively compared with those of a similar article. The results in that article were examined in two cases, with the DR and without it, as presented in Table 4.

As can be seen, after implementing the DR program with the modeling method proposed in this article, the LOL rate decreased from 0.0102 to 0.0056, which indicates the effectiveness of the DR method and also the accuracy of the RLS thermal model. Also, compared to reference [33], the DR method in this article managed to perform better; that is, it increased the LOL index from 0.00692 to 0.0056.

4. CONCLUSION

In this paper, the heavy-load and high-temperature conditions for power transformers were alleviated by DR. The standard thermal model for power transformers based on loading level and ambient temperature was used to investigate the effect of DR programs on the hot spot temperature. On the other hand, a temperature-related failure rate was developed to accurately measure the amount of DR effect on transformer healthy operation. To prevent DR application being tedious for loads, the DR fatigue index was also considered an objective function, and the proposed multi-objective optimization was solved by putting RFI as a constraint with different values. Also, as this article showed, by spending 0.0005 million dollars to implement the load response program, the degradation cost of transformers can be reduced by 33.5664%. This reduction shows the capacity of the method proposed in this article for the optimal use and thermal modeling of the transformer. Hence, the Pareto front of the objective functions was obtained. Numerical studies prove that the proposed method can allocate the DR programs for transformer life extension. On the other hand, the implementation of the DR program in transformers has caused the percentage of the transformer’s loss of life to decrease significantly so that the LOL percentage decreased from 0.0102 to 0.0056. It means that the lifespan of the transformer was improved and increased by about 45%. Finally, it can be said that the important results obtained in this article are as follows:

- The positive effect of implementing the DR program in reducing transformer failures
- Increasing the lifetime of transformers by implementing DR programs
- Reducing the temperature of transformer oil and less need for periodical repairs due to the implementation of DR programs

Table 4: Comparison of the amount of LOL of the transformer.

Without DR			
Maximum load can be delivered (pu)	Hot spot temperature (C)	LOL index in [33] (%)	LOL index this paper (%)
1.65	115	0.00726	0.0102
With DR			
Maximum load can be delivered (pu)	Hot spot temperature (C)	LOL index in [33] (%)	LOL index this paper (%)
1.6	110	0.00692	0.0056

Future researchers are suggested to use the interest rate and the inflation rate to perform economic calculations from a long-term perspective for the economic analysis of the effects of the DR program on the cost of transformer repairs. In addition, this study addressed the effect of consumption time programs for a certain percentage of times, so it is suggested that the percentage of participation be considered as one of the optimization variables in future research. Finally, due to the direct effect of ambient temperature on oil temperature, it is suggested that the design of load response programs be taken into account with regard to ambient temperature changes during the day.

CREDIT AUTHORSHIP CONTRIBUTION STATEMENT

Arash Moghadami: Conceptualization, Data curation, Formal analysis, Funding acquisition, Investigation, Resources, Software, Writing - review & editing. **Davood Azizian:** Formal analysis, Funding acquisition, Project administration, Supervision, Validation, Visualization. **Amin Karimi:** Funding acquisition, Writing – original draft, Writing - review & editing.

DECLARATION OF COMPETING INTEREST

The authors declare that they have no known competing financial interests or personal relationships that could have appeared to influence the work reported in this paper. The ethical issues; including plagiarism, informed consent, misconduct, data fabrication and/or falsification, double publication and/or submission, redundancy has been completely observed by the authors.

REFERENCES

- [1] IEEE Standard C57.91–2011, "IEEE guide for loading mineral-oil-immersed transformers and step-voltage regulators," Mar. 2012.
- [2] IEC Standard 60076–7, "Power transformers part 7: loading guide for oil-immersed power transformers," Aug. 2005.
- [3] H. L. Willis, *Power distribution planning reference book*. CRC press, 1997.
- [4] Grid Week Talk. (Sep 11, 2009). *Investing in our energy future* [Online]. Available: <https://www.energy.gov/articles/investing-our-energy-future>.
- [5] G. Strbac, "Demand side management: benefits and challenges," *Energy Policy*, vol. 36, no. 12, pp. 4419–4426, 2008.
- [6] I. Diahovchenko et al., "Mitigation of transformers' loss of life in power distribution networks with high

- penetration of electric vehicles," *Results in Engineering*, vol. 15, 100592, 2022.
- [7] C. Teja, and P. K. Yemula, "Architecture for demand responsive HVAC in a commercial building for transformer lifetime improvement," *Electric Power Systems Research*, vol. 189, 2020.
- [8] R. Gunasekara, L. Meegahapola, and M. Jalili, "Demand response scheme for distribution transformer load relieving using smart-meter data," in *Australasian Universities Power Engineering*, 2021, pp. 1-6.
- [9] N. Loitongbam, and T. Ghose, "Impact of demand response on transformer loss of life," in *Proc. International Conference on Computer, Electrical & Communication Engineering*, 2020, pp. 1-5.
- [10] J. H. Jürgensen, L. Nordström, and P. Hilber, "Estimation of individual failure rates for power system components based on risk functions," *IEEE Transactions on Power Delivery*, vol. 34, no. 4, pp. 1599-1607, 2019.
- [11] T. D. Poyser, "An on-line microprocessor based transformer analysis system to improve the availability and utilization of power transformers," *IEEE Trans. Power App. Syst.*, vol. PAS-102, no. 4, pp. 957–962, 1983.
- [12] D. Hilshey, P. D. H. Hines, P. Rezaei, and J. R. Dowds, "Estimating the impact of electric vehicle smart charging on distribution transformer aging," *IEEE Trans. Smart Grid*, vol. 4, no. 2, pp. 905–913, 2013.
- [13] M. Humayun, M.Z. Degefa, A. Safdarian, and M. Lehtonen, "Utilization improvement of transformers using demand response," *IEEE Transactions on Power Delivery*, vol. 30, no. 1, pp. 202-210, 2014.
- [14] M. A. Abd-Aziz, M. A. Talib, A. F. Abidin, and S. A. M. Al-Junid, "Development of power transformer health index assessment using feedforward neural network," *Journal of Advanced Research in Applied Sciences and Engineering Technology*, vol. 30, no. 3, pp. 276-289, 2023.
- [15] R. D. Medina, D. A. Zaldivar, A. A. Romero, J. Zuñiga, and E. E. Mombello, "A fuzzy inference-based approach for estimating power transformers risk index," *Electric Power Systems Research*, vol. 209, 108004, 2022.
- [16] H. Yu et al., "A risk assessment method of power transformer based on three-parameter interval grey number decision-making," *Applied Sciences*, vol. 12, no. 7, 3480, 2022.
- [17] F.L. Dixon, and D. Robey, "When to replace aging transformers, Part 2: Guidelines to replace older transformers before failure," *IEEE Industry Applications Magazine*, vol. 29, no. 3, pp. 46-56, 2022.
- [18] A. Nanfak, S. Eke, F. Meghnefi, I. Fofana, G.M. Ngaleu, and C.H. Kom, "Hybrid DGA method for power transformer faults diagnosis based on evolutionary k-means clustering and dissolved gas subsets analysis," *IEEE Transactions on Dielectrics and Electrical Insulation*, vol. 30, no. 3, pp. 2421-2428, 2023.

- [19] c. I. da silva *et al.*, "an online non-invasive condition assessment method of outdoor high-voltage SF6 circuit breaker," *Machines*, vol. 11, no. 3, 323, 2023.
- [20] X. Zhao, F. Gui, H. Chen, L. Fan, and P. Pan, "Life cycle cost estimation and analysis of transformers based on failure rate," *Applied Sciences*, vol. 14, no. 30, 2024.
- [21] V. Vita, G. Fotis, V. Chobanov, C. Pavlatos, and V. Mladenov, "Predictive maintenance for distribution system operators in increasing transformers' reliability," *Electronics*, vol. 12, no. 6, 2023.
- [22] L. Gkatzikis, I. Koutsopoulos, and T. Salonidis, "The role of aggregators in smart grid demand response markets," *IEEE Journal on Selected Areas in Communications*, vol. 31, no. 7, pp. 1247–1257, 2013.
- [23] J. H. Kim, and A. Shcherbakova, "Common failures of demand response," *Energy*, vol. 36, no. 2, pp. 873–880, 2011.
- [24] G. Swift, T. S. Molinski, and W. Lehn, "A fundamental approach to transformer thermal modeling – Part I : Theory and equivalent circuit," *IEEE Transactions on Power Delivery*, vol. 16 no. 2, pp. 171-175, 2001.
- [25] IEEE Standard C57.91.119-2001, "IEEE Recommended Practice for Performing Temperature Rise Tests on Oil-Immersed Power Transformers at Loads beyond Nameplate Ratings," March. 2012.
- [26] L. Paulhiac, and R. Desquens, "Dynamic thermal model for oil directed air forced power transformers with cooling stage representation," *IEEE Transactions on Power Delivery*, vol. 37, no. 5, pp. 4135-4144, 2022.
- [27] M. Abasi, M. Joorabian, A. Saffarian, and S. G Seifossadat, "A comprehensive review of various fault location methods for transmission lines compensated by FACTS devices and series capacitors," *Journal of Operation and Automation in Power Engineering*, vol. 9, no. 3, pp. 213-225, 2021.
- [28] J. Ebrahimi, and M. Abedini, "A two-stage framework for demand-side management and energy savings of various buildings in multi smart grid using robust optimization algorithms," *Journal of Building Engineering*, vol. 53, 104486, 2022.
- [29] M. Sadeghi, and M. Abasi, "Optimal placement and sizing of hybrid superconducting fault current limiter to protection coordination restoration of the distribution networks in the presence of simultaneous distributed generation," *Electric Power Systems Research*, vol. 201, 107541, 2021.
- [30] M. Abasi, A. Torabi Farsani, A. Rohani, and M. Aghazadeh Shiran, "Improving differential relay performance during cross-country fault using a fuzzy logic-based control algorithm," in *Proc. 5th Conference on Knowledge-Based Engineering and Innovation*, 2019.
- [31] J. Ebrahimi, M. Abedini, M. Rezaei, and M. Nasri, "Optimum design of a multi-form energy in the presence of electric vehicle charging station and renewable resources considering uncertainty," *Sustainable Energy, Grids and Networks*, vol. 23, 100375, 2020.
- [32] P. K. Yemula, "Architecture for demand responsive HVAC in a commercial building for transformer lifetime improvement," *Electric Power Systems Research*, vol. 189, 106599, 2020.
- [33] M. Humayun, M. Z. Degefa, A. Safdarian, and M. Lehtonen, "Utilization improvement of transformers using demand response," *IEEE Transactions on Power Delivery*, vol. 30, no. 1, pp. 202-210, 2014.

BIOGRAPHY

Arash Moghadami was born in 1990 in Zanjan, Iran. He received his master's degree in electrical engineering majoring in telecommunications from Aba Abyek Qazvin Higher Education Institute, Iran, in 2014. Currently, He is a Ph.D. candidate at Islamic Azad University of Sanandaj, Iran, in the field of electricity majoring in power. His



current research interests are power transformer loss reduction and demand response.

Davood Azizian received his B.Sc. (2003) and M.Sc. (2005) degrees in electrical engineering from Zanjan University and Ph.D. degree (2012) in electrical engineering from Islamic Azad University, Sciences and Research Branch. He has worked at the Iran Transformer Research Institute, R&D Department and Dry-Type



Technical Office of Iran Transfo Company, and Abhar Branch of Islamic Azad University. His fields of interest include transformer design, electromagnetic modeling, thermal modeling, heuristic algorithms, and optimization. Dr. Azizian is now an Assistant Professor in Abhar Branch, Islamic Azad University, Abhar, Iran.

Amin Karimi received his B.E. degree in Electrical Engineering from the Educational Research Complex of Isfahan, Iran, in 2005 and his M.Sc. degree in Analog Electronic Engineering from Razi University, Kermanshah, Iran, in 2009. He received his Ph.D. degree (2019) in Control of Power Systems from the University of



Kurdistan, Iran. Dr. Karimi is now an Assistant Professor at Sanandaj Branch, Islamic Azad University, Sanandaj, Iran. His current research interests include power electronics, virtual inertia, and robust/intelligent control.

Copyrights

© 2024 Licensee Shahid Chamran University of Ahvaz, Ahvaz, Iran. This article is an open-access article distributed under the terms and conditions of the Creative Commons Attribution –NonCommercial 4.0 International (CC BY-NC 4.0) License (<http://creativecommons.org/licenses/by-nc/4.0/>).





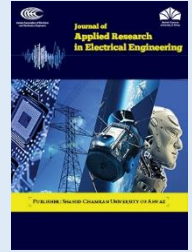
Iranian Association of
Electrical and Electronics
Engineers

Journal of Applied Research in Electrical Engineering

E-ISSN: 2783-2864

P-ISSN: 2717-414X

Homepage: <https://jaree.scu.ac.ir/>



Research Article

Assessing Power System Adequacy and Generation Expansion Planning in the Presence of Wind Power Plants Considering Uncertainties in the DIGSILENT Software Environment

Hamid Reza Safa¹, Ali Asghar Ghadimi^{1,2,*}, and Mohammad Reza Miveh³

¹Department of Electrical Engineering, Faculty of Engineering, Arak University, Arak 38156-8-8349, Iran

²Research Institute of Renewable Energy, Arak University, Arak 38156-8-8349, Iran

³Department of Electrical Engineering, Tafresh University, Tafresh 39518-79611, Iran

* Corresponding Author: a-ghadimi@araku.ac.ir

Abstract: Renewable energy sources are particularly important in clean energy transitions and must be considered in Generation Expansion Planning (GEP) problems due to low cost, ease of installation, and ability to implement Demand Response (DR) programs. However, challenges such as the stochastic nature of renewable energy sources, consumer unawareness regarding participation in DR programs, and difficulties in integrating some resources have posed challenges to the use of these resources in the GEP problem. This paper addresses these challenges by using the Weibull distribution function to model wind power plants' uncertainty and rewards and penalties to motivate consumer participation in the GEP problem. To achieve these objectives, initially, the adequacy assessment of the generation system is performed analytically using the reliability index, which includes Expected Energy Not Supplied (EENS), considering the forced outage rate of generators in the DIGSILENT power factory through Python programming. Subsequently, an optimized GEP model is presented to enhance the generation system's adequacy against short-term demand for the next year. In this model, wind farms and the DR program are integrated and optimized using the genetic algorithm, employing Python programming. The genetic algorithm selects the number of existing turbines in the wind power plant and the level of consumer participation needed to reduce the EENS to the desired value at the minimum cost. Validation of the proposed model is conducted on a 9-bus network. The strength of the presented method lies in its applicability to real-world networks modeled in the DIGSILENT Power Factory.

Keywords: System adequacy assessment, generation expansion planning, wind power plant, uncertainty, demand response, reliability.

Article history

Received 14 February 2024; Revised 10 June 2024; Accepted 23 June 2024; Published online 23 October 2024.

© 20xx Published by Shahid Chamran University of Ahvaz & Iranian Association of Electrical and Electronics Engineers (IAEEE)

How to cite this article

H. R. Safa, A. A. Ghadimi, and M. R. Miveh, "assessing power system adequacy and generation expansion planning in the presence of wind power plants considering uncertainties in the DIGSILENT software environment," *J. Appl. Res. Electr. Eng.*, vol. 3, no. 1, pp. 99-109, 2024. DOI: 10.22055/jaree.2024.46140.1109



1. INTRODUCTION

Electricity as one of the vital energy sources plays a significant role in meeting the daily needs of modern society and ensuring the future development of humanity. Given this issue, the generation segment of the power system must have

sufficient capacity to meet the load demand at any given moment to ensure the reliability of the power system [1]. To achieve reliable generation for the demand sector, it is necessary to first assess the adequacy of the generation network to obtain information about its capability to meet the demand load for the desired horizon (e.g., short-term, such as

the upcoming year). After obtaining sufficient information, a Generation Expansion Planning (GEP) model is employed to address production shortages [2]. In this regard, it is preferable to utilize renewable energy sources and/or demand response programs in the GEP model, as both are proposed solutions for environmental sustainability in the future [3, 4]. The deployment of renewable resources and demand response (DR) programs, due to their environmental benefits, lower costs, and rapid implementation capabilities in short-term horizons, is a highly suitable solution for balancing generation and consumption. However, it comes with challenges that require special attention. Failure to address or adequately model these challenges may result in additional costs or network outages [4, 5]. Regarding wind energy utilization, wind speed exhibits random and variable behavior. Additionally, people lack the necessary awareness to participate in the generation sector in DR programs. Therefore, the use of these resources in generation development planning faces challenges that must be addressed with appropriate methods [6-8].

Another challenge facing power system planners is the large-scale dimensions of power grids, which complicates the optimization of generation planning considering practical parameters and constraints. In such cases, simplifications are employed, and results are extracted [9]. If a method can be implemented on industrial software where the entire power grid at the national or regional level is fully modeled, more realistic results can be provided, thereby reducing future challenges and additional costs imposed on the network. The efficiency indices of power generation can be calculated using deterministic or probabilistic methods. As renewable energy sources and flexible load demand increase gradually, the priority has shifted from deterministic methods to probabilistic ones [10]. Probabilistic methods for assessing adequacy indices are divided into two main approaches: analytical methods and Monte Carlo simulation. Power system adequacy is determined based on the actual presence of power generation units when they are available and capable of generating electricity, as well as during failures or unplanned outages [11]. For adequacy evaluation, the analytical method, if conducted using precise and appropriate models, can provide accurate results with power generation adequacy indices. On the other hand, the Monte Carlo simulation method requires a large number of iterations to achieve more accurate results and typically demands significant computational time, especially when applied to large-scale systems [12]. Therefore, adequacy assessment and generation expansion planning are vital components of the energy infrastructure for modern society, and if not properly evaluated and planned, society will face serious challenges. In reliability assessment, the study of generation adequacy focuses on the system's ability to meet the requested load demand without considering the transmission line facilities and distribution system [13]. After evaluating the adequacy of the network, any future shortages should be addressed through generation expansion planning. In reference [14], the optimization problem of generation expansion planning has been modeled using the General Algebraic Modeling System (GAMS). The GEP problem involves determining the optimal investment in the generation network with various objectives such as maximizing profits, minimizing production costs, reducing outage costs, and increasing the share of renewable

energy resources [15]. In [16], a mathematical model is presented for the optimal measurement of energy storage in GEP for old systems with high penetration of renewable energies to increase production. Also in [17] wind turbine uncertainty and demand response are considered only for the transmission system and the production sector is not considered. Therefore, other suitable approaches can contribute to improving generation planning alongside the use of renewable sources to enhance short-term adequacy. These approaches not only reduce costs but also increase the flexibility in meeting the required load at any given moment. One of these solutions is peak load reduction, where Demand Response (DR) serves as a cost-effective resource, improving system adequacy [18, 19]. Furthermore, in [20], demand response (DR) programs and renewable energy sources have been utilized to enhance network resilience in coping with potential disruptions to input energy carriers, only on a daily basis (one or a few days ahead), optimal planning has been performed. However, in the development of production studies, planning should be done annually (short-term, medium-term, long-term). In [21], thermal generators with similar characteristics are clustered together using clustering techniques. Each cluster shares information among its members and exchanges power, enabling the improvement of power generation adequacy. Furthermore, in [22], energy shifting to periods with lower demand has been utilized to improve adequacy. To achieve this, battery systems are employed to store energy during low-demand periods using the Monte Carlo method.

Based on the above statements, the efforts made by others to improve efficiency indicate that these resources alone are insufficient in increasing efficiency. Therefore, this article simultaneously utilizes two key sources, namely wind power plants and a DR program. To address the stochastic nature of wind speed, the Weibull distribution function has been employed to model the uncertainty of wind power plants. In addition, in the DR program, tools such as rewards are used to encourage consumer participation to participate with the production sector in the proposed GEP model. This model integrates wind power plant and DR program by using a genetic algorithm. The genetic algorithm works in such a way that what percentage of the contribution amount that the consumer can have, along with how many of the existing turbines of the wind power plant, can be chosen so that the EENS is reduced to the desired amount with the minimum cost. The proposed GEP model provides the most optimal mode to the planners so that the planners can make the right decision to increase the network adequacy in the present and short term.

Furthermore, to ensure the practicality of the proposed method, the implementation approach of the proposed method on real-world networks modeled in the DIGSILENT software has been emphasized.

As can be seen in Table 1, past works in the GEP model have not fully evaluated the production adequacy and only renewable resources have been used. But in this article, in the first step, the network adequacy has been investigated. Due to the high importance of Demand Response (DR) due to its cost-effectiveness and zero environmental pollution, it has been added to the GEP model alongside wind power plants. Additionally, in this paper, Python software and DIGSILENT

Table 1: Summary of reviewed articles.

Reference	Adequacy assessment		Consider demand response	Generation Expansion Planning	
	EENS	Solution method		Using renewable energy source	Optimization method
[3]				*	MILP
[4]			*		
[11]	*	Analytical in Python			
[13]				*	MILP
[14]				*	MILP
[15]				*	Gurobi
[16]			*		
[17]	*				
[18]	*				
In this article	*	An Analytical with Python programming in DIgSILENT	*	*	GA

are linked to facilitate computational development. This capability is provided in any real industrial network.

The organization of this paper is as follows: In Section 2, the research methodology is introduced. Section 3 describes the results and simulations. Section 4 discusses the conclusions.

In summary, the innovations and contributions of this paper are as follows:

1- This article evaluates generation adequacy using analytical methods with Python programming in DIgSILENT.

2- Simultaneous use of wind power plant and load response programs to implement the generation expansion planning (GEP) to improve the adequacy of the generation system in the short term.

3- The use of genetic algorithms in GEP.

2. METHODOLOGY

In this section, the formulation of indices for evaluating adequacy, uncertainty, and wind power generation capacity, as well as the development planning of the power plant, is presented.

2.1. Modeling the Adequacy Evaluation Index

In [21, 23], the reliability index (EENS), which is used to assess the adequacy of generation, has been examined.

2.1.1. Expected energy not supplied (EENS)

This index indicates the amount of energy that is not supplied by the electricity generation system in the event of a power outage. Energy non-supply can lead to significant damages and losses for customers and even society as a whole.

The formula for calculating this index is based on the total expected energy that is not supplied under specific conditions and the probability of occurrence of these conditions, along with the unit of energy measurement and the number of specific conditions. By using this index, the amount of lost energy and the damages associated with power outages can be estimated and analyzed.

$$EENS = T * \sum_{i \in S} c_i p_i \quad (1)$$

In (1), c_i represents the capacity that has a probability p_i of not being met within the time period T .

2.2. Wind Power Plant Model

2.2.1. Considering the uncertainty of the wind power plant with the Weibull distribution function

The Weibull distribution is utilized to study and analyze wind characteristics at wind sites. This distribution is well-suited to the wind speed distribution under specific conditions. Therefore, by using the Weibull distribution, the wind power generation at wind sites can be estimated, and wind characteristics can be investigated. The probability density function (PDF) of this distribution is as follows [24, 25].

$$f_v(v) = \frac{k}{c} \left(\frac{v}{c}\right)^{k-1} e^{-\left(\frac{v}{c}\right)^k} \quad (2)$$

In (2), k represents the shape parameter, and c represents the scale parameter.

2.2.2. The relationship between the output power of the wind power plant and the wind speed

The relationship between the power output of wind turbines and wind speed is depicted in Fig. 1. The mathematical equation can be expressed as follows [26, 27].

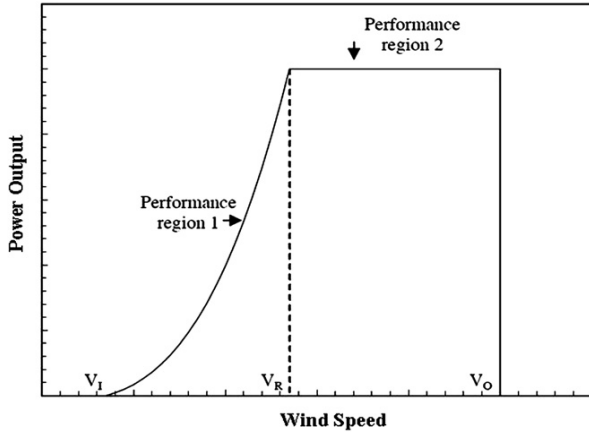


Fig. 1: Power curve vs. wind speed curve showing the overall cost of wind turbines in a wind farm per year.

$$P_T = \begin{cases} 0 & 0 \leq V \leq V_I \\ (A + BV + CV^2) * P_R & V_I \leq V \leq V_R \\ P_R & V_R \leq V \leq V_O \\ 0 & V \geq V_O \end{cases} \quad (3)$$

In (3), V represents the wind speed variable, V_I is the cut-in speed at which the wind turbine begins generating electricity, V_R is the rated speed at which the wind turbine produces maximum power, P_R is the rated power of the wind turbine, and V_O is the cut-out speed, beyond which the wind turbine stops and does not generate any power.

The constants A , B , and C are obtained using the following equations:

$$A = \frac{1}{(V_I - V_R)[V_I + V_R] - 4(V_I V_R) \left(\frac{V_I + V_R}{2V_R}\right)^3} \quad (4)$$

$$B = \frac{1}{(V_I - V_R)^2} \left[4(V_I + V_R) \left(\frac{V_I + V_R}{2V_R}\right)^3 - 3(V_I + V_R) \right] \quad (5)$$

$$C = \frac{1}{(V_I - V_R)^2} \left[2 - 4 \left(\frac{V_I + V_R}{2V_R}\right)^3 \right] \quad (6)$$

2.3. Power Plant Development Planning

2.3.1. Objective function

The total cost (C_{total}), which is used as an objective function to reduce costs (wind turbine, expected energy not supplied, demand response), is expressed as the main objective as follows:

$$C_{total} = C_{wt} + C_{ENS} + C_{DR} \quad (7)$$

2.3.2. Cost Model for Wind Farm

To calculate the cost of wind turbines in a wind farm, a cost model introduced in [28, 29] is employed. In [28], the model assumes that with an increase in the number of turbines (n_{wt}), the cost per year for the turbines decreases, and the maximum reduction reaches one-third of the turbine cost. ($Cost_y$) represents the cost of one wind turbine per year.

$$Cost = n_{wt} \left(\frac{2}{3} + \frac{1}{3} e^{-0.00174n_{wt}^2} \right) \quad (8)$$

$$Cost_{total} = Cost_y \times Cost \quad (9)$$

2.3.3. Energy Not Served Cost

A generating unit may experience outage due to unforeseen failures, referred to as Forced Outage Rate (FOR). This rate represents the percentage of time that a generating unit is unavailable due to unexpected failures. Due to the forced outage rate of generating units and based on demand and available reserves, a portion of the energy demand may not be met. This portion is referred to as Energy Not Supplied (ENS). Its formula is as follows:

$$C_{ENS} = \sum_{t=1}^T Cost_{ENS_t} \times ENS_t \quad (10)$$

2.3.4. Demand Response Cost

In the demand response cost formula C_{DR} represent the amount of power that consumers can actively participate in demand response management. This amount is typically expressed as a percentage of the total consumed load. Here, DR_{level} indicates the amount of power that consumers can reduce in a participatory manner, up to 30% of their load or equivalently, the capacity that is saved through consumer participation in demand reduction.

In this context, $Cost_{DR}$ represents the cost per megawatt of reduced power that the electricity producer receives from consumers' participatory reduction. Therefore, the set of costs C_{DR} in this formula represents the expenses related to consumer participation in load management and power reduction.

$$C_{DR} = Cost_{DR} \times DR_{level} \times Load_{peak} \quad (11)$$

2.3.5. The decision variable

In this article, the decision variables in power plant development planning include the number of wind turbines (n_{wt}) and the level of consumer participation (DR_{Level}) in the power generation network.

2.3.6. Constraints in the problem

The power range of wind turbines (p_{wt}) and the demand response level (DR_{Level}) are constrained by (12) and (13), and the reliability model range in (14) is provided.

$$p_{wt} \leq L \times Peak_{Load} \quad (12)$$

$$DR_{Level} \leq n \times Peak_{Load} \quad (13)$$

$$EENS \leq EENS_{max} \quad (14)$$

2.4. Proposed Methodology Flowchart

The generation of the GEP model's performance flowchart is depicted in Fig. 2. This model, informed by the adequacy assessment data, evaluates the system's capacity to meet the demanded load. Employing a genetic algorithm in Python, it strives to balance generation and demand in the short term (next year) by integrating wind energy and demand response programs.

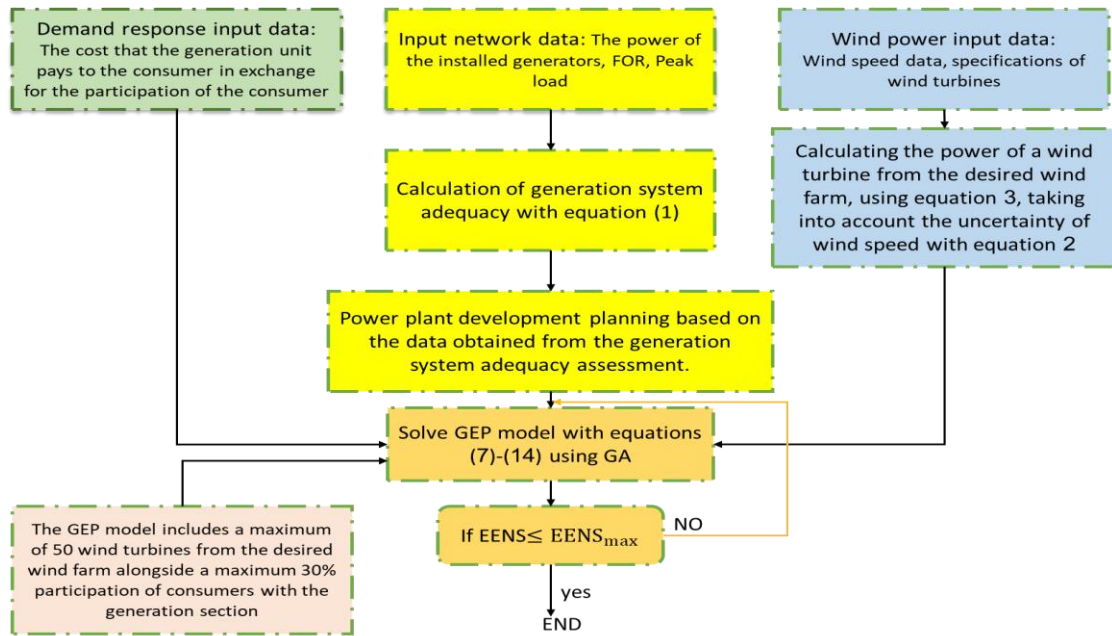


Fig. 2: Flowchart of the proposed GEP model.

3. RESULTS AND SIMULATION

In this section, the examination of the given data (including network type, generators, required software, and system specifications) and simulation for validating the proposed method have been addressed.

3.1. Introduction of Test Network and Production System Model

Using the analytical method, the adequacy of generation units has been evaluated under normal conditions (without forced outages) and based on their forced outage rates. Only generation units and loads are considered in the adequacy assessment, while transmission lines and distribution networks are not taken into account. In this paper, the IEEE 9-bus test system with a peak load of 900 megawatts (Fig. 3) has been utilized in DIgSILENT. The generators in the network under study are listed in Table 2.

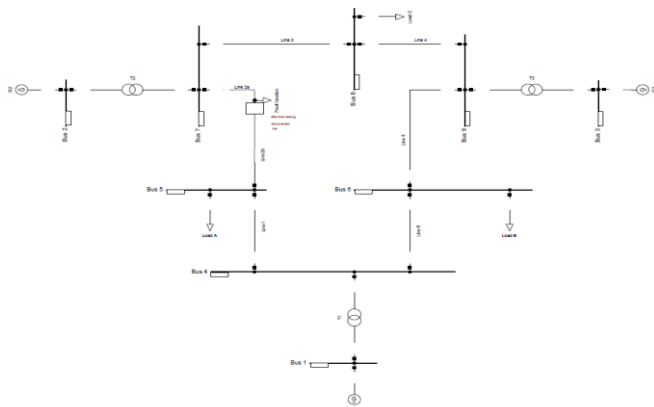


Fig. 3: The 9-bus test network model in DIgSILENT

Table 2: Generator specifications and their forced outage rates

Generating Unit	Generating Capacity (MW)	Forced Outage Rate (FOR)
G ₁	202	0.04
G ₂	200	0.02
G ₃	250	0.01

3.2. Required Software and Systems

Simulations were conducted using Python in the system whose specifications are provided in Table 3 for the short term (one year).

3.3. Simulation Results Related to Adequacy

3.3.1. The value of Expected Energy Not Supplied (EENS)

The load duration curve consists of three parts (base, intermediate, and peak load), as shown in Fig. 4, where all power plants are online but the generation network still has a shortfall of 248 megawatts. The unmet energy is examined in Table 4 for both cases of no generator outages and individual generator outages.

$$ENS = t \times \frac{1}{2} (Load_{peak} - Power_{level}) = 47.310769$$

$$EENS = ENS * q_1 q_2 q_3 = 44.06487198 \text{ (MWh/Year)}$$

Table 3: System specifications

System Model	P553UJ
Processor	Intel(R) Core (TM) i5-6198DU CPU@ 2.30GHZ (4CPUS), ~2.4GHZ
Memory	819MB RAM

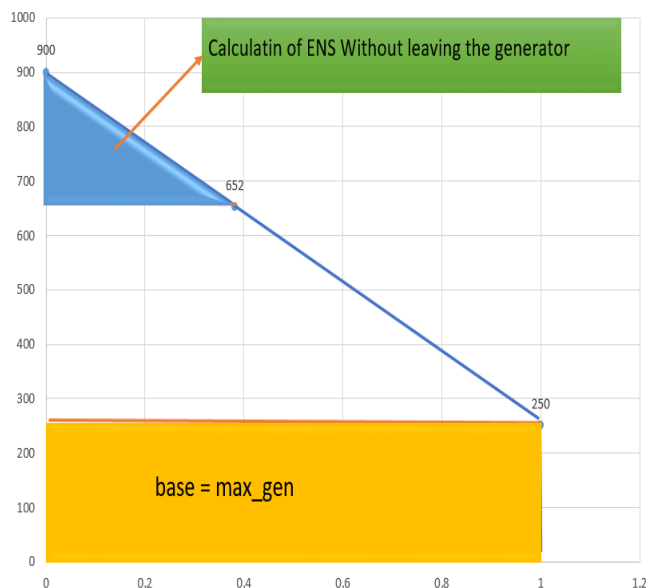


Fig. 4: Load continuity curve in terms of perionite.

Table 4: Results of expected energy not served for the initial network.

Out of capacity (c_i) in MW	Probability (p_i)	t_i	$EENS_i = t_i * \sum_{i \in S} c_i p_i$
0	$0.96 \times 0.98 \times 0.99 = 0.931392$	0.38153546	44.0648719754
202	$0.04 \times 0.98 \times 0.99 = 0.038808$	0.69230769	5.427143327
200	$0.96 \times 0.02 \times 0.99 = 0.019008$	0.68923076	2.620179657
250	$0.96 \times 0.98 \times 0.01 = 9.408 \times 10^{-3}$	0.76615384	1.801993832
			$\sum EENS_i = 54.8393514092$

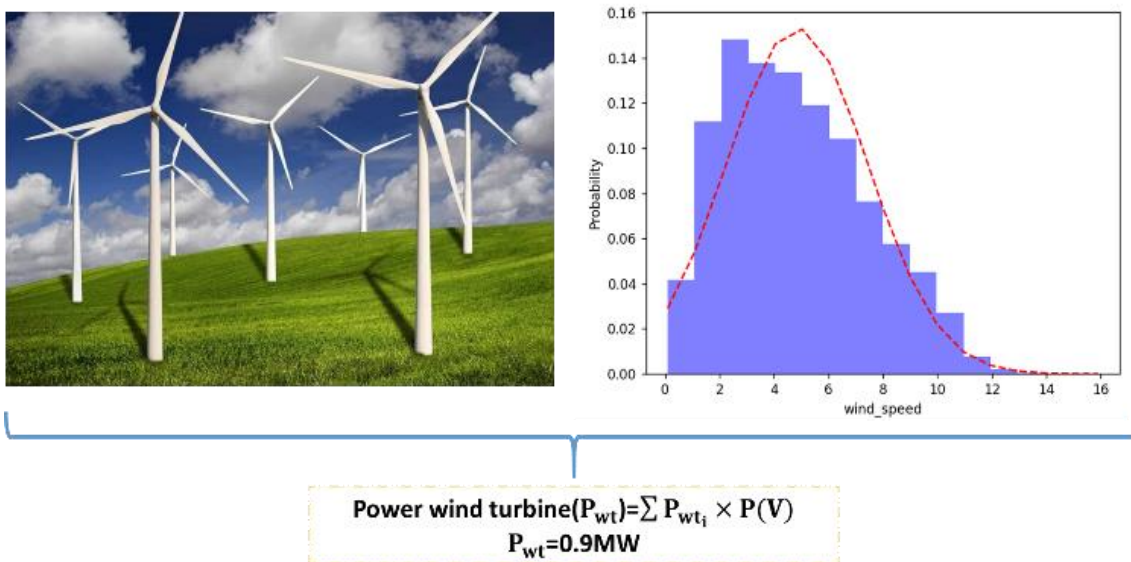


Fig. 5: Average annual power of each wind turbine considering wind speed uncertainty.

3.4. Results of the Wind Power Plant

Wind speed data has been collected by a meteorological station. Considering the specifications of the wind turbine provided in Table 5, the average annual power of each wind turbine (p_{wt}) has been obtained, taking into account the uncertainty of wind speed with the Weibull distribution function as shown in Fig. 5. Its value is equal to 0.9 MW.

3.5. Data Related to the Generation Development

In this section Table 6, the information regarding the wind turbine, including the wind turbine investment cost ($Cost_y$), energy not served cost ($Cost_{ENS_t}$), demand response ($Cost_{DR}$), is provided.

3.6. Simulation Results

Simulation in a 9-node network, as depicted in Fig. 3, has been conducted as follows:

First, the network adequacy in the current state is evaluated in scenarios with and without the generator's exit. Based on this evaluation, the Expected Energy Not Supplied (EENS) is determined. Therefore, after gathering information about the current state of the network, necessary measures have been taken to improve and enhance the network adequacy in the current and short-term periods. These actions have been carried out using the proposed GEP model, as shown in Fig. 2. The model integrates wind power plant and Demand Response (DR) program using the genetic algorithm. The genetic algorithm considers two factors: firstly, Table 6 which includes three costs (the reward cost given to consumers for participation, the installation cost of each wind turbine, and the cost of unsupplied energy); and secondly, the maximum participation power of the consumer, which is 83% higher than the total participation power of wind turbines. In the proposed GEP model, the genetic algorithm operates by determining what percentage of consumer participation, along with how many of the existing wind turbines in the wind power plant, should be selected to reduce the EENS to

the desired level with minimum cost. The results in Table 7 show information about various scenarios of consumer participation along with the participation of wind turbines, along with the costs associated with these scenarios. And the reduced EENS values resulting from these participations are displayed in Table 8. In Table 8, the first column indicates the number of generator outputs, where column A represents the amount of power shortage in the current network state without generator outputs, and G_1 to G_2 are the generators removed from the network. The EENS results in Table 8 are presented under two conditions. $EENS_1$ to $EENS_9$ correspond to participation scenarios, and $EENS_{10}$ represents the scenario without participation. In the power generation system, the baseline load is set equal to the capacity of the generator that exceeds that of the other generators. In this regard, the maximum total participation of consumers and wind power plant is set to be greater than or equal to the capacity of the fixed generator G_3 , which produces more power compared to generators G_1 and G_2 ($P_{gen_{max}} \leq P_{maximum\ contribution}$). In Table 7, the total power of participations corresponding to scenarios 1 to 5 fails to meet this condition. The results in Table 8 ($EENS_1$ to $EENS_5$) indicate that, considering the participation limits set in scenarios 1 to 5, the combination of maximum consumer participation along with wind turbines by the genetic algorithm within this range does not satisfy the condition ($EENS_i \leq 4\ MWh$). However, the total power of participations corresponding to scenarios 6 to 9 satisfies the condition ($P_{gen_{max}} \leq P_{maximum\ contribution}$). The results in Table 8 ($EENS_6$ to $EENS_9$) indicate that, considering the participation limits set in scenarios 6 to 9, the combination of consumer participation with wind turbine participation by the genetic algorithm within these ranges satisfies the condition ($EENS_i \leq 4\ MWh$). The costs associated with these participations in Fig. 7 indicate that they are higher compared to the EENS cost in a year without participation. To ensure that participation in the production sector is profitable, considering that the consumer participation cost is significantly higher compared to the wind turbines, it has been reduced by 42.5%. Based on the new cost for consumer participation, Table 9 re-evaluates the participation scenarios corresponding to scenarios 6 to 9 that satisfy the condition ($EENS_i \leq 4\ MWh$). The proposed model selects the best participation mode for each constraint based on their participation scenarios with the minimum cost, and Table 10 displays the EENS values related to the new participations where the condition ($EENS_i \leq 4\ MWh$) is satisfied. In Table 9, the participation range ($n=46, i=23$) determined by the proposed GEP model is the optimal mode. Considering the newly obtained EENS values (shown in Fig. 6 and Table 10), it can be observed that the condition ($3.91\ MWh \leq 4\ MWh$) is satisfied with the minimum cost within this range. In scenario 2, power production is more profitable compared to other scenarios in Table 9. The costs of all scenarios are compared in Fig. 7.

Table 5 :Wind turbine specifications.

Technical specifications of the 2-megawatt Samen (AV928) wind turbines under license of the Avantis Energy Germany.	
Startup speed	3m/s
Rated speed	9m/s
Cut-off speed	20m/s

Table 6: Costs (wind turbine, EENS, and demand response)

$Cost_y$	1624000 (\$/MW)/25
$Cost_{ENS_t}$	5.5*1000*8760 (\$/MWh)
$Cost_{DR}$	2*1000*8760 (\$/MWh)

Table 7 : Comparison table of the results of the participation of the number of wind turbines next to the participation of the consumer, considering the total costs for improving the adequacy of the electricity generation system

Scenario	$P_{gen_{max}}$ (MW) $P_{gen_{max}}$ (MW) $\leq P_{maximum\ contribution}$	$P_{maximum\ contribution}$ (MW) $= (n \times P_{wt}) +$ $(DR_{level_i} \times Load_{peak})$ Acc. to (12) and (13)	The maximum number of turbines (n) and the maximum load participation percentage (i)	Total cost	Number of wind turbines	Consumer participation percentage
1	250	9+90=99	$n = 10$ $i = 10\%$	2878713513	10	10
2		27+90=117	$n = 30$ $i = 10\%$	2711209422	30	10
3		18+180=198	$n = 20$ $i = 20\%$	3541154965	20	20
4		27+180=207	$n = 30$ $i = 20\%$	3498372560	30	20
5		45+180=225	$n = 50$ $i = 20\%$	3426020585	50	20
6		27+270=297	$n = 30$ $i = 30\%$	4041727163	29	24.4
7		45+270=315	$n = 50$ $i = 30\%$	3933851414	47	23
8		9+270=279	$n = 10$ $i = 30\%$	4294743428	9	26
9		18+270=288	$n=20$ $i=30\%$	4295942587	16	26.11

Table 8: EENS results considering wind turbines and demand response.

Generator exited	Capacity outed (MW) = C_i	$EENS_1$	$EENS_2$	$EENS_3$	$EENS_4$	$EENS_5$	$EENS_6$	$EENS_7$	$EENS_8$	$EENS_9$	$EENS_{10}$ (MWh) $= t_i$ $* \sum_{i \in S} c_i p_i$	$EENS_i \leq EENS_{max}$
A	A (No exit gen)=248	19.14	16.06	2.92	2.22	1.08	0.056	0	0.0002	0.0016	44.064	
A,G ₁	G ₁ =202	23.51	20.18	5.70	4.88	3.52	2.12	1.96	1.97	1.98	50.109	
A,G ₁ ,G ₂	G ₂ =200	25.62	22.18	7.04	6.17	4.70	3.12	2.9	2.92	2.94	53.044	
A,G ₁ ,G ₂ ,G ₃	G ₃ =250	26.99	23.48	7.99	7.09	5.56	3.88	3.63	3.65	3.67	54.839	$EENS_i \leq 4MWh$

Table 9: Comparison table of the results of the participation of the number of wind turbines next to the participation of the consumer, considering the total costs for improving the adequacy of the electricity generation system (Based on the new cost of consumer participation).

Scenario	$P_{gen_{max}}$ (MW) $P_{gen_{max}}$ (MW) $\leq P_{maximum\ contribution}$	$P_{maximum\ contribution}$ (MW) $= (n \times P_{wt}) + (DR_{level_i} \times$ $Load_{peak})$ Acc. to (12) and (13)	The maximum number of turbines (n) and the maximum load participation percentage (i)	total cost	Number of wind turbines	Consumer participation percentage
1	250	27+270=297	$n = 30$ $i = 30\%$	2486809821	29	25.4
2		45+270=315	$n = 50$ $i = 30\%$	2279302873	46	23
3		9+270=279	$n = 10$ $i = 30\%$	2551641219	9	26
4		18+270=288	$n=20$ $i=30\%$	2573663747	18	26

Table 10: EENS results considering wind turbines and demand response (Based on the new cost of consumer participation).

Generator exited	Capacity outed (MW) = C_i	$EENS_1$	$EENS_2$	$EENS_3$	$EENS_4$	$EENS_5$ (MWh) = $t_i * \sum_{i \in S} c_i p_i$	$EENS_i \leq EENS_{max}$
A	A (No exit gen)=248	0.0	0.06	0.05	0.0	44.064	
A,G ₁	G ₁ =202	1.93	2.15	2.13	1.92	50.109	
A,G ₁ ,G ₂	G ₂ =200	2.86	3.15	3.13	2.84	53.044	
A,G ₁ ,G ₂ ,G ₃	G ₃ =250	3.58	3.91	3.89	3.56	54.839	$EENS_i \leq 4MWh$

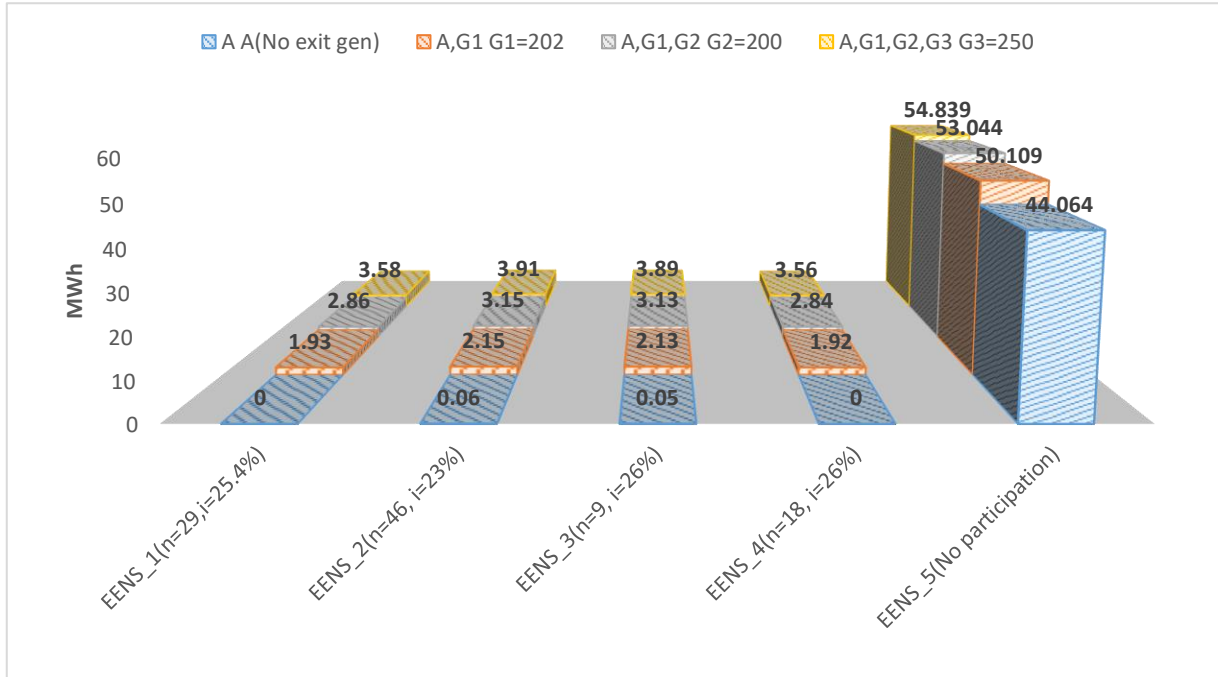


Fig. 6: EENS results for different modes (Based on the new cost of consumer participation).

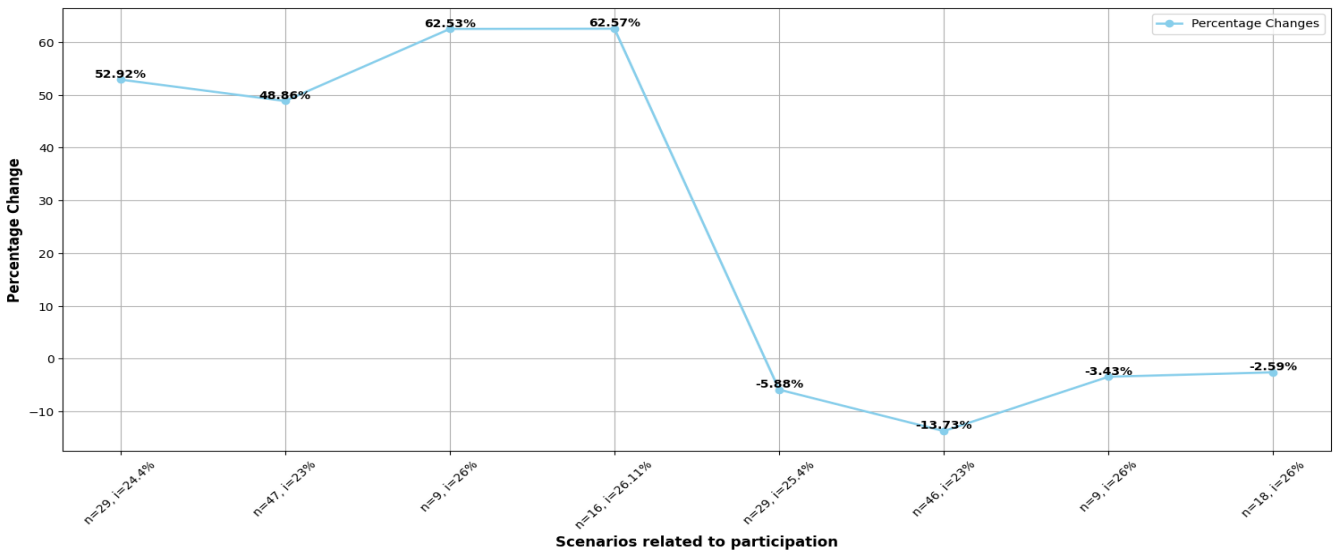


Fig. 7: Comparing the results of the participation costs of the proposed GEP model with the EENS cost in the non-participation mode in a year.

4. Conclusions

In this article, a proposed GEP model has been utilized to enhance network adequacy in the current and short-term periods. Therefore, in this regard, considering Table 6 where

the consumer participation cost exceeds the wind turbine installation cost, and furthermore, the maximum power of consumer participation exceeds the total power of wind turbines in the wind power plant by 83%, the results should favor maximal wind turbine participation, given their lower

costs, compared to maximal consumer participation. The impact of these higher costs and increased consumer power can be observed in Tables 7 and 8. where scenarios of participation that meet the condition ($EENS_i \leq 4\text{MWh}$) are depicted, however, the costs in these participations, as shown in Fig. 7, are high. In order to ensure profitability in the production sector, the consumer participation cost has been reduced by 42.5%. The results obtained in Tables 9 and 10 indicate that the condition ($EENS_i \leq 4\text{MWh}$) has been met, as shown in Fig. 6. The associated costs are shown in Fig. 7, which demonstrate a reduction compared to the EENS cost in a year without participation. The optimal participation mode, as determined by the proposed GEP model while considering the condition ($EENS_i \leq 4\text{MWh}$) with minimum cost within the range ($n=46, i=23\%$), results in a 13.73% reduction in participation cost compared to the EENS cost in a year without participation.

CREDIT AUTHORSHIP CONTRIBUTION STATEMENT

Hamid Reza Safa: Conceptualization, Data curation, Formal analysis, Methodology, Software, Writing - original draft. **Ali Asghar Ghadimi:** Conceptualization, Investigation, Project administration, Supervision, Validation, Writing - review & editing. **Mohammad Reza Miveh:** Conceptualization, Funding acquisition, Resources, Validation, Visualization, Writing – original draft.

DECLARATION OF COMPETING INTEREST

The authors declare that they have no known competing financial interests or personal relationships that could have appeared to influence the work reported in this paper. The ethical issues; including plagiarism, informed consent, misconduct, data fabrication and/or falsification, double publication and/or submission, redundancy has been completely observed by the authors.

References

- [1] M. Shirvani, A. Memaripour, M. Abdollahi, and A. Salimi, "Calculation of generation system reliability index: Expected energy not served," *Life Sci. J.*, vol.9, no.4, pp.3443-3448, 2012.
- [2] H. Seifi, and M. S. Sepasian, "Electric power system planning: issues, algorithms and solutions," *Berlin: Springer*, Vol. 49, 2011.
- [3] O. H. Abdalla, M. A. A. Adma, and A. S. Ahmed, "Generation expansion planning considering high share renewable energies uncertainty," *In 2019 21st International Middle East Power Systems Conference (MEPCON). IEEE*, pp.1-7, December, 2019.
- [4] S. Nolan, and M. O'Malley, "Challenges and barriers to demand response deployment and evaluation," *Applied Energy*, vol.152, pp.1-10, 2015.
- [5] A. H. Shojaei, A. A. Ghadimi, M. R. Miveh, F. Mohammadi, and F. Jurado. "Multi-objective optimal reactive power planning under load demand and wind power generation uncertainties using ϵ -constraint method," *Applied Sciences*, vol.10, no.8, p.2859, 2020.
- [6] P. Paliwal, N. P. Patidar, and R. K. Nema, "A novel method for reliability assessment of autonomous PV-wind-storage system using probabilistic storage model," *International Journal of Electrical Power & Energy Systems*, vol.55, pp.692-703, 2014.
- [7] S. A. Alavi, V. Ilea, A. Saffarian, C. Bovo, A. Berizzi, and S. G. Seifossadat, "Feasible islanding operation of electric networks with large penetration of renewable energy sources considering security constraints," *Energies*, vol.12, no.3, p.537, 2019.
- [8] D. Sloot, N. Lehmann, and A. Ardone, "Explaining and promoting participation in demand response programs: the role of rational and moral motivations among German energy consumers," *Energy Research & Social Science*, vol.84, p.102431, 2022.
- [9] A. H. Shojaei, A. A. Ghadimi, M. R. Miveh, F. H. Gandoman, and A. Ahmadi, "Multiobjective reactive power planning considering the uncertainties of wind farms and loads using information gap decision theory," *Renewable Energy*, vol.163, pp.1427-1443, 2021.
- [10] R. Billinton, and R. N. Allan, *Reliability evaluation of engineering systems*, New York: Plenum press, p.281, 1992.
- [11] R. Billinton, and R. N. Allan, "Power-system reliability in perspective," *Electronics and Power*, vol.30, no.3, pp.231-236, 1984.
- [12] J. Oteng-Adjei, A. M. I. Malori, and E. K. Anto, "August. Generation system adequacy assessment using analytical technique," *In proc. 2020 IEEE PES/IAS PowerAfrica*, pp.1-5, 2020.
- [13] W. Li, "Reliability assessment of electric power systems using Monte Carlo methods," *Springer Science & Business Media*, 2013.
- [14] A. Haseeb, M. M. Ashraf, and A. Arshad, "Emission constrained generation expansion planning considering site-dependent renewable energy sources of Pakistan," *In Proc. 2023 International Conference on Emerging Power Technologies (ICEPT), IEEE*, pp.1-6, May, 2023.
- [15] L. Baringo, M. Carrión, and R. Domínguez, "Generation expansion planning considering renewable energies, in *Electric Vehicles and Renewable Generation: Power System Operation and Planning Under Uncertainty*," Cham: Springer International Publishing, pp. 335-386, 2023.
- [16] X. Wei, D. Liu, S. Ye, F. Chen, J. Weng, "Optimal sizing of energy storage in generation expansion planning of new power system with high penetration of renewable energies," *Energy Reports*, vol.9, pp.1938-1947, 2023.
- [17] A. A. Ghadimi, A. Ahmadi, and M. R. Miveh, "Multiobjective stochastic power system expansion planning considering wind farms and demand response," *International Journal of Energy Research*, article 9962745, 2024.
- [18] T. K. Vrana, and E. Johansson, "Overview of analytical power system reliability assessment techniques," in *Proceedings of the CIGRE Symposium*, Recife, Brasil, pp.3-6, 2011.
- [19] M. Joung, and J. Kim, "Assessing demand response and smart metering impacts on long-term electricity market prices and system reliability," *Applied Energy*, vol.101, pp.441-448, 2013.

[20] S. Rezaei, and A. Ghasemi, "Optimal day-ahead scheduling of a chp and renewable resources-based energy hub with the aim of improving resiliency during input energy carriers' outage," *Journal of Applied Research in Electrical Engineering*, vol.1, no.1, pp.93-111, 2022.

[21] V. Guerrero-Mestre, M. Poncela, and G. Fulli, J. Contreras, "A probabilistic analysis of power generation adequacy towards a climate-neutral Europe," *Energy Reports*, vol.6, pp.3316-3333, 2020.

[22] M. A. J. Alsaedi, H. J. Jabir, and B. M. Albaker, "Load shifting impact on generating adequacy assessment during peak period," *Indonesian Journal of Electrical Engineering and Computer Science*, vol.25, no.3, pp.1217-1226, 2022.

[23] Y. Zhou, P. Mancarella, and J. Mutale, "Generation adequacy in wind rich power systems: Comparison of analytical and simulation approaches," in *Proc. 2014 International Conference on Probabilistic Methods Applied to Power Systems (PMAPS)*, IEEE, pp. 1-6, July, 2014.

[24] C. Carrillo, J. Cidrás, E. Díaz-Dorado, A. F. Obando-Montaño, "An approach to determine the Weibull parameters for wind energy analysis: The case of Galicia (Spain)," *Energies*, vol.7, no.4, pp.2676-2700, 2014.

[25] V. Sohoni, S. C. Gupta, and R. K. Nema, "A critical review on wind turbine power curve modelling techniques and their applications in wind based energy systems," *Journal of Energy*, vol.2016, no.1, article 8519785, 2016.

[26] M. C. Mabel, R. E. Raj, and E. Fernandez, "Adequacy evaluation of wind power generation systems," *Energy*, vol.35, no.12, pp.5217-5222, 2010.

[27] A. A. Ghadimi, M. Amani, M. Bayat, S. Ahmadi, M. R. Miveh, F. Jurado, "Stochastic transmission expansion planning in the presence of wind farms considering reliability and N-1 contingency using grey wolf optimization technique," *Electrical Engineering*, vol.104, no.2, pp.727-740, 2022.

[28] D. Jiang, C. Peng, Z. Fan, Y. Chen, and X. Cai, "Modified binary differential evolution for solving wind farm layout optimization problems," in *Proc. 2013 IEEE Symposium on Computational Intelligence for Engineering Solutions (CIES)*, 2013, pp. 23-28.

[29] L. Wang et al., "Different approaches of applying single-objective binary genetic algorithm on the wind farm design," in *World Congress on Engineering Asset Management*, 2014.

Biography



Hamid Reza Safa received his M.Sc. degree from Arak University in 2023. He is currently a research assistant in the field of power electrical engineering at Arak University. His research interests are Machine and Deep learning, System optimal planning, Renewable Energy, power system protection and FACTS devices.



Ali Asghar Ghadimi received his M.Sc. and Ph.D. degrees in Power Engineering from Tehran Polytechnic University, Tehran, Iran in 2002 and 2008 respectively. He is currently Associate Professor and research member in the Department of Electrical Engineering at Arak University, Arak, IRAN. His current research interests are in the areas of MicroGrid, Renewable Energy, and

Power system optimal planning.



Mohammad Reza Miveh received his Ph.D. degree in Electrical Engineering from Universiti Teknologi Malaysia (UTM), Malaysia in 2017. Currently, he is an Assistant Professor with the Department of Electrical Engineering, at Tafresh University, Iran. His main research interests include the control and protection of large-scale hybrid AC/DC grids, distributed generation, and microgrids.

Copyrights

© 2024 Licensee Shahid Chamran University of Ahvaz, Ahvaz, Iran. This article is an open-access article distributed under the terms and conditions of the Creative Commons Attribution –NonCommercial 4.0 International (CC BY-NC 4.0) License (<http://creativecommons.org/licenses/by-nc/4.0/>).





Iranian Association of
Electrical and Electronics
Engineers

Journal of Applied Research in Electrical Engineering

E-ISSN: 2783-2864

P-ISSN: 2717-414X

Homepage: <https://jaree.scu.ac.ir/>



Research Article

Reliability Evaluation of Power Systems Including Pumped-Storage Generation Units

Amir Ghaedi ^{1,*} , and Mehrdad Mahmoudian ² 

¹ Department of Electrical Engineering, Dariun Branch, Islamic Azad University, Dariun, Iran

² Department of Electrical Engineering, Apadana Institute of Higher Education, Shiraz, Iran

* Corresponding Author: amir.ghaedi@miau.ac.ir

Abstract: In recent years, energy storage systems are increasingly used in power systems to store electricity when the generated power is more than the required load. The advantages of the energy storage systems in the power system include improved reliability, energy storage in non-peak times and production in peak times that results in the peak reduction of the power system, storage at times of low electricity prices, and generate at times of high electricity prices, and storage of the surplus production capacity of renewable energy resources such as wind turbines and photovoltaic systems that their production is not controllable. Among different energy storage systems, pumped-storage generation units can be integrated into electricity networks with high-energy storage capacity and no environmental effects. For this purpose, in this research, the adequacy assessment of power systems, including pumped-storage generation units, is studied. At first, the paper develops a reliability model for these energy storage systems considering the failure of composed components, including the motor-generator, pump-turbine, control, protection, and measurement systems, turbine housing, water channel, up and down reservoir, and transformer. To consider the effect of pumped-storage generation plants on the reliability of the power system, the load duration curve of the system is modified. Then, the proposed model is implemented for assessing the adequacy of power systems, considering the effect of generation and transmission networks using an analytical method through the contingency analysis technique. To study the effectiveness of the suggested reliability model, numerical results related to the reliability assessment of RBTS and IEEE-RTS are presented. It is concluded from numerical outcomes that pumped storage power plants can improve the reliability indices of the power systems. By integrating the understudied pumped storage generation unit into RBTS, the system load can increase up to 15 MW.

Keywords: Contingency analysis, load duration curve, pumped-storage power plant, reliability, transmission system.

Article history

Received 6 February 2024; Revised 6 June 2024; Accepted 24 June 2024; Published online 23 October 2024.

© 2024 Published by Shahid Chamran University of Ahvaz & Iranian Association of Electrical and Electronics Engineers (IAEEE)

How to cite this article

A. Ghaedi, and M. Mahmoudian, "Reliability evaluation of power systems including pumped-storage generation units," *J. Appl. Res. Electr. Eng.*, vol. 3, no. 1, pp. 110-119, 2024. DOI: [10.22055/jaree.2024.46072.1107](https://doi.org/10.22055/jaree.2024.46072.1107)



1. INTRODUCTION

When power system is operated, generated power should be equal to required load for setting frequency of electricity generated within the allowable range. If generated power is more than required demand, frequency of generated electricity increases and so some of generated power of the conventional power plants should be reduced, or generated power of renewable generation units such as photovoltaic systems and wind farms should be wasted. If generated power of power system is less than required load, some of loads must

be curtailed. To solve this problem, energy storage devices can be used in power systems to store surplus generated power from power plants, especially renewable resources whose output is not controllable. These stored energies can then be used during times when generated power is less than the required load. This leads to a reduction in power fluctuations in the system. Other benefits of the energy storage systems in power system include: reliability of power system is increased, energy storage systems can store the electricity at low costs during off-peak times and sell at high costs during peak times, which are both economically viable

and lead to peak reduction of the power system. Among different energy storage systems including batteries, capacitors, water electrolysis device -hydrogen tank- fuel cell system, flywheels, compressed air system, super magnets and pumped-storage systems, pumped-storage generation units can be integrated into power system with high-energy storage capacity. For this purpose, in the current research, impact of pumped-storage generation plants on power system reliability is examined.

For studying impact of pumped-storage systems on different aspects of power system, many researches have been performed. In [1], scheduling plan of a system containing wind units, photovoltaic system and pumped-storage generation unit is performed. In the proposed system, penetration level of renewable energies especially pumped-storage plant is significant and its voltage is extra high level. This paper studied different uncertainties including generated power of wind and photovoltaic units and operating range constraint related to pumped-storage units. Paper [2] proposes an approach for energy management of a hybrid system including wind turbines and pumped-storage generation unit to evaluate economic aspect related to this device. This paper studies economic feasibility related to integration a wind unit into a system containing a pumped-storage generation unit to convert existing system to hybrid system composed of wind and hydro power plants. Reference [3] studies a pumped-storage generation unit with variable speed to determine required reserve of system. To this end, mixed-integer linear programming method considering energy loss of power electronic converters is proposed. Paper [4] studies different electrical converters utilized in pumped-storage generation units with variable speed, especially partial-scale converters used in double fed induction machines. In this research, the topologies, problems and future development of these devices are investigated. In [5], pumped-storage generation plant is used for maximizing generated energy of wind farms in the power systems with transmission constraints. In this paper, transmission congestion and wind power curtailment arisen from mismatch of wind unit and required load are considered. For minimizing the wind power curtailment, pumped-storage generation unit is proposed in the paper. In [6], the characteristics of double fed pumped-storage generation unit with variable speed are performed. This technology is applied to regulate the grid power fluctuations arisen from the renewable resources. In this paper, topology of double fed pumped-storage generation plant is introduced and mathematical presentation associated to plant components is developed. Paper [7] studies operation of pumped-storage generation units at short-circuits conditions. To this end, this paper proposes mixed integer programming method to study the plant at short circuit conditions. Paper [8] studies dynamic characteristics of islanded power systems equipped to pumped-storage generation plants with high penetration level of renewable energies. In the research, understudied pumped-storage generation unit is equipped with Pelton turbines and pumps with fixed speed. In [9], current status of pumped-storage generation units installed in China are studied. In this research, different advantages of these systems are reviewed. In [10], a chronological production simulation platform used for planning of pumped-storage generation plants in power system containing wind units is described. In this research, a unit commitment module is used to simulate daily dispatch

related to different kinds of plants, and then, a simulation of the wind farms operation is interconnected to the unit commitment module to consider its variability impact on daily dispatch program. Paper [11] performs a feasibility study to construct a pumped storage generation plant using abandoned mines. In this research, the natural conditions, mine conditions, safety conditions, economic benefits, resource utilization, ecological restoration and population resettlement of pumped storage plant constructed using Shitai mine are investigated. In [12], multi-method combination site selection of pumped storage generation unit is performed, taking into account the power structure optimization. In this paper, a systematic assessment index system of pumped storage generation unit site selection is developed from power grid expansion planning, economic and environmental benefits, hydrological, topographical, and geological and construction conditions. Paper [13] presents nonlinear modeling and operation stability of pumped storage generation unit based on the variable speed technology. For this purpose, basic equations of variable speed pumped storage power plant are developed. To determine dynamic response of variable speed pumped storage power plant, nonlinear state equation in the form of reactive deviation value considering supplementary conditions is derived. In [14], influencing factors associated with modification potential of abandoned coal mine into pumped storage generation unit is analyzed. According to the principle of pumped storage power plant and the characteristics of coal mine roadway conditions, an analytical hierarchy process is utilized in this paper to assess the main influencing factors including elevation difference between the upper and lower basins, basins capacity, roadway surrounding rock stability, and roadway permeability. Paper [15] presents the prospect of new pumped storage generation unit. In this paper, a new type of pumped storage power plant based on the variable speed technology with faster response speed, wider regulation range and better stability is proposed. Paper [16] studies developments and characteristics of pumped storage generation units constructed in China. In this paper, the current development status of the pumped storage generation unit in some different countries, especially in China, based on their own economic loads and network characteristics are introduced. In [17], the operation of pumped storage generation unit is optimized to boost the absorbability of power grid to the renewable energy. In this research, a novel optimization operation framework for a pumped storage generation unit driven by peak-shaving and valley-filling operation is proposed to boost the power system absorbability to renewable energy inputs. Paper [18] analyzes the coupling mechanisms of the pumped storage generation unit and the eco-environment. For this purpose, the fuzzy comprehensive assessment of the cloud model is established, and the economic model is used to evaluate the influence factors. Paper [19] performs an optimal dispatching of a power system containing wind turbines, photovoltaic systems and mine pumped storage generation units. In this paper, the pumped storage generation units are considered to be utilized from Lingxin coal mine located in Ningxia province of China. The genetic algorithm-dog log optimization method is utilized to minimize the operation cost of the system based on the underground reservoir of mine. In [20], load frequency control of pumped storage generation unit is performed based on the second-order linear active disturbance rejection control

strategy. In this paper, the load frequency model of the two-area reheats steam turbine under nonlinear conditions such as governor dead zone and generation rate constrains is developed.

In the current research, reliability assessment of power systems containing pumped-storage generation plants, considering impact of transmission network, is performed. To this end, the contributions of the research would be as follows:

- Reliability modeling of pumped storage power plants considering failure of composed components is performed.
- A new technique based on the load duration curve modification is introduced for reliability analysis of the power system containing pumped storage power plant.
- Reliability assessment of power system containing pumped storage power plant in HLI and HLII is performed.

According to the aims of the paper, its organization would be as follows: in the second section, structure of pumped-storage generation plants is described. In third section, reliability model of these units is developed, and section four studies adequacy of the power system containing pumped-storage generation plant. Adequacy assessment of RBTS and IEEE-RTS including pumped-storage power plants are presented in 5th section. The last section of the paper is devoted on the research conclusion.

2. PUMPED-STORAGE POWER PLANTS

Fig. 1 presents topology of a typical pumped-storage generation unit. Pumped-storage generation plant includes the lower and upper reservoirs that are usually found naturally in nature and if these reservoirs want to be made artificially, they have to cost a lot. A channel called the penstock is made to transfer the water between lower and upper reservoirs. When the generated power exceeds the required load during off-peak times, the cost of electricity is cheaper, and the generator-motor machine acts as a motor, consuming the excess electricity. In this condition, water moves from lower basin to upper basin by pumping. If the generated power is less than the required load during peak times, the cost of electricity increases, prompting the release of water from the upper basin to rotate the turbine. Thus, turbine and consequently generator turns to generate electricity. Generated power is transmitted to the main grid using of the transformer.

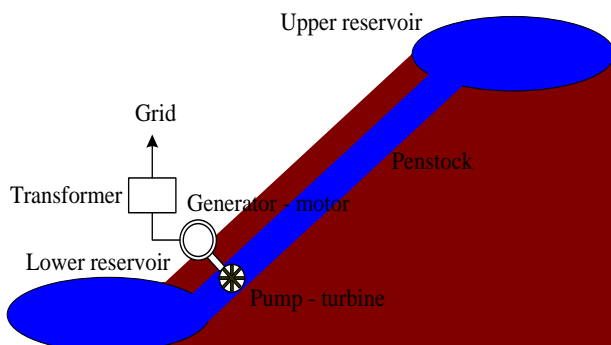


Fig. 1: The structure of pumped-storage generation plant.

Thus, main components of a typical pumped storage generation units are upper and lower reservoirs, the penstock, turbine house, pump – turbine, motor – generator, control-protection and measurement systems and transformer. The pump – turbine and the generator – motor can be a single device that they can be rotated in two directions. It is possible to use from the independent motor and generator, and also independent pump and turbine in the pumped-storage power plants. Different electrical and mechanical losses including the friction of the penstock wall, the friction of the pump, the copper and the stray losses of motor lead the efficiency of the pumped-storage power plant to be less than 100% and so, the electrical power consumed by the motor for pumping water from lower reservoir to upper basin is more than power generated by generator.

3. RELIABILITY MODEL OF PUMPED-STORAGE GENERATION PLANTS

This section develops a reliability model for pumped storage generation plants considering failure of composed components. All components of pumped-storage generation plant including upper and lower reservoirs, penstock, pump – turbine, motor – generator, control – protection and measurement devices and transformer are presented through Markov model with two states as shown in Fig. 2. The proposed model consists of up and down states. Failure rate (λ) presents transition rates from up to down states, and repair rate (μ) presents rate of transitions from down to up states. Availability (A) and unavailability (U) of each component of pumped-storage generation unit can be obtained as [21]:

$$A = \frac{\mu}{\lambda + \mu}, U = 1 - A \tag{1}$$

Failure of each component of pumped-storage generation unit leads transferring water from lower basin to upper basin, rotation of turbine, the electric power generation, or transmitting the generated power to the grid fail and so, if one or more components fails, the electric power of pumped-storage generation unit transmitted to main grid is zero. Thus, in the reliability modeling of plant, all composed components of pumped-storage generation unit as presented in Fig. 3, are series.

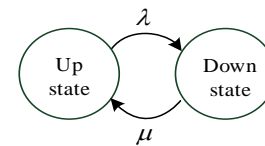


Fig. 2: 2-State Markov model of plant components.

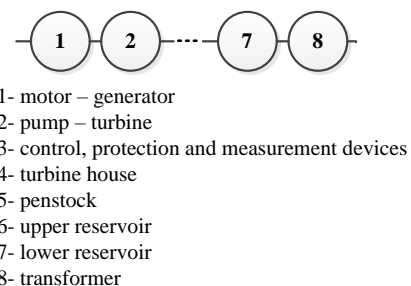


Fig. 3: Reliability model of pumped-storage generation unit considering failure of composed components.

Equivalent failure and repair rates of reliability model of pumped storage generation unit is calculated as [21]:

$$\lambda_{eq} = \sum_{k=1}^8 \lambda_k \tag{2}$$

$$\mu_{eq} = \frac{\lambda_{eq}}{\sum_{k=1}^8 \mu_k} \tag{3}$$

where, λ_{eq} is equivalent failure rate of model, λ_k is failure rate of composed components, μ_{eq} is equivalent repair rate and μ_k is repair rate of composed components. In a power system including N pumped storage generation units, reliability model of these N pumped storage generation units can be presented as Fig. 4. Probability of state k associated to this model including $N+1-k$ up units can be calculated as:

$$P_k = \binom{N}{N+1-k} A^{N+1-k} U^{k-1} \tag{4}$$

4. ADEQUACY ANALYSIS OF POWER SYSTEMS CONTAINING PUMPED-STORAGE GENERATION UNITS

Reliability of power system is defined as providing required load of the power system according to the associated standards. Two aspects of power system reliability are adequacy and security. In adequacy analysis of power system, adequate facilities must be provided for supplying required load. In security studies of power system, response of the power system to various disturbances such as outages of power plants is investigated. Reliability analysis related to power system can be performed in three hierarchical levels. They are reliability study of the generation part (HLI), reliability evaluation of generation and transmission parts (HLII) and reliability assessment of three sections of power system including generation, transmission and distribution parts (HLIII). This paper introduces proposed techniques used for studying power system adequacy in HLI and HLII.

4.1. Adequacy Assessment of Power System Including Pumped-Storage Generation Unit in HLI

For adequacy assessment of power system containing pumped-storage generation plants in HLI, as presented in Fig. 5, all power plants and total load of system are connected to common bus. In this level, reliability of transmission network is considered to be 100% and failure of transmission network is neglected. The model of power plants is presented by capacity outage probability table (COPT). In COPT associated with each unit, capacity and related probability of all possible states are determined. By combining COPTs of different power plants, total COPT of system is constructed. Demand is presented by load duration curve that is a line extended from maximum to minimum peak load during the studied horizon time. By convolving the models of power

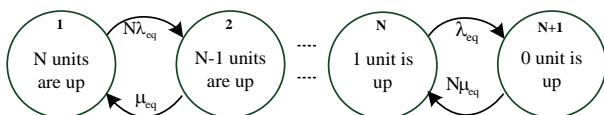


Fig. 4: Reliability model of N pumped storage generation units.

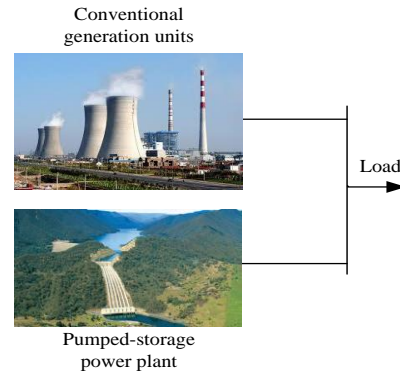


Fig. 5: Adequacy assessment of power system including pumped-storage generation plant in HLI.

plants and demand, reliability indices of power system are obtained. These reliability indices are average times that load is curtailed (loss of load expectation - LOEE) and average energy that is not provided (expected energy not supplied - EENS). Fig. 6 presents load duration curve of the system. For determining power system reliability indices, each state of total COPT is selected and reliability indices associated to each state can be calculated. Then, reliability indices of the power system are obtained by summing these reliability indices weighted by the related probabilities as equations (5) and (6).

$$LOLE = \sum_{i=1}^n t \times P_i \text{ hours/year} \tag{5}$$

$$EENS = \sum_{i=1}^n ENS_i \times P_i \tag{6}$$

where, t and ENS_i are time of year that system load is curtailed and energy of system that is not supplied related to state with generation capacity i and probability P_i . Other reliability indices are peak demand that system can provide (peak load carrying capability - PLCC) and difference in peak demand that system can provide (increase in peak load carrying capability - IPLCC). PLCC is maximum peak load that power system can provide, so that reliability remains in permissible range. IPLCC is amount of increased peak load with addition of new power plant, so that reliability remains in permissible range.

In this part, the impact of pumped storage power plant on the reliability performance of power system is studied. The charging and discharging of storage depends on time and availability of water, which is not independent from load variations. Thus, to accurately study the reliability of power system containing pumped storage power plant, input data including hourly load, hourly generated power of all power plants, and hourly operation of pumped storage power plant in motor or generator states are required. However, in the best case, when the impact of pumped storage power plant on the reliability of power system is maximum, the operation of pumped storage power plant would be as below: the pumped storage power plant acts as load in minimum load to pump water from lower reservoir to the upper reservoir, and acts as generator in maximum load to generate electricity through releasing water from upper reservoir to the lower reservoir.

Thus, in this research, to consider the impact of pumped-storage generation unit on reliability of power system, load duration curve is modified as presented in Fig. 7. At low

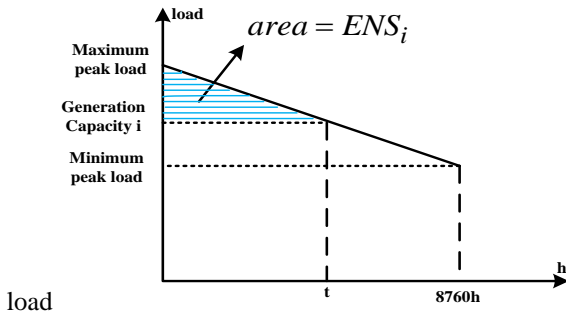


Fig. 6: System load duration curve.

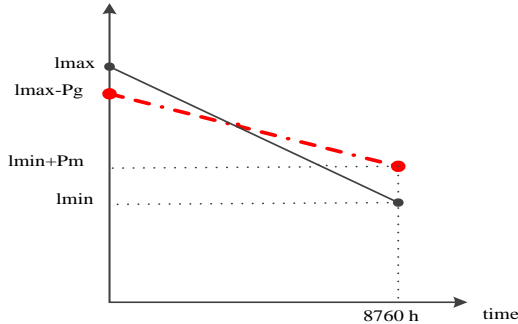


Fig. 7: System load duration curve affected by pumped-storage generation unit in optimal case.

level, pumped storage generation unit acts as a load (the machine acts as a motor and the pump-turbine acts as a pump) that consumes the electric power (P_m) for pumping water from lower reservoir to upper basin. When, load is high, water of upper basin is released and plant acts as a power plant (the machine acts as a generator and the pump-turbine acts as a turbine) that generates the electric power (P_g). In optimal operation of pumped-storage generation unit, plant acts as a load when the load is minimum, and the plant acts as a power plant when the load is maximum. In the current research, optimal operating plan related to pumped-storage generation unit is performed and according to this operation, system load duration curve is modified. Thus, consumed power of pumped-storage generation unit (P_m) is added to minimum load (l_{min}) and the maximum load (l_{max}) is reduced by the amount of generated power of unit (P_g). Efficiency of pumped-storage generation unit is less than 100% and so, value of generated power is less than consumed power of pumped-storage power plant.

Thus, for adequacy analysis of power system containing maximum impact of pumped storage generation plant in HLI, the following procedures should be tracked:

Step. 1. Equivalent failure rate and repair rate of pumped storage generation plant are calculated as (2) and (3).

Step. 2. Capacity outage probability table of all conventional generation units is obtained.

Step. 3. Total capacity outage probability table is obtained by combining all capacity outage probability tables.

Step. 4. Reliability indices of power system without pumped storage generation unit is calculated.

Step. 5. Load duration curve of the system by considering impact of pumped storage generation plant is modified as Fig. 7.

Step. 6. Reliability indices of power system with modified load duration curve is calculated.

Step. 7. To calculate reliability indices of power system containing pumped storage generation plant, the following equation is used:

$$s = s_0U + s_1A \tag{7}$$

In (7), s , s_0 and s_1 are reliability index considering impact of pumped storage generation plant, reliability index without pumped storage generation unit and reliability index considering modified load duration curve, U and A are unavailability and availability of pumped storage generation unit. The flowchart of adequacy analysis of power system containing pumped storage generation unit is presented in Fig. 8.

4.2. Adequacy Assessment of Composite Power System Containing Pumped-Storage Power Plant

To study adequacy of composite power system containing generation and transmission parts, integrated with pumped-storage generation units, contingency analysis approach is proposed. In the current research, power system components such as power plants and transmission lines are modeled by two-state reliability model (with down and up states). Based on this model, composite power systems with n power plants and m transmission lines have 2^{m+n} contingencies. To reduce contingencies associated with large-scale power system, state selection technique is proposed. According to the state selection approach, high-probability contingencies are considered and low-probability contingencies are neglected. In this paper, to analyze different contingencies of the composite power system, DC-type load flow considers transmission lines capacity is implemented. Thus, based on DC-type load flow, each contingency is evaluated. If the contingency makes interruption of load at load points, load shedding program is run for minimizing cost of curtailed loads as (8).

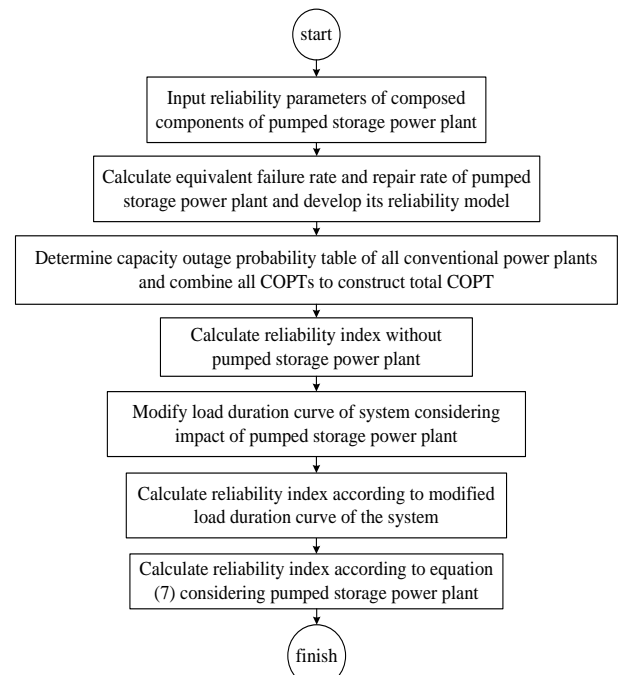


Fig. 8: Flowchart of adequacy analysis of power systems containing pumped-storage generation units in HLI.

$$\text{interrupted load cost} = \sum_{i=1}^n L_i VOLL_i \quad (8)$$

In (8), L_i and $VOLL_i$ are interrupted load and value of lost load in \$/kWh for bus i . For minimizing interrupted loads cost, linear programming approach with interior point method is implemented. Problem constrains includes:

- Balance between generated power and required load minus interrupted load must be established.
- Generated power of all power plants must be within the allowable range.
- The curtailed load must be less than total load of each bus.
- The power transferring by transmission lines must be less than capacity of corresponding line.

According to the proposed approach, adequacy assessment of composite power system containing pumped-storage generation units can be performed. In adequacy evaluation of power system in HLII, load is considered to be constant and equal to maximum value. Thus, to consider the impact of pumped-storage generation plant on the adequacy indices of composite power system, capacity of these units is considered as the generated power of them. In the current research, important reliability indices of composite power system such as probability of interrupted load (Q_s), average time of interrupted load or loss of load expectation ($LOLE$) and average energy not provided or expected energy not supplied ($EENS$) corresponding to load points are determined as:

$$Q_s = \sum_{i=1}^n P_i B_i \quad (9)$$

$$LOLE = \sum_{i=1}^n P_i B_i \times 8760 \quad (10)$$

$$EENS = \sum_{i=1}^n L_i P_i \times 8760 \quad (11)$$

In (10), P_i presents probability related to state i , B_i with 0 and 1 values (0 for events without curtailment and 1 for events lead to load interruption at desired bus). n presents number of contingencies and L_i presents interrupted load at desired load point corresponding to contingency i . Fig. 9 illustrates flowchart for reliability analysis of composite power system containing pumped-storage generation unit.

5. NUMERICAL RESULTS

In this section, numerical outcomes related to adequacy assessment of two power systems including pumped-storage generation units at HLI and HLII are given. To this end, according to the proposed technique, reliability model of understudied pumped-storage generation plant is achieved and used in adequacy analysis of test systems.

5.1. Reliability Modelling of Understudied Pumped-Storage Generation Unit

In this part, a 30MW pumped storage generation unit that generates 120MWh electric energy, and efficiency of 80% is

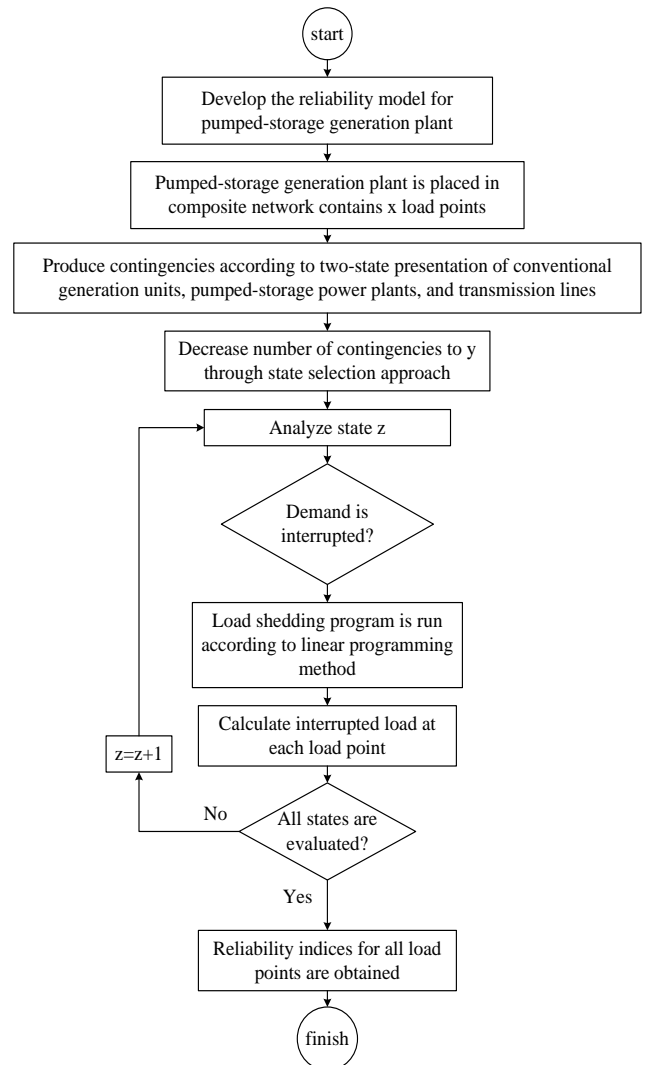


Fig. 9: Flowchart for adequacy analysis of composite power system containing pumped-storage generation units.

Table 1: Failure rate and repair time of composed components of pumped-storage generation unit.

Components	Failure rate (occ./yr)	Repair time (hour)
Upper reservoir	0.25	50
Lower reservoir	0.25	50
Penstock	0.25	50
Turbine house	0.25	50
Pump - turbine	2	100
Generator - motor	1	100
Control, protection and measurement system	0.9	50
Transformer	1	100

considered. Table 1 illustrates failure and repair rates of plant components. Thus, equivalent failure rate and repair time of reliability model of pumped-storage power plant would be 5 failures per year and 80 hours, respectively. Based on (1), availability of pumped-storage power plant would be 0.96.

The efficiency of the plant is 80% and so, the consumed power of the plant when water is transferred from lower basin to upper basin by pumping would be 37.5MW.

5.2. Adequacy Analysis of RBTS

In this part, adequacy analysis of RBTS including mentioned pumped-storage generation unit in HLI and HLII is performed. This test system is shown in Fig. 10. The characteristics of RBTS are given in [22]. Load duration curve is a line continues from 100% to 60% of maximum load.

In this stage, RBTS as Case I and RBTS integrated with understudied pumped-storage generation unit as Case II are studied to calculate adequacy indices including LOLE and EENS of them at HLI for different peak load. The results are illustrated in Figs. 11 and 12, respectively.

PLCC of Case I and Case II provided that expected energy not supplied of system remains less than allowable value is obtained and illustrated in Table 2. IPLCC of system by addition of understudied pumped-storage power plant is obtained and illustrated in Table 3. Numerical results present that pumped-storage generation unit significantly improves reliability indices of power system.

At this stage, adequacy assessment of composite RBTS including pumped-storage generation unit is performed. For reducing number of contingencies, contingencies related to 4 or less power plants failure, 3 or less transmission lines failure and 3 or less power plants or transmission lines failure are investigated. According to the proposed approach, LOLE and EENS related to different load points for initial RBTS are obtained and illustrated in Table 4. As can be seen in the table, the reliability of load point 5 is weak and so, the pumped-storage generation plant should be connected to this load point. According to the proposed method, reliability indices of modified system are obtained and illustrated in Table 5. This table presents that reliability indices of composite power system at bus 5 is improved by addition of the pumped-storage generation unit to this bus.

5.3. Adequacy Analysis of IEEE-RTS

In this part, adequacy assessment of large-scale IEEE-RTS as shown in Fig. 13, including understudied pumped-storage power plant in HLI and HLII is performed. Paper [23] presents characteristics of power plants, transmission lines

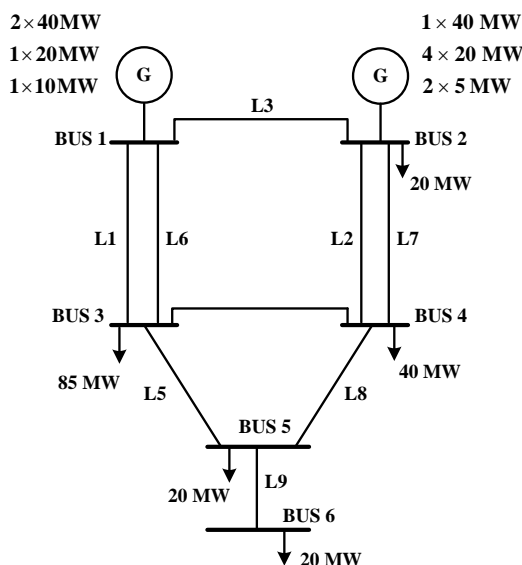


Fig. 10: Roy Billinton Test System (RBTS) [22].

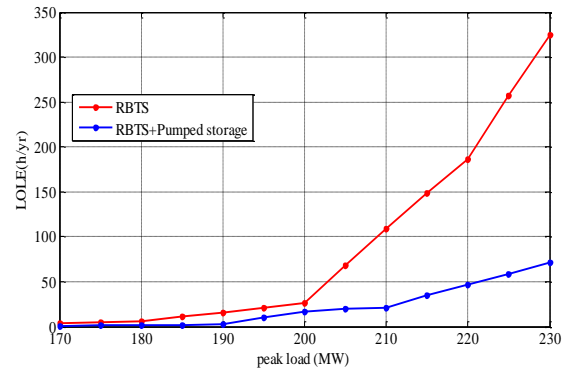


Fig. 11: LOLE for different peak loads.

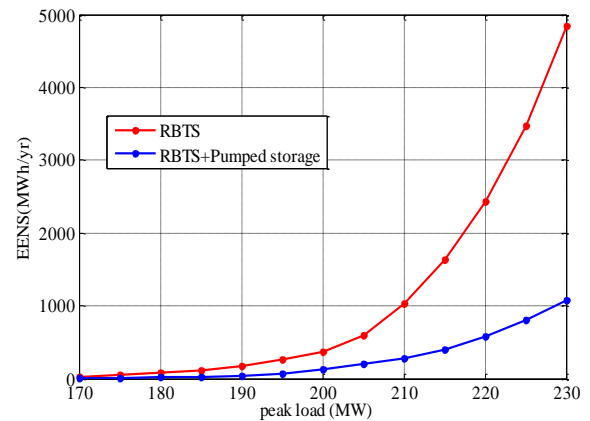


Fig. 12: EENS for different peak loads.

Table 2: PLCC.

Cases / Permissible EENS	100 MWh/yr	200 MWh/yr	300 MWh/yr	400 MWh/yr
Case I	180MW	190MW	195MW	200MW
Case II	195MW	205MW	210MW	210MW

Table 3: IPLCC.

Cases/ Permissible EENS	100 MWh/yr	200 MWh/yr	300 MWh/yr	400 MWh/yr
Case II	15MW	15MW	15MW	10MW

Table 4: Reliability indices of composite RBTS.

Bus	Probability of lost load	LOLE (hrs/yr)	EENS (MWh/yr)
2	0	0	0
3	0.0086	75.34	6403.9
4	0	0	0
5	1.2733e-06	0.01115	0.223
6	0.00113913	9.9787788	199.575576

Table 5: Reliability indices of composite RBTS including the understudied pumped-storage generation unit.

Bus	Probability of lost load	LOLE (hrs/yr)	EENS (MWh/yr)
2	0	0	0
3	0.000363	3.182225	270.5
4	0	0	0
5	1.26E-06	0.011063	0.221
6	0.00113911	9.9786036	199.572072

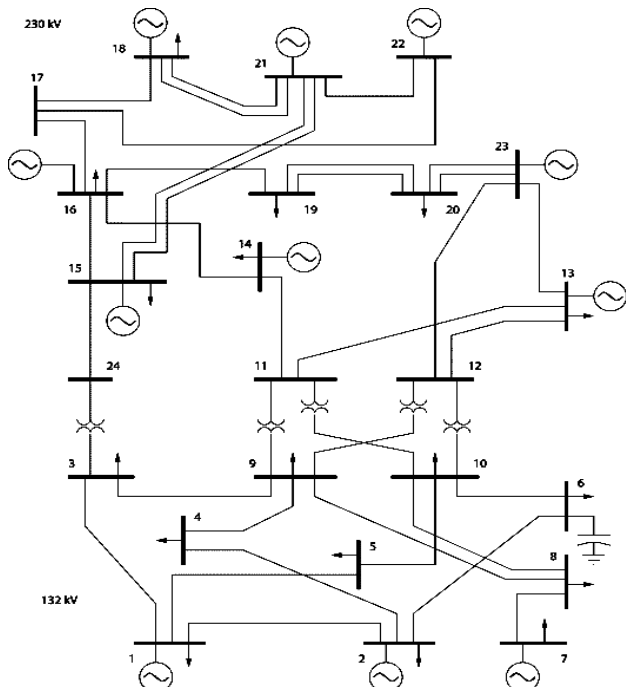


Fig. 13: IEEE Reliability Test System (IEEE-RTS) [23].

and load points of IEEE-RTS. Load duration curve is a line continues 100% and 60% of peak load that is 2850MW. According to the proposed approach, adequacy assessment of IEEE-RTS when different numbers (from 0 to 5) of the understudied pumped-storage power plants are added to it is performed, and different reliability indices including LOLE, EENS, PLCC and IPLCC are calculated and illustrated in Table 6. PLCC and IPLCC of system are obtained when $EENS < 16985 \text{ MWh/yr}$. It is concluded from Table 6 that by addition of pumped-storage power plants, reliability indices of IEEE-RTS improve, significantly.

In this stage, adequacy analysis of composite IEEE-RTS containing pumped-storage generation plant is performed. For reducing number of contingencies, contingencies related to simultaneous failures of up to 2 generation power plants, up to 2 transmission lines and up to 2 generation power plants and transmission lines are taken into account. According to the proposed approach, loss of load probability, loss of load expectation and expected energy not supplied at different load points for initial IEEE-RTS are calculated and illustrated in Table 7. It is deduced from this table that reliability of load point 19 is weak and so, pumped-storage generation plant should be connected to this load point. According to the proposed approach, reliability indices of the modified system are calculated and presented in Table 8. This table presents that reliability indices of the composite power system at load point 19 is improved by addition of pumped-storage generation unit to this load point.

6. CONCLUSION

In the current research, adequacy studies of power system including pumped-storage power units in generation and composite levels of power system are performed. According to the authors' knowledge, reliability of these power plants has not been investigated in any reference. To

Table 6: Reliability indices of IEEE-RTS in HLI.

Number of added plants	LOLE (h/yr)	EENS (MWh/yr)	PLCC (MW)	IPLCC (MW)
0	112.9085	16984	2850	0
1	100.3366	14755	2872	22
2	89.8462	12806	2893	43
3	81.4793	11065	2914	64
4	73.3801	9509	2935	85
5	65.1861	8139	2955	105

Table 7: Reliability indices of composite IEEE-RTS.

Bus	Probability of lost load	LOLE (hrs/yr)	EENS (MWh/yr)
1	0	0	0
2	0	0	0
3	2.35e-7	0.0020586	0.370548
4	4.70e-8	0.0004117	0.030466
5	3.80e-8	0.0003329	0.023636
6	1.86e-7	0.0016294	0.221598
7	0	0	0
8	0	0	0
9	0.0108849	95.3517244	16686.551770
10	0	0	0
13	0	0	0
14	6.01e-8	0.0005265	0.102141
15	0	0	0
16	0	0	0
18	0	0	0
19	0.02198609	192.5981484	34860.264860
20	0	0	0

Table 8: Reliability indices of composite IEEE-RTS including understudied pumped-storage power plant.

Bus	Probability of lost load	LOLE (hrs/yr)	EENS (MWh/yr)
1	0	0	0
2	0	0	0
3	2.25E-07	0.001968	0.35424
4	4.50E-08	0.000395	0.02923
5	3.60E-08	0.000315	0.022365
6	1.78E-07	0.001558	0.211888
7	0	0	0
8	0	0	0
9	0.004573	40.05832	7010.206
10	0	0	0
13	0	0	0
14	5.75E-08	0.000504	0.097776
15	0	0	0
16	0	0	0
18	0	0	0
19	0.021003	183.9865	33301.5565
20	0	0	0

this end, an equivalent two-state reliability model is developed for pumped-storage generation units. This model considers failure of composed components including upper basin, lower reservoirs, penstock, turbine house, motor-generator, pump-turbine, transformer and control, protection and measurement devices. It is concluded from reliability analysis of pumped-storage generation unit that mentioned components makes the plant fails. Thus, in reliability modeling of plant, all components are series. To determine

the impact of pumped-storage generation unit on reliability of power system, load duration curve of system is modified. The minimum load is increased by the amount of consumed power of pumped-storage generation unit and maximum load is reduced by the amount of generated power of the plant. Adequacy studies of generation system is performed through the analytical method based on the COPT of the generation plants and load duration curve of the demand. To perform adequacy analysis of composite power system, contingency analysis methodology is proposed. Besides, for reducing number of contingencies of large-scale composite power system, state selection method is proposed. Numerical outcomes related to the reliability analysis of RBTS and IEEE-RTS conclude that by integration of pumped-storage generation plants into the power system the reliability of power system in both levels, i.e. HLI and HLII, is improved. The reliability of RBTS in load point 5, and IEEE-RTS in load point 19 is weak. By integration the understudied pumped storage power plant into RBTS and IEEE-RTS in these load points, reliability of modified RBTS and IEEE-RTS is improved.

CREDIT AUTHORSHIP CONTRIBUTION STATEMENT

Amir Ghaedi: Conceptualization, Data curation, Formal analysis, Funding acquisition, Investigation, Software, Validation, Writing - original draft. **Mehrdad Mahmoudian:** Methodology, Project administration, Supervision, Visualization, Writing - review & editing.

DECLARATION OF COMPETING INTEREST

The authors declare that they have no known competing financial interests or personal relationships that could have appeared to influence the work reported in this paper. The ethical issues; including plagiarism, informed consent, misconduct, data fabrication and/or falsification, double publication and/or submission, redundancy has been completely observed by the authors.

7. REFERENCES

- [1] M. Xu, M., L. Wu, H. Liu, and X. Wang, "Multi-objective optimal scheduling strategy for wind power, PV and pumped storage plant in VSC-HVDC grid," *The Journal of Engineering*, vol. 2019, no. 16, pp.3017-3021, 2019.
- [2] C. Serrano-Canalejo, R. Sarrias Mina, P. Garcia-Trivino, and L. M. Fernandez-Ramire, "Energy management system design and economic feasibility evaluation for a hybrid wind power/pumped hydroelectric power plant," *IEEE Latin America Transactions*, vol. 17, no. 10, pp. 1686-1693, 2019.
- [3] M. Chazarra, J. I. Pérez-Díaz, and J. Garcia-Gonzalez, "Optimal joint energy and secondary regulation reserve hourly scheduling of variable speed pumped storage hydropower plants," *IEEE Transactions on Power Systems*, vol. 33, no. 1, pp. 103-115, 2017.
- [4] A. Joseph, and T. Raj Chelliah, "A review of power electronic converters for variable speed pumped storage plants: Configurations, operational challenges, and future scopes," *IEEE Journal of Emerging and Selected Topics in Power Electronics*, vol. 6, no. 1, pp. 103-119, 2017.
- [5] M. A. Hozouri, A. Abbaspour, M. Fotuhi-Firuzabad, and M. Moeini-Aghtaei, "On the use of pumped storage for wind energy maximization in transmission-constrained electricity networks," *IEEE Transactions on Power Systems*, vol. 30, no. 2, pp. 1017-1025, 2014.
- [6] Z. Guopeng, Z. Qiang, R. Jiyun, S. Xiaofang, and H. Minxiao, "Modelling and control of doubly fed variable-speed pumped storage units for grid power regulation," *The Journal of Engineering*, vol. 2017, no. 13, pp. 745-750, 2017.
- [7] M. Chazarra, J. I. Pérez-Díaz, and J. García-González, "Optimal energy and reserve scheduling of pumped-storage power plants considering hydraulic short-circuit operation," *IEEE Transactions on Power Systems*, vol. 32, no. 1, pp. 344-353, 2016.
- [8] M. H. Vasconcelos, P. Beires, C. L. Moreira, and J. A. P. Lopes, "Dynamic security of islanded electricity networks with pumped storage power plants for high renewable integration—A study case," *The Journal of Engineering*, vol. 2019, no. 18, pp. 4955-4960, 2019.
- [9] G. Liu, F. L. Zheng, U. F. Xia, L. Kang, and Z. Y. Zhang, "Analysis on operation situation and main functions of pumped-storage power plants in China southern power grid," *The Journal of Engineering*, vol. 2019, no. 16, pp. 2654-2657, 2019.
- [10] N. Zhang, C. Kang, D. S. Kirschen, Q. Xia, W. Xi, Huang, J., Zhang, Q., "Planning pumped storage capacity for wind power integration," *IEEE Transactions on Sustainable Energy*, vol. 4, no. 2, pp. 393-401, 2012.
- [11] X. Lyu *et al.*, "Feasibility study of construction of pumped storage power station using abandoned mines: a case study of the Shitai Mine." *Energies*, vol. 16, no. 1, article 314, 2022:
- [12] L. Ji *et al.*, "Multi-method combination site selection of pumped storage power station considering power structure optimization," *Sustainable Energy Technologies and Assessments*, vol. 49, article 101680, 2022)
- [13] W. Guo, and Z. Daoyi, "Nonlinear modeling and operation stability of variable speed pumped storage power station," *Energy Science & Engineering*, vol. 9, no.10, pp. 1703-1718, 2021.
- [14] D. Shang, and P. Peng, "Analysis of influencing factors of modification potential of abandoned coal mine into pumped storage power station," *Journal of Energy Resources Technology*, vol. 143, no. 11, article 112003., 2021.
- [15] J. Li, Y. Chuanbao, and G. Sujie, "Prospect of new pumped-storage power station," *Global Energy Interconnectio*, vol. 2, no. 3, pp. 235-243, 2019.
- [16] Y. W. Xu, and J. Yang, "Developments and

- characteristics of pumped storage power station in China," in *Proc. IOP Conference Series: Earth and Environmental Science*, vol. 163, no. 1, IOP Publishing, 2018.
- [17] Y. Zhou, Y. Zhu, Q. Luo, Y. Wei, Y. Mei, and F. Chang, "Optimizing pumped-storage power station operation for boosting power grid absorbability to renewable energy," *Energy Conversion and Management*, vol. 299, pp. 117827, 2024.
- [18] S. Li, Y. Hu, and L. Zhang, "Coupling coordination relationship of pumped storage power station and eco-environment system," *Journal of Energy Storage*, vol. 52, article 105029, 2022.
- [19] R Gao *et al.*, "Optimal dispatching of wind-PV-mine pumped storage power station: A case study in Lingxin coal mine in Ningxia province, China," *Energy*, vol. 243, article 123061, 2022.
- [20] K Liu *et al.*, "Load frequency control of pumped storage power station based on LADRC," *Processes*, vol. 8, no. 4, article 380, 2020.
- [21] R. Billinton, R. N. Allan, *Reliability evaluation of electricity networks*. 2nd edition, New York: Plenum Press, 1994.
- [22] R. Billinton *et al.*, "A reliability test system for educational purposes-basic data'," *IEEE Power Engineering Review*, vol. 9, no. 8, pp. 67-68, 1989.
- [23] R. Billinton, and W. Li, *Reliability Assessment of Electric Electricity network Using Monte Carlo*. Plenum Press, New York, 1994.

BIOGRAPHY



Amir Ghaedi was born in 1984 in Kheirabad, a village of Shiraz, and received the M.Sc., and Ph.D. degrees in electrical engineering, power field, from Sharif University of Technology, Tehran, Iran, in 2008, and 2013, respectively. He is currently associate professor in Department of Electrical Engineering, Dariun Branch, Islamic Azad University, Dariun, Iran. His main research interests are the power quality, power system reliability, smart grids, renewable resources and high voltage engineering.



Mehrdad Mahmoudian was born in Iran, in 1990. He received the B.Sc. degree in Electrical Engineering from Shahid Bahonar University, Kerman, Iran, and M.S. degree in Electrical Engineering from Iran University of Science and Technology (IUST), Tehran Iran, in 2012 and 2014 respectively. His research interests include DC/DC Converters, Energy Conversion and Photovoltaic Power System.

Copyrights

© 2024 Licensee Shahid Chamran University of Ahvaz, Ahvaz, Iran. This article is an open-access article distributed under the terms and conditions of the Creative Commons Attribution –NonCommercial 4.0 International (CC BY-NC 4.0) License (<http://creativecommons.org/licenses/by-nc/4.0/>).



Improving the Performance of a VSG in the Distorted Grid Using Third-Order Generalized Integrator Ramin Arjmandzadeh, Mahdi Banejad, Ali Akbarzadeh Kalat	1
Voltage and Frequency Control Considering Disturbance in Input Power of DG Ali Morsagh Dezfuli, Mahyar Abasi, Mohammad Esmaeil Hasanzadeh, Mahmood Joorabian	9
Solving Combined Economic Emission Dispatch Problem Using the Rain Optimization Algorithm Narges Yousefi, Mahmood Joorabian, Mahyar Abasi	19
A New Topological Method for Output Voltage Clamping of Immittance-based Constant Current Load Resonant Converters Alireza Khoshsaadat, Mohammad Abedini	33
Analysis of the Potential of Different Air Conditioner Brands for Piezoelectric Energy Harvesting Daniel Kwegyir, Francis Boafo Effah, Daniel Opoku, Peter Asigri, Yoosi Hayford; Eliezer Owusu Boateng, Kwaku Kessey-Antwi, Nana Maryam Abdul-Bassit Munagah, Kelvin Worlanyo Tamakloe	40
Efficient Responding to Demand and Robust Voltage Control of an Islanded DC Microgrid Under Variations in Load and Supply Sajed Derakhshani Pour, Reza Eslami	51
Conventional DC-DC Converters Through Duality Approach for Current-Based Applications Zahra Gholami, Rahim Ildarabadi, Hamed Heydari-doostabad	64
Consensus-Based Algorithm for Distributed Continuous-Time Convex Optimization Over Undirected and Directed Networks Ehsan Nazemorroaya, Mohsen Shafieirad, Mahdi Majidi, Mahdiah Adeli	74
Improvement of IBC-SHJ Solar Cell Efficiency Based on Back Contacts Geometry Engineering Pegah Paknazar, Maryam Shakiba, Gholamreza Shaloo	83
Demand Response Design for Healthy Operation of Transformers in Heavy-Load and High-Temperature Conditions Arash Moghadami, Davood Azizian, Amin Karimi	90
Assessing Power System Adequacy and Generation Expansion Planning in the Presence of Wind Power Plants Considering Uncertainties in the DIgSILENT Software Environment Hamid Reza Safa, Ali Asghar Ghadimi, Mohammad Reza Miveh	99
Reliability Evaluation of Power Systems Including Pumped-Storage Generation Units Amir Ghaedi, Mehرداد Mahmoudian	110

